

**Experimental Study of Turbulent Natural Convective Condensation In the Presence of
Non-Condensable Gas on Vertical and Inclined Surfaces**

Submitted in partial fulfillment of the requirements for

the degree of

Doctor of Philosophy

in

Mechanical Engineering

Matthew M. Swartz

B.S., Mechanical Engineering, West Virginia University

B.S., Aerospace Engineering, West Virginia University

M.S., Aerospace Engineering, West Virginia University

Carnegie Mellon University
Pittsburgh, PA

May, 2017

© 2017 Westinghouse Electric Company LLC. All Rights Reserved.

Abstract

Experimental Study of Turbulent Natural Convective Condensation In the Presence of Non-Condensable Gas on Vertical and Inclined Surfaces

By

Matthew M. Swartz

Pressurized water reactor nuclear plants, currently under construction, have been designed with passive containment cooling systems. Turbulent, natural-convective condensation, with high non-condensable mass fraction, on the walls of the containment vessel is a primary heat transfer mechanism in these new plant designs. A number of studies have been completed over the past two decades to justify use of the heat and mass transfer analogy for this scenario. A majority of these studies are founded upon natural-convective heat transfer correlations and apply a diffusion layer model to couple heat and mass transfer. Reasonable success in predicting experimental trends for vertical surfaces has been achieved when correction factors are applied. The corrections are attributed to mass transfer suction, film waviness or mist formation, even though little experimental evidence exists to justify these claims.

This work examines the influence of film waves and mass transfer suction on the turbulent, natural-convective condensing flow with non-condensable gas present. Testing was conducted using 0.457 m x 2.13 m and a 0.914 m x 2.13 m condensing surfaces suspended in a large pressure vessel. The test surfaces could be rotated from vertical to horizontal to examine the inclination angle effect. The test facility implements relatively high accuracy calorimetric and condensate mass flow measurements to validate the measured heat and mass transfer rates.

Test results show that application of the Bayley (1955) and Al-Arabi and Sakr (1988) heat transfer correlations using the heat and mass transfer analogy is appropriate for conditions in which the liquid film remains laminar. For transitional and wavy film flows, a clear augmentation in heat transfer was observed due to disruption of the gas layer by film waves. This result has implications for the scalability of existing correlations. A new correlation is proposed and results compared to several other datasets.

Acknowledgement

I would like to express appreciation to my advisor Professor Shi-Chune Yao. Without his guidance and persistent help this dissertation would not have been possible. In addition, I express appreciation to my committee members Professor Alan McGaughey and Professor Sheng Shen for volunteering their time to review my work.

I would like to thank my Westinghouse Electric Company colleagues who supported me throughout this endeavor. Without the help of John Lojek, the design, construction and operation of the pressurized test facility would not have been a success. John acted as a sounding board for many ideas and spent countless hours of his own time helping resolve technical challenges associated with this test program. In addition, Steve Swantner has been a mentor and valuable collaborator. Without Steve's initial advice to pursue my doctorate at Carnegie Mellon University and continued positive reinforcement, I would not have completed this research. Finally, thanks to Bill Turkowski, Tyler Upton and Susan Baier, management at Westinghouse Electric Company, for supporting my research.

I would like to thank my committee member and colleague at Westinghouse Electric Co., Dr. Richard Wright. Rick has acted as a mentor throughout completion of my research and has provided encouragement and motivation to complete this research.

Last but not least, I express deep appreciation to my wife Nichole and two children Graydon and Nygel. Nichole has been my biggest supporter throughout this research, and her understanding and love during this time has made this dissertation possible.

Table of Contents

Abstract	i
Acknowledgement.....	ii
Table of Contents.....	iii
Nomenclature	vi
List of Figures.....	ix
List of Tables.....	x
List of Appendix Figures.....	x
List of Appendix Tables.....	xi
1.0 Introduction.....	1
2.0 Literature Review	5
2.1 Turbulent Natural Convective Condensation Experiments	5
2.1.1 Flat Plate Experiments	5
2.1.2 Cylinder Experiments	7
2.2 Diffusion Layer Theory Model Development	9
2.3 Turbulent Natural Convective Heat Transfer	10
2.3.1 Vertical Surfaces	10
2.3.2 Inclined Surfaces	12
2.4 Influence of Film Waves on Liquid Film Heat Transfer	13
2.5 Influence of Film Waves on Gas Boundary Layer Heat Transfer.....	14
2.6 Summary	15
3.0 Model Description.....	16
3.1 Liquid Film Heat Transfer on the Vertical Plate.....	18
3.2 Gas Diffusion Layer Heat and Mass Transfer	19
3.3 Gas Diffusion Layer Suction Effect.....	22
3.4 Cylindrical Condensing Surfaces.....	23
3.5 Inclined Flat Plate Condensing Surfaces	25
4.0 Experimental Facility	26
4.1 Test Facility Description	26
4.2 Test Article and Cooling Channel Design Details.....	31
4.3 Test Facility Operation.....	37
5.0 Experimental Facility Instrumentation	38
5.1 Test Plate Temperature.....	38
5.2 Tank Environment Conditions	39
5.3 Calorimetric Heat Removal Rate	39
5.4 Collection Tank Mass Flow Rates	39
5.5 Film Applicator Mass Flow Rate and Temperature	40

5.6	Film Thickness.....	40
5.7	Optical Access.....	43
5.8	Inclination Angle Measurement.....	44
5.9	Instrumentation Summary.....	45
6.0	Heat Transfer Coefficient Analysis.....	48
7.0	Experimental Results.....	52
7.1	Test Data Analysis Description.....	55
7.2	Analysis of Vertical Plate Results.....	64
7.3	Analysis of Inclined Plate Results.....	72
8.0	Review of Published Experimental Databases.....	77
8.1	Data Analysis.....	77
8.2	Summary.....	80
9.0	Wavy Film Interface Correction.....	83
10.0	Summary and Conclusions.....	90
11.0	Recommendations for Future Work.....	92
12.0	References.....	94
Appendix A Instrumentation Uncertainty.....		99
A.1	Analog to Digital Conversion.....	99
A.2	Mass Flow Meters.....	99
A.3	Resistance Thermal Detectors.....	100
A.4	Thermocouples.....	101
A.5	Inclinometer.....	101
A.6	Pressure Transducers.....	101
A.7	Summary of Instrumentation Uncertainty.....	102
Appendix B Data Analysis Methodology.....		103
B.1	Gutter and Trough Collection Container Mass Flow Rate.....	103
B.2	Average Condensing Surface Temperature.....	106
B.3	Heat Transfer Rate Analysis Methodology.....	108
B.3.1	Heat Transfer Rate Based on the Calorimetric Balance.....	108
B.3.2	Heat Transfer Rate Based on the Condensate Mass Flow Rate.....	110
B.4	Heat Flux and Heat Transfer Coefficient Analysis Methodology.....	112
Appendix C Analysis of Literature Data.....		113
C.1	Dehbi (1991) Database.....	113
C.2	Kataoka et al. (1994) Database.....	120
C.3	Uchida et al. (1965) Database.....	125
C.4	Tagami (1965) Database.....	127
C.5	Su et al. (2013 and 2014) Database.....	130

C.6	Kim et al. (2009) Database	138
C.7	Liu (1999) Database	143
C.8	Anderson (1998a) Database	144
Appendix D Fluid and Gas Properties.....		148
Appendix E Experimental Results.....		150
E.1	Tabulated Results for 0.457 m Width Plate	150
E.2	Tabulated Results for 0.914 m Width Plate	160
Appendix F Condensation Conductivity Derivation.....		164
Appendix G Average Film Thickness and Wave Velocity Calculation		168

Nomenclature

ACRONYMS

DAS	Data acquisition system
HMTA	Heat and mass transfer analogy
HX	Heat exchanger
IAPWS	International Association for the Properties of Water and Steam
LOCA	Loss of coolant accident
PCS	Passive containment cooling system
PRHR	Passive residual heat removal
PWR	Pressurized water reactor
RCS	Reactor coolant system
SBO	Station blackout
SRSS	Square root sum of squares

VARIABLE DEFINITIONS

A	Area
a_{θ}	Empirically determined inclination angle correction factor
B	Suction parameter
c	Total molar concentration
C_p	Specific heat at constant pressure
D	Binary diffusion coefficient
g	Gravitational acceleration
g_m	Mass transfer coefficient
h	Heat transfer coefficient
i_{fg}	Latent heat of condensation
J	Molar flux
k	Thermal conductivity
L	Length
M	Molecular weight
m	Mass concentration
n	Power law exponent
P	Pressure
q	Heat transfer rate
q''	Heat flux
R	Universal gas constant
R_v	Vapor specific gas constant
R_{air}	Air specific gas constant

R_{N_2}	Nitrogen specific gas constant
T	Temperature
t	Time or total
u	Uncertainty
v_{fg}	Difference between fluid and gas specific volumes
v_v	Vapor molar velocity
W	Weight fraction
x	Mole fraction
z	Distance along condensing surface from top of plate
δ	Boundary layer thickness
γ	Product of diffusion coefficient and density
Γ	Mass flow rate per unit width
μ	Viscosity
π	Pi
φ	Gas / vapor log mean concentration ratio or mixture viscosity parameter
ρ	Density
θ	Inclination angle
θ	Boundary layer suction factor

DIMENSIONLESS GROUPS

Gr	Grashoff number
Ka	Kapitza number
Nu	Nusselt number
Pr	Prandtl number
Sc	Schmidt number
Sh	Sherwood number
Ra	Rayleigh number
Re	Reynolds number

SUBSCRIPTS

avg	Average of log mean
b	Bulk
c	Condensation
dl	Diffusion layer
eff	Effective
f	Film of final
g	Non-condensable gas
i	Interface or initial
l	Latent heat

m	Mass
ref	Reference condition
s	Sensible heat
t	Total
ts	Test surface
v	Vapor
w	Wall

List of Figures

Figure 1-1 AP1000 Passive System Response to Station Blackout Event	2
Figure 3-1 Schematic of Natural Convective Condensation with Non-Condensable Gas Present	17
Figure 3-2 Thermal Network Representing Condensation with Non-Condensable Gas Present.....	17
Figure 4-1 Test Facility Overview	27
Figure 4-2 Overview Image of Test Facility	28
Figure 4-3 Test Facility Piping and Instrumentation Diagram.....	30
Figure 4-4 Air Motor and Gear Box Connection with Test Plate.....	31
Figure 4-5 Cooling Channel Image	32
Figure 4-6 Cooling Plate Assembly Dimensional Detail (Dimensions in Inches).....	33
Figure 4-7 Cooling Channels Assembled on Rear of Test Plate with Coolant Tubing Installed.....	34
Figure 4-8 Insulation Box viewed from Back of Test Plate	35
Figure 4-9 Front Side of Test Plate Installed in Vessel with Insulation Shown on Sides	36
Figure 5-1 Test Plate Surface Temperature Measurement Locations.....	38
Figure 5-2 Chromatic Confocal Film Thickness Measurement Method.....	42
Figure 5-3 View Window Lighting (Left) and Forced Air Heater (Right)	43
Figure 5-4 Inclinometer Housing Installed on 0.914 m Width Plate Shaft	44
Figure 5-5 Inclinometer Housing Design.....	45
Figure 6-1 Comparison of Heat Flux Measurement Methods.....	51
Figure 7-1 Test T456_026 Tank Temperatures	56
Figure 7-2 Test T456_026 Absolute Pressure	57
Figure 7-3 Test T456_026 Cooling Channel Inlet and Outlet Temperatures.....	58
Figure 7-4 Test T456_026 Cooling Channel Mass Flow Rates	58
Figure 7-5 Test T456_026 Gutter Collection Tank Differential Pressure.....	59
Figure 7-6 Test T456_026 Trough Collection Tank Differential Pressure	60
Figure 7-7 Test T456_026 Upper Vertical Test Plate Temperatures.....	61
Figure 7-8 Test T456_026 Lower Vertical Test Plate Temperatures.....	61
Figure 7-9 Test T456_026 Applied Film Mass Flow Rate.....	62
Figure 7-10 Test T456_026 Applied Film Temperature.....	62
Figure 7-11 Test T456_026 Upper Lateral Test Plate Temperatures.....	63
Figure 7-12 Test T456_026 Lower Lateral Test Plate Temperatures.....	63
Figure 7-13 Laminar Liquid Film Results compared to Equation 3-21 Suction Parameter	65
Figure 7-14 Laminar Liquid Film Results compared to Equation 3-23 Suction Parameter	66
Figure 7-15 Laminar Liquid Film Results Compared to Equation 3-20.....	66
Figure 7-16 Images Showing Full Width of 0.457 m Plate at $P_b = 0.97$ bar, $T_b = 87^{\circ}\text{C}$ and $T_i = 52^{\circ}\text{C}$: Re=1.8 (Top Left) Re=14.2 (Top Right) Re=115 (Lower Left) Re=220 (Lower Right)	68
Figure 7-17 Experimental Gas Diffusion Layer Heat Transfer Coefficient with Respect to the Wave Free	

Gas Diffusion Layer Heat Transfer Coefficient Prediction from Equation 3-20 Showing the Effect of Liquid Film Waves on Heat Transfer Enhancement for Increasing Film Reynolds Number	69
Figure 7-18 Chromatic Confocal Thickness Results for Transitional Wavy Film	70
Figure 7-19 Chromatic Confocal Thickness Results for Wavy Film Regime	71
Figure 7-20 Plate Inclination Effect on Gas Boundary Layer Heat Transfer Coefficient with Respect to the Vertical Plate for Liquid Film Reynolds Number Less than 10	74
Figure 7-21 Heat Transfer Enhancement at Various Reynolds Numbers with Respect to Low Reynolds Number Conditions at Different Inclination Angles	76
Figure 8-1 Comparison of Published Flat Plate Experimental Data to Equation 3-20.....	77
Figure 8-2 Comparison of 2 m Height Experiments to Equation 3-25 Prediction	79
Figure 8-3 Comparison of 3.5 and 0.65 m Height Experiments to Equation 3-25 Prediction	79
Figure 9-1 Current Experimental Results along with Results of Su et al. (2013), Dehbi (1991), Kim et al. (2009), Liu (1999) and Anderson (1998) Showing the Experimental Gas Diffusion Layer Heat Transfer Coefficient with Respect to the Wave Free Gas Diffusion Layer Heat Transfer Coefficient Prediction from Equation 3-20 for Wavy Liquid Film Conditions Only ($Re > 2.2Ka^{1/10}$) as a Function of the Ratio of Gas Diffusion Layer to Liquid Film Length Scale	84
Figure 9-2 Total Heat Transfer Coefficient Predicted Using the Equation 9-3 Gas Diffusion Layer Model Corrected for Film Waves and the Equation 3-4 Liquid Film Model versus the Measured Total Heat Transfer Coefficient.....	87
Figure 9-3 Total Heat Transfer Coefficient Predicted Using the Equation 9-4 Model from Dehbi (2015) versus the Measured Total Heat Transfer Coefficient	88

List of Tables

Table 5-1 Instrumentation Summary for 0.457 m Wide Plate Experiments.....	46
Table 5-2 Instrumentation Summary for 0.914 m Wide Plate Experiments.....	47
Table 6-1 Summary of Heat Transfer Coefficient Measurement Uncertainty Analysis	50
Table 7-1 Test Matrix Summary for 0.914 m Width Plate	52
Table 7-2 Test Matrix Summary for 0.457 m Width Plate	53
Table 7-3 Summary of Vertical Plate Experiments Nominal Conditions.....	64
Table 7-4 Summary of Inclined Plate Experiments Nominal Conditions	73
Table 8-1 Summary of Published Experimental Databases for Condensation on Vertical Surfaces	82

List of Appendix Figures

Figure C-1 Kataoka et al. (1994) Measured Condensation Heat Transfer Coefficients	120
Figure C-2 Kataoka et al. (1994) Measured Wetwell and Outer Pool Temperatures	121
Figure C-3 Uchida et al. (1965) Measured Heat Transfer Coefficients	125

Figure C-4 Tagami (1965) Measured Heat Transfer Coefficients.....	127
Figure C-5 Su et al. (2013) Measured Heat Transfer Coefficients at 6 bar	130
Figure C-6 Su et al. (2013) Measured Heat Transfer Coefficients at 2 and 4 bar	131
Figure C-7 Su et al. (2014) Measured Heat Transfer Coefficients	132
Figure C-8 Kim et al. (2009) Results at 4 bar and 50°C Wall Sub-cooling	138
Figure C-9 Kim et al. (2009) Results at 7 bar and 50°C Wall Sub-cooling	139
Figure C-10 Kim et al. (2009) Results at 12 bar and 50°C Wall Sub-cooling	139
Figure C-11 Kim et al. (2009) Results at 15 bar and 55°C Wall Sub-cooling	140
Figure C-12 Kim et al. (2009) Results at 20 bar and 60°C Wall Sub-cooling	140
Figure G-1 Wave Feature Tracking to Determine Average Wave Velocity for Test T457_048.....	168

List of Appendix Tables

Table A-1 Data Acquisition System Analog Input Module Configuration.....	99
Table A-2 Data Acquisition System Analog Input Module Accuracies	99
Table A-3 Mass Flow Meter Accuracies	100
Table A-4 Pressure Transducer Accuracies	101
Table A-5 Summary of Combined Instrumentation Accuracies	102
Table B-1 Collection Tank 1 Dimensions	103
Table B-2 Collection Tank 2 Dimensions	104
Table B-3 Collection Tank 3 Dimensions	104
Table B-4 Summary of Collection Tank Cross Sectional Areas	104
Table B-5 Collection Tank Cross Sectional Area Uncertainties.....	105
Table C-1 Summary of Dehbi (1991) Experimental Results for 1.16 m Height	114
Table C-2 Summary of Dehbi (1991) Experimental Results for 3.5 m Height	117
Table C-3 Summary of Kataoka et al. (1994) Measured Heat Transfer Coefficients	121
Table C-4 Kataoka et al. (1994) Interface Temperature Calculation Results	124
Table C-5 Kataoka et al. (1994) Dataset Analysis Summary	124
Table C-6 Uchida et al. (1965) Air Data.....	126
Table C-7 Uchida et al. (1965) Nitrogen Data.....	126
Table C-8 Tagami (1965) 0.3 m Height Cylinder Data	128
Table C-9 Tagami (1965) 0.9 m Height Cylinder Data	129
Table C-10 Su et al. (2013) Experimental Results at 6 bar	133
Table C-11 Su et al. (2013) Experimental Results at 2 and 4 bar	136
Table C-12 Su et al. (2014) Experimental Results	137
Table C-13 Kim et al. (2009) Experimental Results.....	141
Table C-14 Liu (1999) Experimental Results	143
Table C-15 Anderson (1999a) Atmospheric Facility Averaged Experimental Results	144

Table C-16 Anderson (1999a) Pressurized Facility Averaged Experimental Results	145
Table C-17 Anderson (1999a) Pressurized Facility Local Experimental Results	146
Table E-1 Inclination, Pressure and RTD Results for 0.457 m Width Plate	151
Table E-2 Thermocouple Results for 0.457 m Width Plate.....	153
Table E-3 Mass Flow Rate Results for 0.457 m Width Plate	156
Table E-4 Heat Transfer Coefficient Results for 0.457 m Width Plate	158
Table E-5 Inclination, Pressure and Temperature Results for 0.914 m Width Plate	161
Table E-6 Mass Flow Rate Results for 0.914 m Width Plate.....	162
Table E-7 Heat Transfer Coefficient Results for 0.914 m Width Plate	163
Table G-1 Wave Velocity Results for T457_048.....	169
Table G-2 Nusselt Laminar Film Calculation Results for T457_048.....	170

1.0 Introduction

As an advanced Gen III+ plant, the AP1000® pressurized water reactor (PWR) nuclear plant is equipped with passive containment and core cooling systems. These passive systems utilize natural convection to transfer heat from the reactor core to the environment in the event of an accident (Schulz, 2006). During a postulated loss of coolant accident (LOCA), the reactor coolant system (RCS) coolant would be expelled into the containment, pressurizing the containment vessel. Steam condensation on the externally cooled, inner walls of the containment vessel limits pressurization of the containment. The steel containment pressure vessel must transfer the initial energy release from the reactor coolant system to the environment and continue to transfer decay heat throughout the course of the accident event.

The AP1000 PWR is equipped for a number of non-LOCA accident scenarios. One such scenario is the extended station blackout (SBO) event similar to what occurred at the Fukushima-Daiichi plants in March of 2011. Figure 1-1 shows a schematic of the AP1000 containment following a SBO. In the event of a SBO, the heat removal function would be accomplished by the passive residual heat removal (PRHR) heat exchanger (HX) located in the in-containment refueling water storage tank (IRWST). The PRHR HX is designed to remove decay heat from the RCS to the water in the IRWST, which increases in temperature and eventually boils. Steam from the IRWST is vented to the containment atmosphere and actuates the passive containment cooling system (PCS), which is used to apply water to the outside of the steel containment vessel and passively remove heat via evaporation to the environment. Steam that is condensed on the inside surface of the containment vessel forms a water film that flows down the containment wall and is returned to the IRWST using a system of water collection gutters and piping. The PRHR system must be capable of removing core decay heat for up to 30 days following such an event.

Effective operation of the PRHR HX and PCS to remove decay heat from the reactor to the environment depends on the ability to maintain water in the IRWST. Uncovering the PRHR HX could result in a failure to reach safe shutdown conditions. Film condensed on the containment wall that is not collected and returned to the IRWST is lost into the sump and is not recoverable without active equipment (e.g. pumps).

® AP1000 is a trademark or registered trademark of Westinghouse Electric Company LLC, its affiliates and/or its subsidiaries in the United States of America and may be registered in other countries throughout the world. All rights reserved. Unauthorized use is strictly prohibited. Other names may be trademarks of their respective owners.

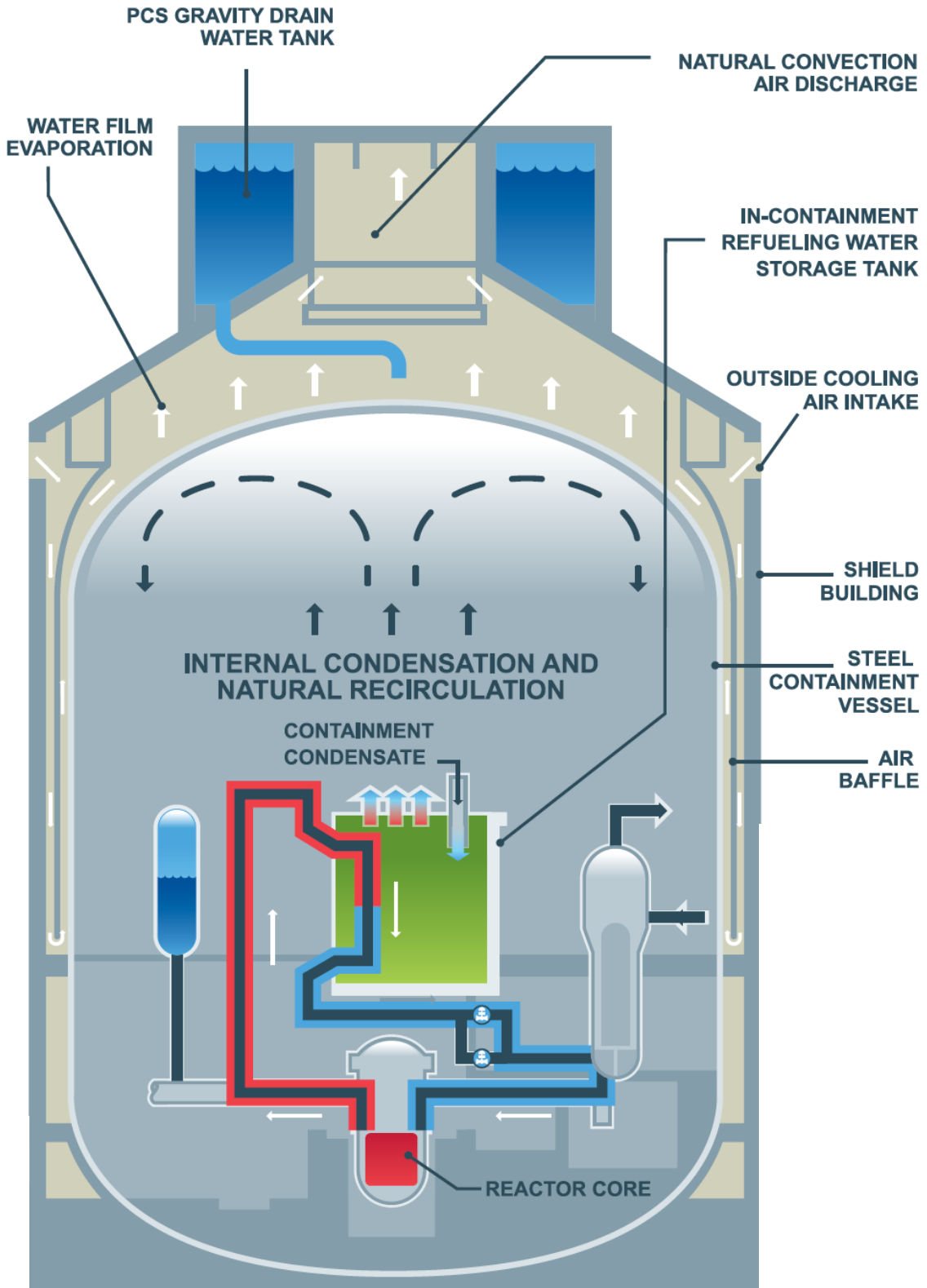


Figure 1-1 AP1000 Passive System Response to Station Blackout Event

The most substantial source of condensate loss from the containment inner surface occurs in the dome region where the film must flow in an inverted configuration at inclination angles ranging from vertical to horizontal. Film loss from the dome can be due to pendent rivulet drips or flow over obstructions such as weld seams and structural attachments to the containment. To determine the coping time limits following an extended SBO, it is necessary to better understand the condensate distribution in the dome region of the containment vessel in order to accurately account for various loss mechanisms.

Non-condensable gas results in a substantial resistance to condensation heat transfer, since vapor must diffuse through the non-condensable gas prior to condensing on the surface. An important factor in the condensation heat transfer characteristics of the passive plant containment are the presence of a significant mass fraction of non-condensable gas. Due to the air environment inside the containment, condensation occurs with significant air mass fraction. Air sequestration in containment compartments and the potential for hydrogen generation during a severe accident lead to variability in the non-condensable mass fraction, dependent upon the plant design and accident scenario.

Experimental studies have focused on post-LOCA heat flux. For these conditions, the liquid film Reynolds number is relatively high and the film disrupts the gas diffusion layer resulting in enhanced heat transfer. This effect has not been explicitly studied for the turbulent natural convective condensation scenario. Due to the height of prototypical containment vessels compared to experimental facilities, this effect can cause a distortion when applying the results to predict plant response. Finally, the film Reynolds number varies over an order of magnitude comparing short term and long term post-accident operation, and the effect may have a significant influence when using semi-empirical correlations proposed in the literature to predict heat transfer for SBO operation.

Heat and mass transfer in the dome region of the containment vessel is of significant importance for the SBO scenario. Gravitational film instabilities exist that cause a different effect than the vertical condition. This influence has been hypothesized by a number of researchers, but no separate studies have been performed. Due to the lack of data available to quantify condensation heat transfer as a function of inclination, this has prompted further investigation into the condensation heat transfer characteristics on inclined surfaces.

The influence of the liquid film on disruption of the turbulent gas boundary layer has not been adequately addressed for the natural convective condensation problem. As outlined in the Section 2.0 literature review, there have been no studies on this effect in the turbulent natural convective condensing flow. This work extends the available database of turbulent natural convective condensation heat transfer experiments in the presence of non-condensable gas to low heat flux, consistent with long term post-LOCA and SBO operation. By extending the available database to low heat flux conditions, the film Reynolds number can be reduced to the extent where film hydrodynamic effects are unimportant. Then, by parametrically varying the film flow Reynolds number and heat flux over a wide range, the effects of the film disruption phenomenon can be clearly observed. This experimental method is used for both vertical and inclined surfaces.

Section 3.0 defines the baseline model used to predict the experimental results of this study and those reported in the literature. Various forms of the baseline model are developed to model condensation on vertical and inclined flat plates as well as cylinders.

The experimental facility is described in Sections 4.0 and 5.0. By employing a direct measurement of the condensate mass flow rate to determine the latent heat flux, relatively low measurement uncertainty is achieved compared to uncertainties reported in the literature. This allows close examination of the plate inclination and film disruption effects that would not be possible with other experimental methods.

Section 7.0 provides the analysis of experimental results. A clear enhancement in heat transfer, above that predicted by the Section 3.0 model, is observed due to surface waves. The influence of film waves is observed visually and through local film thickness measurements. The first of a kind application of a chromatic confocal film thickness measurement device in a condensing environment is demonstrated.

Section 8.0 summarizes the results of a thorough analysis of the available literature. Experimental trends and explanations for deviations from the prediction are provided. Section 9.0 develops an empirically based adjustment to the Section 3.0 baseline model to account for film surface waves and compares the new model to the entirety of the published literature database. Finally, Section 10.0 summarizes the results and conclusion of this research and Section 11.0 provides recommendations for future work.

2.0 Literature Review

The primary focus areas of this review are experiments and modeling of turbulent natural convective condensation in the presence of non-condensable gas. An emphasis has been placed on reviewing the experimental methods and uncertainty assessments. A recent review of this topic is also provided by de la Rosa et al. (2009a), which is less critical of the experimental methods and measurement uncertainty. Given the reliance on the heat and mass transfer analogy for predicting condensation heat flux in this regime, published correlations for turbulent natural convective heat transfer on vertical and inclined flat plates as well as cylinders are also reviewed.

2.1 Turbulent Natural Convective Condensation Experiments

2.1.1 Flat Plate Experiments

Uchida et al. (1965) published some of the first experimental data available for condensing heat transfer under nuclear containment conditions. Uchida et al. (1965) used a 0.14 m wide by 0.3 m length condensing plate. The short vertical height resulted in conditions close to the gas layer laminar turbulent transition as discussed in Section 8.0. There is limited documentation of the experimental apparatus and no statement of uncertainty that was identified as part of this review. The Uchida et al. results have been used to develop empirical correlations to predict containment heat transfer using the vapor to non-condensable gas weight ratio as the correlating parameter. More recent studies (Peterson, 1996 and Herranz et al., 1998) have demonstrated that the form of the empirical correlation is an artifact of the test procedure, which restricts the usefulness to conditions in which the non-condensable partial pressure is 1 atmosphere at standard conditions. This is problematic when considering any number of effects such as non-condensable gas generation, stratification or sequestration. Nonetheless, the weight ratio correlation based on the Uchida et al. dataset is used widely in nuclear plant safety analyses as a standard for predicting containment response.

Kataoka et al. (1991, 1992 and 1994) published results in the turbulent natural convective regime for a 4.5 m high vertical wall. No statements of experimental uncertainty are provided. Temperature difference across the condensing wall and the wall material thermal conductivity were used to calculate the experimental heat transfer coefficient. Typically, this measurement method results in errors in the range of

10-20%, however, uncertainties can be much higher depending temperature difference magnitude, selection of instrumentation and precautions taken during calibration. It was noted that K-type thermocouples were used, which do not provide optimal accuracy for the measured temperature range. Even though the measurement uncertainties are questionable, results from Kataoka et al. (1994) are of significant importance due to the high Rayleigh numbers that were developed in the facility that are not available from other flat plate experimental programs.

Anderson (1998a), Anderson et al. (1998b) and Herranz et al. (1998) reported the results of testing that modeled a 1:12 scale radial slice of the AP600 nuclear plant containment vessel. The test geometry included vertical, inclined and horizontal condensing surfaces. The condensing surface was fabricated from aluminum and coated with inorganic zinc coating, which is similar to the zinc coated carbon steel surfaces standard for the AP600/AP1000 containment vessel. The test facility was 2.9 m height and 0.33 m width. The sides of the test facility were enclosed; however there was no treatment of the enclosure / sidewall effect.

Anderson (1998a) utilized two independent methods of heat flux measurement. Average measurement accuracy of 10% was reported for each method. This level of accuracy could not be validated. The local heat flux was based on measurement of the temperature gradient across the condensing plate. However, this method inherently accepts the uncertainty in measured thermal conductivity, which was not reported. Furthermore, the standard deviation in temperature measurements was used to quantify temperature measurement error, which appears incorrect. Coolant channel energy balance results were provided for each of the 14 plate locations. The flow measurement accuracy was reported to be 8%. However, no method of calibration was referenced for the Dwyer RMC 141 rotameter. In addition, the range of the rotameter is stated as 0.1 to 1 gpm, and it appears that the meter was used to report values greater than 1 gpm. Finally, a detailed assessment of the Anderson database indicates that a number of the measured results using the coolant channel and plate temperature gradient methods did not agree within the reported measurement uncertainty, as shown in Appendix C.8 of this report. No explanation was provided for discrepancy between the two measurement methods that exceed 50% in several cases.

A reasonable range of total pressure and wall temperature was included in the test matrix that covered

post-LOCA blowdown conditions. The model proposed by Anderson (1998a) was shown to reasonably predict results from the vertical portion of the test facility and the results for the inclined dome region of the facility were reported to increase the heat transfer coefficient. However, the effect of inclination was reported to be second order even though detailed review of the results indicates up to a 50% increase in heat transfer coefficient due to inclination angle. It was hypothesized that the film structure played a role in the increased heat transfer. However, no analysis of the inclined plate results was presented and the magnitude of the liquid film disturbance effect was not discussed.

From an experimental standpoint, results taken from inclined plates of the Anderson AP600 scale model experiments are difficult to use directly for assessing the effects of inclination. This is due to variable boundary conditions on each plate. Differences in inlet flow profile, insulation and conduction boundaries resulted in experimental variability that make it difficult discriminate between results at different plate angles. Finally, the film flow regimes observed for the Anderson pressurized facility (Anderson et al., 1998b) were complex, with rivulets and rolling waves. These patterns would not develop on a vertical condensing surface.

2.1.2 Cylinder Experiments

Tagami (1965) reports results for condensation on 0.3 m and 0.9 m height, 15 cm diameter vertical cylinders. For access to the experimental data and a description of the facility the Tagami (1965) results are also provided by Corradini (1984). Like the Uchida et al. (1965) data, the Tagami (1965) data has been used widely based on an empirical fit of the dataset relating the heat transfer coefficient to the non-condensable to vapor weight ratio. Tagami (1965) does not provide sufficient details of the experimental apparatus to assess possible sources of experimental bias or a statement of the measurement uncertainty. Gido and Koestel (1983) note that the configuration of the baffle plate, which diverts the blowdown flow entering the Tagami (1965) test vessel, strongly influenced the convection patterns around the test cylinders.

Dehbi (1991) performed testing under turbulent natural convective conditions using 3.5 m tall, 3.8 cm diameter cylinder. The Dehbi experiments covered a total pressure range of 1.5 ATM to 4.5 ATM, air mass fraction from 25 to 90% and sub-cooling from 15 to 50°C. Dehbi reported an experimental

measurement uncertainty of approximately 15% using a coolant channel energy balance. The uncertainty evaluation considered standard deviation of thermocouple measurements acquired at a rate of 40 samples per second and averaged over a 2 minute interval. The standard deviation of this measurement was used to quantify the temperature measurement uncertainty. It appears as if this uncertainty is simply a quantification of the noise level in the measurement. Furthermore, the uncertainty did not consider accuracy of the J type thermocouples used or statistical combination of the accuracy with the analog to digital converter. There was no mention of the method used to calibrate the thermocouples or the flow meter used for the coolant channel energy balance.

Dehbi (1991) reports a heat transfer coefficient measurement error of 15% based on the coolant energy balance. The error analysis reported by Dehbi assumes a coolant temperature rise of 10°C between stations and indicated that the rise in coolant temperature was in the range of 40°C to 90°C. Assuming the stated Reynolds number of 1500 in the coolant loop, this coolant temperature rise range was not maintained. As a result, the experimental accuracy of 15% is questionable at heat transfer rates below 8000 W/m².

Liu (1999) and Liu et al. (2000) report experimental results for condensation on a 2 m height, 0.038 m diameter vertical cylinder. Results are given over a pressure range of 2.5 to 4.5 bar and bulk non-condensable weight fraction range of 0.17 to 0.75. Liu (1999) reports measurement error ranging from 7 to 18%. However, this heat transfer coefficient measurement accuracy measurement uncertainty range is not supported by the experimental results provided. As shown in Appendix C.7, in some cases the bulk to wall temperature differential was less than 4°C and Liu (1999) states that manufacturer calibrations were accepted for thermocouple readings.

Kim et al. (2009) reports experimental results for condensation on a 0.65 m height, 0.038 m diameter vertical cylinder. Results are given over a pressure range of 4 to 20 bar and bulk non-condensable weight fraction range of approximately 0.01 to 0.71. The data is reported with an experimental error of ±25%. Kim et al. (2009), reported coolant channel calorimetric based results and indicated that condensate mass based results were also available, but did not show a comparison. The coolant channel calorimetric measurement may have been biased due to insulation losses or conduction to the vessel

wall. Finally, the interface temperatures were only reported as nominal values for a range of given test conditions.

Su et al. (2013 and 2014) reports the experimental results of condensation on a 2.0 m height, 0.038 m diameter vertical cylinder. Test results are provided over an absolute pressure range of 2 to 6 bar with bulk non-condensable weight fraction ranging from 0.07 to 0.59. Su et al. reported experimental results with a maximum measurement error of 19.4%. No independent measurement method was reported to confirm the heat transfer coefficients.

2.2 Diffusion Layer Theory Model Development

Peterson et al. (1993) published a diffusion layer theory that considers the effect of non-condensable gas on condensation heat transfer. A theoretical derivation was used to relate the vapor velocity at the liquid gas interface to the gas diffusion layer thickness. The relationship for vapor velocity was then formulated in terms of an effective condensation thermal conductivity. Using the heat and mass transfer analogy (HMTA), an appropriate correlation for natural convection heat transfer could be used to predict the condensing heat flux. Peterson selected the correlation proposed by Bayley (1955) for turbulent natural convection on a vertical plate to formulate the heat and mass transfer correlation. The resulting mechanistic model was reported to fit data reported by Kataoka et al. (1991) within a standard deviation of $\pm 4\%$.

Anderson (1998a) and Herranz et al. (1998) provided an improvement to the theory established by Peterson et al. (1993) that more accurately accounts for the variation in vapor specific volume through the diffusion layer. They also extended the model to account for boundary layer suction. Boundary layer suction results in a reduction of the boundary layer thickness due to the vapor velocity towards the plate. Application of the HMTA utilized the McAdams (1954) correlation for natural convection on a vertical plate, which differs only in the empirical constant from the Bayley (1955) correlation used by Peterson. No discussion on the usage of the McAdams correlation versus the Bayley correlation was provided.

A good description of the influence of wall suction on the application of the heat and mass transfer analogy is provided by Kays et al. (2005) and Bird et al. (2007). The Herranz et al. (1998) model utilizes the suction factor based on laminar Couette flow as described by Kays (2005). de la Rosa et al. (2009b)

has proposed modification to the suction parameter to account for over-prediction of the suction parameter in the turbulent regime. These suction factors are discussed in detail in Section 3.3.

2.3 Turbulent Natural Convective Heat Transfer

2.3.1 Vertical Surfaces

There are a number of experimental datasets, empirical correlations and theoretical expressions to predict the heat transfer rate from vertical flat plates by natural convection. Eckert and Jackson (1950) proposed a correlation in the following form:

$$\text{Nu}_s = 0.021\text{Ra}_s^{0.4} \quad \text{Equation 2-1}$$

, where Ra_s is the Rayleigh number and Nu_s is the Nusselt the number. The expressions used to evaluate these parameters are discussed in Section 3.0.

Bayley (1955) proposed a correlation based on an empirical fit of data from Saunders (1936) and supported the correlation theoretically. The Bayley correlation is given as:

$$\text{Nu} = 0.1\text{Ra}_s^{1/3} \quad \text{Equation 2-2}$$

McAdams (1954) and Kutateladze (1964) also proposed a correlation that is independent of the plate length with a different empirical constant. The McAdams correlation is given as:

$$\text{Nu} = 0.13\text{Ra}_s^{1/3} \quad \text{Equation 2-3}$$

Equation 2-1 is consistent with Equation 2-2 near a Rayleigh number of 10^{10} and consistent with Equation 2-3 at a Rayleigh number of 10^{12} .

Warner and Arapaci (1968) compared several correlations including those of Bayley and McAdams to their experimental data. The showed that the Bayley correlation was appropriate using a 0.6 m wide by 3.7 m tall test geometry, covering a range of Rayleigh numbers from 10^8 to 10^{12} in air at atmospheric pressure. The McAdams correlation was shown to over-predict heat transfer rates by approximately 30%. The Warner and Arpaci experiments implemented measures to minimize early transition to turbulent flow

and determined a critical Grashof number of 3×10^9 to 4×10^9 using smoke trace studies. They noted that this transition criterion was as high as eight to ten times that reported by other investigators as a result of the precautions taken to avoid early transition.

The Equation 2-2 and Equation 2-3 predictions indicate that the heat transfer coefficient is independent of the plate length when the gas boundary layer is turbulent. Therefore, application of these relations to predict the local or plate averaged heat transfer coefficient is appropriate. However, depending on measures taken to promote or avoid transition to turbulence at the top of the plate, a laminar boundary layer may be present on the upper portion of the plate. As a result, application of these relations to predict the plate averaged heat transfer coefficient assumes that the influence of this laminar region is small. Al-Arabi and Sakr (1988) compare the local and plate averaged heat transfer methods and propose a slightly higher transition criterion when applying the correlation to predict plate averaged heat transfer coefficient. The transition criterion of 2×10^9 for the plate averaged prediction is suggested by Al-Arabi and Sakr (1988). As described in the Section 4.2 test article description, the experiments conducted for this program implement a boundary layer trip to promote turbulent flow at the upper region of the test plate and avoid the laminar gas layer region altogether.

Clausing (1983) showed that differences between the Eckert and Jackson, Bayley and McAdams correlations could be explained by two primary factors, in addition to a number of secondary effects. First, the basis for gas properties used in the various experiments to calculate the dimensionless Nusselt and Rayleigh numbers (e.g. thermal conductivity, viscosity) is different simply due to the availability of accurate thermo-physical property databases at the time the experimental databases were published. The variation of gas properties across the boundary layer is not accounted for in these simple formulations.

Clausing (1983) conducted experiments in a cryogenic facility in order to assess the variable property influence. Although the condition of no variable properties across the boundary layer can only be approached experimentally, Clausing provides convincing evidence that the variable property influence inherent in the application of the Eckert and Jackson, McAdams and Bayley correlations are significant. Clausing correlated his data and the data from several other studies in the following form:

$$Nu = 0.082Ra_s^{1/3} f \quad \text{Equation 2-4}$$

$$f = -0.9 + 2.4 \left(\frac{T_w}{T_b} \right) - 0.5 \left(\frac{T_w}{T_b} \right)^2 \quad \text{Equation 2-5}$$

, where T_w and T_b are the wall and bulk temps. The variable f describes the variable property influence and is based only on natural convection of gaseous air or nitrogen. The form of Equation 2-4 is similar to that proposed by Siebers et al. (1985) to consider the variable properties influence.

The influence of variable properties on the turbulent natural convective mass transfer scenario examined as part of this research has not been experimentally addressed in the literature for the condensing air water system. This research does not attempt to resolve this deficiency; however, it is noted as a possible explanation for deviations from the theoretical application of the heat and mass transfer analogy.

2.3.2 Inclined Surfaces

Natural convection on inclined plates has received less attention than the vertical configuration. However, several reasonably well developed experimental efforts exist that can be used to form the basis for a correlation using the HMTA. Vliet (1969) conducted natural convection studies on an inclined plate in water. The test plate was 1.22 m tall and 0.914 m wide. Results for plate inclination angles from vertical to 30 degrees from horizontal were reported. The transition Grashoff number, from laminar to turbulent flow, was observed to vary significantly over the range of tested inclination angles.

Fujii and Imura (1972) conducted natural convection heat transfer studies in the turbulent regime using plates of 30 cm height x 15 cm width and 5 cm height x 10 cm width. Results were reported in terms of average Rayleigh number and average Nusselt number. Heated plate tests were conducted with upward and downward configurations. Here, the heated upward plate is consistent with the cooled downward surface for the current research. Empirical correlations for the Nusselt number as a function of Rayleigh number and critical Rayleigh number for transition to turbulence were reported. The form of the correlations results in a dependence on plate length. Furthermore, for Rayleigh numbers much greater than the critical Rayleigh number, the influence of plate inclination is negligible.

Al-Arabi and Sakr (1988) conducted a comprehensive study of natural convection on heated vertical and inclined plates facing upwards using a 1.3 m long by 0.65 m wide plate. Guarded test plate sides were used to assure results were independent of test plate width. Local heat flux measurements at 13 stations along the plate length were used to monitor the transition from laminar to turbulent flow. Correlations for the transition Rayleigh number as a function of inclination angle were provided. Furthermore, a general correlation for the Nusselt number in terms of the Rayleigh number and plate inclination angle was provided for the turbulent regime. In comparison to the Fujii and Imura correlation, the Al-Arabi and Sakr correlation was reported independent of plate length. In addition, the influence of plate inclination was shown to be important regardless of the magnitude of Rayleigh number with respect to the transition point.

2.4 Influence of Film Waves on Liquid Film Heat Transfer

Kutateladze and Gogonin (1979) comprehensively review the effect of surface waves for pure vapor on vertical and horizontal cylinders. The results presented for the vertical cylinder are directly applicable to the vertical plate configuration that is the focus of this research. The results are presented in terms of an empirical correction to the Nusselt laminar film theory that is a function of the film Reynolds number. Kutateladze and Gogonin (1979) indicate that between Reynolds numbers of approximately 100 to 1000, results are highly scattered, and assuming a constant enhancement factor is appropriate.

The Kutateladze and Gogonin (1979) correlation is defined using the Reynolds number evaluated at the bottom of the condensing surface. The experimental conditions summarized by Kutateladze and Gogonin (1979) would have resulted in a developing film flow starting from a Reynolds number of zero at the top of the condensing surface. The result is that a Reynolds number at the bottom of the vertical condensing surface that is sufficient to develop a wavy film interface, would also include a laminar, wave-free region at the top. By characterizing the film wave effect using the Reynolds number at the bottom of the condensing surface, the effect of film waves is somewhat washed out. Although discretizing the surface and assessing the flow regime at each point along the vertical surface would result in a clearer delineation of the film wave enhancement effect, the experimental database is not suitable for validating such an approach. Therefore, given the wide acceptance of the Kutateladze and Gogonin (1979)

correlation to correct for the film wave effect, it is implemented, as described in Section 3.1 to analyze the results of this study.

For inclined and horizontal surfaces, pendent drops and rivulets form due to gravitational instabilities (Gerstmann and Griffith, 1965 and 1967; Rockroth, 1968; Indeikina et al., 1997). Depending on the angle of inclination and film Reynolds number, drops may fall from the surface. The analysis and corrections proposed by Gerstmann (1965) appear to be the most appropriate for assessing the liquid film thermal resistance on inclined plates under condensing conditions.

2.5 Influence of Film Waves on Gas Boundary Layer Heat Transfer

Surface waves can cause a disruption of the gas boundary layer in a manner that enhances heat transfer. The process is similar to the enhancement that occurs in the liquid film. Gido and Koestel (1983) performed an analytical study to explain the deviations from small scale tests to large scale integral tests. The Gido and Koestel model includes a functional variation with liquid height to the 0.7 power to account for increases in liquid flow rate along the wall.

No experimental studies were identified in which the liquid film wave interaction with the turbulent, natural convective boundary layer was examined; however, several studies have noted this influence as part of the experimental results discussion. Kataoka et al. (1994) attributed the experimentally observed increase in heat transfer as a function of height to the film thickness increase. Dehbi (1991) reported an increase in heat transfer due to increased film flow rate.

This film disruption effect has been studied experimentally in the forced convection regime by a number of researchers, but no theoretical predictions were identified. Kang and Kim (1994) studied this effect experimentally, considering condensation on a nearly horizontal, upward facing surface. The condensing surface was 0.15 m width and 1.52 m length. Steam and air mixtures were injected at 3 m/s into the rectangular test section at varying mass fractions. The effect of surface waves was considered by varying the liquid film flow rate. The results indicated up to a factor of two influence of film Reynolds number on the heat transfer coefficient.

Recently, Park et al. (1996 and 1997) experimentally examined the influence of surface waves on forced

convection heat transfer on a vertical plate. The condensing surface was 0.15 m width and 1.52 m length. The results were correlated in terms of a correction factor applied to the heat transfer coefficient. The correction factor was defined as a function of both the film Reynolds number and bulk gas Reynolds number.

For the inclined surface, Huhtiniemi (1991), Huhtiniemi et al. (1993) and Anderson (1998a) hypothesize that pendent rivulet drips are the cause of increased heat transfer when comparing tests conducted at inclination compared to the vertical. No analysis or separate experimentation has been conducted to support these claims.

2.6 Summary

Studies focusing on turbulent natural convective condensation heat transfer in the presence of non-condensable gas are limited. The experiments of Uchida et al. (1965), Tagami (1965) and Kataoka et al. (1994) do not include a measurement uncertainty statement and there are only few details of the experimental apparatuses available. The experimental facilities of Anderson (1998a) and Tagami (1965) implement test geometries that would develop complex flow patterns that may distort the results compared to naturally driven flow on a vertical wall. Measurement uncertainties reported by Dehbi (1991), Anderson (1998a) and Liu (1999) are questionable based on the detailed reports that are available for these studies. The accuracy of a model benchmarked to these datasets should be considered with respect to this assessment. Nonetheless, the combined datasets cover a wide range of conditions relevant to operating and advanced reactor containment designs, and observed trends that span multiple of these reported datasets add confidence in understanding the underlying physical phenomena.

No literature identified for modeling or predicting the heat transfer coefficient for inclined surfaces in the turbulent natural convective condensation regime, considering the influence of non-condensable gas. Furthermore, no experimental studies, specifically aimed at assessing the influence of liquid film waves on the gas boundary layer were identified. Both of these deficiencies are considered as part of this research.

3.0 Model Description

Figure 3-1 shows a schematic of the condensing steam air system. The heat flux, q'' , and total heat transfer coefficient, h_t , are a function of the liquid and gas properties and the bulk temperature, T_b , to wall temperature, T_w , difference. The model can be viewed as a simple thermal network as shown in Figure 3-2, where parallel sensible and latent heat transfer occurs in the gas boundary layer and the gas and liquid layer resistances act in series.

The model assumes that the air steam environment is saturated with steam at T_b and saturated conditions exist through the gas boundary layer to the liquid film interface, T_i . As such, the non-condensable gas mole fraction, x_{nc} , must increase in the direction of the interface. This is the physical explanation for the strong influence of non-condensable gas on vapor condensation, since the vapor must diffuse through the non-condensable gas layer.

The limit as the non-condensable mole fraction approaches zero is the pure steam condensation scenario. In this scenario, the gas layer latent and sensible heat transfer resistances are negligible and the liquid film thermal resistance is the only thermal resistance between the bulk and interface. For conditions in which the film thermal resistance is significant, the model used to assess the liquid film heat transfer coefficient is increasingly important.

Considering high non-condensable mole fraction, the resistance to latent heat transfer, driven by the diffusion of vapor through the non-condensable gas, is the dominant resistance. Furthermore, the temperature gradient that arises in the gas layer necessitates the consideration of sensible heat transfer. Depending on the magnitude of the gas layer and liquid film thermal resistances, the liquid film thermal resistance may be negligible for the high non-condensable mole fraction scenario.

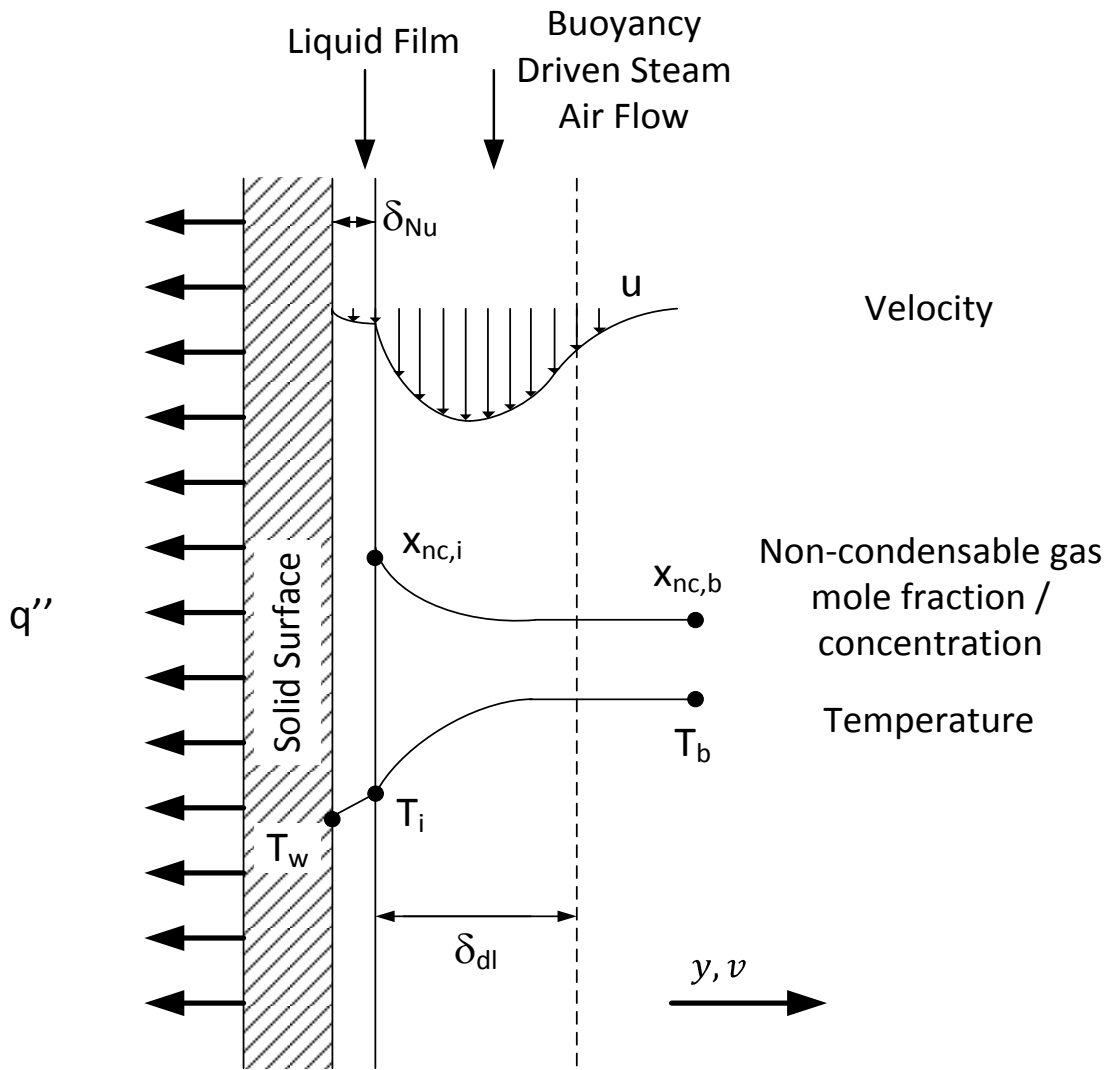


Figure 3-1 Schematic of Natural Convective Condensation with Non-Condensable Gas Present

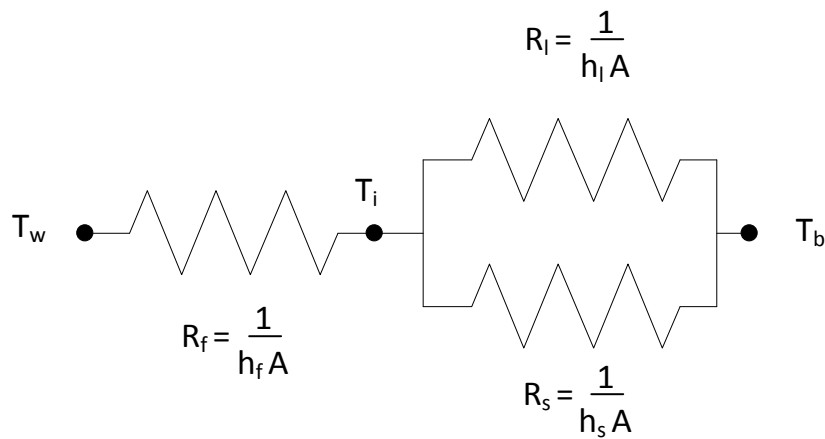


Figure 3-2 Thermal Network Representing Condensation with Non-Condensable Gas Present

To assess the relative importance of the gas layer and liquid film thermal resistances, the baseline model accounts for all three thermal resistances shown in Figure 3-2. First, the liquid film heat transfer coefficient is defined in Section 3.1 in terms of published empirical correlations applicable to laminar and wavy film flows. In Section 3.2, the heat and mass transfer analogy is applied to the flat plate geometry to define the gas layer heat transfer coefficient, without waviness or suction corrections. Various forms of the mass transfer suction factor are reviewed in Section 3.3 that are subsequently assessed in the experimental results discussion provided in Section 7.0. Finally, correlations for the cylindrical and inclined plate geometries are presented in Section 3.4 and 3.5.

3.1 Liquid Film Heat Transfer on the Vertical Plate

The gas diffusion layer and liquid film act as series heat transfer resistances between the bulk, T_b and wall temperature, T_w . Therefore, the heat flux through the diffusion layer and liquid film must be equal. Correlations for the liquid film heat transfer coefficient, h_f , and the gas diffusion layer heat transfer coefficient, h_{dl} , can be used to determine the heat flux by iterating the liquid film interface temperature, T_i , until the heat flux through the gas layer and liquid film are equal:

$$q'' = h_t(T_b - T_w) = h_{dl}(T_b - T_i) = h_f(T_i - T_w) \quad \text{Equation 3-1}$$

The average liquid film thickness, δ_{Nu} , and average heat transfer coefficient are approximated using the Nusselt laminar film theory as described by Collier and Thome (1994).¹

$$h_f = \frac{\delta_{Nu}}{k_f} = 0.943 \left[\frac{\rho_f(\rho_f - \rho_g)g i_{fg} k_f^3}{\mu_f L (T_i - T_w)} \right]^{1/4} \quad \text{Equation 3-2}$$

, where L is the length of the condensing surface, μ_f is the fluid viscosity, ρ_f is the fluid density, ρ_g is the gas density, g is gravitational acceleration, i_{fg} is the latent heat of vaporization and k_f is the thermal conductivity of the liquid film. The Nusselt theory can also be formed to relate the film Nusselt number to the Reynolds number:

¹ Note that experiments were performed with film applied to the plate. The local Nusselt solution is used in these instances to calculate film thickness and heat transfer coefficient as described in Appendix G.

$$Nu_f = \frac{h_f}{k_f} \left[\frac{\mu_f^2}{\rho_f(\rho_f - \rho_g)g} \right] = 0.925 Re_\Gamma^{-1/3} \text{ for } Re_\Gamma \leq 5 \quad \text{Equation 3-3}$$

, where $Re_\Gamma = \Gamma/\mu_f$ is the film Reynolds number and Γ is the liquid film mass flow rate per unit width at the bottom of the condensing surface.

Above a film Reynolds number of approximately five, it is necessary to account for heat transfer enhancement due to film waves. Kutateladze and Gogonin (1979) suggest an empirical correction to the Nusselt theory that is dependent on the film Reynolds number.

$$Nu_f = 0.925 Re_\Gamma^{-1/3} Re_\Gamma^{0.04} \text{ for } 5 < Re_\Gamma \leq 50 \quad \text{Equation 3-4}$$

Above a Reynolds number of 50 the experimental data exhibits significant scatter. For Reynolds numbers between 100 and 1000 Kutateladze and Gogonin (1979) suggest that a constant heat transfer coefficient represents the experimental data well. For this study, the film Nusselt number of 0.28 is assumed for the Reynolds number range of 50 to 400, which agrees well with the results of Kutateladze and Gogonin.

3.2 Gas Diffusion Layer Heat and Mass Transfer

To determine the diffusion layer heat transfer coefficient under saturated bulk conditions, sensible and latent heat transfer are assumed to act as parallel resistances such that the sensible heat transfer coefficients, h_s and latent heat transfer coefficient, h_l , are additive.

$$q'' = h_{dl}(T_b - T_i) = (h_s + h_l)(T_b - T_i) \quad \text{Equation 3-5}$$

For natural convection on a vertical plate, the Nusselt number, Nu_s , can be determined using the Bayley (1955) correlation:

$$Nu_s = \frac{h_s L}{k_g} = 0.1 Ra_s^{1/3} \quad \text{Equation 3-6}$$

, where k_g is average thermal conductivity in the diffusion layer. The thermal convection Rayleigh number is defined as a function of Grashoff and Prandtl number:

$$Ra_s = Gr_L \cdot Pr \quad \text{Equation 3-7}$$

$$Gr_L = \frac{g\rho_{ave}(\rho_i - \rho_b)L^3}{\mu_g^2} \quad \text{Equation 3-8}$$

$$Pr = \frac{C_{p,g}\mu_g}{k_g} \quad \text{Equation 3-9}$$

, where ρ_b is the bulk gas density, ρ_i is the gas density at the interface, ρ_{ave} is the average of the bulk and interface gas densities, μ_g is average gas viscosity in the boundary layer and $C_{p,g}$ is the average specific heat at constant pressure in the boundary layer.

Equation 3-6 is only applicable to the turbulent regime. The lower limit of applicability is defined based on experimental investigations of the laminar to turbulent transition. Warner and Arpaci (1968) experimentally evaluated the Bayley (1955) correlation and compared the results to a number of studies over a Rayleigh number range of approximately 1×10^8 to 1×10^{12} . The Warner and Arpaci experiments implemented measures to minimize early transition to turbulent flow and determined a critical Grashof number of 3×10^9 to 4×10^9 using smoke trace studies. They noted that this transition criterion was as high as eight to ten times that reported by other investigators as a result of the precautions taken to avoid early transition.

The heat and mass transfer analogy is used to develop a relationship for the condensing heat transfer coefficient in a form similar to Equation 3-6. The mass transfer Sherwood number, Sh , is defined in a manner similar to the Nusselt number:

$$Sh = \frac{g_m \cdot L}{\gamma} = \frac{(g_m/\rho) \cdot L}{D} \quad \text{Equation 3-10}$$

, where g_m is the mass transfer coefficient and γ is the product of the diffusion coefficient, D , and density, ρ .² The mass transfer coefficient is analogous to the heat transfer coefficient and is given by:

² Note that the ratio of g_m/ρ in Equation 3-10 is sometimes referred to as the mass transfer coefficient, k . The terminology used here avoids the use of the commonly used variable, k , to represent the mass transfer coefficient and is consistent with the terminology used by Kays (2005).

$$g_m = \frac{\left(\gamma \cdot \frac{\partial m}{\partial y}\right)_i}{(m_b - m_i)} \quad \text{Equation 3-11}$$

, where m is the mass concentration within the diffusion boundary layer.

The form of the mass transfer coefficient given by Equation 3-10 is not convenient for problems with both heat and mass transfer since the driving force for heat transfer is the temperature gradient and the driving force for mass transfer is the concentration gradient. Considering a boundary layer in which the gas remains saturated through the layer, a simplification can be made by relating the concentration gradient to the temperature gradient. In this manner the Sherwood number can be redefined in the same form as the Nusselt number:

$$Sh = \frac{h_c \cdot L}{k_c} \quad \text{Equation 3-12}$$

, where k_c is an effective condensation thermal conductivity.³ Because k_c represents resistance to mass transfer, it is a function of bulk and interface gas properties as well as the binary diffusion coefficient. Peterson et al. (1993) theoretically derived a relationship for k_c by integrating the Clapeyron equation over the diffusion boundary layer. This derivation was later modified by Anderson (1998a). The formulation for k_c as derived by Anderson (1998a) is given by:

$$k_c = \frac{1}{\varphi T_b T_i^2} \left(\frac{P_b D_{fg}^2}{R_v^2} \right) \quad \text{Equation 3-13}$$

, where R_v is the vapor specific gas constant and P_b is the absolute bulk pressure. The quantity φ is given by:

$$\varphi = \frac{x_{nc,avg}}{x_{v,avg}} = - \frac{\ln[(1 - x_{nc,b})/(1 - x_{nc,i})]}{\ln[x_{nc,b}/x_{nc,i}]} \quad \text{Equation 3-14}$$

, where $x_{nc,b}$ and $x_{nc,i}$ are the mole fractions of non-condensable gas in the bulk mixture and at the

³ The variable k_c should not be confused with the binary diffusion coefficient, D . The variable k_c represents an effective thermal conductivity due to mass transfer. The form of Equation 3-12 is different from Equation 3-10 in that it represents an effective heat transfer due to mass transfer. Determination of the effective condensation thermal conductivity, k_c , requires solution of the boundary layer equations.

interface respectively. To avoid confusion associated with the basis for the condensation thermal conductivity, the derivation is provided in Appendix F.

Now, applying the heat and mass transfer analogy to Equation 3-6 yields the following equation for the condensation heat transfer coefficient.

$$Sh = \frac{h_c L}{k_c} = 0.1 Ra_c^{1/3} \quad \text{Equation 3-15}$$

The definition of mass transfer Rayleigh number has also been introduced as:

$$Ra_c = Gr_L \cdot Sc \quad \text{Equation 3-16}$$

$$Sc = \frac{\mu_g}{\rho_{ave} D} \quad \text{Equation 3-17}$$

The diffusion layer Nusselt number, which includes heat and mass transfer components, can now be formed in terms of the summation of convective and condensing components.

$$Nu_{dl} = \frac{L}{\delta_{dl}} = \frac{q''L/(T_b - T_i)}{k_{eff}} = 0.1 Ra_c^{1/3} \quad \text{Equation 3-18}$$

, where δ_{dl} represents the diffusion layer thickness and k_{eff} has been defined as:

$$k_{eff} = k_c + \left(\frac{Pr}{Sc}\right)^{\frac{1}{3}} k_g \quad \text{Equation 3-19}$$

3.3 Gas Diffusion Layer Suction Effect

The underlying correlations used to apply the heat and mass transfer analogy do not consider an additional convective component towards the interface due to mass diffusion. For low mass transfer rates this effect can be neglected and Equation 3-18 is applicable. However, at high mass transfer rates this effect cannot be neglected. To account for this effect, a suction factor, Θ , is applied as a direct multiplier to Equation 3-18.

$$\text{Nu}_{dl} = 0.1 \cdot \theta \cdot \text{Ra}_c^{1/3} \quad \text{Equation 3-20}$$

Considering a laminar Couette flow, Kays et al. (2005) demonstrates that the suction factor can be formulated as follows:

$$\theta_{\text{Kays}} = \frac{\ln(1 + B)}{B} \quad \text{Equation 3-21}$$

$$B = \frac{W_{v,i} - W_{v,b}}{1 - W_{v,i}} \quad \text{Equation 3-22}$$

, where $W_{v,i}$ and $W_{v,b}$ are the weight fraction of vapor at the interface and bulk conditions respectively. This formulation of the mass transfer suction factor has been implemented in a number of studies (e.g. Dehbi, 2015; Anderson, 1998a). Application is justified for turbulent flows since a significant portion of the concentration gradient lies within the laminar sub-layer.

de la Rosa et al. (2009b) proposed an alternate form of the suction factor. The underlying hypothesis that justifies the de la Rosa factor is that gas concentration profiles in the turbulent boundary layer are not influenced by the additional convective component caused by suction. As a result the driving force for mass transfer is altered compared to the Couette flow analysis and the suction factor is given by:

$$\theta_{\text{de la Rosa}} = \frac{1}{W_{nc,i}} \quad \text{Equation 3-23}$$

, where $W_{nc,i}$ is the weight fraction of non-condensable gas at the liquid film interface. Both forms of the suction parameter discussed here are assessed as part of the experimental data analysis.

3.4 Cylindrical Condensing Surfaces

The cylindrical test apparatus eliminates convective edge effects, distorted convection flow patterns due to sidewalls and enclosures as well as issues associated with heat loss to the surroundings that must be addressed for the flat plate geometry. The majority of experimental investigations have implemented cylindrical test geometries for these reasons in addition to their cost effectiveness. Due to the limited availability of flat plate experimental data, it is useful to compare the current flat plate experimental results

to cylindrical test results reported by other investigators.

Recently, Popiel (2008) reviewed free convection heat transfer from vertical cylinders. For cylinders in which the thermal boundary layer is thin compared to the diameter of the cylinder, the cylinder can be treated as a flat plate and Equation 3-20 is applicable. Typically, the criterion used to assess whether curvature should be considered is given as:

$$\text{Gr}_L^{0.25} \frac{D}{L} \leq 35 \quad \text{Equation 3-24}$$

, where D is the cylinder diameter. When this criterion is true, the curvature effect must be considered. Popiel notes that for turbulent free convection on a vertical cylinder, when curvature effects are important, there is a significant disparity in the published literature. The generalized correlations recommended by Popiel for this scenario appear to be inadequate since they do not include a parameter to account for the curvature effect.

Al-Arabi and Khamis (1982) conducted turbulent natural convection experiments using cylinders with 11 different lengths ranging from 0.3 to 2.0 m and six different diameters ranging from 12.75 to 51 mm. The ranges of cylinder length and diameter are appropriate for application of the heat and mass transfer analogy to the published results examined as part of this study. Furthermore, the experimental results of Tagami (1965) meet the flat plate criterion. Therefore, the Al-Arabi and Khamis correlation is used to assess the cylindrical results for this study. The Nusselt number for a cylindrical geometry with suction effect taken into account is:

$$\text{Nu}_{dl} = 0.47\theta \text{Gr}_D^{-1/12} \text{Ra}_c^{1/3} \quad \text{Equation 3-25}$$

, where Gr_D is the Grashoff number given in Equation 3-8 with the cylinder diameter as the length scale. For transition to turbulence, the critical Rayleigh number of 2.7×10^9 is suggested by Al-Arabi and Khamis and the correlation is applicable for $1.08 \times 10^4 \leq \text{Gr}_D \leq 6.9 \times 10^5$ and $2.7 \times 10^9 \leq \text{Ra}_L \leq 2.95 \times 10^{10}$.

For larger Gr_D or Ra_L , the Al-Arabi and Khamis (1982) correlation does not approach the flat plate result as would be expected by Equation 3-24. Therefore, caution is warranted when extrapolating the result to

larger Gr_D and Ra_L . For conditions in which extrapolation is necessary, implications are necessarily evaluated.

3.5 Inclined Flat Plate Condensing Surfaces

For inclined surfaces, Equation 3-26 provides the general form of the model proposed by Al-Arabi and Sakr (1988).

$$h_s = (0.1 + a_\theta) \frac{k}{L} Ra_s^{1/3} \quad \text{Equation 3-26}$$

The empirical parameter a_θ describes the influence of inclination angle. Al-Arabi and Sakr proposed a simple linear function for a_θ :

$$a_\theta = \frac{0.05\theta}{\pi} \quad \text{Equation 3-27}$$

, where θ is the angle of inclination from vertical in radians. For the vertical wall condition, the Al-Arabi and Sakr model reduces to the Bayley model.

4.0 Experimental Facility

A flat plate test facility has been constructed at the Westinghouse research laboratory in Churchill, PA for the purposes of investigating condensation heat transfer and film hydrodynamics. The test facility design corrects many of the issues associated with prior experimental efforts:

- Flat plate test article is housed within a large pressure vessel to minimize vessel wall effects
- Thermal bridging to non-isolated components of the facility minimized by using a rotating test plate with single shaft attachment
- Enclosed environment permits collection of condensation from the insulation, which allows precise characterization of insulation heat losses
- Direct measurements of condensation mass flow rate due to insulation losses and condensation on the test surface provide precision characterization of heat flux that can be directly compared to the coolant channel energy balance and heat flux monitored by conduction through the test plate
- Labyrinth cooling channels on the rear of the test article, along with a thick carbon steel test plate, promote uniform temperature distribution on the test plate
- High accuracy Coriolis mass flow measurements and platinum resistance thermal detectors are used for the coolant channel energy balance
- Uniformly distributed steam supply from a lower heated and mixed water pool minimizes influence of heat input to system on the natural convection process

Details of the test facility design are provided in the following sections.

4.1 Test Facility Description

Testing was conducted using 0.457 m x 2.13 m and a 0.914 m x 2.13 m condensing surfaces. The test plates are fabricated from carbon steel and coated with inorganic zinc coating. Each flat plate is suspended, using a central shaft, within a 2.59 m diameter, 4.88 m tall stainless steel pressure vessel. The test vessel is separable near the bottom shell via a large body flange to allow for installation and removal of large components. The vessel has 13, borosilicate view windows for optical access, and implements window heating to prevent condensation from obstructing the view.

The pressure vessel is rated to 4 bar (gage) and temperature of 155°C. The vessel is sized such that the test plates can be centered within the vessel and rotated 90° without contacting the vessel sidewalls. Figure 4-1 shows a model of the test facility with solid and transparent vessel walls. Figure 4-2 shows an image of the test facility.

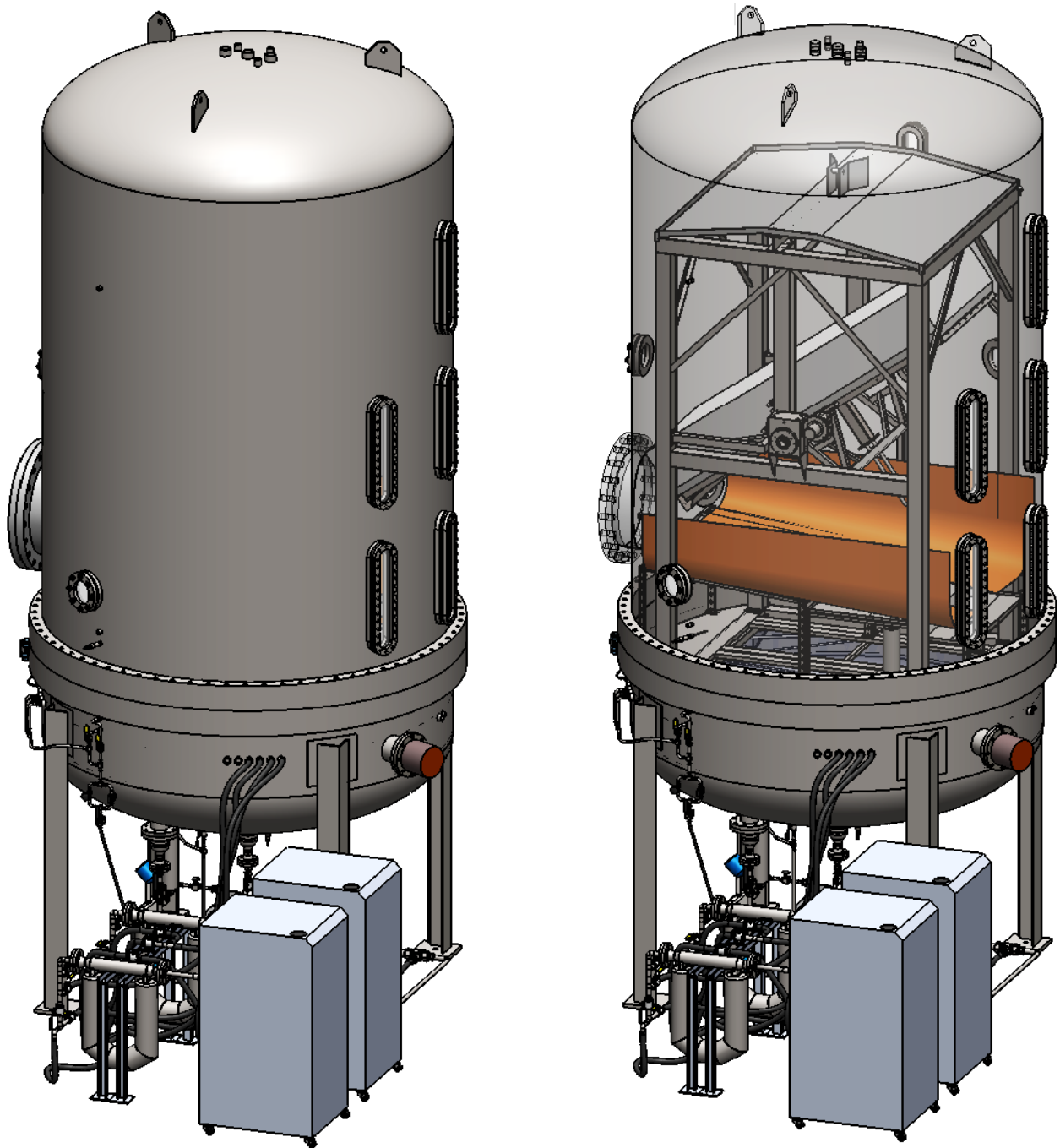


Figure 4-1 Test Facility Overview



Figure 4-2 Overview Image of Test Facility

The test plate is rotated by an air motor connected to one end of the test plate shaft. Compressed air is provided from outside of the vessel to turn the air motor, and air is discharged outside of the vessel such that there is no effect on the non-condensable mass fraction. A high temperature, sealed, digital inclinometer is used to precisely monitor the angle of the plate.

Heat addition to the test vessel is from a 120 kW immersion heater located at the bottom of the vessel submerged in a pool of water. Heat removal from the back of the test plate is accomplished with labyrinth cooling channels that promote uniform temperature distribution.

Cooling channels aligned vertically on the backside of the test plate are used to control condensing surface temperature. The cooling channels are machined out of solid blocks of stainless steel. The channels are mounted and sealed directly to the back of the test plate which allows the coolant water to contact the test plate. The cooling channels are supplied with water circulated through two Thermo Scientific 10 kW TF100D chillers.

All condensation that drips from the test plate surface, insulation and shaft connections is collected by a drip pan beneath the test plate and diverted to Tank 2. All condensation on the test plate surface that flows to the bottom of the plate is captured by a gutter and routed to a condensate collection tank, Tank 1. The rate at which condensate is collected is monitored with differential pressure transmitters.

To study the effect of the liquid film Reynolds number, film is applied to the top of the condensing surface via a porous film applicator. The film applicator is installed flush with the test plate surface and is fabricated out of porous stainless steel welded to a stainless steel channel. A pump draws suction from the gutter condensate collection tank and discharges through a heat exchanger that supplies the film applicator.

A platform within the vessel supports the weight of the large condensing test plate, support structure, collection tanks and drip pan. A roof is installed above the test plate to divert any water condensing and falling off of the upper dome section of the test vessel that could distort the test results. Figure 4-3 shows a diagram of the test facility.

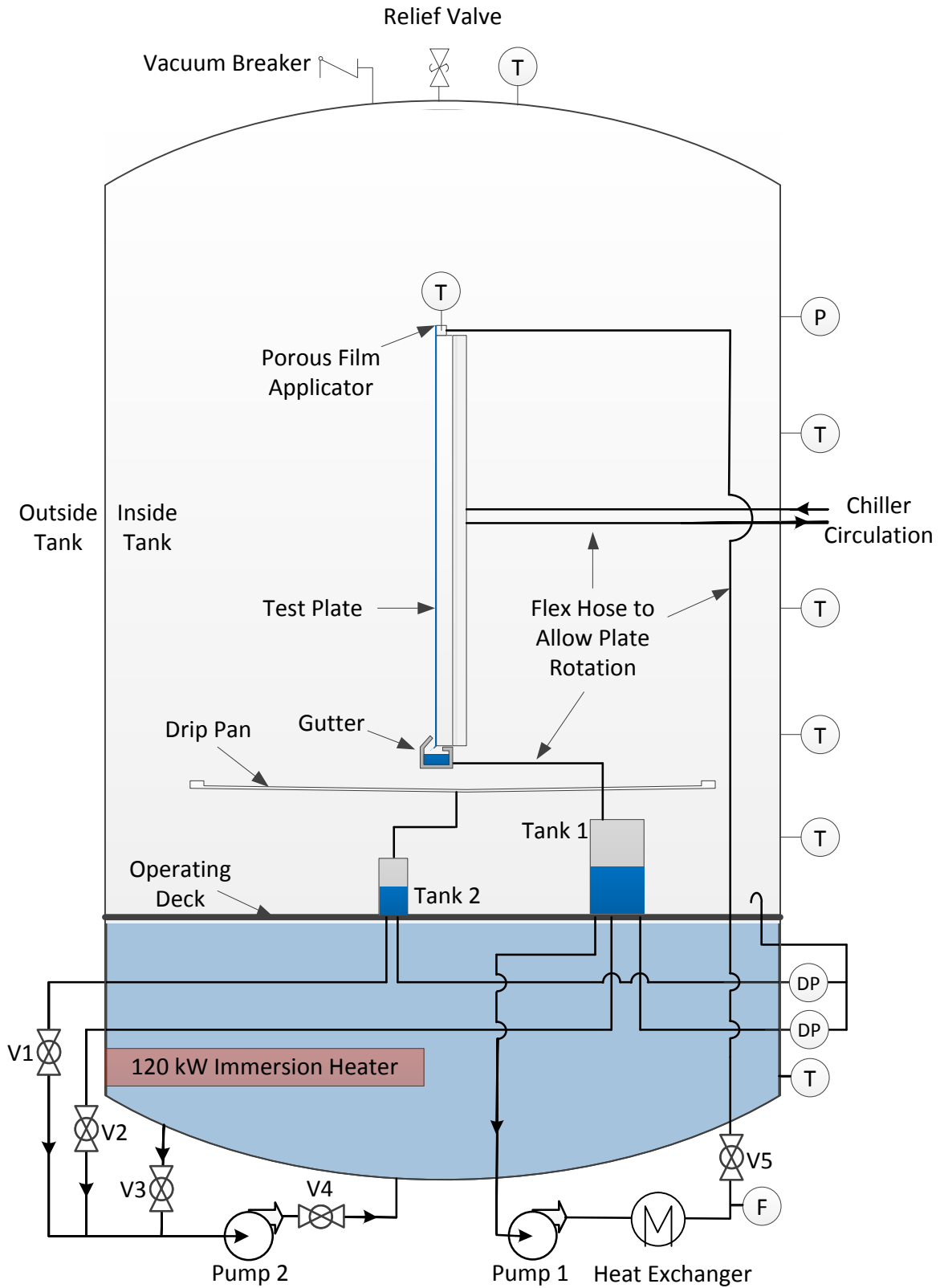


Figure 4-3 Test Facility Piping and Instrumentation Diagram

4.2 Test Article and Cooling Channel Design Details

The 0.914 m x 2.13 m condensing plate was fabricated from 4.13 cm thick AISI 1020 carbon steel and coated with Carbozinc 11HSN inorganic zinc. The 0.457 m x 2.13 m condensing plate was fabricated from 2.54 cm thick ASTM A36 carbon steel and coated with Carbozinc 11HSN inorganic zinc. The early 4.13 cm thick plate design was initially selected to be consistent with the AP1000 containment vessel thickness and to support a large temperature differential across the test plate for heat flux monitoring. The weight of the 4.13 cm thick test article, with cooling channels installed, was approximately 1 metric ton. To reduce fabrication and installation costs, the 0.457 m width plate was constructed from 2.54 cm thick carbon steel.

Test plate rotation is accomplished by fixing a shaft near the center of gravity of the plate, placing the ends of each shaft through fixed pillow block bearing supports and connecting to a gear reduced air motor as shown in Figure 4-4. All components of the motor, gear assembly and bearing supports are capable of withstanding the harsh, pressurized, condensing steam environment that exists in the vessel during testing.



Figure 4-4 Air Motor and Gear Box Connection with Test Plate

At the top of the test plate, a thin piece of stainless steel sheet metal is placed on the outside of the insulation that protrudes 3 cm out from the test plate surface and spans the width of the test plate. The sheet metal is thermally isolated from the test plate and acts to disturb the gas layer flow to assure turbulent gas layer flow along the length of the plate. This avoids the development of a short laminar layer on the upper portion of the condensing surface.

Four cooling channels aligned vertically on the backside of the test plate are used to control condensing surface temperature. The cooling channels are machined out of solid blocks of stainless steel measuring 0.457 m x 0.533 m x 1.90 cm. The channels are mounted and sealed directly to the back of the test plate and allow the coolant water to contact the rear of the test plate. Each cooling plate has an inlet and outlet connection for coolant flow as well as several penetrations for bolting and instrumentation. Figure 4-5 shows the cooling channel plate labyrinth geometry. Figure 4-6 shows the cooling channel dimensional detail. Figure 4-7 shows the cooling channels assembled on the test plate with coolant tubing and temperature measurements installed.

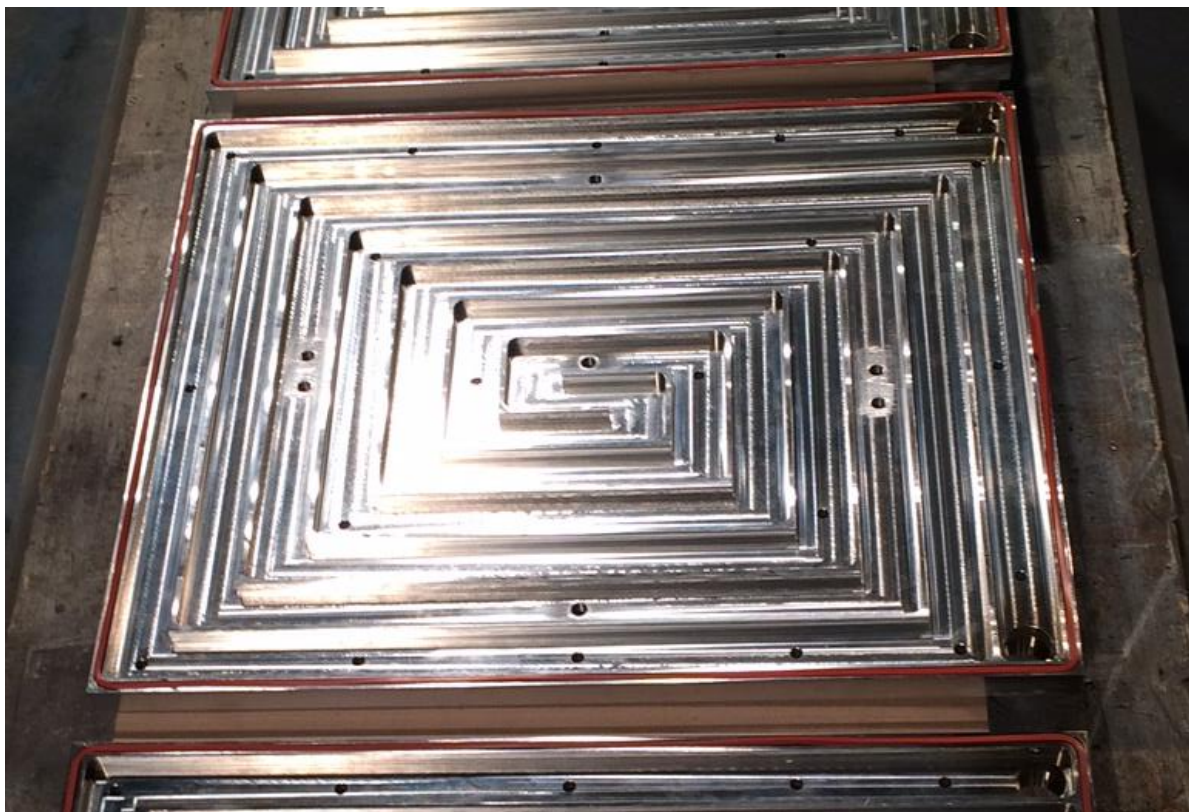


Figure 4-5 Cooling Channel Image

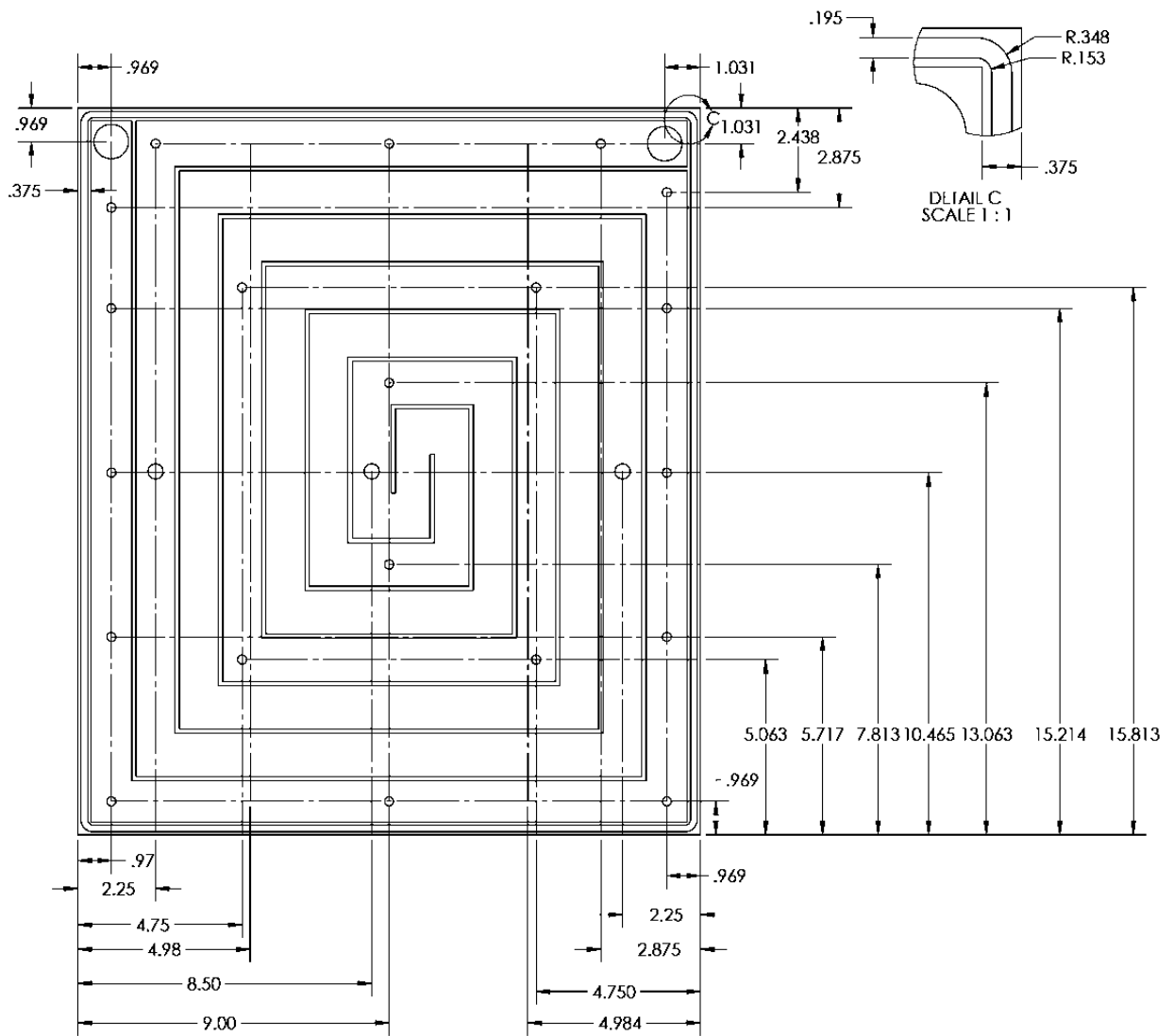


Figure 4-6 Cooling Plate Assembly Dimensional Detail (Dimensions in Inches)

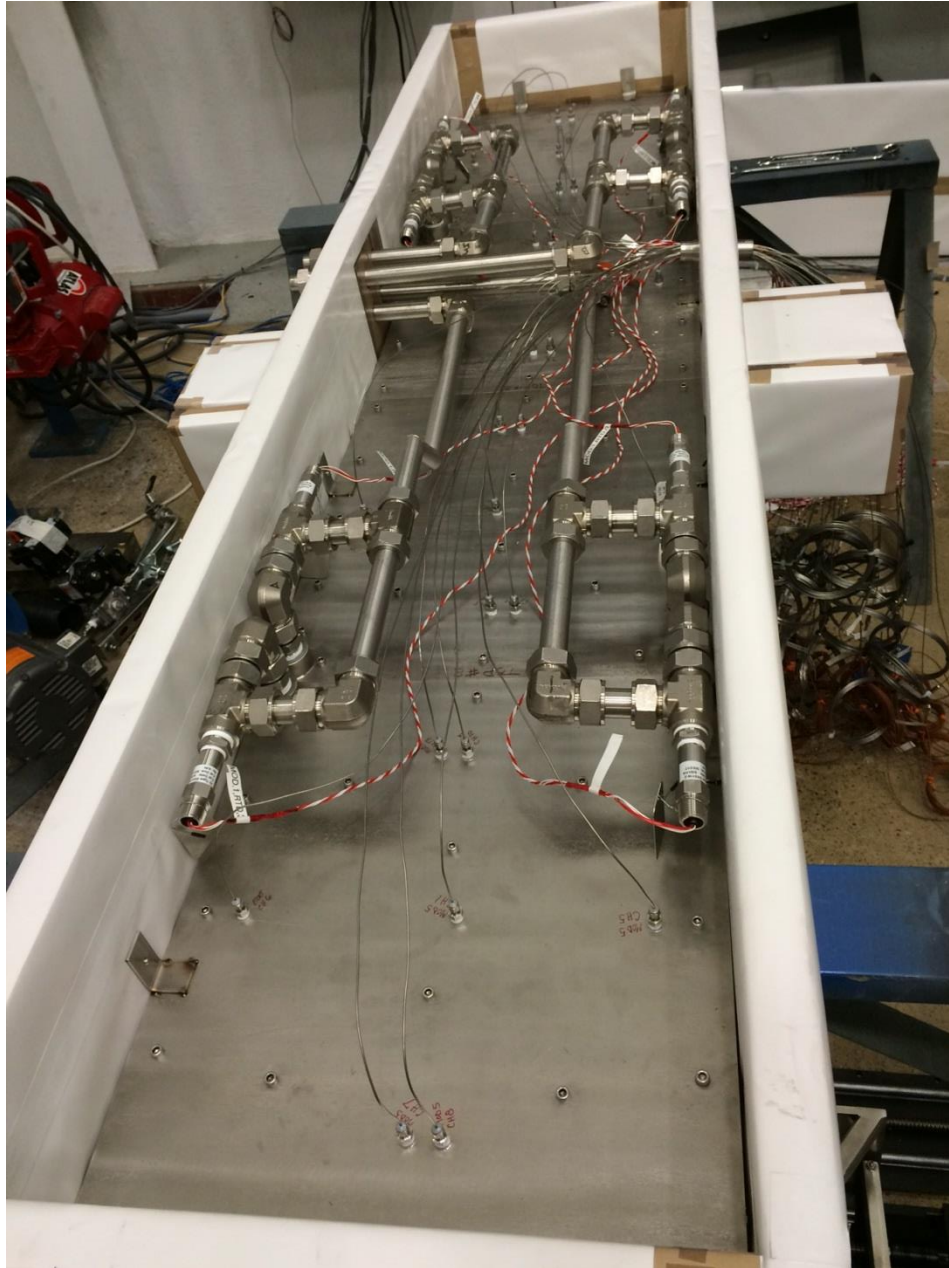


Figure 4-7 Cooling Channels Assembled on Rear of Test Plate with Coolant Tubing Installed

The test plate and cooling channels are insulated with TRYMER 6000® insulation wrapped in Saran® film. The TRYMER® insulation has a high compressive strength and will not crush under the pressurized conditions of the test vessel. The Saran® film provides an effective moisture barrier for the insulation. All gaps are sealed with silicone adhesive Teflon® tape or silicon caulking. Figure 4-8 shows the insulation installed on the back side of the test plate. Figure 4-9 shows the front side of the test plate.



Figure 4-8 Insulation Box viewed from Back of Test Plate



Figure 4-9 Front Side of Test Plate Installed in Vessel with Insulation Shown on Sides

4.3 Test Facility Operation

In preparation for a test, the vessel is initially filled to a level approximately 16 cm above the heater with deionized water. Conditions within the vessel are controlled by closing the system and heating the water to the desired temperature. For adjusting the non-condensable gas mass fraction upwards, compressed air is injected into the vessel in increments until the desired saturation temperature and pressure are attained. For adjusting the non-condensable gas mass fraction downward, the vent valve on the top of the tank is opened to release an air steam mixture to the environment. Throughout heat up of the vessel, cooling water flow through the cooling channels is initiated to control the condensing surface temperature.

Steady state conditions are confirmed prior to starting an experiment via continuous readouts from the cooling channel calorimetric data, temperature measurements located at various elevations within the test vessel, total pressure and collection tank differential pressure measurements. The process of adjusting the tank bulk non-condensable mass fraction and condensing surface temperature can take several hours for steady state, saturated conditions to develop. The tank environment is well mixed as a result of the geometric arrangement of the condensing surface within the vessel, uniformly distributed steam source from the lower pool and open operating deck. Prior to conducting an experiment, the vessel atmosphere temperature gradient is confirmed uniform, to within the measurement accuracy of the instruments.

Once steady state conditions are reached, the condensate collection tanks are drained before starting a test. The test is then initiated by closing the collection tank drain valves and starting data acquisition. Draining the collection tanks before starting data acquisition assures that the tests can be operated for as long as possible, without over-filling, to reduce uncertainty in the condensate mass measurement.

Maintaining a smooth film interface at low Reynolds number is ideal for comparison to the theoretical model. During initial condition setting, it was sometimes necessary to wipe the surface with a high liquid flow rate before operating tests at low Reynolds number. This action always resulted in a smooth, mirror-like film interface in the laminar liquid film regime. When these actions were not implemented, rivulets and other complex film regimes were observed and there was a measurable influence on the heat transfer rate. It is proposed that this type of behavior is one source of experimental variability that impacts results reported in literature.

5.0 Experimental Facility Instrumentation

5.1 Test Plate Temperature

For the 0.457 m x 2.13 m plate, surface temperature is monitored with 16 thermocouples installed into the test plate. Special limits of error, 1.59 mm diameter, grounded T-type thermocouples are used. The T-type thermocouple provides the highest measurement accuracy available for a thermocouple of $\pm 0.5^\circ\text{C}$, using a linear calibration, over the operating temperature range. The 1.59 mm diameter thermocouple is installed into a 3.17 mm diameter hole drilled into the test plate from the back side. During installation, thermally conductive grease (Dow Corning TC5622) is installed in the hole to minimize contact resistance.

Along the test plate centerline, 12 thermocouples are installed at 9.65, 26.7, 43.7, 63.0, 80.0, 97.0, 116.3, 133.3, 150.4, 169.7, 186.7 and 203.7 cm from the top of the test plate. A total of four thermocouples are installed 5.7 cm from the plate edge on either side at 80.0 cm and 133.3 cm from the top of the test plate. The tip of the surface temperature thermocouples are installed 4 mm from the test surface. The surface temperature thermocouple readings are corrected to the test surface temperature using the measured heat flux and plate thermal conductivity. Figure 5-1 shows the thermocouple installation layout for the 0.457 m width test plate.

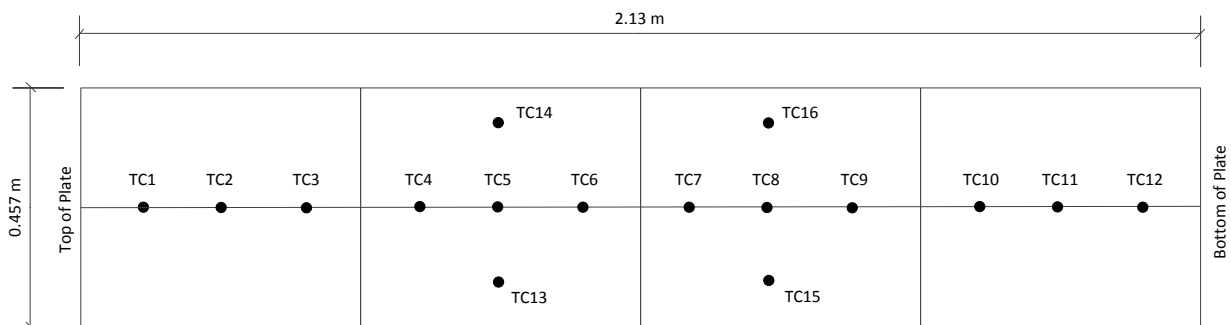


Figure 5-1 Test Plate Surface Temperature Measurement Locations

Thermocouples are installed using the same installation method in the 0.914 m x 2.13 m plate. However, only one thermocouple, TC6, located 35 cm from the bottom of the plate was available. Other thermocouples were installed, but these failed due to overtightening of the compression fittings that

severed the small thermocouple wiring. Teflon ferrules were used for later experiments to avoid this issue.

All plate surface temperature thermocouples are calibrated against a reference standard platinum resistance temperature detector of higher accuracy in a Fluke 9171 metrology well.

5.2 Tank Environment Conditions

The test vessel water temperature and vessel atmosphere temperature at the bottom elevation of the test plate are monitored with Rosemount model 0068 Pt-100 platinum resistance temperature detectors (RTDs). The vessel atmosphere temperature gradient is monitored with special limits of error, 1.59 mm diameter, grounded T-type thermocouples. All thermocouples and resistance thermal detectors are calibrated against a reference standard platinum resistance thermal detector of higher accuracy in a Fluke 9171 metrology well. The vessel absolute pressure is monitored with a Rosemount 3051CA absolute pressure transmitter with sensing line sloped upwards to avoid condensate build-up. All pressure instrumentation is calibrated at an ISO-17025 certified laboratory.

5.3 Calorimetric Heat Removal Rate

The heat removal rate from each chiller is monitored separately. Mass flow is monitored with two Micromotion CMF200 Coriolis flow meters. Temperature differential across each of the cooling channels is monitored using Rosemount model 0068 Pt-100 platinum RTDs. The RTDs were installed directly at the inlet and outlet of each cooling channel. The flow instrumentation is calibrated at an ISO-17025 certified laboratory. All cooling channel RTDs are calibrated against a reference standard platinum RTD of higher accuracy in a Fluke 9171 metrology well.

5.4 Collection Tank Mass Flow Rates

The collection tank mass flow rates are monitored with Rosemount model 3051S differential pressure transducers referenced to the tank atmosphere. The tank atmosphere sensing line is installed with an inverted J-tube placed above the water level. With the tube opening facing downward and the tube routed underwater, no condensate can accumulate inside the tubing. The differential pressure instrumentation is calibrated at an ISO-17025 certified laboratory.

5.5 Film Applicator Mass Flow Rate and Temperature

The film application flow rate is monitored with a Micromotion CMFS025 Coriolis sensor downstream of the pump. Using the gutter condensate collection tank to supply film, level changes within the condensate collection tank are only due to condensation on the test surface. This assures high accuracy condensation rate measurement. Due to some heat transfer along the flow circuit, the porous film applicator is installed with a T-type thermocouple in the channel to assure an accurate energy balance. The film applicator thermocouple is calibrated against a reference standard platinum RTD of higher accuracy in a Fluke 9171 metrology well. The flow meter is calibrated at an ISO-17025 certified laboratory.

5.6 Film Thickness

Water film thickness is measured using a chromatic confocal displacement sensor. A summary of this measurement method is provided by Lel et al. (2005). Figure 5-2 shows a schematic of the measurement method. A white light source is passed, via a fiber optic cable, to an optical probe. The optical probe consists of a series of lenses that act to focus various light wavelengths at different distances from the probe. Light is reflected from the measurement interface back through the fiber optic cable, and is returned, via a dichroic mirror, to the measurement head. The measurement head measures the intensity of light for the entire wavelength spectrum and correlates the wavelengths with highest intensities to a distance using a calibration curve that relates light wavelength to focal distance. To measure film thickness, light reflected from the plate interface and the film interface must both be within the optical measuring range of the probe. This results in two intensity peaks at different wavelengths. The corresponding distance between these two peaks is determined from the probe calibration and a correction to account for the refractive index of water is necessary as described by Lel et al. (2005).

A Precitec Chrocodile M4 module with LED light source is used for confocal displacement sensor measurement. The selected probe head provides a spatial resolution of 4 μ m with a measurement rate of 4000 Hz. To apply this measurement technique in a pressurized condensing environment, custom probes were manufactured by Precitec. The probes have a weep hole for pressure equalization within the series of lenses to avoid pressure forces acting on the optics. Furthermore, it is necessary to heat the optical

probe to temperatures slightly above the pressurized steam environment such that condensation does not occur on the optics.

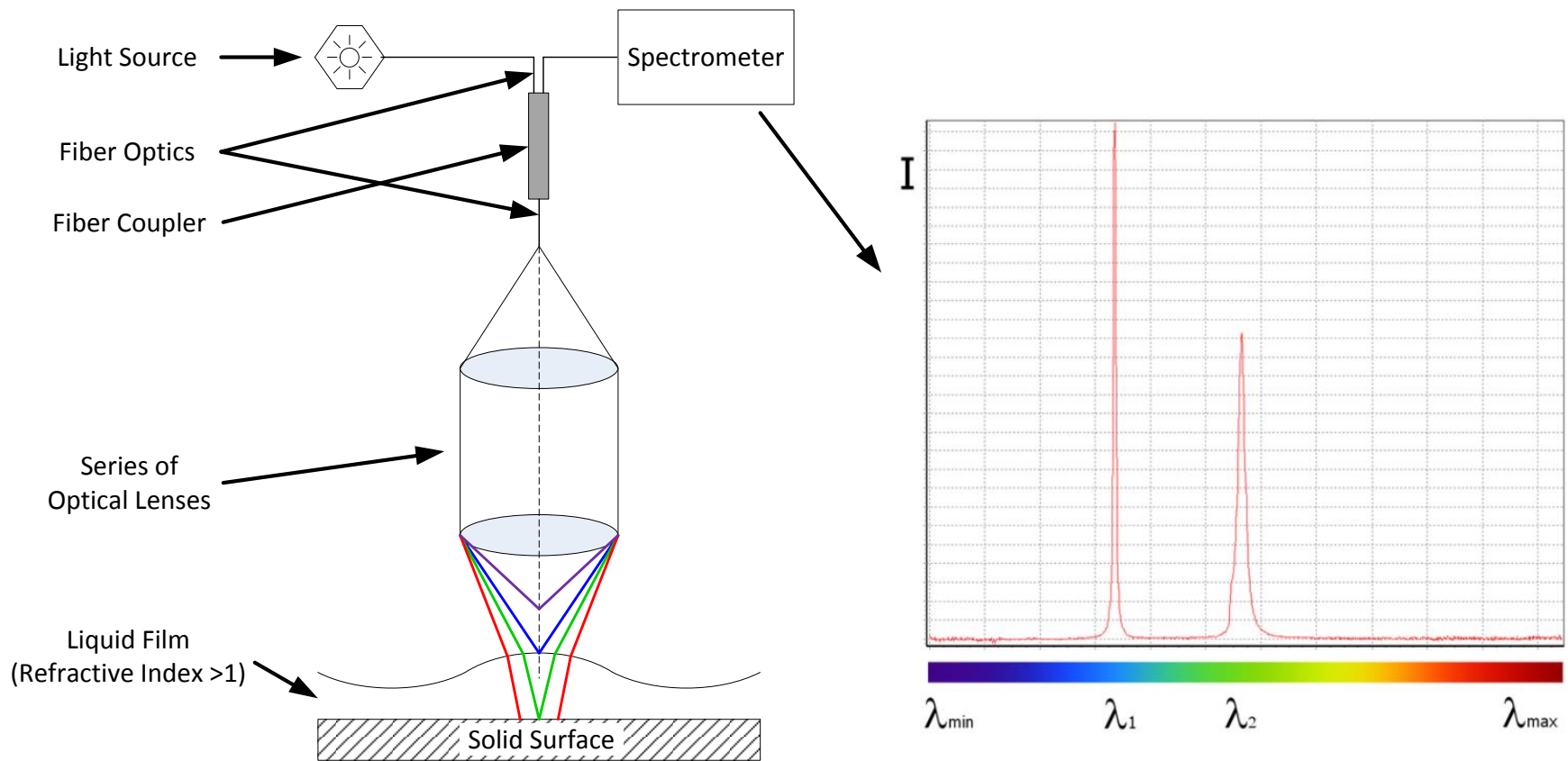


Figure 5-2 Chromatic Confocal Film Thickness Measurement Method

5.7 Optical Access

The test vessel has a total of eight, 4" x 24" obround view windows and five, 6" circular view windows. The view windows are strategically placed to allow for straight-on, side, angled and rear viewing of the test plate. All obround view windows are placed for front, side and angled viewing of the test plate at various elevations. The circular view windows are placed at angled and rear locations for lighting and viewing purposes.

Four view windows, two with a front view and two with a side view of the test plate, are heated via 1000 Watt air circulation heaters. The view windows are heated to prevent condensation from occurring on the inside. This allows clear observation and video recording. Figure 5-3 shows one of the view window heaters.

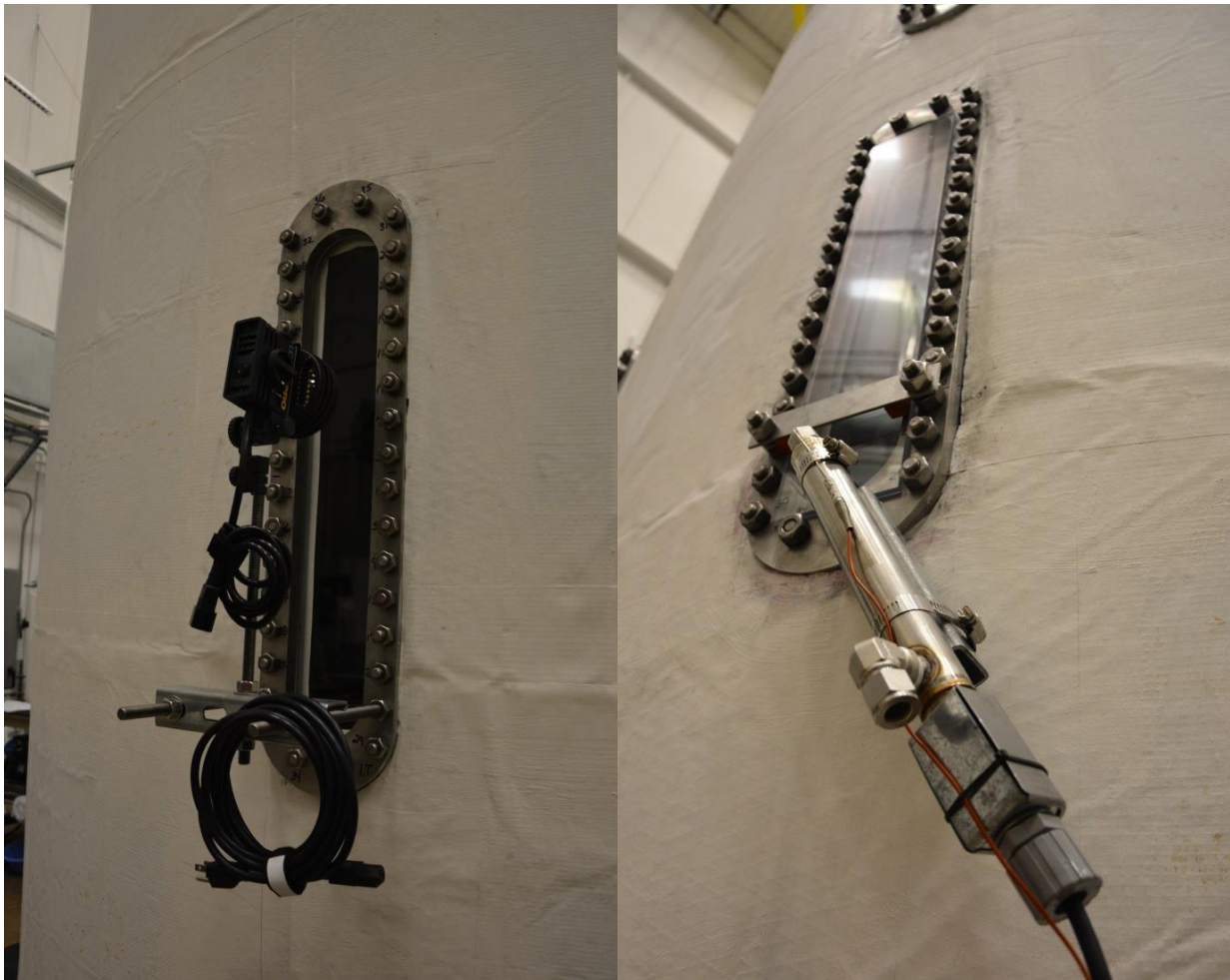


Figure 5-3 View Window Lighting (Left) and Forced Air Heater (Right)

5.8 Inclination Angle Measurement

The angle of the test plate is measured using the $\pm 60^\circ$ inclinometer. The inclinometer is positioned at an offset of 45° . This was done such that the inclinometer could cover the full span of rotation for the test plate (0° to 90°). Figure 5-4 shows the inclinometer housing connected to the test plate shaft. Figure 5-5 shows an illustration of the inclinometer housing internals. Figure 5-5 shows two inclinometers installed; however, only one is used for the experimental results reported here.

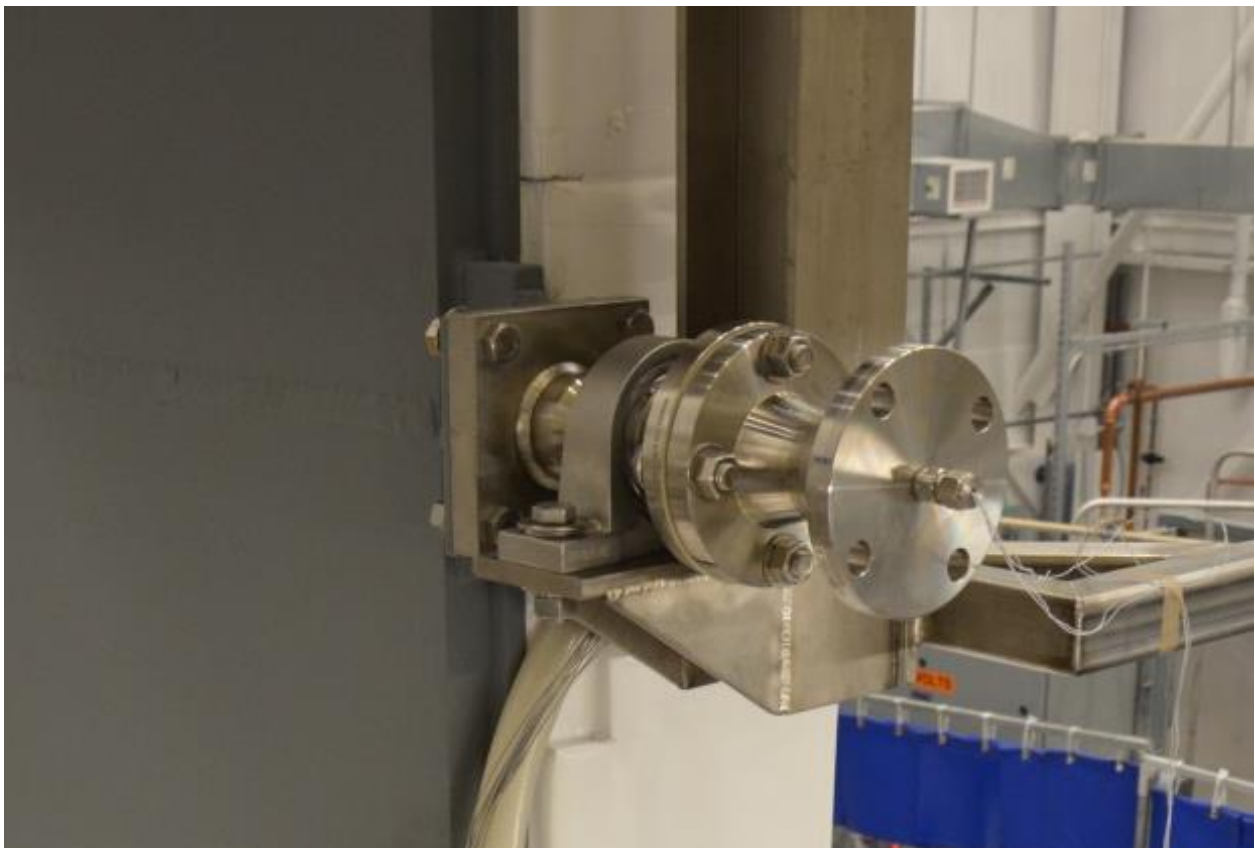


Figure 5-4 Inclinometer Housing Installed on 0.914 m Width Plate Shaft

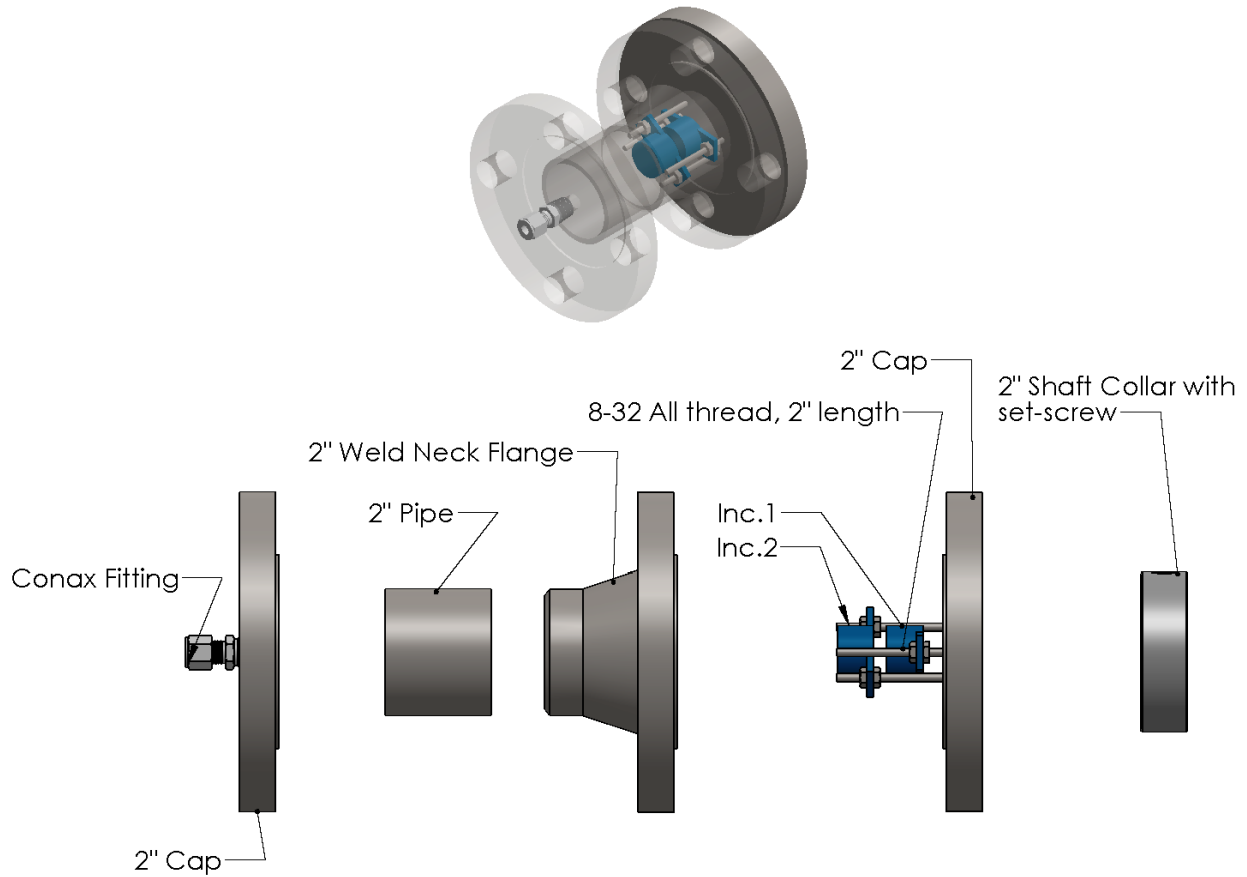


Figure 5-5 Inclinometer Housing Design

5.9 Instrumentation Summary

Table 5-1 provides a list of the instrumentation used for the 0.457 m width plate experiments. Table 5-2 gives the instrumentation for the 0.914 m width plate experiments. These lists show all instrumentation that was connected to the data acquisition system and recorded continuously for each experiment. A separate acquisition system was used for the film thickness measurement. A complete listing of the instrumentation model and serial numbers along with accuracy statement is provided in Appendix A.

Table 5-1 Instrumentation Summary for 0.457 m Wide Plate Experiments			
Instrument ID	Type	Manufacturer	Location description
RTD1	Resistance Temperature Detector	Rosemount	Cooling channel 1 outlet temperature
RTD2	Resistance Temperature Detector	Rosemount	Cooling channel 2 outlet temperature
RTD3	Resistance Temperature Detector	Rosemount	Cooling channel 1 inlet temperature
RTD4	Resistance Temperature Detector	Rosemount	Cooling channel 2 inlet temperature
RTD5	Resistance Temperature Detector	Rosemount	Cooling channel 3 inlet temperature
RTD6	Resistance Temperature Detector	Rosemount	Cooling channel 4 inlet temperature
RTD7	Resistance Temperature Detector	Rosemount	Cooling channel 3 outlet temperature
RTD8	Resistance Temperature Detector	Rosemount	Cooling channel 4 outlet temperature
RTD9	Resistance Temperature Detector	Rosemount	Inserted 10 cm from bottom of tank below water level
RTD10	Resistance Temperature Detector	Rosemount	Inserted 10 cm from side of tank above water level at 1.4 m above bottom of tank
TC1-12	T-Type Thermocouple	Omega	Test plate centerline (see Figure 5-1)
TC13-16	T-Type Thermocouple	Omega	Test plate lateral (see Figure 5-1)
TC17	T-Type Thermocouple	Omega	Applied film temperature
TC18	T-Type Thermocouple	Omega	Inserted above main tank water level, 20 cm from side of tank at 3.8 m elevation above bottom of tank
TC19	T-Type Thermocouple	Omega	Inserted above main tank water level, 20 cm from side of tank at 2.0 m from bottom of tank
CFM1	Coriolis Flow Meter	Rosemount	Chiller 1 mass flow rate
CFM2	Coriolis Flow Meter	Rosemount	Chiller 2 mass flow rate
CFM3	Coriolis Flow Meter	Rosemount	Film applicator mass flow rate
P1	Absolute Pressure Transmitter	Rosemount	Tank atmosphere pressure
DP1	Differential Pressure Transmitter	Rosemount	Gutter collection tank level
DP2	Differential Pressure Transmitter	Rosemount	Drip pan collection tank level
Inc	Inclinometer	Penny & Gilles	Test plate shaft

Table 5-2 Instrumentation Summary for 0.914 m Wide Plate Experiments			
Instrument ID	Type	Manufacturer	Location description
RTD1	Resistance Temperature Detector	Rosemount	Inserted 10 cm from bottom of tank below water level
RTD2	Resistance Temperature Detector	Rosemount	Chiller 2 cooling channel inlet header temperature
RTD3	Resistance Temperature Detector	Rosemount	Chiller 1 cooling channel outlet header temperature
RTD5	Resistance Temperature Detector	Rosemount	Chiller 2 cooling channel outlet header temperature
RTD7	Resistance Temperature Detector	Rosemount	Chiller 1 cooling channel inlet header temperature
RTD12	Resistance Temperature Detector	Rosemount	Inserted 10 cm from side of tank above water level at 1.42 m above bottom of tank
TC6	T-Type Thermocouple	Omega	Test plate surface temperature inserted from back of plate, 35 cm from bottom of plate
TC13	T-Type Thermocouple	Omega	Inserted above main tank water level, 20 cm from side of tank at 3.78 m elevation above bottom of tank
TC14	T-Type Thermocouple	Omega	Inserted above main tank water level, 20 cm from side of tank at 2.49 m from bottom of tank
TC16	T-Type Thermocouple	Omega	Inserted below main tank water level, 20 cm from side of tank at 0.76 m from bottom of tank
CFM1	Coriolis Flow Meter	Rosemount	Chiller 1 mass flow rate
CFM2	Coriolis Flow Meter	Rosemount	Chiller 2 mass flow rate
CFM3	Coriolis Flow Meter	Rosemount	Film applicator mass flow rate
P1	Absolute Pressure Transmitter	Rosemount	Tank atmosphere pressure
DP1	Differential Pressure Transmitter	Rosemount	Gutter collection tank level
DP2	Differential Pressure Transmitter	Rosemount	Drip pan collection tank level
Inc	Inclinometer	Penny & Gilles	Test plate shaft

6.0 Heat Transfer Coefficient Analysis

The average error in heat transfer coefficient measurement reported by Dehbi (1991) was $\pm 15\%$. The analysis of uncertainty by Dehbi only accounted for the random variability of the temperature measurements and not the instrument accuracies as compared to a reference standard. Liu (1999) reports measurement error ranging from 7 to 18%. This measurement uncertainty range is not supported by the experimental results provided. As shown in Appendix C.7, in some cases the bulk to wall temperature differential was less than 4°C and Liu (1999) states that manufacturer calibrations were accepted for thermocouple readings. Su et al. (2014) reports measurement uncertainty of $\pm 20\%$ and Kim et al. (2009) reports a measurement uncertainty of $\pm 25\%$. Anderson (1998a) reports the results of two independent measurement methods and states an accuracy of $\pm 15\%$ for each method; however, as shown in Appendix C.8, discrepancies between the coolant energy balance and local heat flux measurement methods are well in excess of $\pm 15\%$. Kataoka et al. (1994), Tagami (1965) and Uchida et al. (1965) do not report uncertainties. The analysis of experimental uncertainty presented here demonstrates an improvement compared to the reviewed studies.

Three independent methods of determining the heat transfer coefficient are implemented. The most accurate method is via direct measurement of the condensate mass flow from the test surface. A coolant channel energy balance and a measure of the thermal conduction through the test plate are also employed.

For the coolant channel energy balance, each of the cooling channels is instrumented with RTDs installed in the inlet and outlet fittings. The cooling channels are combined into two sets with header tubing and the feed flow to each set of cooling channels is monitored with Coriolis mass flow meters. To calculate the heat transfer coefficient from the coolant channel energy balance, it is necessary to account for the enthalpy change of film applied to the test surface for experiments with liquid film applied and correct for heat loss to the surroundings. The applied film enthalpy difference is corrected using measured temperatures. Heat losses are corrected using measured condensate loss rates from the trough collection container.

Local heat flux is monitored by analyzing conduction through the test plate at each surface temperature

measurement location. Knowing the thermal conductivity of the test plate and temperature on the backside of the test plate, the local heat flux can be calculated. The temperature distribution on the backside of the test plate can be accounted for by using T-type thermocouples installed in each cooling channel to monitor coolant temperature at intermediate points along the length of the channel. This method is relatively inaccurate since the temperature differential across the cooling channels is small, the thermal conductivity of the plate was only determined to within $\pm 15\%$ and a model of the convective heat transfer coefficient between the cooling channel fluid and the test plate surface must be solved.

Measurement using the condensate mass flow is the most accurate method of determining the heat transfer coefficient. The latent heat transfer rate is calculated from measured quantities by multiplying the condensate mass flow rate by the latent heat of condensation, assuming saturated conditions at the condensing interface. The sensible heat transfer rate is determined using the model presented in Section 3.0 and added to the latent heat transfer rate. Since the sensible heat transfer makes up a very small fraction of the overall heat transfer rate, a relatively high uncertainty of $\pm 30\%$ can be applied to this term with little effect on the overall uncertainty.

The uncertainty analysis for each of the three methods is carried out in accordance with the guidance provided in ASME PTC 19.1-2013. The measurement uncertainty from each measured quantity, including the device and analog to digital conversion, is propagated using the law of propagation of uncertainty to determine the heat transfer coefficient measurement uncertainty. In addition to the uncertainty in predicted sensible heat rate, the condensate mass flow rate based measurement uncertainty includes components to account for the uncertainty in the collection tank cross sectional area, thermal expansion of the collection tanks, differential pressure, temperature and latent heat uncertainty of 0.2% using the IAPWS-95 formulation from Wagner et al. (2002).

For conditions in which the measurement results from each method did not agree within the expected measurement uncertainty, the results were evaluated and typically discarded. As a result, many more experiments were conducted that were discarded than kept in the final dataset. In some cases it was evident that equilibrium conditions had not been reached and in others there were issues with equipment that required correction.

Table 6-1 summarizes results of the uncertainty analysis for the vertical plate conditions. Table 6-1 does not include results for conditions in which film was applied. The condensate mass based uncertainties are essentially the same under these conditions and the calorimetric results are slightly worse when film is applied. This is due to the increased uncertainty from the correction required to account for the sensible heat change of the applied film flow.

Table 6-1 Summary of Heat Transfer Coefficient Measurement Uncertainty Analysis							
T_b	T_i	P_b	h_t (Condensate Mass)		h_t (Calorimetric)		Difference
°C	°C	bar	W/m ² -K	Uncertainty	W/m ² -K	Uncertainty	
94.3±0.3	59.5±0.6	0.980±0.004	359.0	±2.1%	371.8	±7.0%	3.5%
86.1±0.3	60.1±0.6	0.972±0.004	193.6	±2.7%	198.0	±17.0%	2.3%
87.4±0.3	52.2±0.6	0.974±0.004	200.8	±2.1%	203.5	±12.5%	1.3%
76.3±0.3	19.6±0.6	0.977±0.004	77.8	±2.2%	85.5	±18.0%	9.0%
84.8±0.3	35.1±0.6	0.964±0.004	139.3	±1.9%	143.9	±12.6%	3.2%
118.1±0.3	88.6±0.6	2.792±0.004	395.0	±2.5%	405.8	±7.7%	2.7%
75.3±0.3	58.0±0.6	1.609±0.004	74.0	±4.5%	75.7	±24.4%	2.2%
101.8±0.3	69.9±0.6	2.317±0.004	166.3	±3.2%	160.0	±6.2%	3.9%
75.4±0.3	66.1±0.6	1.583±0.004	77.9	±9.0%	97.6	±33.2%	20.2%

For the majority of experimental results reported, the uncertainty in the condensate mass based method is better than ±5%. For the last condition shown Table 6-1 the uncertainty is ±9%. This relatively high uncertainty was driven almost entirely by the accuracy of measuring the small bulk to interface temperature difference. Figure 6-1 shows a comparison of the condensate mass and calorimetric based heat transfer coefficient measurement methods for the vertical plate test conditions. The error bars represent the calorimetric measurement uncertainty. For a complete description of the analysis methodology refer to Appendix B. For a summary of measurement and uncertainty analysis results for all experiments, refer to Appendix E.

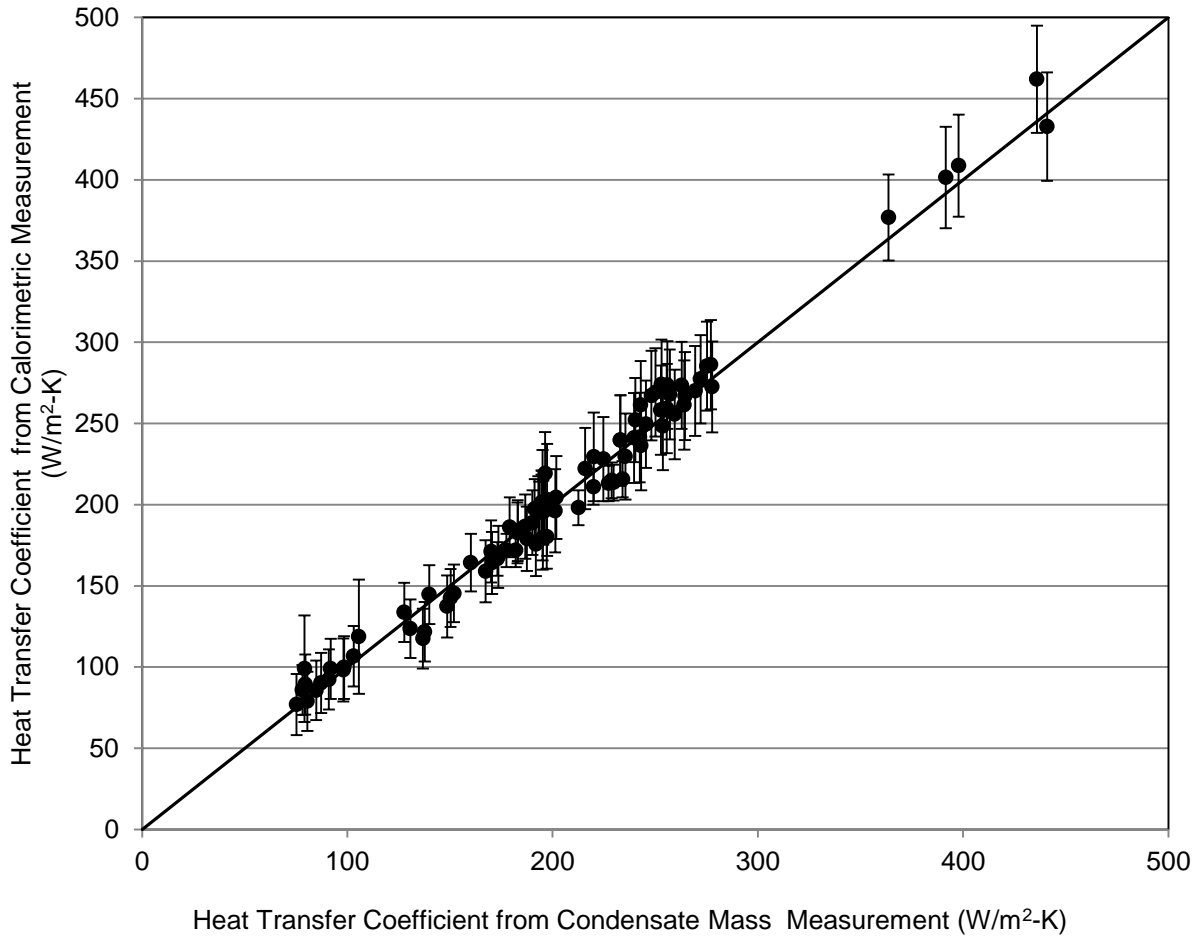


Figure 6-1 Comparison of Heat Flux Measurement Methods

7.0 Experimental Results

Table 7-1 and Table 7-2 provide a list of experimental conditions with primary measurement and calculation results presented. The methods used to calculate the wall temperature, T_w , and total heat transfer coefficient, h , from measurement results are given in Appendix B. The quantity, \dot{m}_{ap} , represents the mass flow rate of water applied at the top of the plate from the porous film applicator. The bulk vapor and non-condensable weight fractions, $W_{v,b}$ and $W_{nc,b}$, are determined assuming saturated conditions using the gas properties as defined in Appendix D. All other measurement results are provided in Appendix E. The Reynolds number, Re_r , is determined at the mid-plate elevation.

Test ID	Inc	P_b	\dot{m}_{ap}	Re_r	T_b	T_w	h	$W_{v,b}$	$W_{nc,b}$
	°				bar	kg/hr	°C		
T914_001	82	1.606	0	1.2	75.5	57.3	79	0.169	0.831
T914_002	80	1.604	0	1.3	75.5	57.4	83	0.169	0.831
T914_003	78	1.603	0	1.4	75.4	57.4	90	0.169	0.832
T914_004	78	2.371	0	7.6	101.5	70.2	222	0.342	0.659
T914_005	78	2.366	0	7.5	101.4	70.0	221	0.341	0.659
T914_006	75	1.601	0	1.6	75.3	57.4	102	0.168	0.832
T914_007	75	2.372	0	7.6	101.5	70.3	223	0.342	0.659
T914_008	57	1.587	0	0.9	75.2	66.2	104	0.170	0.831
T914_009	57	2.369	0	7.7	101.7	70.6	227	0.345	0.656
T914_010	50	1.592	0	1.5	75.4	58.3	97	0.170	0.830
T914_011	37	1.592	0	1.5	75.4	58.2	97	0.170	0.830
T914_012	37	2.356	0	7.2	101.5	70.2	212	0.345	0.656
T914_013	15	1.594	0	1.3	75.8	58.1	86	0.173	0.827
T914_014	15	2.355	0	7.1	101.7	70.0	205	0.347	0.653
T914_015	0	2.300	0	6.1	101.9	70.1	175	0.361	0.639
T914_016	0	1.609	0	1.1	75.3	58.0	74	0.167	0.833
T914_017	0	2.317	0	5.8	101.8	69.9	166	0.356	0.645
T914_018	0	1.596	0	1.2	75.8	58.1	78	0.173	0.828
T914_019	0	1.583	0	0.7	75.4	66.1	78	0.172	0.829
T914_020	0	2.357	0	6.0	101.8	69.5	171	0.349	0.652

Table 7-2 Test Matrix Summary for 0.457 m Width Plate

Test ID	Inc	P _b	m _{ap}	Re _Γ	T _b	T _w	h	W _{v,b}	W _{nc,b}
	°	bar	kg/hr		°C	°C	W/m ² -K		
T457_001	0	0.980	0	12.0	94.3	59.5	359	0.768	0.232
T457_002	0	0.978	0	4.8	85.7	60.1	196	0.494	0.506
T457_003	0	0.972	0	4.8	86.1	60.1	194	0.509	0.491
T457_004	0	0.970	0	5.8	87.4	52.6	199	0.543	0.457
T457_005	15	0.970	0	6.7	87.2	53.4	233	0.539	0.461
T457_006	30	0.970	0	7.1	86.8	53.7	252	0.527	0.473
T457_007	45	0.970	0	7.5	86.5	54.0	267	0.519	0.481
T457_008	60	0.970	0	7.6	86.2	54.0	276	0.512	0.488
T457_009	75	0.970	0	7.1	85.7	53.4	258	0.500	0.500
T457_010	75	0.970	67	87.4	86.2	54.4	257	0.512	0.489
T457_011	75	0.971	56	73.0	85.8	52.6	255	0.501	0.500
T457_012	60	0.971	54	70.9	85.5	52.7	252	0.493	0.507
T457_013	45	0.972	58	74.6	85.6	52.6	238	0.496	0.505
T457_014	45	0.972	61	80.1	85.7	54.5	254	0.499	0.502
T457_015	45	0.972	58	75.4	85.7	53.2	246	0.498	0.503
T457_016	0	0.974	0	6.4	88.0	52.7	215	0.557	0.444
T457_017	15	0.974	0	7.0	87.6	53.4	239	0.546	0.455
T457_018	31	0.974	0	7.4	86.9	53.8	262	0.528	0.472
T457_019	45	0.973	0	7.7	86.5	54.0	274	0.519	0.482
T457_020	60	0.973	0	7.7	86.5	54.0	276	0.518	0.483
T457_021	75	0.973	0	7.6	86.6	53.9	271	0.521	0.479
T457_022	75	0.973	44	60.1	86.2	53.4	264	0.510	0.491
T457_023	60	0.972	11	20.8	86.0	53.7	263	0.505	0.495
T457_024	76	0.972	54	71.0	85.9	53.2	249	0.503	0.497
T457_025	60	0.972	51	67.8	85.5	53.4	252	0.494	0.506
T457_026	0	0.971	80	101.7	86.1	53.3	242	0.508	0.492
T457_027	0	0.971	202	246.5	86.1	53.3	236	0.509	0.491
T457_028	0	0.970	0	5.6	86.5	52.1	195	0.520	0.480
T457_029	0	0.974	0	5.9	87.4	52.2	201	0.542	0.459
T457_030	15	0.974	0	6.5	87.4	52.8	224	0.543	0.458
T457_031	30	0.973	0	7.0	86.9	53.3	244	0.529	0.472
T457_032	45	0.974	0	7.1	86.3	53.4	252	0.513	0.487
T457_033	60	0.975	0	7.1	86.1	53.4	256	0.506	0.494
T457_034	75	0.974	0	7.1	86.1	53.3	255	0.507	0.493
T457_035	75	0.974	55	71.0	85.6	52.8	242	0.494	0.507
T457_036	45	0.974	102	127.0	85.4	52.9	232	0.488	0.512
T457_037	45	0.974	102	127.0	85.4	52.9	232	0.488	0.512
T457_038	30	0.974	103	128.0	85.5	53.0	239	0.490	0.510

Table 7-2 Test Matrix Summary for 0.457 m Width Plate Continued

Test ID	Inc	P _b	m _{ap}	Re _Γ	T _b	T _w	h	W _{v,b}	W _{nc,b}
	°	bar	kg/hr		°C	°C	W/m ² -K		
T457_039	15	0.973	102	127.7	85.7	53.0	242	0.498	0.503
T457_040	0	0.972	102	126.4	85.7	52.7	219	0.497	0.503
T457_041	0	0.977	0	1.8	76.3	19.6	78	0.309	0.691
T457_042	0	0.974	233	155.0	74.5	22.4	92	0.285	0.716
T457_043	0	0.973	104	78.0	74.7	27.2	91	0.287	0.713
T457_044	0	0.975	0	5.0	87.6	36.4	159	0.545	0.455
T457_045	0	0.974	4	8.5	87.3	36.4	151	0.539	0.462
T457_046	0	0.974	9	12.3	87.2	36.5	149	0.536	0.465
T457_047	0	0.973	40	42.2	86.3	37.9	182	0.513	0.488
T457_048	0	0.973	42	44.0	86.2	37.8	182	0.510	0.490
T457_049	0	0.972	121	113.1	85.6	36.6	183	0.494	0.506
T457_050	0	0.972	238	214.7	85.2	36.0	179	0.485	0.516
T457_051	15	0.972	243	219.2	84.8	36.0	191	0.476	0.524
T457_052	30	0.971	249	223.2	83.9	35.6	193	0.455	0.545
T457_053	30	0.971	0	5.7	84.9	37.2	192	0.479	0.521
T457_054	30	0.969	56	56.3	83.8	37.6	194	0.455	0.545
T457_055	45	0.969	57	57.0	83.2	37.5	194	0.440	0.560
T457_056	61	0.968	58	57.7	83.0	37.1	195	0.437	0.563
T457_057	75	0.967	0	5.6	83.5	36.9	196	0.448	0.553
T457_058	75	0.966	25	27.8	83.4	37.4	196	0.446	0.554
T457_059	60	0.966	23	25.6	83.0	36.9	191	0.438	0.562
T457_060	60	0.965	0	5.5	83.1	36.8	194	0.441	0.560
T457_061	60	0.966	59	57.2	82.4	36.7	186	0.425	0.576
T457_062	45	0.966	54	53.3	82.4	37.0	189	0.425	0.575
T457_063_A	45	0.966	125	116.6	82.5	36.8	195	0.427	0.574
T457_063_B	45	0.966	123	114.7	82.4	36.7	187	0.426	0.574
T457_064_A	0	0.966	122	113.4	83.6	36.4	173	0.452	0.548
T457_064_B	0	0.966	121	112.0	83.7	36.3	169	0.453	0.547
T457_065_A	0	0.966	52	51.0	83.8	36.7	170	0.457	0.543
T457_065_B	0	0.966	50	49.5	83.9	36.8	167	0.458	0.542
T457_066	0	0.964	0	4.1	84.8	35.1	139	0.481	0.520
T457_067	0	0.962	5	7.9	84.8	34.7	130	0.481	0.519
T457_068	0	0.963	12	14.2	84.3	35.3	136	0.469	0.531
T457_069	0	0.962	18	19.6	84.0	34.9	137	0.463	0.538
T457_070	0	0.962	30	30.2	83.6	36.1	148	0.454	0.547
T457_071	0	0.971	0	3.7	84.1	34.5	127	0.460	0.541
T457_072	0	2.792	0	16.7	118.1	88.6	395	0.563	0.437

Clear fluorinated ethylene propylene (FEP) tubing was installed in the line connecting the gutter collection tank and pump 1, as shown in Figure 4-3. During testing, with pump 1 supplying flow to the film applicator, small bubbles were observed to form in the tubing. This was attributed to non-condensable gas dissolution as a result of localized pressure reduction near fittings installed in the tubing. Between each experimental condition, the flow path was flushed with high velocity flow to clear the bubbles. To confirm this phenomenon had no impact on the test results, a series of experiments were conducted to examine different methods of draining the gutter collection tank. The experimental conditions T457_063, 064 and 065 labeled “_A” were operated with the normal drain path through pump 2, which does not flush the pump 1 suction line. The experimental conditions labeled “_B” were flushed with a high flow through the pump 1 suction line, through pump 1 and discharged to the tank via a separate isolation valve that was opened only for flushing and draining. The second method, “_B”, was only used for this study since it results in an undesirable thermal transient in the film applicator tubing. The conclusion of this small parametric was that the influence of the non-condensable gas buildup during an individual experiment was negligible as shown in Table 7-1.

7.1 Test Data Analysis Description

The calculation steps necessary to convert the measurement results to heat transfer rates and coefficients are provided in Appendix B. This section provides a high level review of the data analysis and evaluation and provides detailed graphical results for one of the experiments to aid in understanding the measurement methods.

After setting the initial conditions for each experiment, the tank environment and test plate temperatures are allowed to stabilize for several hours before collecting data. Once this process is complete, the data file name is set and data acquisition is commenced for that experiment. Typically, data is recorded over a period of 20 minutes to 1 hour depending on the fill rates of the condensate collection containers. During this time, data is acquired at a rate of 200 Hz and then averaged every second such that the data records are in 1 Hz format. This process eliminates high frequency noise.

Figure 7-1 and Figure 7-2 show the measured tank atmosphere temperatures and atmosphere pressure, with instrument IDs consistent with those provided in Table 5-1 for the 0.457 m width plate experiments.

Figure 7-1 shows that there is a temperature difference of 8°C between the lower pool, RTD9, and the atmosphere temperature. Comparing the three measurement locations at different elevations in the tank atmosphere, RTD10, TC18 and TC19, thermal gradients within the tank are negligible, and within the measurement accuracy of the instruments. This evaluation assures that the conditions within the vessel are well mixed and the tank has reached thermal equilibrium.

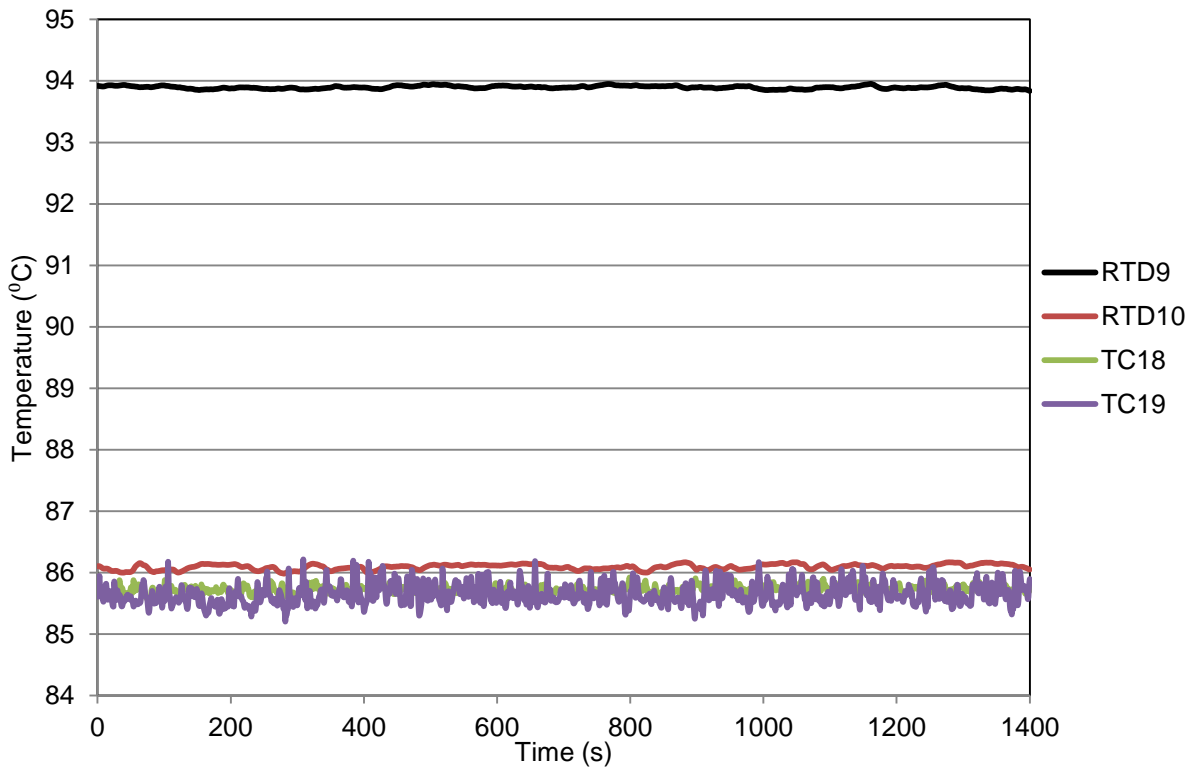


Figure 7-1 Test T456_026 Tank Temperatures

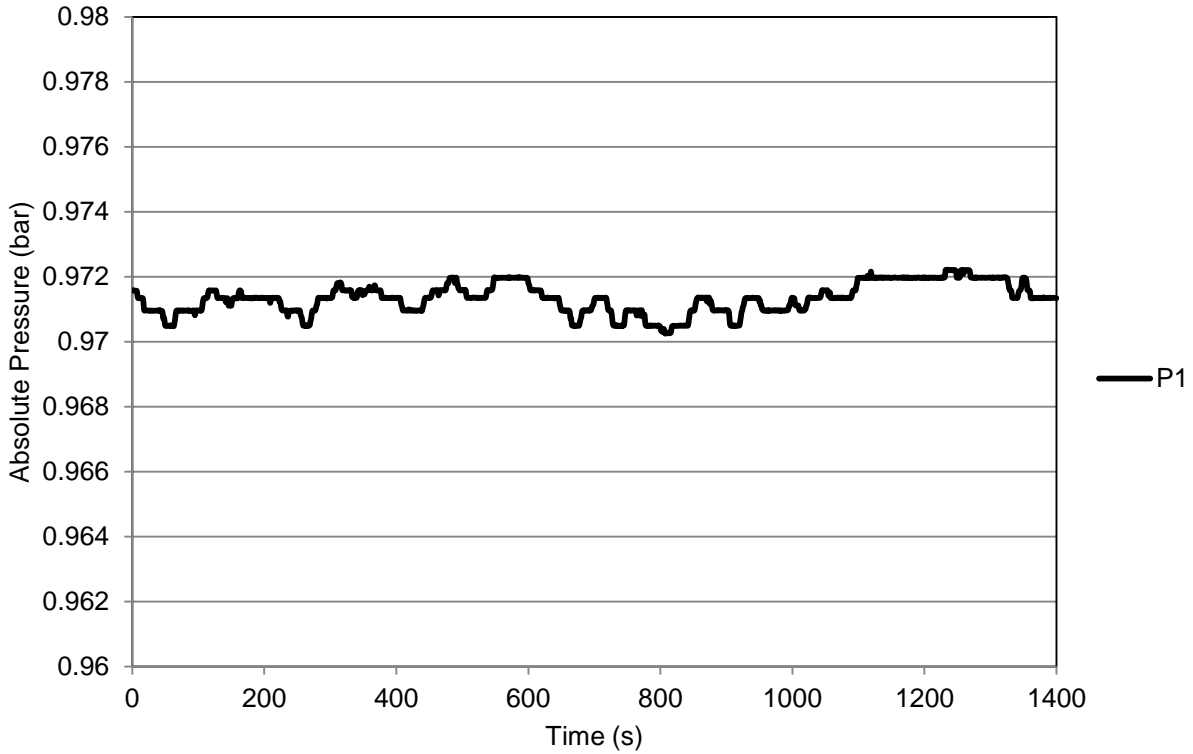


Figure 7-2 Test T456_026 Absolute Pressure

Figure 7-3 shows the cooling channel inlet and outlet temperatures and Figure 7-4 shows the cooling channel mass flow rates. Some small amplitude oscillations are observed in the cooling channel inlet and outlet temperatures. These are attributed to the chiller temperature controller and could not be eliminated. The cooling channel mass flow rates, which are monitored with Coriolis flow meters, exhibit noise levels that are approximately 1.5% of the measured rate. This noise was attributed to the close proximity of the film applicator pump. Later experiments included a flexible rubber hose that acts as a hydraulic dampener between the pump and flow meter to reduce the noise level.

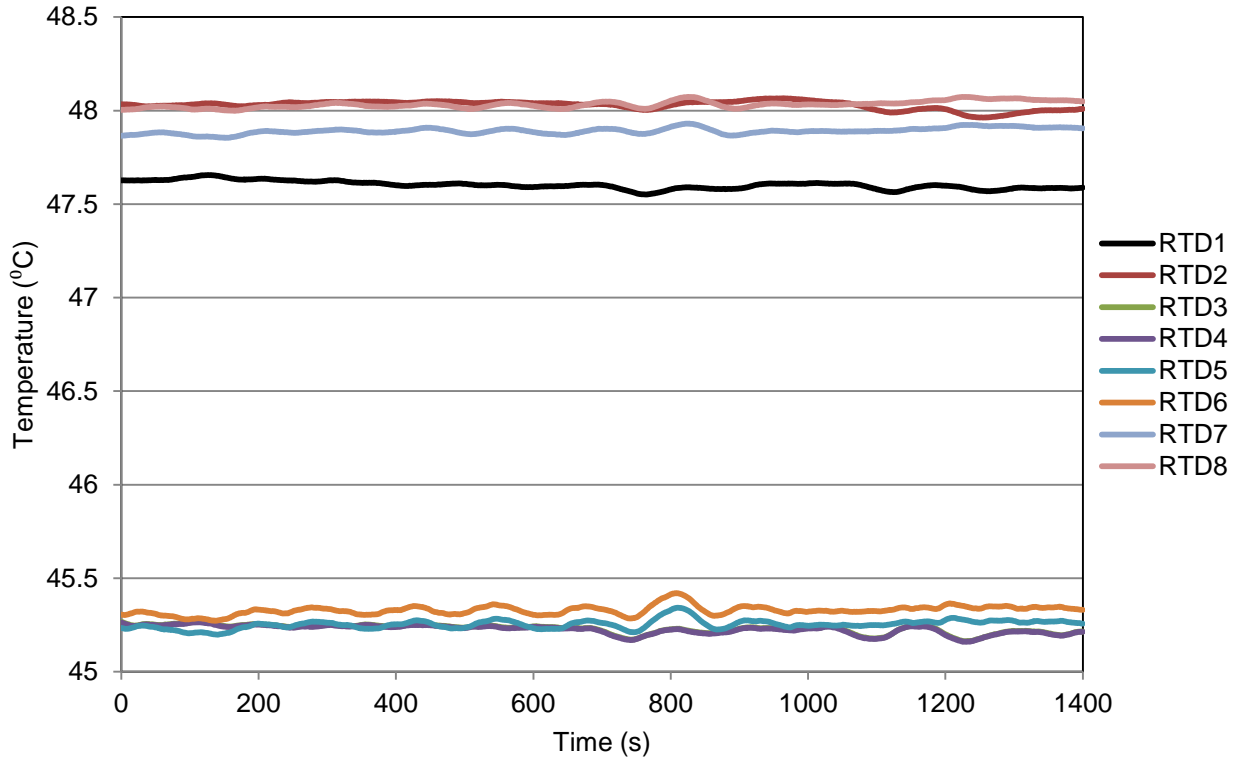


Figure 7-3 Test T456_026 Cooling Channel Inlet and Outlet Temperatures

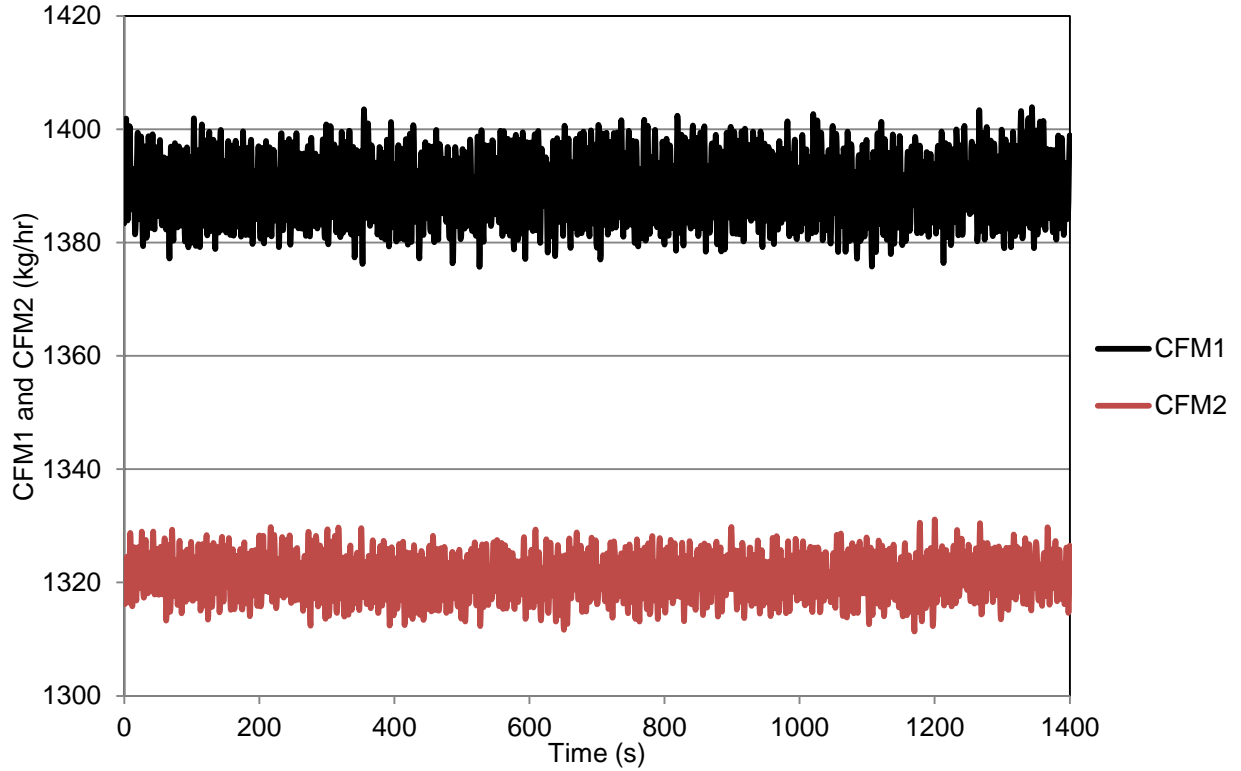


Figure 7-4 Test T456_026 Cooling Channel Mass Flow Rates

Figure 7-5 and Figure 7-6 show the measured differential pressure across the gutter and trough collection tanks. For this experiment, the gutter was drained and refilled twice, while the trough container was only drained and filled once. The calculated mass flow rates based on these measurements are provided in Appendix E.1. Noting that different collection container cross sectional areas apply to the gutter and trough flow rate calculations, the gutter mass flow rate is 0.00318 kg/s and the trough mass flow rate is 0.00005 kg/s for this experiment. A simple analysis of the insulation losses can be conducted by comparing the ratio of the trough flow rate to the total condensate flow rate. This analysis shows that the insulation losses were only 1.5% for this experiment. This confirms good performance of the insulation material and test article design to minimize losses.

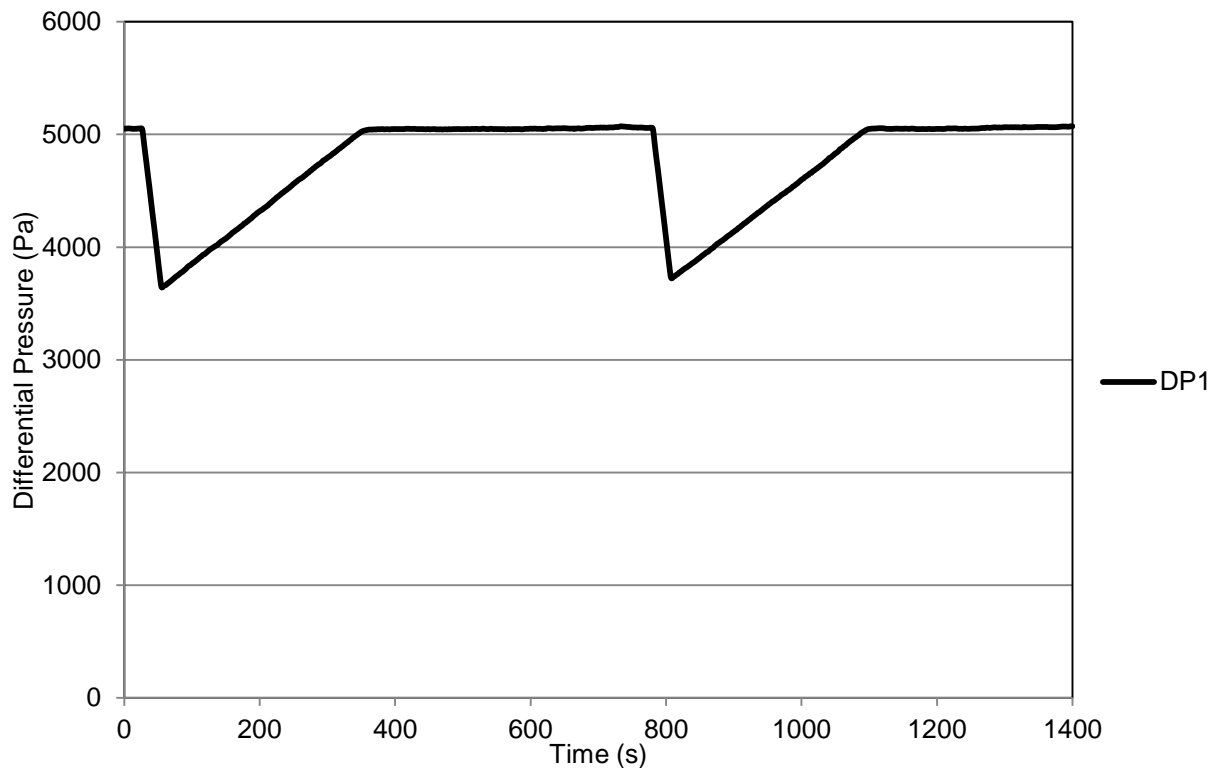


Figure 7-5 Test T456_026 Gutter Collection Tank Differential Pressure

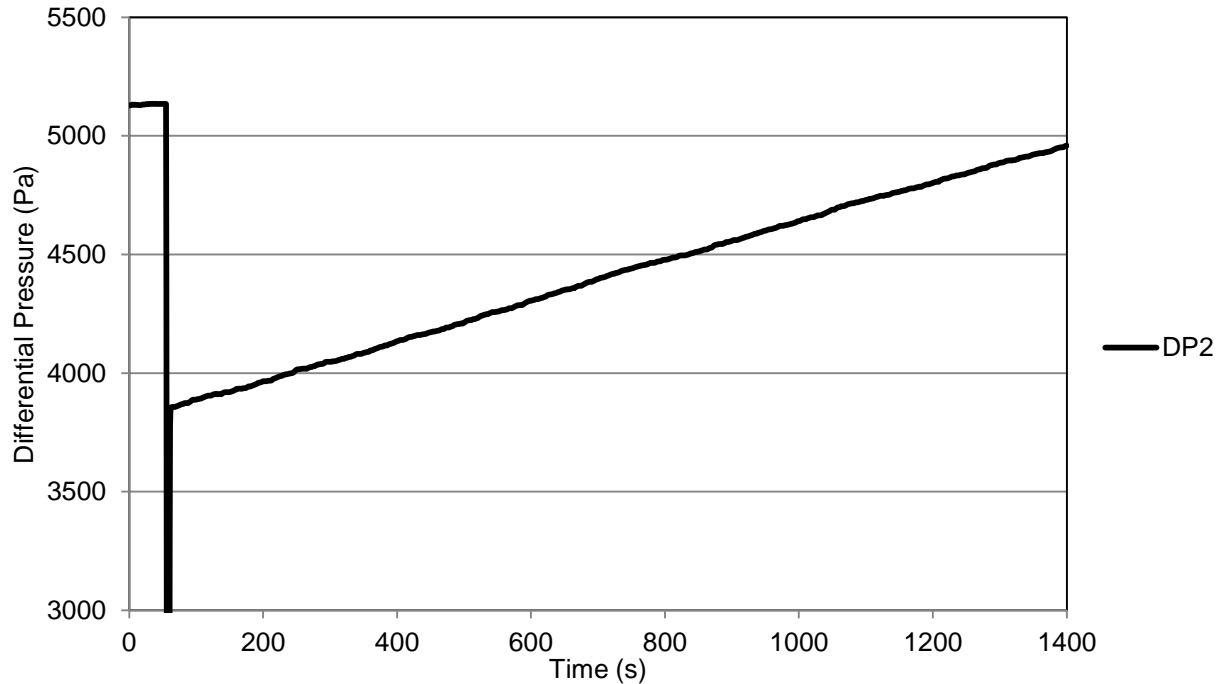


Figure 7-6 Test T456_026 Trough Collection Tank Differential Pressure

Figure 7-7 and Figure 7-8 give the measured centerline temperatures along the vertical length of the test plate as shown in Figure 5-1. Figure 7-9 shows the applied film mass flow rate and Figure 7-10 shows the applied film temperature as the water enters the film applicator. For this experiment, the applied film temperature was controlled to approximately equal to the measured plate temperature. This resulted in a relatively uniform temperature along the entire condensing surface, with variation held to within 2.5°C. It is worth noting here that when the gutter collection tank was drained, as shown in Figure 7-5, this corresponds to a small thermal transient that is detected in the applied film flow rate measurement, the film applicator temperature measurement and the uppermost plate surface temperature measurement, T1. Nonetheless, the magnitude of the transient is considered negligible.

Figure 7-11 and Figure 7-12 show the lateral temperature gradients. For this experiment, there were no clear trends associated with the lateral temperature gradients. However, reviewing the entirety of tabulated results shown in Appendix E.1, some of the experiments showed a gradient with slightly lower temperature in the center of the plate than on the edges. However, the gradient was always small with respect to the bulk to interface temperature difference.

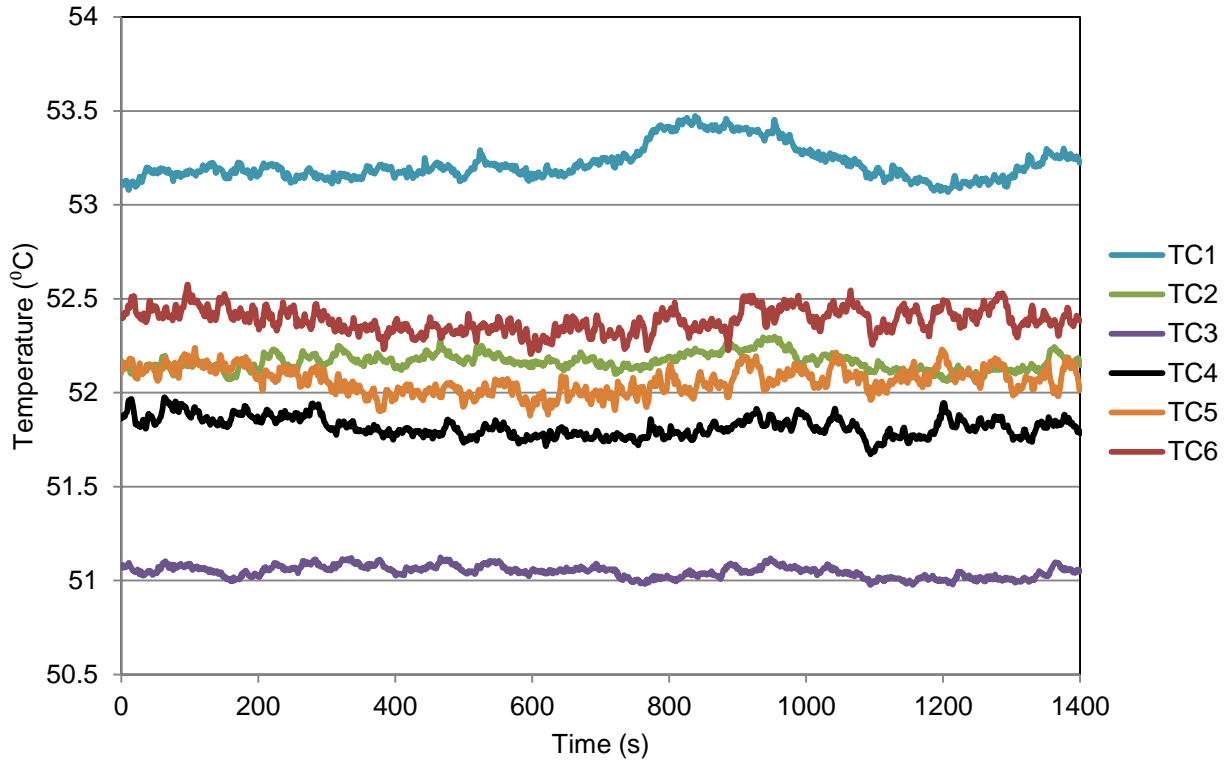


Figure 7-7 Test T456_026 Upper Vertical Test Plate Temperatures

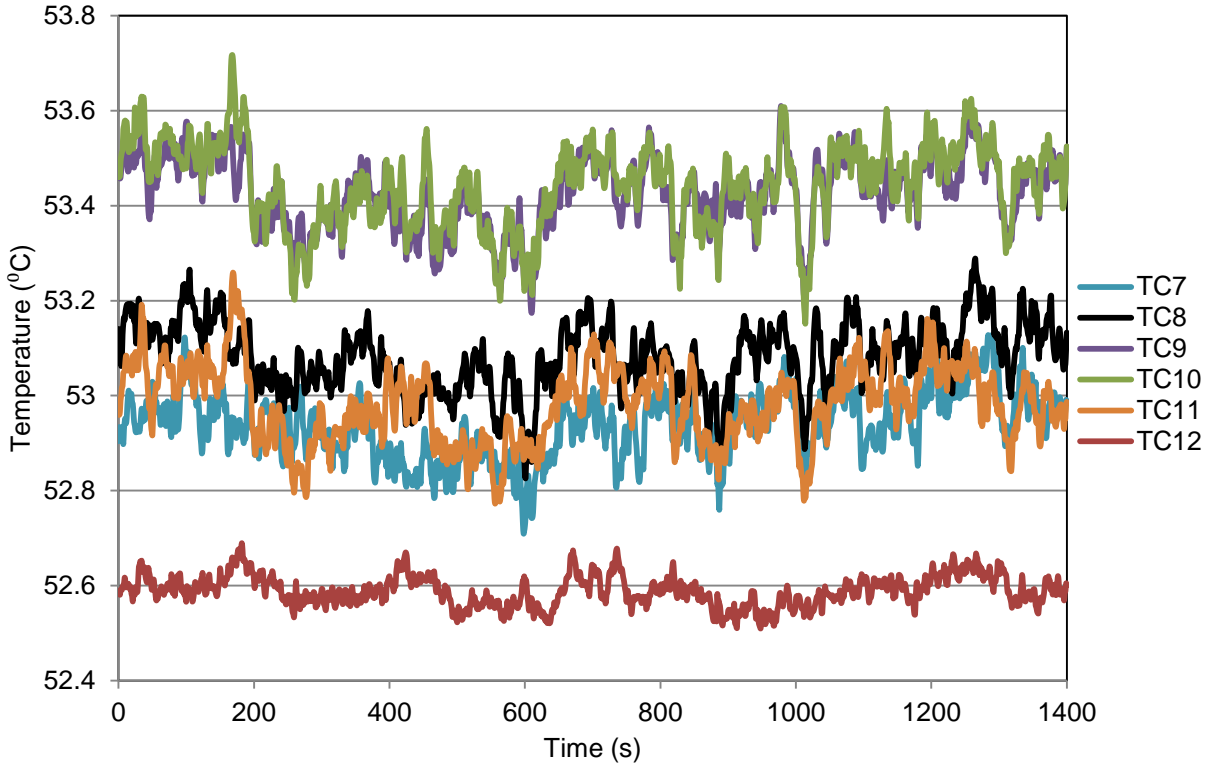


Figure 7-8 Test T456_026 Lower Vertical Test Plate Temperatures

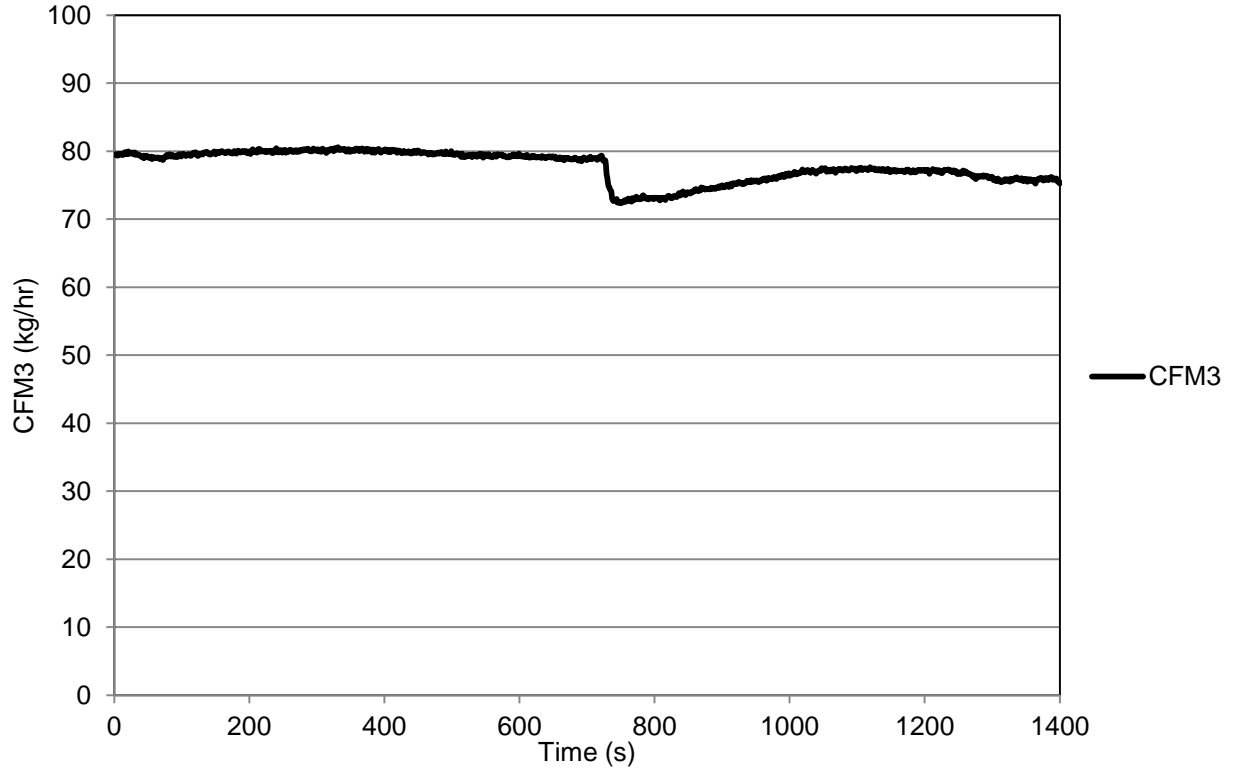


Figure 7-9 Test T456_026 Applied Film Mass Flow Rate

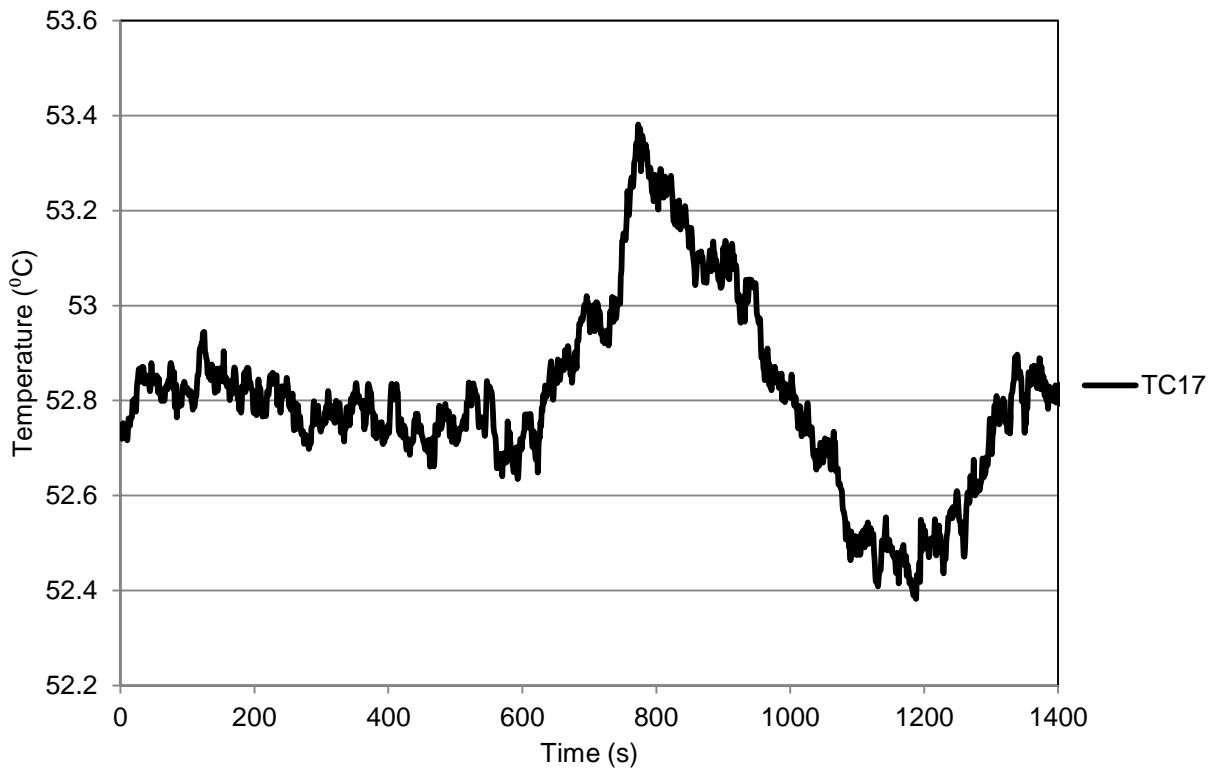


Figure 7-10 Test T456_026 Applied Film Temperature

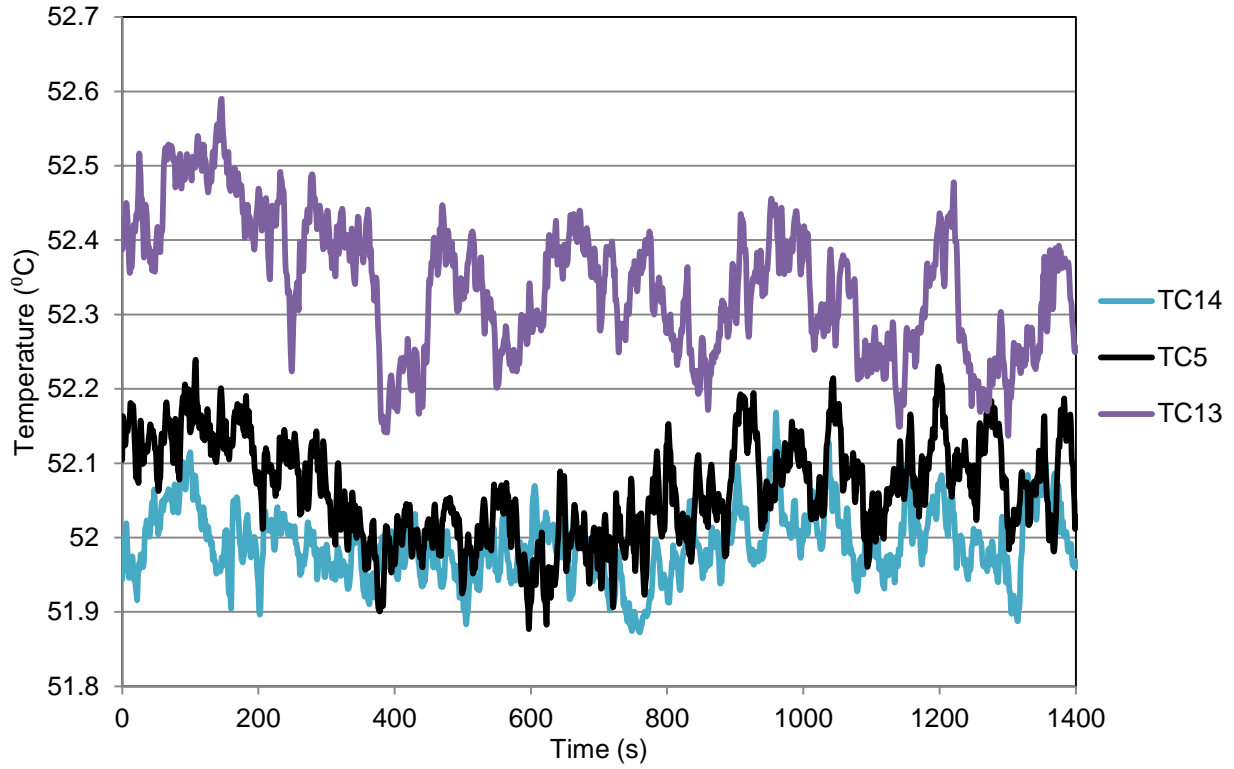


Figure 7-11 Test T456_026 Upper Lateral Test Plate Temperatures

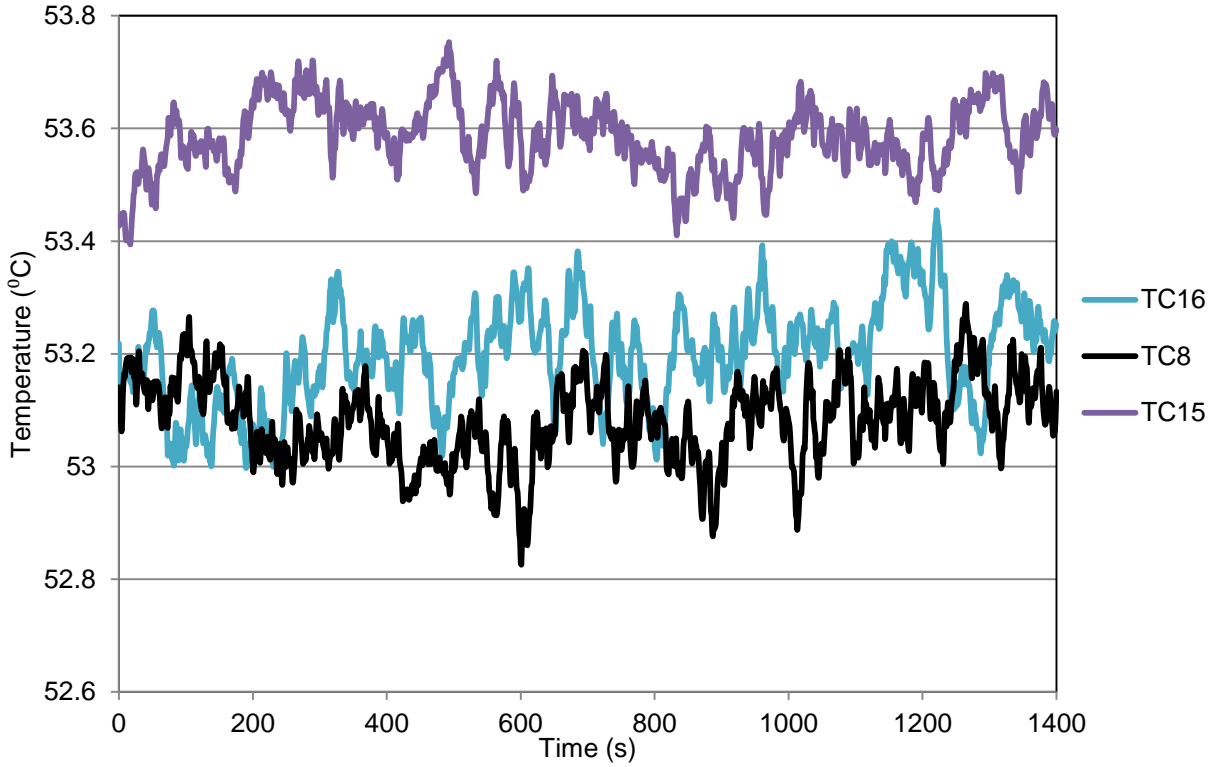


Figure 7-12 Test T456_026 Lower Lateral Test Plate Temperatures

A review of the experimental data trends and a comparison to the model discussed in Section 3.0 is presented in the following sections. The analysis has been divided into an analysis of the vertical plate results and inclined plate results.

7.2 Analysis of Vertical Plate Results

The influence of film hydrodynamic interaction on the diffusion layer heat transfer coefficient was examined by varying the film Reynolds number. Table 7-3 shows a summary of the vertical experiments with nominal test conditions to provide a perspective of the range of conditions examined. The actual temperatures and pressures varied slightly as the Reynolds number was varied as shown in Table 7-1 and Table 7-2.

Table 7-3 Summary of Vertical Plate Experiments Nominal Conditions					
Test IDs	T_b (°C)	T_w (°C)	P (bar)	Ra_c	Re_T
T457_001	94.3	59.5	0.980	5.08E+10	12.0
T457_002, T457_003	86.1	60.1	0.972	3.67E+10	4.8
T457_004 to T457_040 (vertical only)	87.4	52.2	0.974	4.58E+10	5.9 - 250.1
T457_041 to T457_043	76.3	19.6	0.977	5.65E+10	1.8 - 157.2
T457_044 to T457_071 (vertical only)	84.8	35.1	0.964	5.45E+10	4.1 - 219.5
T457_072	118.1	88.6	2.792	2.37E+11	16.8
T914_016	75.3	58.0	1.609	4.56E+10	1.1
T914_015, T914_017, T914_020	101.8	69.9	2.317	1.65E+11	5.8
T914_019	75.4	66.1	1.583	2.57E+10	0.7

As described in Section 5.0, the film Reynolds number was varied by holding all other variables essentially constant using the porous film applicator. Since film application takes suction from the gutter collection container, the measured condensation rate was unaffected by the applied film flow rate magnitude and could be measured accurately using a differential pressure sensor installed on the collection container. Furthermore, the film supply temperature could be controlled to approximately equal the plate surface temperature since the system continuously circulates the condensed fluid and a heat exchanger is used to adjust for heat transfer along the flow circuit.

Results from the 0.457 m and 0.914 m wide plate tests with Reynolds number below 17, which may be considered laminar liquid film results based on experimental observation, are shown in Figure 7-13 and

Figure 7-14. Figure 7-13 shows the enhancement factor, represented as the ratio of measured to predicted Nusselt number from Equation 3-18, as a function of the Equation 3-21 suction parameter. Figure 7-14 shows the enhancement factor plotted as a function of the de la Rosa suction factor given by Equation 3-23. The Equation 3-21 suction factor over-predicts heat transfer enhancement due to suction by as much as 67%. The de la Rosa suction factor predicts the appropriate trend although the results are scattered and offset. Therefore, the Equation 3-23 suction factor is used for the remainder of the reported results. Figure 7-15 shows all results for the laminar liquid film compared to the Equation 3-20 prediction.

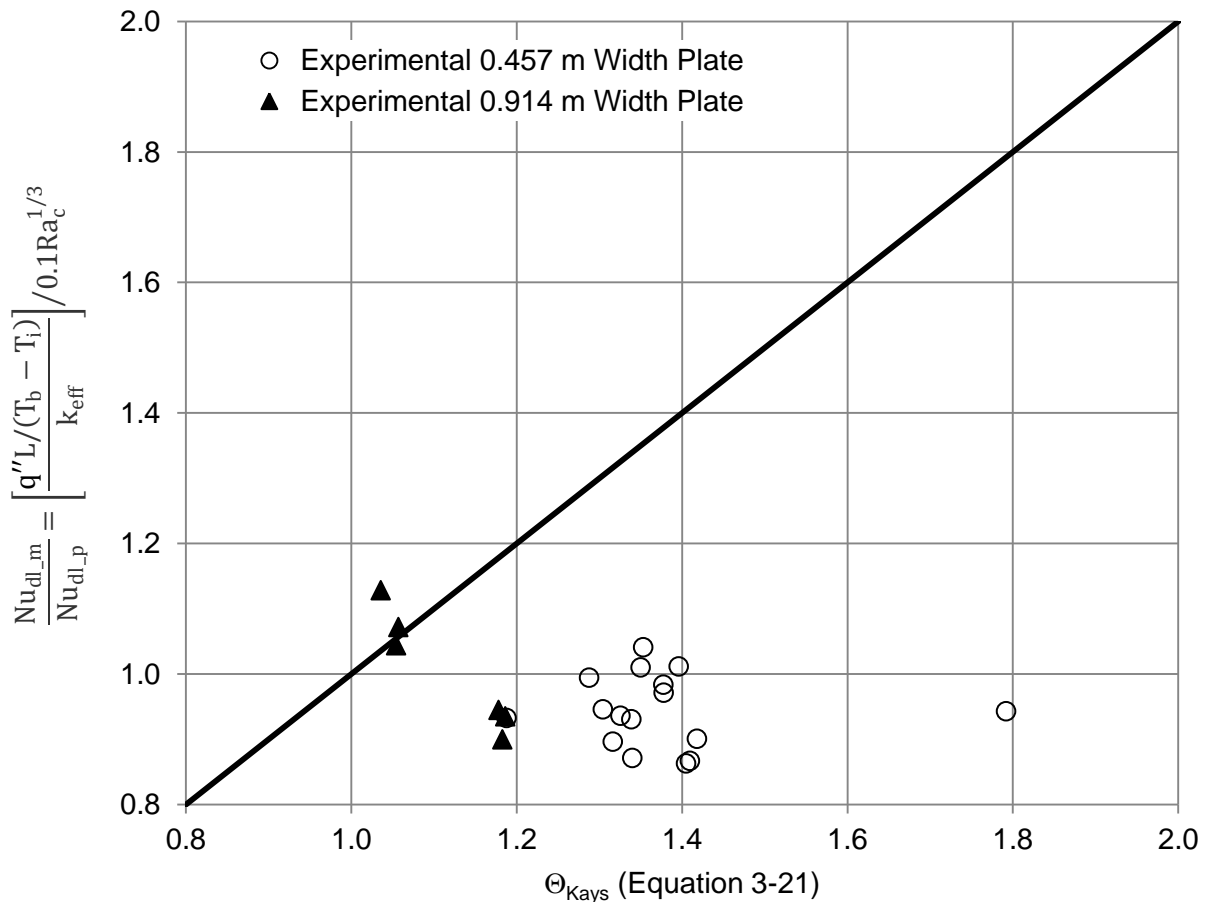


Figure 7-13 Laminar Liquid Film Results compared to Equation 3-21 Suction Parameter

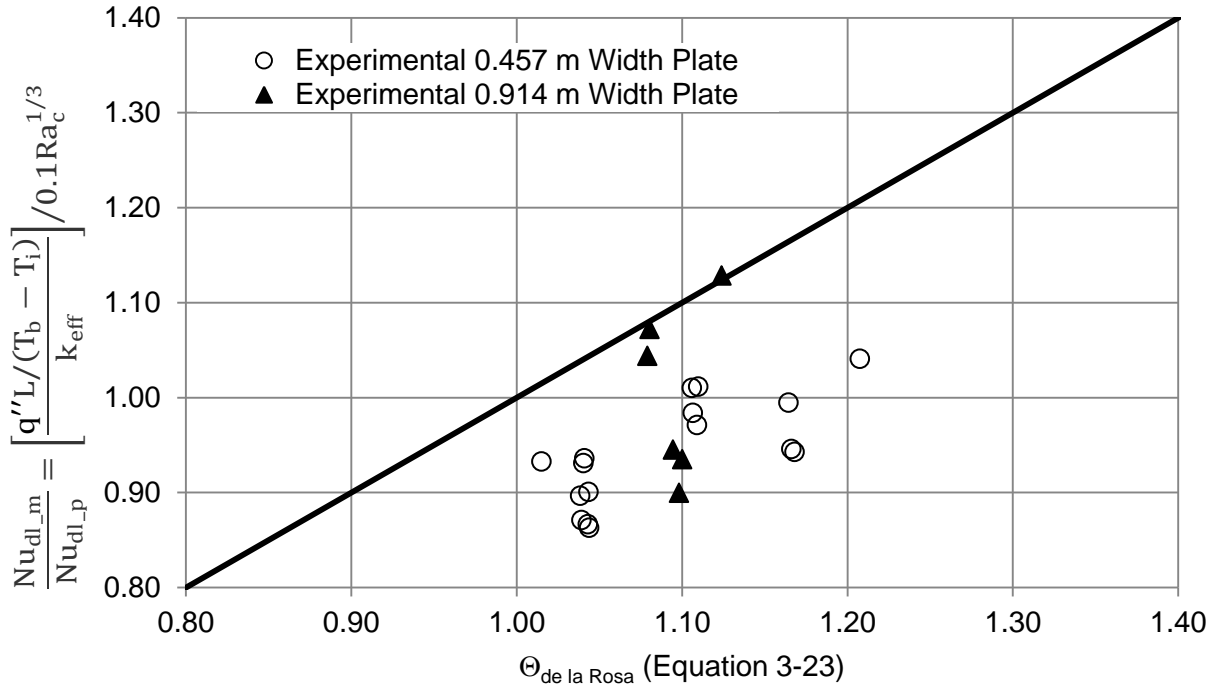


Figure 7-14 Laminar Liquid Film Results compared to Equation 3-23 Suction Parameter

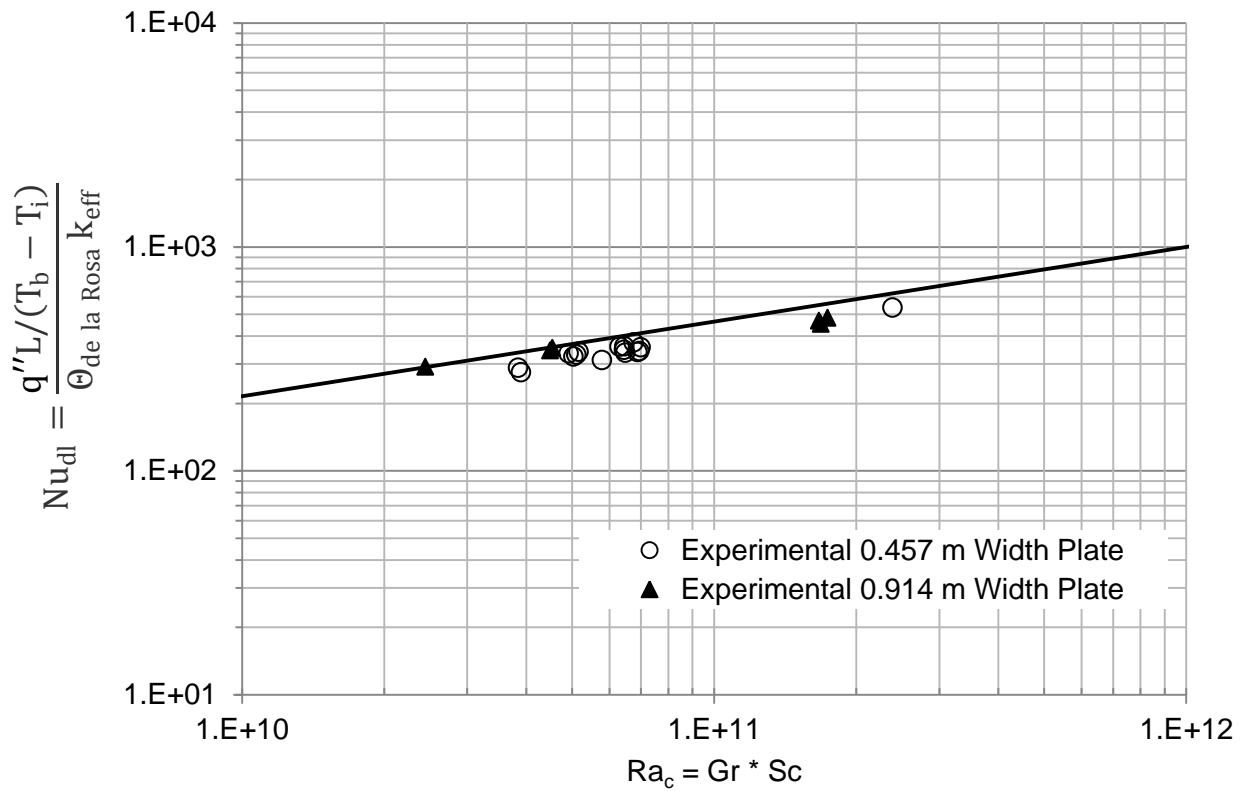
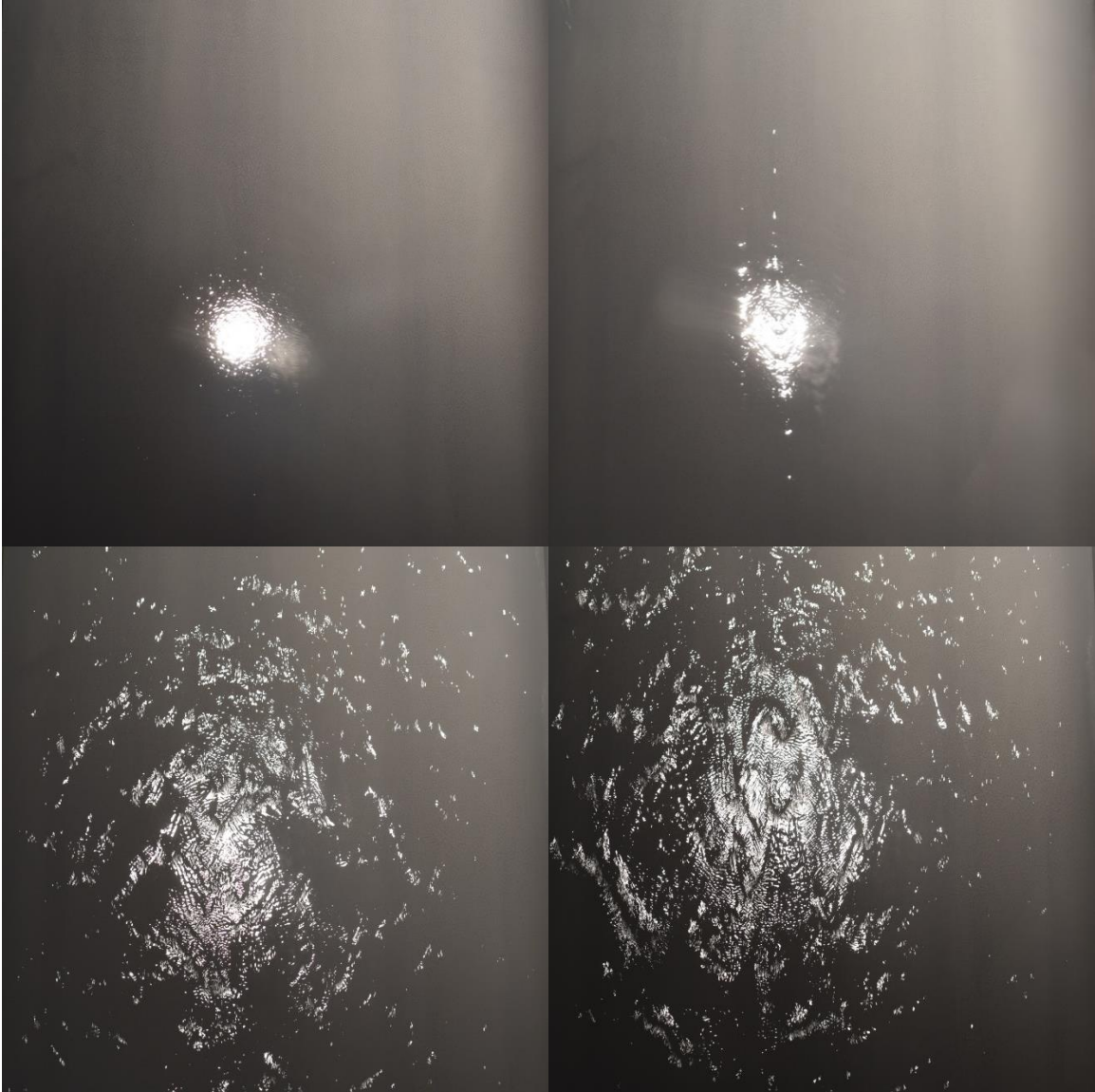


Figure 7-15 Laminar Liquid Film Results Compared to Equation 3-20

The Figure 7-15 laminar liquid film results are lower than predicted by Equation 3-20. A best fit of the Figure 7-15 data results in a coefficient of 0.088 compared to 0.1 in Equation 3-20. Given the measurement uncertainty and uncertainties in application of the liquid film thermal resistance model and suction factor correction, this difference is marginally significant. It is noted that a form consistent with the Clausen (1983) model presented in Equation 2-4 may be appropriate. However, in the absence of a good description of the variable properties influence, no changes are made to the model proposed by Equation 3-20.

At Reynolds numbers above approximately 17, the film transitions to a wavy interface. This transition was observed visually, through the heated view windows. Figure 7-16 shows images taken during the tests. The backlighting appears as a white spot near the center of the image for low Reynolds numbers. As the Reynolds number increases, the reflection becomes distorted due to surface waves.

Figure 7-18 shows the measured film thickness for increasing Reynolds numbers over the Reynolds number range of 7.1 to 48.5. Note that the Reynolds number reported for the film thickness measurements are based on flow rates at the sensor location. The measured film thickness profiles are consistent with the visually observed transition from laminar flow at a Reynolds number of 7 to 15. The laminar film thickness measurements were consistent with the Nusselt theory within 10%, demonstrating the accuracy of the measurement method.



**Figure 7-16 Images Showing Full Width of 0.457 m Plate at $P_b = 0.97$ bar, $T_b = 87^\circ\text{C}$ and $T_i = 52^\circ\text{C}$:
 $Re=1.8$ (Top Left) $Re=14.2$ (Top Right) $Re=115$ (Lower Left) $Re=220$ (Lower Right)**

At Reynolds numbers above the transition Reynolds number, a clear increase in the enhancement factor was measured. The enhancement factor increased over the Reynolds number range of 15 to approximately 32, consistent with the measured film wave amplitude increase shown in Figure 7-18. Above a Reynolds number of approximately 32, no further increase in heat transfer coefficient was observed. This was consistent with the measured plateau in peak wave height and a second transition in the film flow regime as measured by the film thickness sensor. Figure 7-19 shows the measured film

thickness results over the Reynolds number range of 48.5 to 223. The film regime transition is consistent with a breakup of the film waves into double humped, and more complex wave patterns. Figure 7-17 shows the ratio of measured Nusselt number to that predicted by Equation 3-20 for all test conditions. The enhancement due to the wavy interface ranged from 20 to 30% compared to the laminar liquid film condition.

Two independent heat flux measurement methods, measurement of the liquid film thickness and visual observation all confirm the enhancement due to surface waves. There are a number of physical explanations for the observed enhancement. First, waves act to disrupt the laminar sub-layer and can reduce the sub-layer effective thickness. Second, waves cause an increase in momentum transfer between the liquid film and gas layer that is greater than the wave free condition. Appendix G demonstrates that the wave velocities are much higher than the interface liquid velocity. Finally, waves increase the interface area for heat and mass transfer. Determining the importance of each of these mechanisms may be the subject of future work.

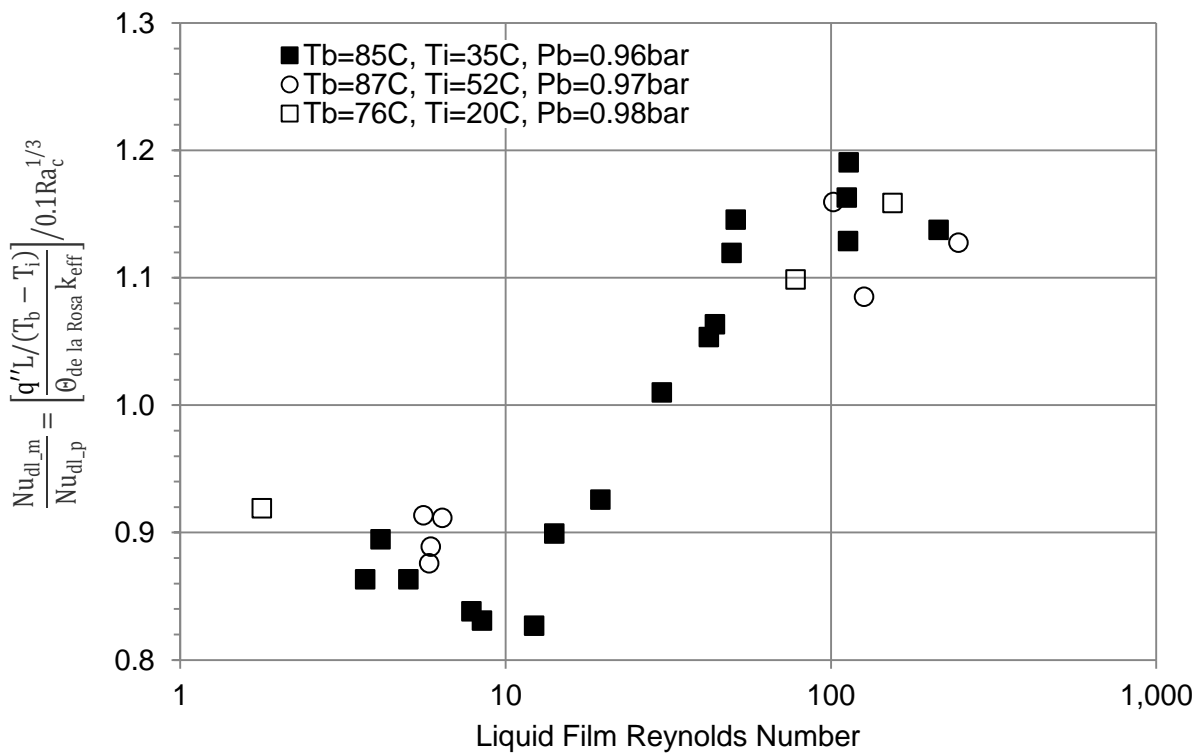


Figure 7-17 Experimental Gas Diffusion Layer Heat Transfer Coefficient with Respect to the Wave Free Gas Diffusion Layer Heat Transfer Coefficient Prediction from Equation 3-20 Showing the Effect of Liquid Film Waves on Heat Transfer Enhancement for Increasing Film Reynolds Number

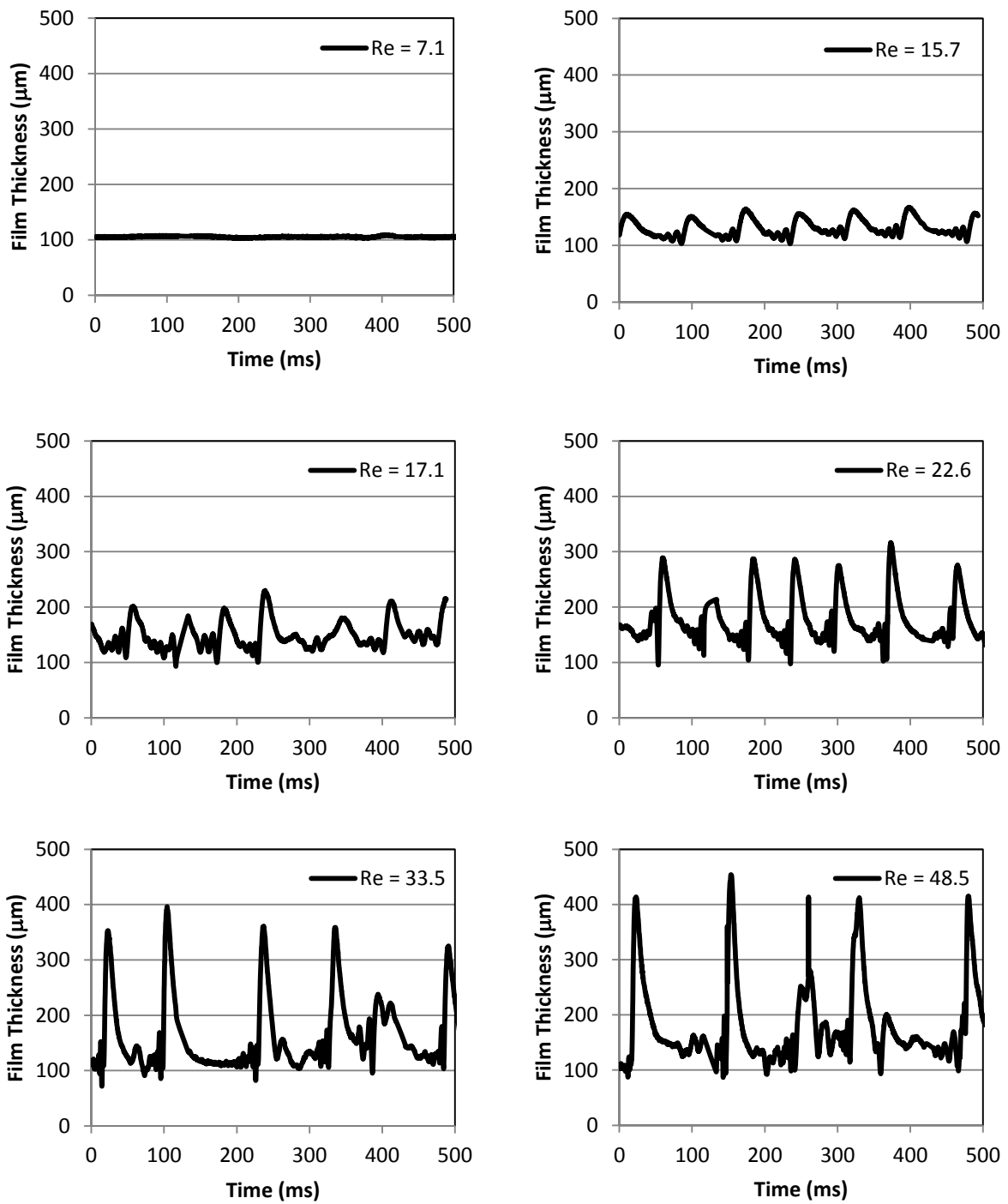


Figure 7-18 Chromatic Confocal Thickness Results for Transitional Wavy Film

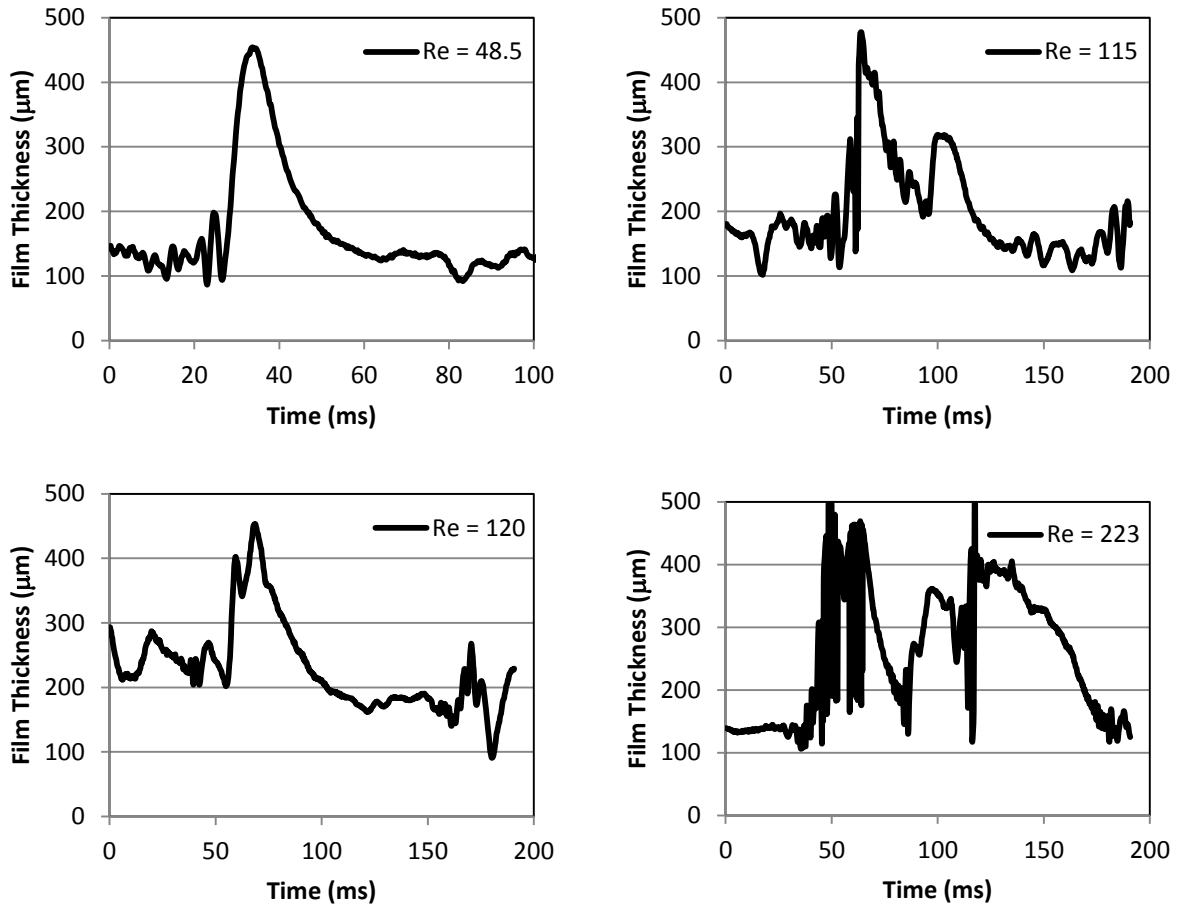


Figure 7-19 Chromatic Confocal Thickness Results for Wavy Film Regime

Finally, it is useful to compare the magnitudes of the various heat transfer resistances to assess the importance of each component of the Section 3.0 model. From Equation 3-1 and Equation 3-5, the fraction of the total thermal resistance between the bulk and wall due to the liquid film, φ_{film} , is:

$$\varphi_{film} = \frac{1/h_f}{1/h_t} = \frac{h_t}{h_f} \quad \text{Equation 7-1}$$

Considering parallel sensible and latent heat transfer through the gas layer, the fraction of total heat transfer resistance due to sensible heat transfer, φ_s and latent heat transfer, φ_l , are:

$$\varphi_s = (1 - \varphi_{film}) \frac{h_s}{(h_s + h_l)} \quad \text{Equation 7-2}$$

$$\varphi_l = (1 - \varphi_{film}) \frac{h_l}{(h_s + h_l)} \quad \text{Equation 7-3}$$

The heat transfer resistance fractions are calculated for each of the experimental conditions. Based on this calculation, the sensible heat transfer fraction ranges from 1 to 7% of the total heat transfer resistance and the latent heat transfer is the primary transfer resistance ranging from 91 to 96%. The liquid film thermal resistance ranges from 0.4 to 4.7% of the total heat transfer resistance considering all of the vertical experiments. This relatively low thermal resistance due to the liquid film is primarily driven by the relatively high non-condensable mass fraction. Therefore, for the selected experimental conditions, the result is not highly sensitive to uncertainties in the film resistance model presented in Section 3.1. However, this is not the case for many of the experimental studies referenced as discussed in Section 8.0. Many of these experimental studies include low non-condensable mass fraction conditions, where the liquid film thermal resistance is dominant.

7.3 Analysis of Inclined Plate Results

As discussed in Section 7.2, the influence of liquid film thermal resistance is small for the vertical plate experiments. This is demonstrated using the Kutateladze and Gogonin (1979) correlation given by Equation 3-4, and can also be demonstrated for the inclined plate experiments. Gerstmann and Griffith (1965) examined the liquid film thermal resistance for the inclined plate and compared their experimental results to the Nusselt laminar film theory given by Equation 3-2, with the gravitational acceleration term, g , replaced by $g \cdot \cos(\theta)$. They showed that the Nusselt laminar film theory slightly under-predicts the heat transfer coefficient for inclination angles up to 80 degrees from vertical and significantly under predicts for near horizontal conditions. Applying the Nusselt laminar film theory prediction to the current experimental data set, it can be shown that the liquid film thermal resistance is less than 5% of the total resistance for all experimental conditions. Therefore, for simplicity, the analysis of the inclined plate results neglects the influence of the liquid film thermal resistance.

Although the model presented by Gerstmann and Griffith (1965 and 1967) has a strong experimental basis, the model does not approach the appropriate limits for the vertical flat plate. Since the liquid film thermal resistance is neglected, extension of the analysis presented in the section to conditions in which the liquid film thermal resistance is large may require further research to resolve the deficiencies in existing models such as the Gerstmann and Griffith model. For instance, neglecting the liquid film thermal resistance to assess the effect of inclination for the high pressure, low non-condensable mass fraction conditions examined by Kim et al. (2009) is not appropriate.

The inclined plate results are presented in a manner similar to the vertical plate results. First, the low liquid film Reynolds number conditions are reviewed followed by the wavy film regime. In an effort to clearly define the inclination effect, and considering the observation that the results in Section 7.2 indicate an offset from Bayley correlation, the inclined plate results are normalized to the vertical plate results. Table 7-4 shows a summary of the experimental conditions.

Table 7-4 Summary of Inclined Plate Experiments Nominal Conditions						
Test IDs	T_b ($^{\circ}\text{C}$)	T_w ($^{\circ}\text{C}$)	P (bar)	Ra_c	Re_{Γ}	Plate Angle
T457_004 to T457_040	87.4	52.2	0.974	4.58E+10	5.9 - 250.1	0,15,30,45,60,75
T457_044 to T457_071	84.8	35.1	0.964	5.45E+10	4.1 - 219.5	0,15,30,45,60,75
T914_001,2,3,6,10,11,13,16,18	75.3	58.0	1.609	4.56E+10	1.1	0,15,37,50,75,80
T914_004,5,7,9,12,14,15,17,20	101.8	69.9	2.317	1.65E+11	5.8	0,15,37,57,75
T914_008,19	75.4	66.1	1.583	2.57E+10	0.7	0,57

Figure 7-20 shows the ratio of measured Nusselt number to that predicted by Equation 3-20 for all conditions with a Reynolds number below 10. These results have been normalized to the average results at the vertical position for each test condition. The enhancement due to plate inclination is as high as 54% for the range of conditions examined.

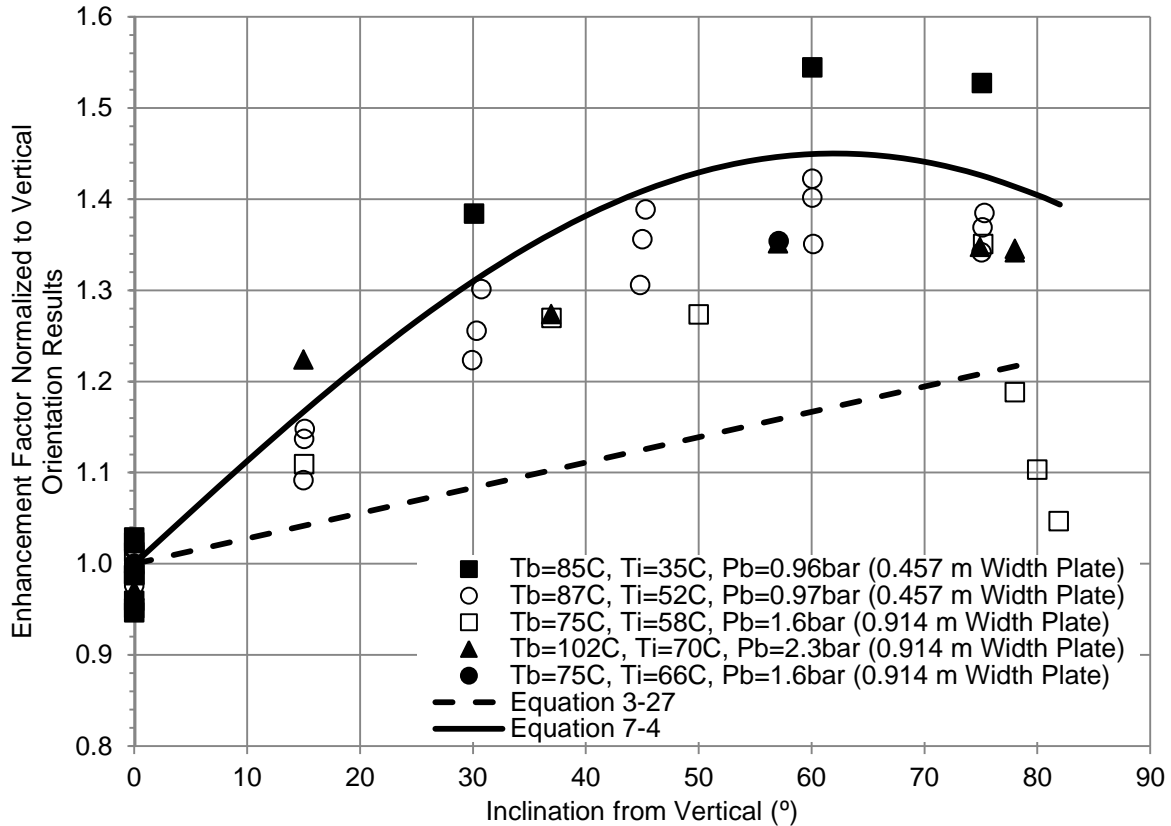


Figure 7-20 Plate Inclination Effect on Gas Boundary Layer Heat Transfer Coefficient with Respect to the Vertical Plate for Liquid Film Reynolds Number Less than 10

Figure 7-20 also shows the predicted enhancement factor based on Equation 3-27 as proposed by Al-Arabi and Sakr (1988). Equation 3-27 predicts the appropriate trend; however, a closer fit of the measurement results is found with the following correlation for the correction factor:

$$a_{\theta} = 0.045 * \sin(1.45\theta) \quad \text{Equation 7-4}$$

, where θ is the angle from vertical in radians and a_{θ} is the correction factor as applied in Equation 3-26. Above an angle of 80° the enhancement factor decreases. Due to the design of the test apparatus, useful data could not be collected at an inclination angle much above 80° since drips begin to fall from the test surface and the collection trough can no longer be used to measure insulation losses. Therefore, the range of applicability of Equation 7-4 is only from 0 to 80° . For unrelated reasons, this is also the range of

applicability of the Al-Arabi and Sakr correlation given by Equation 3-27.

There are a number of possible explanations for the experimental transfer rates higher than those predicted by Equation 3-27. First, the onset of film waves occurs at lower Reynolds numbers due to gravitational instabilities and the Equation 7-4 correlation may include some component associated with film disruption. Second, the Al-Arabi and Sakr correlation, given by Equation 3-27, is based on a limited dataset, and there are few other studies for comparison. There could be an error in the Equation 3-27 correlation or additional parameters that are not taken into account. Finally, the suction effect may influence the transfer processes differently for the inclined condition than the vertical condition. These issues are not resolved as part of this work and may be the topic of future research. Nonetheless, the usefulness of Equation 7-4 as an engineering tool for approximating condensation heat transfer on an inclined plate is significant, since there are no other models reported in the literature for this scenario.

To examine the influence of film disruption on the gas boundary layer for the inclined plate condition, the liquid film Reynolds number was varied along with the plate inclination angle for two of the conditions listed in Table 7-4. Figure 7-21 shows the results of this study. To clearly identify the influence of film disruption, the results with film applied have been normalized to the results with no film applied ($Re < 10$) at each tested inclination angle.

The Figure 7-21 results show that enhancement due to film surface waves is most significant for the vertical plate and decreases as a function of inclination angle. The enhancement is less for slight inclination and essentially no enhancement is observed for inclination angles greater than 30° from vertical.

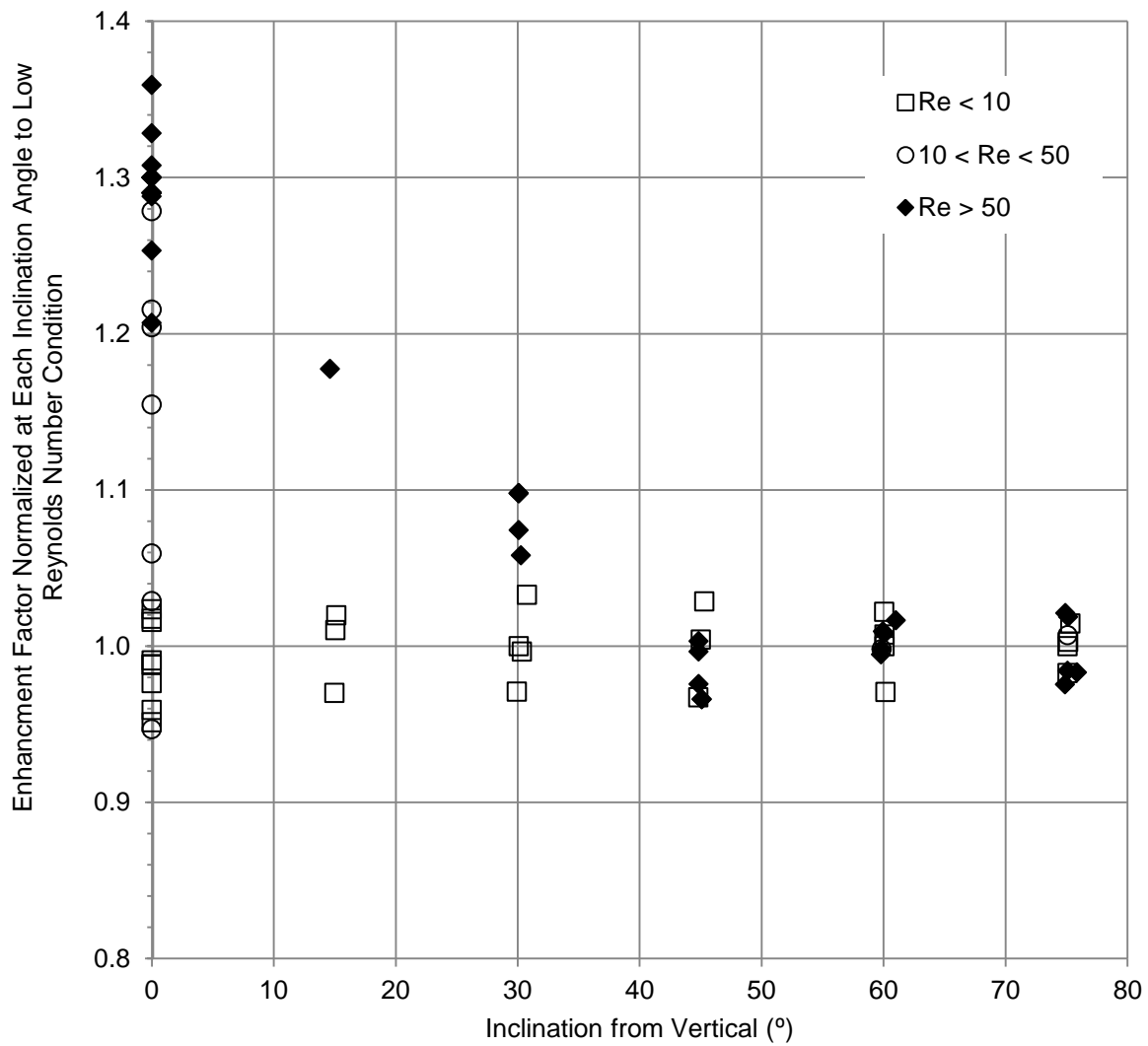


Figure 7-21 Heat Transfer Enhancement at Various Reynolds Numbers with Respect to Low Reynolds Number Conditions at Different Inclination Angles

8.0 Review of Published Experimental Databases

8.1 Data Analysis

The experimental flat plate results of Uchida et al. (1965), Kataoka et al. (1994) and Anderson (1998a) are shown in Figure 8-1 using Equation 3-20 with the Equation 3-23 suction factor applied. The liquid film thermal resistance is accounted for using Equation 3-4. In addition, the large diameter cylinder results of Tagami (1965) are shown since they meet the criterion defined in Equation 3-24 for application of the flat plate correlations. The methods used to extract data from these sources are described in Appendix C.

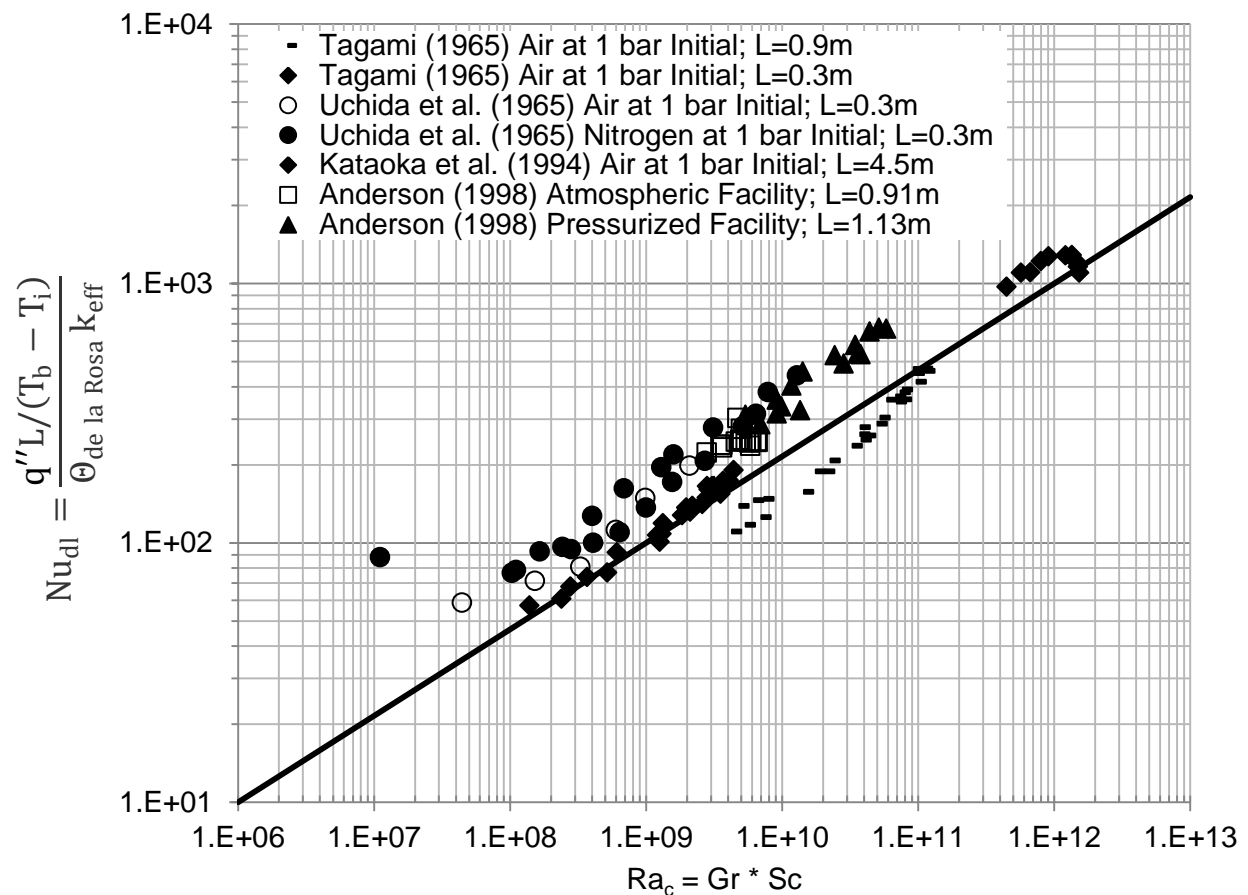


Figure 8-1 Comparison of Published Flat Plate Experimental Data to Equation 3-20

The Tagami results shown in Figure 8-1 indicate a functional variation with height that is not expected for turbulent natural convection on a flat plate over the Rayleigh number range of 1×10^8 to 1×10^{11} . Tagami does not provide sufficient details of the experimental apparatus to assess possible sources of

experimental bias or a statement of the measurement uncertainty. As such, explanations for the deviation from the prediction are only speculation.

Uchida et al. (1965) used a 0.14 m wide by 0.3 m length condensing plate. The short vertical height resulted in conditions close to the gas layer laminar turbulent transition as evident in Figure 8-1, below a Rayleigh number of 1×10^8 . Above a Rayleigh number of 1×10^8 the expected trend is observed, but the model under predicts the heat transfer coefficient by approximately 80%. Uchida et al. (1965) does not provide details of the experimental apparatus or a statement of the measurement uncertainty. As such, explanations for the deviation from the prediction are only speculation.

Kataoka et al. (1994) reports results of condensation on a 0.5 m wide, 4.5 m height vertical wall. Due to the transient nature of the Kataoka et al. experiments, the first three data points at the start of the transient are excluded as a result of high suppression pool rate of temperature change with time. Kataoka et al. (1994) did not define the measurement uncertainty or assess the influence of the transient on the measured heat transfer coefficients.

Anderson (1998a) reports results of testing that modeled a 1:12 scale radial slice of the AP600 nuclear plant containment vessel. The length of the vertical condensing surface for the atmospheric facility is 0.91 m and the vertical component of the pressurized facility is 1.13 m. Anderson (1998a) utilized two independent methods of heat flux measurement. The measurement results from both methods are averaged for this assessment as described in Appendix C. Finally, only the vertical component of the test facility was used for this assessment as described in Appendix C.

The experimental results for cylindrical test geometries reported by Su et al. (2013 and 2014) and Liu (1999) are shown in Figure 8-2 using the Equation 3-25 model with the Equation 3-23 suction factor applied. The liquid film thermal resistance is accounted for using Equation 3-4. Similarly, the experimental results of Dehbi (1991) and Kim et al. (2009) are shown in Figure 8-3. The methods used to extract data from these sources are described in Appendix C.

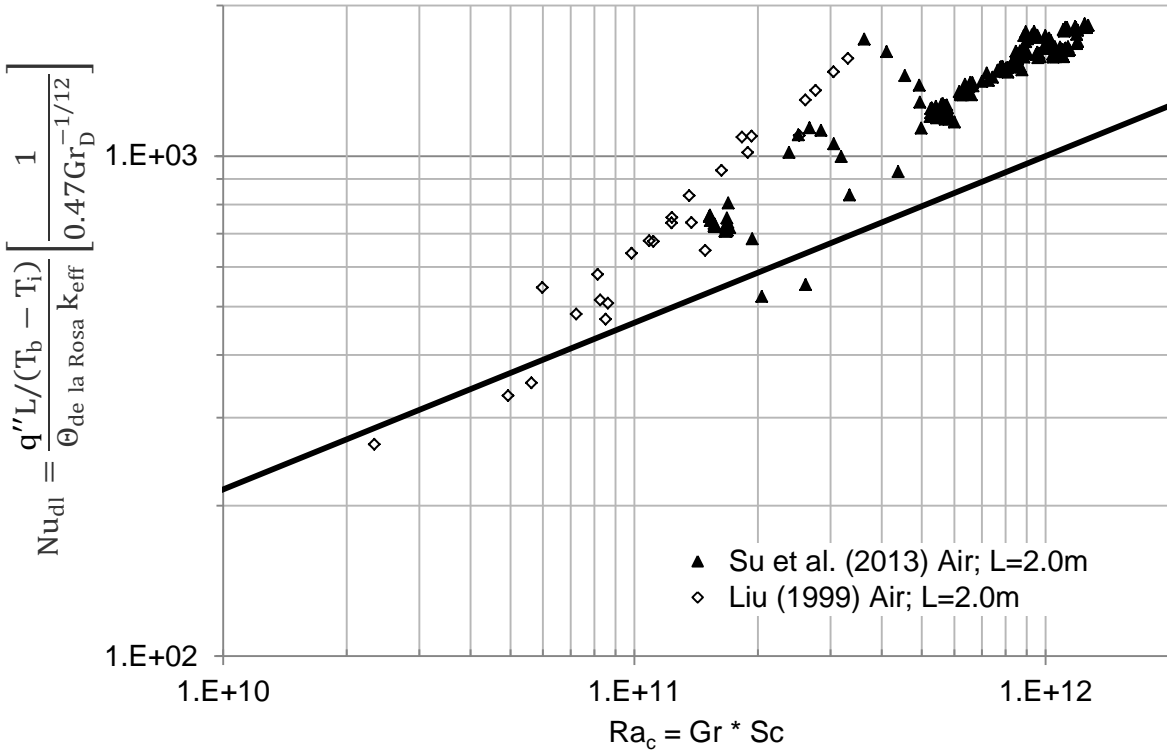


Figure 8-2 Comparison of 2 m Height Experiments to Equation 3-25 Prediction

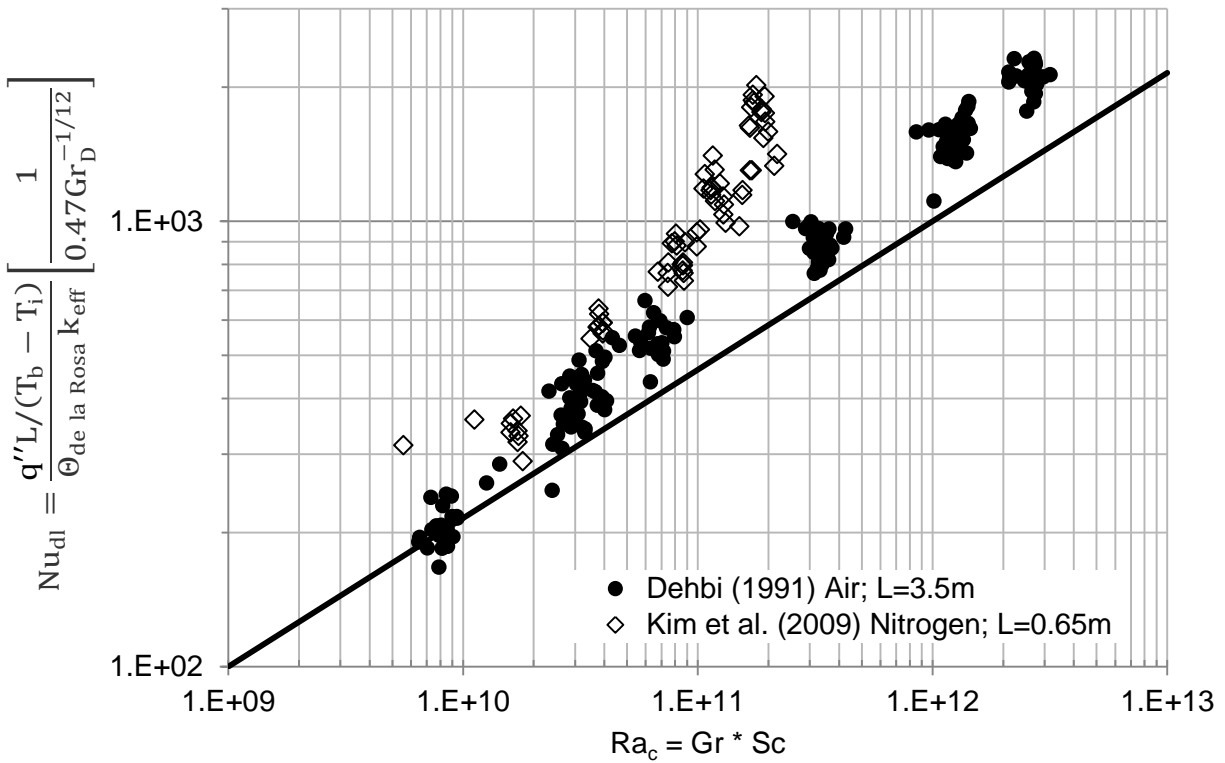


Figure 8-3 Comparison of 3.5 and 0.65 m Height Experiments to Equation 3-25 Prediction

Dehbi (1991) reports experimental results for condensation on a 3.5 m height, 0.038 m diameter vertical cylinder. Heat transfer coefficients are reported for the upper 1.16 m height of the facility and for the full facility height separately. Both upper and lower heat transfer results are represented in Figure 8-3. Based on the Equation 3-25 prediction, several of the data points from this dataset indicate sensible heat transfer rates that make up greater than 10% of the overall gas layer heat transfer.

Dehbi (1991) reports a heat transfer coefficient measurement error of 15% based on the coolant energy balance. The error analysis reported by Dehbi assumes a coolant temperature rise of 10°C between stations and indicated that the rise in coolant temperature was in the range of 40°C to 90°C. Assuming the stated Reynolds number of 1500 in the coolant loop, this coolant temperature rise range was not maintained. As a result, the experimental accuracy of 15% is questionable at heat transfer rates below 8000 W/m². Therefore, these results are not shown in Figure 8-3. The results at lower heat flux follow the same trend, but are significantly more scattered.

Kim et al. (2009) reports experimental results for condensation on a 0.65 m height, 0.038 m diameter vertical cylinder. As noted by Kim et al. (2009), the ideal gas law prediction at the 20 bar test conditions results in significant model prediction error. As described in Appendix A, gas properties are determined using a script based on the International Association for the Properties of Water and Steam (IAPWS) 1995 formulation for steam, and nitrogen properties are determined using the National Institute of Standards and Technology (NIST) Fluid Thermodynamic and Transport Properties (REFPROP) database. Based on the analysis presented here, the liquid film thermal resistance exceeds 50% of the overall heat transfer resistance for several of the Kim et al. data points, necessitating the application of the Kutateladze and Gogonin (1979) correlation to account for film waves.

8.2 Summary

The published literature for flat plates is limited. The datasets of Tagami (1965), Uchida et al. (1965) and Kataoka et al. (1994) are reported with no statement of measurement uncertainty. The Kataoka experiments were collected from transient experiments in which the assumption of thermal equilibrium cannot be validated. The results of Anderson (1998a) are reported with a measurement uncertainty of 10%, which is in contradiction with the tabular results reported for each measurement method. Finally, the

Anderson (1998a) results are distorted due to the gas flow patterns and liquid film interface characteristics that vary significantly from the ideal flat plate scenario.

The published literature for cylinders is much more comprehensive. The datasets of Dehbi (1991), Su et al. (2013 and 2014), Kim et al. (2009) and Liu (1999) are all conducted using 0.038 m diameter cylinders. It is noted that that no confirmatory measurements of the heat transfer coefficient are reported for any of these studies, and where details of the experimental apparatus are provided, the reported uncertainties are questionable. However, the cylindrical apparatus is significantly less prone to the sources of experimental bias associated with heat losses and disruptive convection patterns due to sidewalls.

The data of Su et al. (2013 and 2014), Kim et al. (2009) and Liu (1999), exhibit a significant upward trend away from the model prediction as Rayleigh number increases. The data of Dehbi (1991) exhibits a mild upward trend. Consideration may be given to the fact that the Equation 3-25 model must be extrapolated to higher Rayleigh number to assess the influence of cylinder diameter as a possible explanation for the deviation. Considering the dataset of Kim et al. (2009), the model prediction error is as high as a factor of 3 at a Rayleigh number of 2×10^{11} . At this condition, the correction for the diameter effect is negligible and Equation 3-24 indicates that the flat plate correlation may be applied. Intuitively, as the Rayleigh number increases, the boundary layer thickness will decrease and the results should approach those of the flat plate. This is consistent with the discussion provided by Popeil (2008) of turbulent free convection over a vertical cylinder that cites the theory of Na and Chou (1980). Therefore, it is concluded that the physical explanation for the deviation is unrelated to extrapolation of the Equation 3-25 prediction.

Table 8-1 gives a summary of the literature along with the experimental results from this project. Using Equation 7-1 through Equation 7-3, the fraction of total heat transfer resistance between the bulk and wall is calculated for each test condition and the ranges are provided in Table 8-1. Review of these results demonstrates the need to consider all three heat transfer resistances when comparing results across all datasets.

Table 8-1 Summary of Published Experimental Databases for Condensation on Vertical Surfaces									
Data Source	# of Experiments	Test Geometry	Height	NC Gas	P _b (bar)	W _{nc,b}	% of Total Resistance ⁸		
							Liquid Film	Latent	Sensible
0.457 m Width Experiments	31	0.457 m Wide Suspended Plate	2.13 m	Air	1 to 2.8	0.23 to 0.72	1.1 to 4.7%	91 to 96%	1 to 6%
0.914 m Width Experiments	6	0.914 m Wide Suspended Plate	2.13 m	Air	1.6 to 2.4	0.64 to 0.83	0.4 to 1.6%	93 to 94%	4 to 7%
Anderson Atmospheric Facility (1998a) ^{1,2}	16	0.30 m Wide Enclosure	0.91 m	Air	1	0.41 to 0.86	0.4 to 2.8%	90 to 94%	3 to 10%
Anderson Pressurized Facility (1998a) ^{1,2,3}	17	0.30 m Wide Enclosure	1.13 m	Air	1 to 3.1	0.40 to 0.83	0.8 to 5.3%	90 to 96%	1 to 9%
Su (2013 and 2014)	164	0.038 m Diameter Cylinder	2 m	Air	2 to 6	0.07 to 0.59	6.6 to 45%	55 to 90%	0 to 5%
Kataoka et al. (1994) ⁴	10	0.50 m Wide Enclosure	4.5 m	Air	1.4 to 3	0.51 to 0.83	0.8 to 4.6%	92 to 94%	2 to 7%
Kim et al. (2009)	72	0.038 m Diameter Cylinder	0.65 m	N ₂	4 to 20	0.01 to 0.71	2.4 to 76%	24 to 91%	0 to 8%
Dehbi (1991) ⁵	108	0.038 m Diameter Cylinder	3.5 m	Air	1.5 to 4.6	0.25 to 0.91	0.7 to 14%	84 to 95%	1 to 14%
Tagami (1965) 0.3 m Cylinder	24	0.15 m Diameter Cylinder	0.3 m	Air	1.5 to 4.7	0.38 to 0.85	0.3 to 4.3%	92 to 93%	4 to 8%
Tagami (1965) 0.9 m Cylinder	28	0.15 m Diameter Cylinder	0.9 m	Air	1.5 to 4.8	0.39 to 0.84	0.3 to 5.4%	91 to 93%	4 to 8%
Liu (1999) ¹	26	0.038 m Diameter Cylinder	2 m	Air	2.5 to 4.6	0.17 to 0.75	1.8 to 25.7%	74 to 95%	1 to 5%
Uchida et al. (1965) Air ⁷	20	0.14 m Wide Plate ⁶	0.3 m	N ₂	1.3 to 3.5	0.50 to 0.91	0.1 to 3.7%	90 to 93%	5 to 10%
Uchida et al. (1965) Nitrogen	6	0.14 m Wide Plate ⁶	0.3 m	Air	1.2 to 8.8	0.23 to 0.93	0.1 to 18.7%	79 to 93%	3 to 11%

¹Helium results also available

²Height based on vertical condensing plates only

³Total of 47 averaged and 17 local results sets provided. The localized results are necessary to separate the vertical and inclined results.

⁴Transient experiment with 13 results reported at intermediate times. Only 10 results are considered quasi steady.

⁵Results for upper portion reported separate from entire length (216 conditions included in data analysis)

⁶Anderson (1998a) indicates that the Uchida (1965) flat plate was housed in a 6.4m height x 3.4 m diameter vessel.

⁷Argon results also available

⁸Calculations based on Equation 7-1 through Equation 7-3

9.0 Wavy Film Interface Correction

As shown in Figure 7-17, a clear enhancement is observed as the film transitions from laminar flow to wavy flow. Therefore, to correlate the experimental results, regime transition criteria are defined. Ishigai et al. (1972) performed testing to examine the film dynamics of water flowing down a 2 m long vertical cylinder. The regime transition criteria match closely with those reported in Figure 7-17 and are defined as follows:

- 1) Purely laminar flow, $Re_f \leq 0.47Ka^{1/10}$
- 2) First transition region, $0.47Ka^{1/10} \leq Re_f \leq 2.2Ka^{1/10}$
- 3) Stable wavy flow, $2.2Ka^{1/10} \leq Re_f \leq 75$
- 4) Second transition region, $75 \leq Re_f \leq 400$
- 5) Fully turbulent flow, $400 \leq Re_f$

The Kapitza number, Ka , is solely a function of the fluid properties and is given as:

$$Ka = \frac{\sigma^3}{\rho_f^3 \nu_f^4 g} \quad \text{Equation 9-1}$$

, where σ is the surface tension and ν_f is the kinematic viscosity.

In the Region 1 laminar film flow, the film can be considered wave free, although some long wavelength waves may be observed. For all of the experimental conditions examined as part of this study and those evaluated as part of the literature review, the quantity $0.47Ka^{1/10}$ ranges from five to nine. Practically, the transition from laminar to transitional flow can be assumed to occur at a Reynolds number of 5 for condensed water over a wide range of conditions. This criterion is also consistent with that used by Kutateladze and Gogonin (1979) as discussed in Section 3.1.

The first transition region consists of an approximately linear increase in wave height as a function of Reynolds number as shown in Figure 7-18. The first transition region extends to a Reynolds number corresponding to $2.2Ka^{1/10}$. For the experimental conditions examined as part of this study and those evaluated as part of the literature review, the quantity $0.47Ka^{1/10}$ ranges from 25 to 44.

To evaluate the wavy film influence the gas diffusion layer thickness is compared to the characteristic length of the liquid film disturbances for the wavy liquid film regime using the criteria given above. Since detailed measurements of the liquid film profile are not available for the published literature, the laminar film thickness given by Equation 3-2 is used to represent this length scale. The diffusion layer Nusselt number, Equation 3-20, represents the ratio of the characteristic system dimension to the thermal and mass diffusion length scale. The enhancement factor shown as a function of the ratio of the measured diffusion layer length scale divided by the film length scale is shown in Figure 9-1.

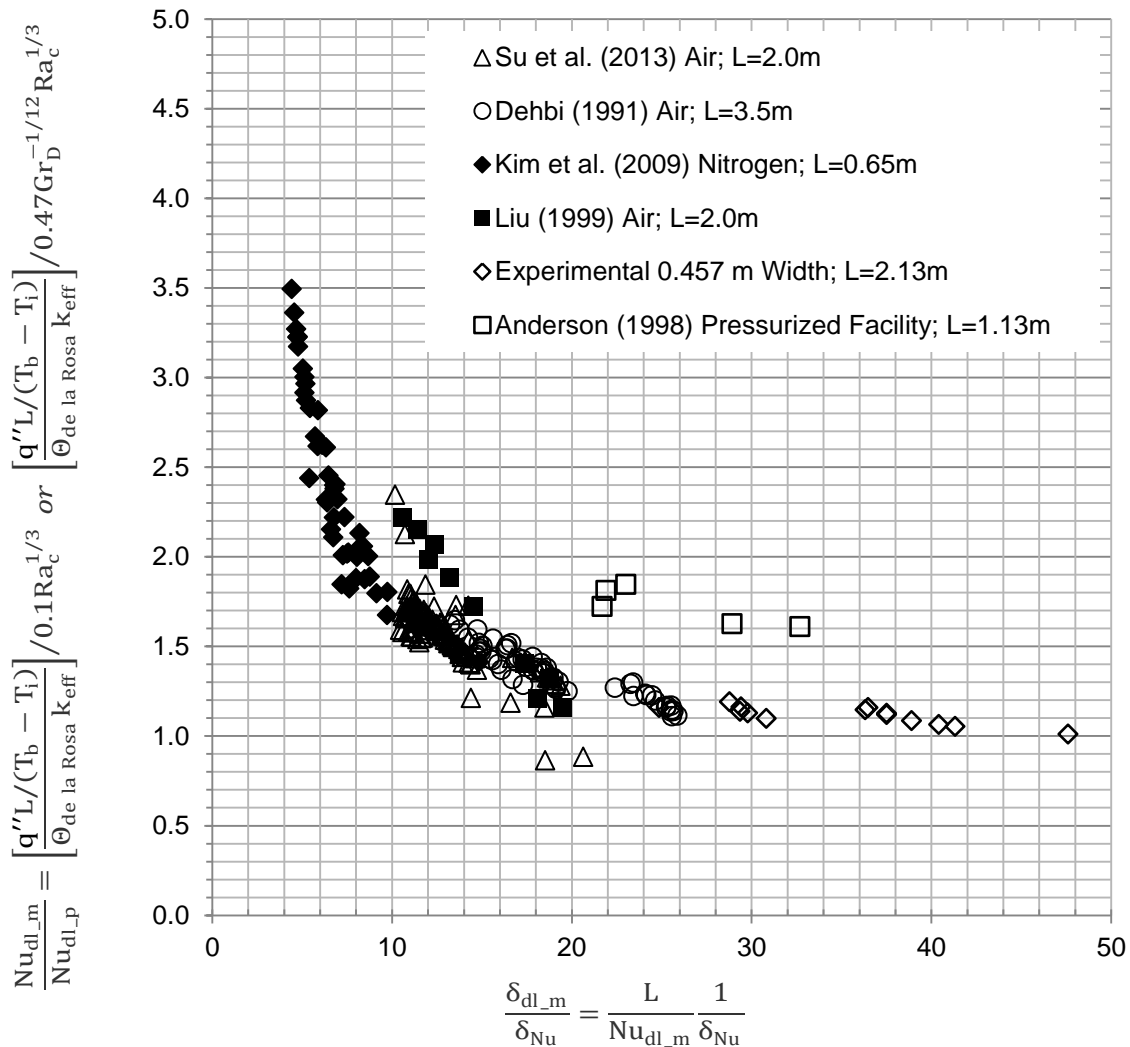


Figure 9-1 Current Experimental Results along with Results of Su et al. (2013), Dehbi (1991), Kim et al. (2009), Liu (1999) and Anderson (1998) Showing the Experimental Gas Diffusion Layer Heat Transfer Coefficient with Respect to the Wave Free Gas Diffusion Layer Heat Transfer Coefficient Prediction from Equation 3-20 for Wavy Liquid Film Conditions Only ($Re > 2.2Ka^{1/10}$) as a Function of the Ratio of Gas Diffusion Layer to Liquid Film Length Scale

Figure 9-1 shows that the results of Su et al. (2013 and 2014), Dehbi (1991), Liu (1999), Kim et al. (2009) and the current experimental results essentially collapse to form a single curve. The Anderson (1998a) pressurized facility results are offset, but exhibit the same trend. The Uchida et al (1965), Kataoka et al. (1994), Tagami (1965), atmospheric facility results of Anderson (1998a) and the current experimental results for the 0.914 m width test plate are not shown since they do not extend into the wavy film regime.

Physically, Figure 9-1 implies that as the diffusion layer thickness approaches the length scale of the liquid film, the enhancement factor increases. In addition, as the diffusion layer thickness becomes large with respect to the film length scale, the enhancement effect becomes negligible. Finally, when the length scale ratio is large, such as for the results of Dehbi (1991) and the 0.457 m width plate results, the enhancement factor is significant, up to 50%, but is not a strong function of the liquid film length scale.

A model for the diffusion layer heat transfer coefficient is proposed to account for the enhancement due to film waviness. The model applies a correction to the baseline model described in Section 3.0. Figure 9-1 suggests that the enhancement factor for the wavy film flow may be represented as an implicit function. However, a reasonable fit of the enhancement effect can be given as an explicit function of the predicted Nusselt number, Nu_{dl} , defined using either Equation 3-20 for a flat plate or Equation 3-25 for a cylinder as follows:

$$\alpha = \frac{Nu_{dl_wavy}}{Nu_{dl}} = 2300 \cdot \left(Nu_{dl} \frac{\delta_{Nu}}{L} \right)^{2.75} + 1 \quad \text{Equation 9-2}$$

The regime transition for laminar to wavy film flow occurs at a Reynolds number of 5. Between a Reynolds number of 5 and approximately 45, Figure 7-17 shows that the enhancement increases linearly. As a result, a good fit of the current experimental data is attained using a linear interpolation between Reynolds numbers of 5 and 45. However, given the lack of available data to assess the transitional wavy regime for thin gas diffusion layers, and to simplify application of the model, it is reasonable to assume that wavy film correction factor can be applied at all Reynolds numbers above 5. Finally, a Reynolds number of 400 is suggested as the upper limit for the proposed model consistent with the results of Ishigai et al. (1972) and considering the range of experimental conditions included in the study. For a flat plate, the model is given as follows:

$$\text{Nu}_{\text{dl}} = \frac{q''L/(T_b - T_i)}{\Theta_{\text{de la Rosa}}k_{\text{eff}}} = 0.1\text{Ra}_c^{1/3} \quad \text{for} \quad \text{Re} \leq 5$$

Equation 9-3

$$\text{Nu}_{\text{dl}} = \frac{q''L/(T_b - T_i)}{\Theta_{\text{de la Rosa}}k_{\text{eff}}} = 0.1\alpha\text{Ra}_c^{1/3} \quad \text{for} \quad 5 < \text{Re} \leq 400$$

Figure 9-2 shows the measured total heat transfer coefficient versus the predicted heat transfer coefficient using the Equation 9-3 gas layer prediction, the Equation 3-3 laminar liquid film and Equation 3-4 wavy liquid film prediction. These equations are solved iteratively by varying the liquid film interface temperature such that Equation 3-1 is valid. The model predicts all reported data, with the exception of the Uchida et al. (1965) laminar gas layer results, within 38% at 95% confidence. Eliminating the Uchida et al. data, Tagami 0.9 m length data and the Dehbi (1991) results below 8000 W/m², the 95% confidence interval is ±30%.

Dehbi (2015) recently reported the results of a study that fit the data of Kim et al. (2009), Su et al. (2013 and 2014), Uchida et al. (1965), Anderson (1998a), Liu (1999) and Dehbi (1991). The study did not consider the results of Tagami (1965) or Kataoka et al. (1994). Dehbi neglects the influence of liquid film thermal resistance and gas layer sensible heat transfer. Furthermore, the model uses a correlation based on laminar flow over a vertical cylinder to assess turbulent conditions. Finally, Dehbi (2015) excludes the high steam fraction results of Kim et al. (2009). The Dehbi model is given by:

$$h_t = 0.185D^{2/3}(\rho_w + \rho_b) \left(\frac{\rho_w - \rho_b}{\mu_g} \right)^{1/3} \frac{i_{fg}}{(T_b - T_w)} \ln \left(\frac{1 - W_{v,i}}{1 - W_{v,b}} \right)$$

Equation 9-4

Figure 9-3 shows the results of Equation 9-4 compared to the current database. In order to reproduce the results of Dehbi (2015), it is necessary to use the ideal gas law to predict the results of Kim et al. (1999) at pressures up to 20 bar. Figure 9-3 is a reasonable reproduction of Dehbi's result considering the large number of data points that must be extracted from graphically reported results.

As reported by Dehbi (2015) the model fit is within ±30% for the database of conditions examined. However, the high steam fraction results of Kim et al. (2009), the data of Tagami (1965), results of Kataoka et al. (1994) and the current experimental data all fall outside of the reported uncertainty of the model. The error is as high as 170% for the Tagami data and 120% for the current experimental data.

- Kataoka et al. (1994) Air at 1 bar Initial Pressure; L=4.5m
- Su et al. (2013) Air; L=2.0m
- Dehbi (1991) Air; L=3.5m
- Kim et al. (2009) Nitrogen; L=0.65m
- Tagami (1965) Air; L=0.3m
- Tagami (1965) Air; L=0.9m
- Uchida et al. (1965) Nitrogen at 1 bar Initial Pressure; L=0.3m
- Uchida et al. (1965) Air at 1 bar Initial Pressure; L=0.3m
- Liu (1999) Air; L=2.0m
- △ Anderson (1998) Atmospheric Facility; L=0.91m
- Anderson (1998) Pressurized Facility; L=1.13m
- Experimental 0.457 m Width; L=2.13m
- Experimental 0.914 m Width; L=2.13m

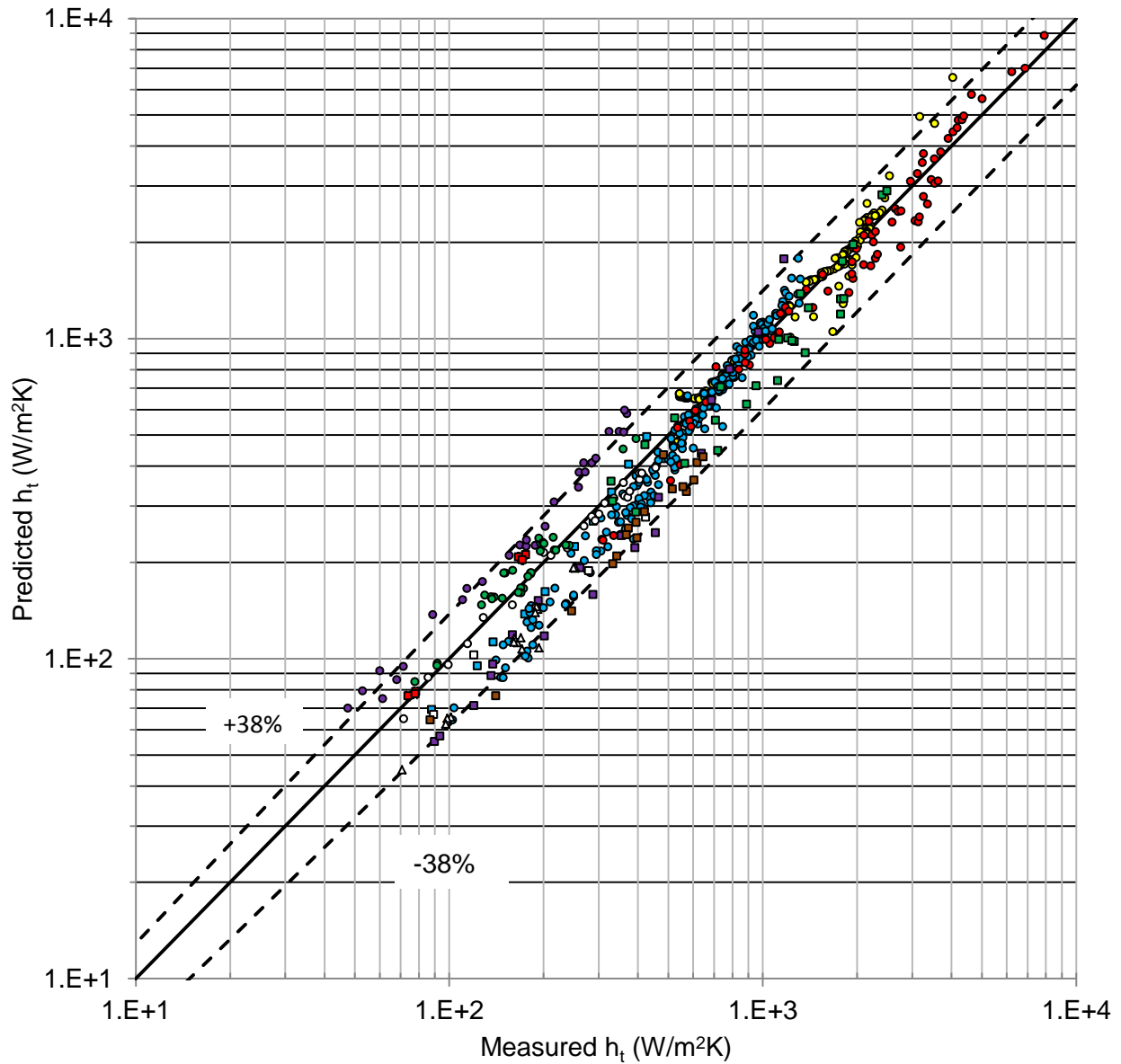


Figure 9-2 Total Heat Transfer Coefficient Predicted Using the Equation 9-3 Gas Diffusion Layer Model Corrected for Film Waves and the Equation 3-4 Liquid Film Model versus the Measured Total Heat Transfer Coefficient

- Kataoka et al. (1994) Air at 1 bar Initial Pressure; L=4.5m
- Su et al. (2013) Air; L=2.0m
- Dehbi (1991) Air; L=3.5m
- Kim et al. (2009) Nitrogen; L=0.65m
- Tagami (1965) Air; L=0.3m
- Tagami (1965) Air; L=0.9m
- Uchida et al. (1965) Nitrogen at 1 bar Initial Pressure; L=0.3m
- Uchida et al. (1965) Air at 1 bar Initial Pressure; L=0.3m
- Liu (1999) Air; L=2.0m
- Experimental 0.457 m Width; L=2.13m
- Experimental 0.914 m Width; L=2.13m
- △ Anderson (1998) Atmospheric Facility; L=0.91m
- Anderson (1998) Pressurized Facility; L=1.13m

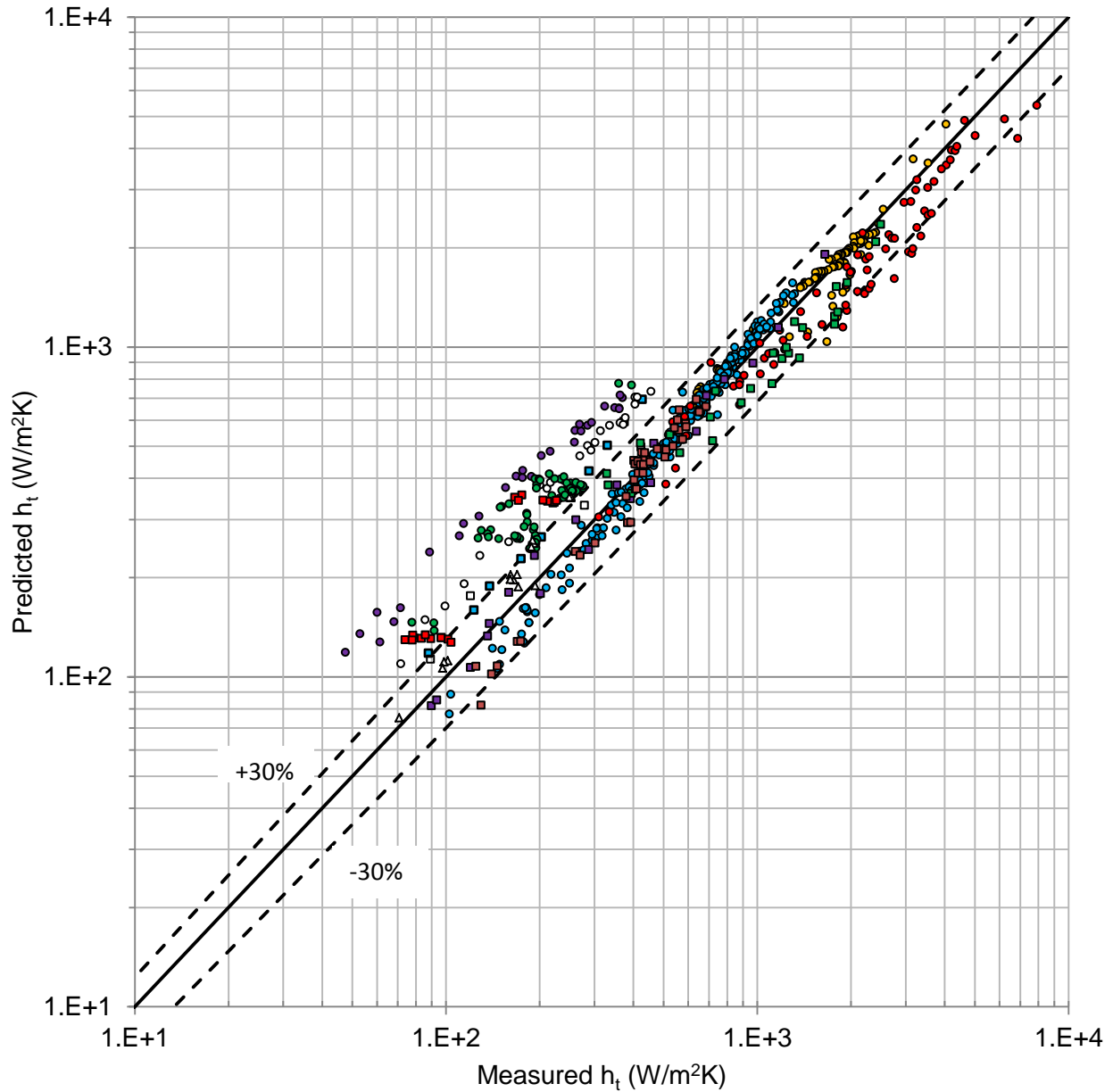


Figure 9-3 Total Heat Transfer Coefficient Predicted Using the Equation 9-4 Model from Dehbi (2015) versus the Measured Total Heat Transfer Coefficient

The model proposed by Dehbi (2015) does not approach the correct limits for either the negligible mass transfer scenario or a pure steam condensation condition since sensible heat transfer and liquid film thermal resistance are neglected. The proposed model approaches the appropriate limits for both conditions. In fact, the Equation 9-3 gas layer model coupled with the Equation 3-4 liquid film model can be used to predict the heat transfer results of Warner and Arpaci (1968) and pure steam condensation results of Kutateladze and Gogonin (1979).

10.0 Summary and Conclusions

The condensate mass flow rate based measurement method results in measurement uncertainty that is generally less than 5%. This allows characterization of the heat and mass transfer enhancement attributed to suction, film interface waves and plate inclination. Based on the laminar liquid film results, the suction factor proposed by de la Rosa et al. (2009) appears appropriate for application to the turbulent diffusion boundary layer.

The experimental results demonstrate a diffusion layer heat transfer enhancement due to surface waves in the range of 10% to 30%. Using visual observations and direct measurement of the condensate film thickness profile, a clear separation between results with laminar, transitional wavy and wavy liquid film regimes is observed. These regime transitions are consistent with those reported by Ishigai et al. (1972).

The diffusion layer heat and mass transfer enhancement due to surface wave disruption is more pronounced as the diffusion layer thickness approaches the characteristic length of the film. A comprehensive review of the available literature databases shows a clear trend between the heat transfer enhancement factor and the ratio of the diffusion layer thickness to the liquid film length scale for Reynolds numbers above the wavy transition criteria.

A model to correct for the wavy film enhancement effect on vertical surfaces has been proposed in Equation 9-2 and Equation 9-3. Application of the model must consider the liquid film thermal resistance as given by Equation 3-4, which requires iteration of the interface temperature to solve. The model is shown to predict the current experimental results and all results from the literature within 38% at 95% confidence interval. The model approaches the appropriate limits for the scenario with no mass transfer and the scenario of pure steam condensation. This model is in agreement the hypotheses outlined by Gido and Koestel (1983) as to the effects of the wavy film flow. However, the functional relationship between the diffusion layer and liquid film length scales is not captured by the Gido and Koestel model, which uses a continuous function dependent upon the condensing surface height.

The heat and mass transfer analogy applied to the Al-Arabi and Sakr (1988) heat transfer correlation for vertical and inclined conditions describe the inclination effect appropriately for liquid film Reynolds numbers less than 10. However, a best fit of the data from this program results in a slightly different

correlation as given by Equation 7-4. As film flow Reynolds number increases, a clear enhancement to heat and mass transfer is observed for the vertical plate. The enhancement is less for slight inclination and essentially no enhancement is observed for angles less than 30° from horizontal. This result implies that the gravitational instabilities that disrupt the diffusion layer for the inclined condition, which are well known for the heat transfer case, disrupt the diffusion layer in a similar manner to the wavy film interface.

Results of this research may be used to more accurately predict the heat transfer and condensation distribution within the containment vessel for SBO conditions. This will allow accurate tracking of condensate film on the containment wall and dome, which is significant with respect to the AP1000 plant SBO coping strategy. Furthermore, this work will support containment response prediction improvements, which has numerous benefits for plant design and margin.

11.0 Recommendations for Future Work

The testing conducted during this project was time intensive and this impacted the total number of experiments that could be conducted. Ideally, several hundred or more experiments would have been conducted to assess the influence of liquid film disturbances on the gas layer. This was not feasible with the facility design. Considering the relatively low cost of automated valves and programmable logic controllers, strong consideration should be given to fully automating the test facility to increase the number of experiments while minimizing worker costs.

Future work may consider a cylindrical apparatus to examine the influence of film waves for the vertical wall. Although a cylindrical apparatus would not be suitable for evaluating the inclined plate, it would simplify the test facility design and allow more detailed investigations of the wavy film interface for the vertical wall over a wider range of temperatures and pressures. The apparatus should be larger in diameter than the 0.038 m diameter cylinder experiments, common in the published literature, such that the results can be treated as a flat plate without question. A diameter of 0.1 to 0.2 m, similar to the experimental apparatus of Tagami (1965), would be sufficient. Ideally, the experimental database would be extended to conditions of turbulent gas layer Rayleigh number with a thin gas diffusion layer, such as the conditions reported by Kim et al. (2009). Parametrically varying the liquid film Reynolds number could be conducted in a similar manner to what was done here. However, at high heat transfer rates, it may be necessary to withdrawal liquid film to avoid transition to wavy film flows. New experimental techniques would need developed to conduct experiments in this manner.

The use of the chromatic confocal measurement method was relatively successful for this program, considering the first time application in a condensing steam environment. The heated lens apparatus performed well and valuable data was gathered to support understanding of the wavy liquid film influence on the gas boundary layer. However, after long periods of usage, the lens began to develop water spots that were difficult to remove and affected the optical grade coating on the lens. This effect, coupled with the grey test surface that is not an ideal reflector, caused low signal to noise ratio. It is hypothesized that the water spots were caused by mist in the vessel that existed during transient between experimental conditions. To address these concerns, an automated lens cover could be installed and a more reflective

condensing surface used. Finally, future efforts should strongly consider installing at least two sensors in close proximity such that the signals can be cross correlated to attain a direct measure of the liquid film wave velocity.

The study of the inclination angle effects necessitated the flat plate geometry for this program. As stated in Section 7.3, the inclination angle study was conducted under conditions in which the liquid film thermal resistance is negligible. For conditions where the film resistance is no longer negligible, further work is needed to develop an improved model compared to the one reported by Gerstmann and Griffith (1965 and 1967). The model should approach the results obtained by Kutateladze and Gogonin (1979) for the vertical plate scenario. Further studies in this area will likely require a traversing film thickness probe. This was attempted as part of this program using a shaft screw translation stage. However, the Teflon on stainless steel screw sleeve seized in the hot condensing environment before sufficient data could be collected.

Finally, the observed heat transfer enhancement due to the development of film waves indicates that engineered features that promote disruption of the gas boundary layer may warrant further study. For instance, hydrophilic coatings may be implemented to reduce both the liquid film thermal resistance and to promote disruption of the gas boundary layer by the development of drop-wise condensation. Another possibility is the installation of small ridges in the surface, either machined or with specialized coatings, to promote disruption of the gas layer. These topics may be the subject of future research.

12.0 References

- Al-Arabi, M. and Khamis, M., 1982. Natural convection heat transfer from inclined cylinders. *International Journal of Heat and Mass Transfer*, 25(1), pp. 3-15.
- Al-Arabi, M. and Sakr, B., 1988. Natural convection heat transfer from inclined isothermal plates. *International Journal of Heat and Mass Transfer*, 31(3), pp. 559-566.
- Anderson, M.H., 1998a. Steam condensation on cold walls of advanced PWR containments. University of Wisconsin - Madison, PhD dissertation.
- Anderson, M.H., Herranz, L.E. and Corradini, M.L., 1998b. Experimental analysis of heat transfer within the AP600 containment under postulated accident conditions. *Nuclear Engineering and Design*, 185, pp. 153-172.
- Bayley, F.J., 1955. An analysis of turbulent free-convection heat transfer. *Proceedings of the Institution of Mechanical Engineers*, 169, pp. 361-370.
- Bird, R.B., Stewart, W.E. and Lightfoot, E.N., 2007. *Transport phenomena*. John Wiley & Sons.
- Clausing, A.M., 1983. Natural convection correlations for vertical surfaces including influences of variable properties. *Journal of Heat Transfer*, 105(1), pp.138-143.
- Collier, J.G. and Thome, J.R., 1994. *Convective boiling and condensation*. Clarendon Press.
- Corradini, M.L., 1984. Turbulent condensation on a cold wall in the presence of a noncondensable gas. *Nuclear Technology*, 64(2), pp.186-195.
- de la Rosa, J.C., et al., 2009a. Review on condensation on the containment structures. *Progress in Nuclear Energy*, 51, pp. 32-56.
- de la Rosa, J.C., Herranz, L.E. and Muñoz-Cobo, J.L., 2009b. Analysis of the suction effect on the mass transfer when using the heat and mass transfer analogy. *Nuclear Engineering and Design*, 239, pp. 2042-2055.

- Dehbi, A.A., 1991. The effects of noncondensable gases on steam condensation under turbulent natural convection conditions. Massachusetts Institute of Technology, Department Nuclear Engineering, PhD dissertation.
- Dehbi, A.A., 2015. A generalized correlation for steam condensation rates in the presence of air under turbulent free convection. *International Journal of Heat and Mass Transfer*, 86, pp. 1-15.
- Eckert, E.R. and Jackson, T.W., 1950. Analysis of turbulent free-convection boundary layer on flat plate (No. NACA-TN-2207). National Advisory Committee for Aeronautics. Washington, DC.
- Fujii, T. and Imura, H., 1972. Natural convection heat transfer from a plate with arbitrary inclination. *International Journal of Heat and Mass Transfer*, 15, pp. 755-767.
- Gerstmann, J. and Griffith, P., 1965. The effect of surface instabilities on laminar film condensation. Massachusetts Institute of Technology, Technical Report No. 5050-36.
- Gerstmann, J. and Griffith, P., 1967. Laminar film condensation on the underside of horizontal and inclined surfaces. *International Journal of Heat and Mass Transfer*, 10, pp. 567-580.
- Gido, R.G. and Koestel, A., 1983. Containment condensing heat transfer. Second International Topical Meeting on Nuclear Reactor Thermal-Hydraulics, Santa Barbara, CA.
- Herranz, L.E., Anderson, M.H. and Corradini, M.L., 1998. A diffusion layer model for steam condensation within the AP600 containment. *Nuclear Engineering and Design*, 183, pp. 133-150.
- Huhtiniemi, I., 1991. Condensation in the presence of noncondensable gas: effect of surface orientation. University of Wisconsin - Madison, PhD dissertation.
- Huhtiniemi, I. and Corradini, M., 1993. Condensation in the presence of noncondensable gases. *Nuclear Engineering and Design*, 141, pp. 429-446.
- Indeikina, A., Veretennikov, I. and Chang, H., 1997. Drop fall-off from pendent rivulets. *Journal of Fluid Mechanics*, 338, pp. 173-201.
- Ishigai, S., Nakanisi, S., Koizumi, T. and Oyabu, Z., 1972. Hydrodynamics and heat transfer of vertically falling liquid films. *Bulletin of the Japan Society of Mechanical Engineers*, 15(83), pp. 594-601.

- Kang, H.C. and Kim, M.H., 1994. Effect of non-condensable gas and wavy interface on the condensation heat transfer in a nearly horizontal plate. *Nuclear Engineering and Design*, 149, pp. 313-321.
- Kataoka, Y., Fukui, T., Hatamiya, S., Nakao, T., Naitoh, M. and Sumida, I., 1991. Experimental study on convection heat transfer along a vertical flat plate between different temperature pools. *ANS National Heat Transfer Conference*, pp. 99-106.
- Kataoka, Y., Fukui, T., Hatamiya, S., Nakao, T., Naitoh, M. and Sumida, I., 1992. Experiments on convection heat transfer along a vertical flat plate between pools with different temperatures. *Nuclear Technology*, 99(3), pp.386-396.
- Kataoka, Y., Fujii, T., Murase, M. and Tominaga, K., 1994. Experimental study on heat removal characteristics for water wall type passive containment cooling system. *Journal of Nuclear Science and Technology*, 31(10), pp.1043-1052.
- Kays, W.M., Crawford, M.E. and Weigand, B., 2005. *Convective heat and mass transfer*. McGraw-Hill, New York.
- Kim, J., Lee, Y., Ahn, H. and Park, G., 2009. Condensation heat transfer characteristic in the presence of noncondensable gas on natural convection at high pressure. *Nuclear Engineering and Design*, 239, pp. 688-698.
- Kutateladze, S.S., 1964. *Fundamentals of heat transfer*. Academic Press Inc. New York, NY.
- Kutateladze, S.S. and Gogonin, I.I., 1979. Heat transfer in film condensation of slowly moving vapour. *International Journal of Heat and Mass Transfer*, 22(12), pp.1593-1599.
- Lel, V.V., Al-Sibai, F. and Renz, U., 2005. Local thickness and wave velocity measurement of wavy films with a chromatic confocal imaging method and a fluorescence intensity technique. *Experiments in Fluids*, 39, pp. 856-864.
- Liu, H., 1999. An experimental investigation of a passive cooling unit for nuclear plant containment (Master's dissertation), MIT Department of Nuclear Engineering, Cambridge, MA.
- Liu, H., Todreas, N.E. and Driscoll, M.J., 2000. An experimental investigation of a passive cooling unit for nuclear plant containment. *Nuclear Engineering and Design*, 199(3), pp.243-255.

- McAdams, W. H., 1954. Heat Transmission, 3rd Edition, McGraw-Hill, New York.
- Na, T.Y. and Chiou, J.P., 1980. Turbulent natural convection over a slender circular cylinder. Heat and Mass Transfer, 14(3), pp.157-164.
- Park, S.K., Kim, M.H. and Yoo, K.J., 1996. Condensation of pure steam and steam-air mixture with surface waves of condensate film on a vertical wall. International Journal of Multiphase Flow, 22, pp. 893-908.
- Park, S.K., Kim, M.H. and Yoo, K.J., 1997. Effects of wavy interface on steam-air condensation on a vertical surface. International Journal of Multiphase Flow, 23(6), pp. 1031-1042.
- Peterson, P.F., Schrock, V.E. and Kageyama, T., 1993. Diffusion layer theory for turbulent vapor condensation with non-condensable gas. Transactions of the ASME, 115, pp. 998-1003.
- Peterson, P.F., 1996. Theoretical basis for the Uchida correlation for condensation in reactor containments. Nuclear Engineering and Design, 162, pp. 301-306.
- Poling, B.E., Prausnitz, J.M. and O'Connell, J.P., 2001. The properties of gases and liquids. McGraw-Hill, New York.
- Popiel, C.O., 2008. Free convection heat transfer from vertical slender cylinders: a review. Heat Transfer Engineering, 29(6), pp.521-536.
- Rothrock III, D.A., 1968. A study of flows down the underside of an inclined plane. University of Cambridge, PhD dissertation.
- Schulz, T.L., 2006. Westinghouse AP1000 advanced passive plant. Nuclear Engineering and Design, 236, pp. 1546-1557.
- Saunders, O.A., 1936. The effect of pressure upon natural convection in air. Proceedings of the Royal Society of London. Series A, Mathematical and Physical Sciences, 157(891), pp. 278-291.
- Siebers, D.L., Moffatt, R.F. and Schwind, R.G., 1985. Experimental, variable properties natural convection from a large, vertical, flat surface. ASME Journal of Heat Transfer. 107(1), pp. 124-132.

- Su, J., Sun, Z., Fan, G. and Ding, M., 2013. Experimental study of the effect of non-condensable gases on steam condensation over a vertical tube external surface. *Nuclear Engineering and Design*, 262, pp.201-208.
- Su, J., Sun, Z., Ding, M., Fan, G., 2014. Analysis of experiments for the effect of noncondensable gases on steam condensation over a vertical tube external surface under low wall subcooling. *Nuclear Engineering and Design*, 278, pp. 644-650.
- Tagami, T., 1965. Interim report on safety assessments and facilities establishment project for June 1965, No. 1. Japanese Atomic Energy Research Agency.
- Uchida, H., Oyama, A., Togo, Y., 1965. Evaluation of post-incident cooling systems of light-water power reactors. *Proceedings of the Third International Conference on the Peaceful Uses of Atomic Energy*, 13, pp. 93-102.
- Vliet, G.C., 1969. Natural convection local heat transfer on constant-heat-flux inclined surfaces. *Journal of Heat Transfer*, 91(4), pp. 511-516.
- Wagner, W. and Pruß, A., 2002. The IAPWS formulation 1995 for the thermodynamic properties of ordinary water substance for general and scientific use. *Journal of Physical and Chemical Reference Data*, 31(2), pp. 387-535.
- Warner, C.Y. and Arpaci, V.S., 1968. An experimental investigation of turbulent natural convection in air at low pressure along a vertical heated flat plate. *International Journal of Heat and Mass Transfer*, 11(3), pp. 397-406.

Appendix A Instrumentation Uncertainty

A.1 Analog to Digital Conversion

A national instruments data acquisition system (DAS) is used to acquire data from all instrumentation. The DAS consists of two, NI cDAQ-9188, 8 slot Ethernet chassis. Table A-1 summarizes the analog input cards used for testing. Table A-2 summarizes the vendor specified accuracy for each of the analog input card models.

Table A-1 Data Acquisition System Analog Input Module Configuration					
Chassis	Slot	Model #	Serial #	# Channels	Type
1	Slot 1	NI 9217	19168EE	4	RTD
	Slot 2	NI 9217	19168D1	4	RTD
	Slot 3	NI 9217	19168C8	4	RTD
	Slot 4	NI 9214	18FBBA3	12	TC
	Slot 5	NI 9214	18FBBC3	12	TC
	Slot 6	NI 9203	1890ED3	8	Current
	Slot 7	NI 9219	190FD33	4	Current
	Slot 8	NI 9219	190FD0F	4	Current
2	Slot 6	NI-9239	190448E	4	Voltage

Table A-2 Data Acquisition System Analog Input Module Accuracies					
Measurement Type	Manufacturer	Model #	Range	Reading (Gain) Error	Range (Offset) Error
Voltage	National Instruments	NI 9239	± 10 V	$\pm 0.04\%$	± 1.35 mV
Current	National Instruments	NI 9219	± 25 mA	$\pm 0.1\%$	± 0.00075 mA
Current	National Instruments	NI 9203	± 21.5 mA	$\pm 0.04\%$	± 0.0043 mA
RTD	National Instruments	NI 9217	-200 to 850°C	N/A	± 0.15 °C
Thermocouple	National Instruments	NI 9214	-200 to 350°C	N/A	± 0.33 °C

A.2 Mass Flow Meters

Two Rosemount CMF200 Coriolis flow meters are used to monitor chiller 1 and chiller 2 flow rates. One Rosemount CMFS025 is used to monitor film applicator flow rate. Table A-3 provides the summary of instrument accuracies.

Table A-3 Mass Flow Meter Accuracies						
ID	Device	Serial Number	Accuracy Above Cutoff (% of Rate)	Accuracy Cutoff (kg/hr)	Accuracy Below Cutoff (kg/hr)	Span (kg/hr)
CFM3	Transmitter	25467055	±0.10	19	±0.019	1,134
	Meter	12096713				
CFM2	Transmitter	25467089	±0.10	2,177	±2.2	11,340
	Meter	14390859				
CFM1	Transmitter	25410343	±0.10	2,177	±2.2	11,340
	Meter	14405959				

All Coriolis flow meters are calibrated using a reference standard meter as described in ISO 10790:1999E by an ISO 17025 accredited laboratory.

The NI 9219 mA input card used to acquire signals from the Coriolis flow meters has an accuracy of ±0.1% of the measured current ± 0.00075 mA. The combined accuracy of the flow meter and analog input card is calculated using the square root sum of squares (SRSS) error of the NI 9219 analog input module and the Coriolis sensor accuracy. To simplify the analysis, the analog input module accuracy can be evaluated at the instrument span to be equal to 0.06% of reading (0.0004 + 0.0043 mA/20mA). For CFM1, CFM2 and CFM3 the accuracy above the accuracy cutoff is then 0.117% of reading $(0.1^2+0.06^2)^{0.5}$. Below the accuracy cutoff the accuracy due to analog input module can be considered negligible.

A.3 Resistance Thermal Detectors

Four wire, 100 Ω, platinum RTDs are used to measure cooling channel fluid and tank environmental temperatures. Manufacturer accuracy for the RTDs considering calibration, hysteresis and repeatability is stated as 0.22°C maximum over a 0 to 200°C temperature range. Combining the RTD and NI-9217 analog input module accuracy from Table A-2 using the SRSS yields a combined accuracy of ±0.27°C.

Pre-test calibration results are in terms of measured resistance versus temperature over a range of temperatures. The calibration standard used for all calibrations had a combined accuracy of 0.114°C from 0 to 100°C and 0.14°C from 100 to 200°C. A curve fit in the form of Equation A-1 was used to relate temperature to resistance.

$$T = a * R^2 + b * R + c \quad \text{Equation A-1}$$

During pre-test calibration, the maximum difference between measured temperature and calculated using Equation A-1 was less than 0.01°C.

A.4 Thermocouples

Omega special limits of error T-type thermocouples are used to monitor temperature at various locations in the test facility. The uncorrected thermocouple accuracy is ±0.5°C. The thermocouples are calibrated as a system with the NI 9214 modules using a linear fit. The combined accuracy of the thermocouples and NI-9214 module is ±0.6°C.

A.5 Inclinometer

Plate inclination is monitored with a Penny and Giles sealed tilt sensor model # STT280/60/P5 with ±60° measurement range. The ±60° measurement range instrument was installed with a 45° offset. This allowed the entire range of plate inclination to be monitored with 1.2° accuracy.

Calibration of the sensor is performed at 0°, 45° and 90° degrees using a spirit level and all results were within manufacturer specifications. The manufacturer stated temperature effect was confirmed by monitoring the inclination angle during heat-up of the test facility with the plate at various angles.

A.6 Pressure Transducers

Table A-4 below provides the span and accuracy for each pressure transducers. The accuracy values shown in Table A-4 consider the instrument reference accuracy, long term stability, line pressure effect and ambient temperature effect.

Table A-4 Pressure Transducer Accuracies			
ID	Model #	Span	Accuracy (Pa)
DP1	3051CD2A02A1AS5M5Q4	6.90 kPa (differential)	±6.70
DP2	3051CD2A02A1AS5M5Q4	6.90 kPa (differential)	±6.70
P1	3051CA2A22A1AM5B4P8Q4	345 kPa (absolute)	±279

The combined accuracy of the pressure instrumentation and analog input modules can be calculated by statistically combining the uncertainties. To simplify the assessment, the analog input module accuracy is conservatively evaluated using the instrument span.

For DP1 and DP2 the uncertainty in measured pressure difference is $\pm 6.90 \text{ kPa} \cdot (0.0004 + 0.0043 \text{ mA}/20 \text{ mA})$ or $\pm 4.24 \text{ Pa}$. Therefore, the combined accuracy for DP1 and DP2 is $(4.24^2 + 6.70^2)^{0.5}$ or $\pm 7.9 \text{ Pa}$. For P1 the uncertainty in measured pressure difference is $\pm 345 \text{ kPa} \cdot (0.0004 + 0.0043 \text{ mA}/20 \text{ mA})$ or 212 Pa . Therefore, the combined accuracy for P1 is $(212^2 + 279^2)^{0.5}$ or $\pm 350 \text{ Pa}$.

A.7 Summary of Instrumentation Uncertainty

Table A-5 below summarizes the uncertainty of all instrumentation. These values account for the combined uncertainty of the instrument and analog input module accuracy. The measurement uncertainty could have been improved by using digital instrument communications, however the existing analog system was deemed acceptable for this work. Furthermore, the measurement uncertainty of thermocouples could have been improved by using a polynomial fit rather than a linear fit.

Table A-5 Summary of Combined Instrumentation Accuracies			
Instrument	Accuracy	Accuracy Cutoff	Accuracy Below Cutoff
CFM3	$\pm 0.117\%$ of Rate	19 kg/hr	$\pm 0.019 \text{ kg/hr}$
CFM1, CFM2	$\pm 0.117\%$ of Rate	2,177 kg/hr	$\pm 2.2 \text{ kg/hr}$
RTD1-10	$\pm 0.27^\circ\text{C}$	N/A	N/A
TC1-30	$\pm 0.6^\circ\text{C}$	N/A	N/A
Inc	$\pm 1.2^\circ$	N/A	N/A
DP1 and DP2	$\pm 7.9 \text{ Pa}$	N/A	N/A
P1	$\pm 350 \text{ Pa}$	N/A	N/A

Appendix B Data Analysis Methodology

This Appendix documents the calculation steps for converting the test measurements to heat transfer rates and coefficients. The analysis of test uncertainty is included for each parameter using the methods described in ASME PTC 19.1-2013. The analysis results are provided in tabular form in Appendix E.

B.1 Gutter and Trough Collection Container Mass Flow Rate

Condensate remaining attached to the test plate is collected in the gutter and drained to the gutter collection tank. Condensate that falls from the plate is collected in catch troughs and drained to a collection tank. Condensate mass flow rate to these collection tanks is monitored with differential pressure transducers DP1 and DP2 for the gutter and trough respectively.

Tank dimensions for each of the collection tanks were taken using a calibrated caliper with an accuracy of 0.5 mm. Dimensions were taken at several elevations and diameters. Table B-1 through Table B-3 summarize the measured values. The tanks used for the 0.457 m width plate experiments were different from the 0.914 m plate widths as indicated in Table B-4 in an effort to improve the accuracy of the .457 m width plate experiments. Table B-4 also summarizes the calculated cross sectional area along with the maximum deviation in measured area for each collection tank. The deviation in average cross sectional area as a function of height was treated as an uncertainty for simplicity.

Table B-1 Collection Tank 1 Dimensions					
Distance from top (cm)	Diameter measurements (cm)			Average diameter (cm)	Average area (cm ²)
	#1	#2	#3		
0.0	2.766	2.758	2.761	2.761	5.987
7.6	2.753	2.774	2.753	2.761	5.987
15.2	2.764	2.776	2.771	2.771	6.031
22.9	2.776	2.741	2.761	2.758	5.976
27.9	2.766	2.774	2.771	2.771	6.031

Table B-2 Collection Tank 2 Dimensions					
Distance from top (cm)	Diameter measurements (cm)			Average diameter (cm)	Average area (cm ²)
	#1	#2	#3		
0.0	9.172	9.182	9.167	9.174	66.11
5.1	9.182	9.177	9.187	9.182	66.22
10.2	9.177	9.169	9.180	9.174	66.11
15.2	9.169	9.180	9.169	9.172	66.07
20.3	9.187	9.187	9.164	9.180	66.18
27.9	9.172	9.154	9.169	9.164	65.96

Table B-3 Collection Tank 3 Dimensions						
Distance from top (cm)	Diameter measurements (cm)				Average diameter (cm)	Average area (cm ²)
	#1	#2	#3	#4		
2.5	23.745	23.856	23.856	23.802	23.815	445.44
7.6	23.818	23.876	23.823	23.807	23.830	446.01
15.2	23.843	23.804	23.778	23.807	23.807	445.16
22.9	23.843	23.851	23.782	23.785	23.815	445.44
30.5	23.802	23.774	23.853	23.815	23.813	445.35
38.1	23.774	23.783	23.802	23.785	23.787	444.40

Table B-4 Summary of Collection Tank Cross Sectional Areas				
Collection Tank	Position for 0.457 m Width Plate Experiments	Position for 0.914 m Width Plate Experiments	Average Cross Sectional Area	Maximum Measured Deviation from Average
			cm ²	%
Tank 1	Trough	N/A	6.003	0.43%
Tank 2	Gutter	Trough	66.11	0.21%
Tank 3	N/A	Gutter	445.3	0.21%

Thermal expansion of the tanks occurs from the room temperature conditions that existed at the time data in Table B-1 through Table B-3 was recorded. Considering a maximum possible collection tank temperature of 130 °C, the maximum temperature difference from room temperature is 110°C. Assuming thermal equilibrium of the tank wall and a thermal expansion coefficient of $16 \times 10^{-6} \text{ }^\circ\text{C}^{-1}$ for the stainless steel collection tanks, this results in a 0.36% increase in the total cross sectional area (this result is independent of tank diameter). Rather than attempting to correct for thermal expansion, this effect was

treated as an uncertainty. Therefore, the total uncertainty associated with tank cross sectional area was taken as the addition of uncertainty due to cross sectional area non-uniformities and thermal expansion.

Table B-5 summarizes these results.

Table B-5 Collection Tank Cross Sectional Area Uncertainties				
Collection Tank	Uncertainty due to Non-Uniformities	Uncertainty Due to Thermal Expansion	Combined Uncertainty	
Tank 1	±0.43%	±0.36%	±0.79%	±0.047 cm ²
Tank 2	±0.21%	±0.36%	±0.57%	±0.38 cm ²
Tank 3	±0.21%	±0.36%	±0.57%	±2.54 cm ²

Mass flow rate for the trough collection tank, \dot{m}_t , and gutter collection tank, \dot{m}_g , was calculated using Equation B-1 and Equation B-2:

$$\dot{m}_t = \frac{A_t \cdot (\Delta P_{tf} - \Delta P_{ti})}{g \cdot \Delta t} \quad \text{Equation B-1}$$

$$\dot{m}_g = \frac{A_g \cdot (\Delta P_{gf} - \Delta P_{gi})}{g \cdot \Delta t} \quad \text{Equation B-2}$$

, where

- g Gravitational acceleration
- ΔP_{tf} Trough collection tank pressure differential at the end of the test
- ΔP_{ti} Trough collection tank pressure differential at the beginning of the test
- ΔP_{gf} Gutter collection tank pressure differential at the end of the test
- ΔP_{gi} Gutter collection tank pressure differential at the beginning of the test
- A_t Trough collection tank cross sectional area
- A_g Gutter collection tank cross sectional area
- Δt Elapsed time from the start to the end of the test

The combined uncertainty in condensate mass flow for the trough, u_{mt} , and gutter, u_{mg} collection tanks is calculated using the law of propagation of uncertainties which results in Equation B-3 and Equation B-4:

$$u_{mt} = \sqrt{\left(\frac{A_t}{g \cdot \Delta t}\right)^2 u_{\Delta P}^2 + \left(\frac{\Delta P_{tf} - \Delta P_{ti}}{g \cdot \Delta t}\right)^2 u_{A_t}^2} \quad \text{Equation B-3}$$

$$u_{mg} = \sqrt{\left(\frac{A_g}{g \cdot \Delta t}\right)^2 u_{\Delta P}^2 + \left(\frac{\Delta P_{gf} - \Delta P_{gi}}{g \cdot \Delta t}\right)^2 u_{A_g}^2} \quad \text{Equation B-4}$$

, where

- $u_{\Delta P}$ Uncertainty of measured pressure differential
- u_{A_t} Uncertainty of trough collection tank area
- u_{A_g} Uncertainty of gutter collection tank area

B.2 Average Condensing Surface Temperature

T-type thermocouples, 1.59 mm diameter, are inserted into the test plate from the back side for measurement of condensing surface temperature. The 3.18 mm diameter machined holes are filled with Dow Corning TC5622 thermally conductive grease. The thermocouples are inserted with the tip located 4.45 mm from the condensing surface. For a known, 1-D heat transfer rate, q_{ts} , through the test plate, the temperature of the condensing surface can be related to the temperature measured 4.45 mm from the test surface using Equation B-5, which can be solved for temperature of the condensing surface as shown in Equation B-6. Note that the total heat transfer rate is used in Equation B-5 for simplicity. The difference between the total heat transfer rate and heat transfer rate through the test surface is negligible for this assessment since the 1st term on the right hand side of Equation B-6 is small.

$$q_{tot} = k \cdot A_{ts} \cdot \frac{(T_w - T_4)}{L} \quad \text{Equation B-5}$$

$$T_w = \frac{L \cdot q_{tot}}{A_{ts} \cdot k} + T_4 \quad \text{Equation B-6}$$

Where,

- k Thermal conductivity of the AISI 1020 carbon steel test plate (51.9 W/m-K)
- T_w Temperature of condensing surface
- T_4 Temperature (average of measurement locations) 4.45 mm from the condensing surface
- L Distance from thermocouple tip to condensing surface (4.45 mm)
- A_{ts} Area of the condensing surface (0.973 m² or 1.95 m²)

Considering the influence of the 1.59 mm diameter thermocouple, thermally conductive grease and 3.18 mm diameter hole machined into the test plate, a disturbance will exist in the test plate due to the thermocouple. A finite element analysis was conducted to quantify these multidimensional effects using properties of the thermocouple, grease and carbon steel plate. The analysis considered the range of heat fluxes examined as part of this test program. For the conditions examined, maximum effect was less than 0.1°F. Therefore, this analysis assumes no correction is needed to account for the thermocouple disturbance.

Uncertainty in the calculated surface temperature, u_{T_w} , based on Equation B-6 can be estimated by using the law of propagation of uncertainty:

$$u_{T_w} = \sqrt{u_{T_4}^2 + u_{q_{ts}}^2 \left(\frac{L}{A \cdot k} \right)^2 + u_k^2 \left(\frac{L \cdot q_{ts}}{A \cdot k^2} \right)^2} \quad \text{Equation B-7}$$

Where

- u_k^2 Uncertainty of AISI 1020 carbon steel thermal conductivity
- u_{T_4} Uncertainty of temperature measurement

Considering conservatively high uncertainties for thermal conductivity and heat transfer rate through the condensing surface of ±20% indicates that the uncertainty due to these parameters is negligible compared to the uncertainty in temperature measurement. Therefore, Equation B-7 can be reduced to

$$u_{T_w} = u_{T_4}$$

B.3 Heat Transfer Rate Analysis Methodology

Three methods were available to calculate the total heat transfer rate through the test surface. The two most accurate methods and the uncertainty analysis for each method are presented in the following sections. The third method consists of calculating the heat transfer rate through the test plate using the measured temperature difference across the plate and the carbon steel material thermal conductivity. This method is the least accurate since the material thermal conductivity could only be determined within $\pm 10\%$, the temperature difference across the plate is small with respect to the thermocouple accuracy and a convective heat transfer model must be used to determine the thermal resistance between the coolant and test plate.

B.3.1 Heat Transfer Rate Based on the Calorimetric Balance

A calorimetric balance based on flow rate and temperature difference of the coolant pumped through the cooling channels is used to calculate the total heat removal rate. The total heat removal rate, q_{tot} , is calculated by adding the heat removal rate from each of the cooling channel sets. Equation B-8 is used to calculate the total heat removal rate:

$$q_{tot} = \dot{m}_1(i_{out_1} - i_{in_1}) + \dot{m}_2(i_{out_2} - i_{in_2}) \quad \text{Equation B-8}$$

Where

\dot{m}_1	Measured chiller 1 coolant channel mass flow rate from CFM1 sensor
\dot{m}_2	Measured chiller 2 coolant channel mass flow rate from CFM2 sensor
i_{out_1}	Chiller 1 outlet enthalpy
i_{out_2}	Chiller 2 outlet enthalpy
i_{in_1}	Chiller 1 inlet enthalpy
i_{in_2}	Chiller 2 inlet enthalpy

The combined uncertainty in total heat transfer rate, $u_{q_{tot}}$, based on Equation B-8 was calculated using the law of propagation of uncertainties which results in Equation B-9:

$$u_{q_{tot}} = \sqrt{C_{p11}^2 (\Delta T_1^2 \cdot u_{\dot{m}_1}^2 + \dot{m}_1^2 \cdot u_{\Delta T}^2) + C_{p12}^2 (\Delta T_2^2 \cdot u_{\dot{m}_2}^2 + \dot{m}_2^2 \cdot u_{\Delta T}^2)} \quad \text{Equation B-9}$$

, where

C_{p1}	Specific heat of coolant in Chiller 1 cooling channels
C_{p2}	Specific heat of coolant in Chiller 2 cooling channels
ΔT_1	Temperature difference across Chiller 1 cooling channels (RTD3 minus RTD7)
ΔT_2	Temperature difference across Chiller 2 cooling channels (RTD5 minus RTD2)
u_{m1}	Uncertainty in Chiller 1 mass flow rate measurement
u_{m2}	Uncertainty in Chiller 2 mass flow rate measurement
$u_{\Delta T}^2$	Temperature difference uncertainty (Table A-5, $\pm [(2*(0.27^\circ\text{C})^2)^{0.5}]$ or 0.38°C)

To determine the component of the heat transfer through the test plate, it is necessary to correct the total heat transfer rate by subtracting heat losses to the surroundings and heat transfer to the film applied to the test plate:

$$q_{ts} = q_{tot} - q_{loss} - q_{film} \quad \text{Equation B-10}$$

, where

q_{tot}	Total heat transfer rate through the control volume
q_{ts}	Heat transfer rate through the test surface only
q_{film}	Heat transfer rate required to cool applied film
q_{loss}	Heat transfer to surfaces other than test surface (e.g. insulation and test plate shaft)

Heat loss to the surroundings, q_{loss} , for each experiment was calculated based on the ratio of the trough condensate mass flow rate to the total mass flow rate into the trough and gutter collection tanks. This method of determining the heat losses assumes that the ratio of the sensible and latent heat transfer rates to the test surface and heat loss surfaces is the same. Furthermore, the method assumes that sensible heat differences in the condensed liquid are small. These assumptions have a negligible effect on the calculation since the majority of the enthalpy difference is due to latent heat of condensation and not sensible heat.

Film flow applied to the test plate was pumped to the plate from a penetration near the bottom of the test vessel. The temperature of the film entering the test plate was monitored with a thermocouple. The

temperature of the film exiting the test plate can be estimated based on the average condensing surface temperature (as discussed in Appendix B.2). Given the measured applied film flow rate, the total heat transfer rate required to cool the film from the applied temperature to the temperature exiting the test plate, T_s , is calculated using Equation B-11, and the total heat transfer rate through the test surface is calculated using Equation B-12.

$$q_{\text{film}} = \dot{m}_{\text{ap}} C_p (T_{\text{in}} - T_s) \quad \text{Equation B-11}$$

$$q_{\text{ts}} = q_{\text{tot}} - \frac{\dot{m}_t}{\dot{m}_t + \dot{m}_g} q_{\text{tot}} - \dot{m}_{\text{ap}} C_p (T_{\text{in}} - T_s) \quad \text{Equation B-12}$$

For simplicity, since the first term on the right hand side of Equation B-12 is large compared to the second and third terms, the uncertainty in the heat transfer rate through the test surface is assumed to be equal to the uncertainty in total heat transfer rate, $u_{q_{\text{ts}}} = u_{q_{\text{tot}}}$, evaluated using Equation B-9.

B.3.2 Heat Transfer Rate Based on the Condensate Mass Flow Rate

The measured condensate mass flow rate can be used to calculate the heat transfer rate through the test surface due to latent heat transfer to the test surface. This measure does not include the sensible heat transfer component. Therefore, an estimate of the sensible heat transfer component, based on the model presented in Section 3.2, is used to determine the total heat transfer rate with this method. Since the fraction of sensible heat transfer to overall heat transfer rate is small, the uncertainty in the sensible heat transfer estimate has a small effect on the overall heat transfer rate. Finally, as a result of this analysis method, the test results analysis becomes iterative.

The condensing heat flux can be directly calculated by multiplying the condensate mass flow rate by the latent heat of condensation assuming saturated conditions at the condensing interface using the measured plate surface temperature. From Wagner (2002) the latent heat can be assumed accurate within 0.2% for the range of conditions examined. The following equation is used to calculate the condensing heat flux:

$$q_l = \dot{m}_g i_{lg} \quad \text{Equation B-13}$$

, where i_{lg} is evaluated at the average interface temperature. The law of propagation of uncertainty results in the following

$$u_{q_l} = \sqrt{u_{\dot{m}_g}^2 i_{lg}^2 + u_{i_{lg}}^2 \dot{m}_g^2} \quad \text{Equation B-14}$$

The total heat transfer rate is calculated assuming parallel sensible and latent heat transfer using as discussed in Section 3.0. From Equation 3-19, the ratio of condensation heat transfer to total heat transfer rate can be calculated, and the sensible heat transfer rate is calculated using Equation B-16:

$$q_{\text{ratio}} = \frac{q_l}{q_l + q_s} = \frac{k_c}{k_c + \left(\frac{Pr}{Sc}\right)^{\frac{1}{3}} k} \quad \text{Equation B-15}$$

$$q_s = \frac{q_l}{q_{\text{ratio}}} - q_l \quad \text{Equation B-16}$$

The uncertainty estimate for the sensible heat transfer rate calculated using Equation B-16, is estimated to be $\pm 30\%$ based on published literature. Finally, the total heat transfer rate and uncertainty are determined by the summation of summation of sensible and latent heat components:

$$q_{ts} = q_l + q_s \quad \text{Equation B-17}$$

$$u_{q_{ts}} = \sqrt{u_{q_l}^2 + u_{q_s}^2} \quad \text{Equation B-18}$$

B.4 Heat Flux and Heat Transfer Coefficient Analysis Methodology

The heat flux can be determined by dividing the heat transfer rate through the test surface by the condensing surface area as shown in Equation B-19. No uncertainty was assumed in the condensing surface area calculation. The heat transfer coefficient is calculated by dividing the heat flux by the bulk to wall temperature difference as shown in Equation B-20. The uncertainty in heat transfer rate, bulk temperature and interface temperature can be propagated using the law of propagation of uncertainty as shown in Equation B-21.

$$q'' = \frac{q_{ts}}{A} \quad \text{Equation B-19}$$

$$h = \frac{q''}{(T_b - T_w)} = \frac{q_{ts}}{A(T_b - T_w)} \quad \text{Equation B-20}$$

$$u_h = \sqrt{u_{q_{ts}}^2 \left[\frac{1}{A(T_b - T_w)} \right]^2 + u_{T_b}^2 \left[\frac{q_{ts}}{A(T_b - T_w)^2} \right]^2 + u_{T_w}^2 \left[\frac{q_{ts}}{A(T_b - T_w)^2} \right]^2} \quad \text{Equation B-21}$$

Appendix C Analysis of Literature Data

The following sections define the methodology for converting data reported by various authors to a form that is useful for comparison to the proposed model. In most cases, this process required digitizing plots and in some cases tabulated data was reported. Finally, additional analyses were required in some instances.

C.1 Dehbi (1991) Database

Dehbi (1991) reports experimental results for condensation on a 3.5 m height, 0.038 m diameter vertical cylinder. Test results are provided in tabular form in Appendix A of the report. Heat transfer coefficients are reported for the upper 1.16 m height of the test geometry and for the full height separately. Both upper and lower heat transfer results are included here.

Experiments were conducted at isobaric conditions at pressures of 1.52, 3.04 and 4.56 bar. Bulk to interface temperature differences were reported for each test condition along with the bulk air weight fraction. The heat transfer coefficient was reported for each test condition corrected for the cylinder curvature. Section 2.4.2 of Dehbi (1991) indicates that the reported heat transfer coefficients were divided by a factor of 0.8 to account for the cylindrical effect. Therefore, the Appendix A results must be multiplied by a factor of 1.25 to attain the measured result. This correction of the Dehbi (1991) dataset is consistent with the correction described by Dehbi (2015).

Dehbi (1991) uses the ideal gas law to calculate steam and air densities. The method used to determine saturated steam partial pressure at a given temperature was not defined. Therefore, the IAPWS script is used for this purpose. Table C-1 and Table C-2 provide a complete reproduction of the results of Dehbi (1991) using the ideal gas law for density calculation and IAPWS script for saturated steam partial pressure.

Table C-1 Summary of Dehbi (1991) Experimental Results for 1.16 m Height

Test ID	P _b	0.8·h _{tot}	W _{nc}	T _b -T _w	h _{tot}	T _b	T _w	P _{v,b}	P _{nc,b}	ρ _{nc,b}	ρ _{v,b}	ρ _b
	bar	W/m ² -C		°C	W/m ² -°C	°C	°C	bar	bar	kg/m ³	kg/m ³	kg/m ³
A1	1.52	632	0.445	11.8	790	100.0	88.2	1.01	0.51	0.47	0.59	1.1
A2	1.52	353	0.632	16.6	441	91.2	74.6	0.73	0.78	0.75	0.44	1.2
A3	1.52	117	0.877	17.4	146	67.4	50.0	0.28	1.24	1.27	0.18	1.4
A4	1.52	451	0.506	15.6	564	97.5	81.9	0.93	0.59	0.56	0.54	1.1
A5	1.52	246	0.712	16.1	308	85.9	69.8	0.60	0.92	0.89	0.36	1.3
A6	1.52	142	0.817	20.2	178	76.0	55.8	0.40	1.12	1.12	0.25	1.4
A7	1.52	168	0.793	19.5	210	78.7	59.2	0.45	1.07	1.06	0.28	1.3
A8	1.52	278	0.688	15.1	348	87.6	72.5	0.64	0.88	0.85	0.38	1.2
A9	1.52	336	0.623	12.7	420	91.7	79.0	0.75	0.77	0.74	0.44	1.2
A10	1.52	388	0.586	13.5	485	93.7	80.2	0.81	0.71	0.68	0.48	1.2
A11	1.52	82	0.905	25.3	103	62.0	36.7	0.22	1.30	1.35	0.14	1.5
A12	1.52	113	0.857	21.1	141	70.6	49.5	0.32	1.20	1.22	0.20	1.4
A13	1.52	272	0.676	15.1	340	88.4	73.3	0.66	0.86	0.83	0.40	1.2
A14	1.52	670	0.392	16.4	838	101.9	85.5	1.08	0.44	0.40	0.63	1.0
A15	1.52	758	0.353	14.7	948	103.2	88.5	1.13	0.39	0.36	0.65	1.0
A16	1.52	940	0.280	14.7	1175	105.3	90.6	1.22	0.30	0.27	0.70	1.0
A17	1.52	881	0.306	16.7	1101	104.6	87.9	1.19	0.33	0.30	0.68	1.0
A18	1.52	748	0.347	14.2	935	103.4	89.2	1.14	0.38	0.35	0.66	1.0
A19	1.52	662	0.368	16.2	828	102.7	86.5	1.12	0.40	0.38	0.64	1.0
A20	1.52	707	0.391	12.4	884	101.9	89.5	1.09	0.43	0.40	0.63	1.0
A21	1.52	614	0.436	14.1	768	100.3	86.2	1.03	0.49	0.46	0.60	1.1
A22	1.52	497	0.498	17.5	621	97.9	80.4	0.94	0.58	0.54	0.55	1.1
A23	1.52	605	0.452	15.4	756	99.7	84.3	1.00	0.52	0.48	0.58	1.1
A24	1.52	748	0.332	13.5	935	103.8	90.3	1.16	0.36	0.33	0.67	1.0
A25	1.52	145	0.818	9.0	181	75.9	66.9	0.40	1.12	1.12	0.25	1.4
A26	1.52	216	0.749	13.5	270	82.9	69.4	0.53	0.99	0.97	0.32	1.3
A27	1.52	282	0.718	10.3	353	85.4	75.1	0.59	0.93	0.91	0.36	1.3
A28	1.52	336	0.671	13.7	420	88.8	75.1	0.67	0.85	0.82	0.40	1.2
A29	1.52	347	0.657	12.1	434	89.7	77.6	0.69	0.83	0.79	0.41	1.2
A30	1.52	361	0.591	17.8	451	93.5	75.7	0.80	0.72	0.68	0.47	1.2
A31	1.52	444	0.561	14.7	555	95.0	80.3	0.85	0.67	0.64	0.50	1.1
A32	1.52	420	0.540	13.8	525	96.0	82.2	0.88	0.64	0.61	0.52	1.1
A33	1.52	461	0.527	13.2	576	96.6	83.4	0.90	0.62	0.59	0.53	1.1
A34	1.52	539	0.506	10.9	674	97.5	86.6	0.93	0.59	0.56	0.54	1.1
A35	1.52	523	0.480	13.8	654	98.6	84.8	0.96	0.55	0.52	0.56	1.1
A36	1.52	581	0.462	11.8	726	99.3	87.5	0.99	0.53	0.50	0.58	1.1
A37	1.52	564	0.427	17.6	705	100.6	83.0	1.04	0.48	0.45	0.60	1.1
A38	1.52	615	0.372	24.1	769	102.5	78.4	1.11	0.41	0.38	0.64	1.0
A39	1.52	732	0.374	14.0	915	102.5	88.5	1.11	0.41	0.38	0.64	1.0

Table C-1 Summary of Dehbi (1991) Experimental Results for 1.16 m Height Continued

Test ID	P _b	0.8·h _{tot}	W _{nc}	T _b -T _w	h _{tot}	T _b	T _w	P _{v,b}	P _{nc,b}	ρ _{nc,b}	ρ _{v,b}	ρ _b
	bar	W/m ² -C		°C	W/m ² -°C	°C	°C	bar	bar	kg/m ³	kg/m ³	kg/m ³
A40	1.52	617	0.409	15.6	771	101.3	85.7	1.06	0.46	0.43	0.61	1.0
A41	1.52	649	0.343	27.8	811	103.5	75.7	1.15	0.37	0.35	0.66	1.0
B1	3.04	148	0.862	36.0	185	86.9	50.9	0.62	2.42	2.34	0.38	2.7
B2	3.04	200	0.810	30.7	250	94.5	63.8	0.83	2.21	2.09	0.49	2.6
B3	3.04	364	0.642	28.8	455	110.1	81.3	1.44	1.60	1.46	0.81	2.3
B4	3.04	323	0.678	31.1	404	107.4	76.3	1.32	1.72	1.58	0.75	2.3
B5	3.04	444	0.605	24.4	555	112.4	88.0	1.56	1.48	1.34	0.87	2.2
B6	3.04	498	0.565	22.5	623	114.8	92.3	1.68	1.36	1.22	0.94	2.2
B7	3.04	543	0.541	20.1	679	116.1	96.0	1.75	1.29	1.15	0.98	2.1
B8	3.04	595	0.511	18.1	744	117.6	99.5	1.84	1.20	1.07	1.02	2.1
B9	3.04	689	0.493	19.4	861	118.5	99.1	1.89	1.14	1.02	1.05	2.1
B10	3.04	226	0.778	31.2	283	98.3	67.1	0.95	2.08	1.96	0.56	2.5
B11	3.04	257	0.764	25.9	321	99.9	74.0	1.01	2.03	1.90	0.59	2.5
B12	3.04	282	0.726	25.8	353	103.5	77.7	1.15	1.89	1.75	0.66	2.4
B13	3.04	303	0.707	24.0	379	105.1	81.1	1.22	1.82	1.68	0.70	2.4
B14	3.04	400	0.625	23.9	500	111.2	87.3	1.49	1.55	1.40	0.84	2.2
B15	3.04	539	0.530	16.2	674	116.7	100.5	1.79	1.25	1.12	0.99	2.1
B16	3.04	550	0.521	20.4	688	117.1	96.7	1.81	1.23	1.09	1.01	2.1
B17	3.04	1041	0.306	14.4	1301	125.9	111.5	2.38	0.65	0.57	1.30	1.9
B18	3.04	429	0.542	29.6	536	116.1	86.5	1.75	1.29	1.15	0.97	2.1
B19	3.04	548	0.518	25.2	685	117.3	92.1	1.82	1.22	1.09	1.01	2.1
B20	3.04	650	0.481	21.6	813	119.0	97.4	1.93	1.11	0.99	1.06	2.1
B21	3.04	681	0.457	20.7	851	120.1	99.4	1.99	1.05	0.93	1.10	2.0
B22	3.04	722	0.440	18.9	903	120.9	102.0	2.04	1.00	0.88	1.12	2.0
B23	3.04	801	0.349	26.5	1001	124.4	97.9	2.28	0.76	0.67	1.24	1.9
B24	3.04	787	0.377	21.3	984	123.4	102.1	2.21	0.83	0.73	1.21	1.9
B25	3.04	795	0.405	16.8	994	122.3	105.5	2.14	0.90	0.80	1.17	2.0
B26	3.04	119	0.906	13.7	149	77.7	64.0	0.43	2.61	2.59	0.27	2.9
B27	3.04	143	0.891	13.2	179	81.1	67.9	0.50	2.54	2.50	0.30	2.8
B28	3.04	146	0.865	11.7	183	86.4	74.7	0.61	2.43	2.35	0.37	2.7
B29	3.04	222	0.801	16.6	278	95.7	79.1	0.87	2.17	2.05	0.51	2.6
B30	3.04	310	0.764	12.2	388	99.9	87.7	1.01	2.03	1.90	0.59	2.5
B31	3.04	329	0.708	20.6	411	105.1	84.5	1.21	1.83	1.68	0.69	2.4
B32	3.04	420	0.661	17.3	525	108.7	91.4	1.37	1.66	1.52	0.78	2.3
B33	3.04	481	0.615	21.0	601	111.8	90.8	1.52	1.52	1.37	0.86	2.2
B34	3.04	465	0.590	18.6	581	113.4	94.8	1.60	1.43	1.29	0.90	2.2
B35	3.04	628	0.494	16.8	785	118.5	101.7	1.89	1.15	1.02	1.05	2.1
B36	3.04	616	0.476	25.4	770	119.3	93.9	1.94	1.10	0.98	1.07	2.0
B37	3.04	677	0.424	21.8	846	121.5	99.7	2.09	0.95	0.84	1.15	2.0

Table C-1 Summary of Dehbi (1991) Experimental Results for 1.16 m Height Continued

Test ID	P _b	0.8·h _{tot}	W _{nc}	T _b -T _w	h _{tot}	T _b	T _w	P _{v,b}	P _{nc,b}	ρ _{nc,b}	ρ _{v,b}	ρ _b
	bar	W/m ² -C		°C	W/m ² -°C	°C	°C	bar	bar	kg/m ³	kg/m ³	kg/m ³
B38	3.04	764	0.388	26.3	955	123.0	96.7	2.18	0.86	0.76	1.19	1.9
B39	3.04	812	0.372	24.7	1015	123.6	98.9	2.22	0.82	0.72	1.21	1.9
B40	3.04	1055	0.307	20.5	1319	125.8	105.3	2.38	0.66	0.57	1.29	1.9
C1	4.56	293	0.744	29.9	366	113.8	83.9	1.62	2.93	2.64	0.91	3.6
C2	4.56	424	0.665	25.6	530	120.8	95.2	2.04	2.52	2.23	1.12	3.4
C3	4.56	524	0.622	21.5	655	124.0	102.5	2.25	2.31	2.03	1.23	3.3
C4	4.56	597	0.617	24.0	746	124.3	100.3	2.28	2.28	2.00	1.24	3.2
C5	4.56	236	0.803	28.9	295	106.8	77.9	1.29	3.27	3.00	0.73	3.7
C6	4.56	327	0.748	17.5	409	113.3	95.8	1.60	2.96	2.67	0.90	3.6
C7	4.56	188	0.850	27.2	235	99.8	72.6	1.01	3.55	3.32	0.59	3.9
C8	4.56	140	0.902	22.6	175	89.2	66.6	0.68	3.88	3.73	0.41	4.1
C9	4.56	119	0.893	22.3	149	91.4	69.1	0.74	3.82	3.65	0.44	4.1
C10	4.56	352	0.742	18.2	440	114.0	95.8	1.64	2.92	2.63	0.92	3.5
C11	4.56	360	0.732	17.6	450	115.0	97.4	1.69	2.87	2.58	0.94	3.5
C12	4.56	373	0.714	19.2	466	116.7	97.5	1.79	2.77	2.48	0.99	3.5
C13	4.56	419	0.691	16.2	524	118.7	102.5	1.91	2.65	2.36	1.05	3.4
C14	4.56	408	0.670	25.3	510	120.4	95.1	2.01	2.54	2.25	1.11	3.4
C15	4.56	441	0.642	22.6	551	122.6	100.0	2.15	2.40	2.12	1.18	3.3
C16	4.56	482	0.604	24.9	603	125.3	100.4	2.34	2.22	1.94	1.27	3.2
C17	4.56	570	0.584	22.2	713	126.5	104.3	2.44	2.12	1.85	1.32	3.2
C18	4.56	519	0.562	31.3	649	127.9	96.6	2.54	2.02	1.76	1.37	3.1
C19	4.56	627	0.526	28.5	784	129.9	101.4	2.70	1.86	1.61	1.45	3.1
C20	4.56	644	0.507	26.8	805	130.9	104.1	2.78	1.78	1.53	1.49	3.0
C21	4.56	718	0.483	25.4	898	132.2	106.8	2.88	1.68	1.44	1.54	3.0
C22	4.56	672	0.467	35.0	840	133.0	98.0	2.95	1.61	1.38	1.57	3.0
C23	4.56	831	0.422	25.0	1039	135.0	110.0	3.13	1.42	1.22	1.66	2.9
C24	4.56	842	0.402	29.7	1053	135.9	106.2	3.21	1.34	1.15	1.70	2.8
C25	4.56	928	0.380	26.2	1160	136.8	110.6	3.30	1.26	1.07	1.74	2.8
C26	4.56	949	0.363	25.9	1186	137.5	111.6	3.36	1.19	1.01	1.77	2.8
C27	4.56	991	0.354	22.3	1239	137.9	115.6	3.40	1.16	0.98	1.79	2.8

Table C-2 Summary of Dehbi (1991) Experimental Results for 3.5 m Height

Test ID	P _b	0.8·h _{tot}	W _{nc}	T _b -T _w	h _{tot}	T _b	T _w	P _{v,b}	P _{nc,b}	ρ _{nc,b}	ρ _{v,b}	ρ _b
	bar	W/m ² -C		°C	W/m ² -°C	°C	°C	bar	bar	kg/m ³	kg/m ³	kg/m ³
A1	1.52	597	0.425	24.2	746	100.7	76.5	1.04	0.48	0.45	0.60	1.0
A2	1.52	319	0.595	29.2	399	93.3	64.1	0.79	0.73	0.69	0.47	1.2
A3	1.52	121	0.858	26.6	151	70.4	43.8	0.32	1.20	1.22	0.20	1.4
A4	1.52	464	0.456	28.4	580	99.6	71.2	1.00	0.52	0.49	0.58	1.1
A5	1.52	274	0.638	27.7	343	90.8	63.1	0.72	0.79	0.76	0.43	1.2
A6	1.52	160	0.795	28.9	200	78.5	49.6	0.45	1.07	1.06	0.27	1.3
A7	1.52	174	0.767	29.5	218	81.2	51.7	0.50	1.02	1.00	0.30	1.3
A8	1.52	296	0.660	26.2	370	89.5	63.3	0.69	0.83	0.80	0.41	1.2
A9	1.52	361	0.586	25.2	451	93.7	68.5	0.81	0.71	0.68	0.48	1.2
A10	1.52	385	0.547	26.0	481	95.7	69.7	0.87	0.65	0.62	0.51	1.1
A11	1.52	83	0.888	33.3	104	65.4	32.1	0.25	1.26	1.30	0.16	1.5
A12	1.52	124	0.833	31.0	155	74.0	43.0	0.37	1.15	1.15	0.23	1.4
A13	1.52	310	0.644	25.8	388	90.5	64.7	0.71	0.80	0.77	0.43	1.2
A14	1.52	664	0.356	25.7	830	103.1	77.4	1.13	0.39	0.36	0.65	1.0
A15	1.52	747	0.320	24.3	934	104.2	79.9	1.18	0.34	0.32	0.67	1.0
A16	1.52	938	0.250	23.1	1173	106.2	83.1	1.26	0.26	0.24	0.72	1.0
A17	1.52	885	0.280	21.7	1106	105.3	83.6	1.22	0.30	0.27	0.70	1.0
A18	1.52	766	0.311	23.8	958	104.4	80.6	1.19	0.33	0.31	0.68	1.0
A19	1.52	680	0.334	25.8	850	103.8	78.0	1.16	0.36	0.33	0.67	1.0
A20	1.52	671	0.364	23.3	839	102.8	79.5	1.12	0.40	0.37	0.65	1.0
A21	1.52	605	0.398	25.0	756	101.7	76.7	1.08	0.44	0.41	0.62	1.0
A22	1.52	508	0.463	27.9	635	99.3	71.4	0.99	0.53	0.50	0.58	1.1
A23	1.52	582	0.418	26.1	728	101.0	74.9	1.05	0.47	0.44	0.61	1.0
A24	1.52	838	0.293	22.7	1048	105.0	82.3	1.21	0.31	0.29	0.69	1.0
A25	1.52	200	0.796	18.0	250	78.3	60.3	0.44	1.08	1.07	0.27	1.3
A26	1.52	244	0.723	24.2	305	85.0	60.8	0.58	0.94	0.92	0.35	1.3
A27	1.52	292	0.693	22.1	365	87.3	65.2	0.63	0.89	0.86	0.38	1.2
A28	1.52	322	0.639	25.1	403	90.8	65.7	0.72	0.80	0.76	0.43	1.2
A29	1.52	336	0.631	24.0	420	91.3	67.3	0.74	0.78	0.75	0.44	1.2
A30	1.52	367	0.558	28.7	459	95.2	66.5	0.85	0.67	0.63	0.50	1.1
A31	1.52	439	0.532	25.9	549	96.4	70.5	0.89	0.63	0.59	0.52	1.1
A32	1.52	469	0.503	24.8	586	97.7	72.9	0.93	0.59	0.55	0.54	1.1
A33	1.52	489	0.496	24.2	611	98.0	73.8	0.94	0.58	0.54	0.55	1.1
A34	1.52	540	0.469	22.3	675	99.1	76.8	0.98	0.54	0.50	0.57	1.1
A35	1.52	547	0.446	24.5	684	99.9	75.4	1.01	0.51	0.47	0.59	1.1
A36	1.52	584	0.430	22.9	730	100.5	77.6	1.03	0.49	0.45	0.60	1.1
A37	1.52	577	0.398	27.2	721	101.7	74.5	1.08	0.44	0.41	0.62	1.0
A38	1.52	644	0.333	31.0	805	103.8	72.8	1.16	0.36	0.33	0.67	1.0
A39	1.52	727	0.337	23.5	909	103.7	80.2	1.15	0.37	0.34	0.66	1.0

Table C-2 Summary of Dehbi (1991) Experimental Results for 3.5 m Height Continued

Test ID	P _b	0.8·h _{tot}	W _{nc}	T _b -T _w	h _{tot}	T _b	T _w	P _{v,b}	P _{nc,b}	ρ _{nc,b}	ρ _{v,b}	ρ _b
	bar	W/m ² -C		°C	W/m ² -°C	°C	°C	bar	bar	kg/m ³	kg/m ³	kg/m ³
A40	1.52	652	0.375	25.2	815	102.5	77.3	1.11	0.41	0.38	0.64	1.0
A41	1.52	704	0.310	31.7	880	104.5	72.8	1.19	0.33	0.31	0.68	1.0
B1	3.04	146	0.844	44.3	183	89.8	45.5	0.70	2.34	2.25	0.42	2.7
B2	3.04	196	0.778	43.0	245	98.3	55.3	0.95	2.08	1.96	0.56	2.5
B3	3.04	323	0.678	43.2	404	107.4	64.2	1.32	1.72	1.58	0.75	2.3
B4	3.04	371	0.611	41.4	464	112.1	70.7	1.54	1.50	1.36	0.86	2.2
B5	3.04	443	0.571	38.2	554	114.5	76.3	1.66	1.38	1.24	0.93	2.2
B6	3.04	501	0.544	36.2	626	115.9	79.7	1.74	1.29	1.16	0.97	2.1
B7	3.04	552	0.484	35.1	690	118.9	83.8	1.92	1.12	0.99	1.06	2.1
B8	3.04	618	0.459	32.8	773	120.0	87.2	1.99	1.05	0.93	1.10	2.0
B9	3.04	611	0.454	32.8	764	120.2	87.4	2.00	1.04	0.92	1.10	2.0
B10	3.04	218	0.755	33.2	273	100.8	67.6	1.04	2.00	1.86	0.60	2.5
B11	3.04	264	0.725	43.6	330	103.6	60.0	1.15	1.89	1.75	0.66	2.4
B12	3.04	287	0.689	39.9	359	106.6	66.7	1.28	1.76	1.62	0.73	2.3
B13	3.04	310	0.679	40.1	388	107.4	67.3	1.31	1.73	1.58	0.75	2.3
B14	3.04	415	0.601	38.7	519	112.7	74.0	1.57	1.47	1.33	0.88	2.2
B15	3.04	537	0.510	37.8	671	117.7	79.9	1.85	1.19	1.06	1.02	2.1
B16	3.04	580	0.495	30.8	725	118.4	87.6	1.89	1.15	1.02	1.05	2.1
B17	3.04	1046	0.286	33.3	1308	126.5	93.2	2.43	0.61	0.53	1.32	1.8
B18	3.04	461	0.521	26.5	576	117.1	90.6	1.81	1.23	1.09	1.01	2.1
B19	3.04	534	0.485	40.2	668	118.9	78.7	1.92	1.12	1.00	1.06	2.1
B20	3.04	628	0.446	37.4	785	120.6	83.2	2.02	1.02	0.90	1.11	2.0
B21	3.04	663	0.429	33.6	829	121.3	87.7	2.07	0.97	0.85	1.14	2.0
B22	3.04	735	0.415	31.1	919	121.9	90.8	2.11	0.93	0.82	1.16	2.0
B23	3.04	824	0.318	36.0	1030	125.5	89.5	2.36	0.68	0.60	1.28	1.9
B24	3.04	808	0.347	32.0	1010	124.5	92.5	2.28	0.75	0.66	1.24	1.9
B25	3.04	802	0.377	29.8	1003	123.4	93.6	2.21	0.83	0.73	1.21	1.9
B26	3.04	142	0.890	25.3	178	81.3	56.0	0.50	2.54	2.50	0.31	2.8
B27	3.04	155	0.866	25.3	194	86.1	60.8	0.60	2.44	2.36	0.36	2.7
B28	3.04	189	0.846	23.6	236	89.5	65.9	0.69	2.35	2.26	0.41	2.7
B29	3.04	236	0.781	30.0	295	98.0	68.0	0.94	2.10	1.97	0.55	2.5
B30	3.04	306	0.741	25.7	383	102.1	76.4	1.09	1.95	1.81	0.63	2.4
B31	3.04	344	0.678	33.6	430	107.4	73.8	1.32	1.72	1.58	0.75	2.3
B32	3.04	413	0.635	30.7	516	110.5	79.8	1.46	1.58	1.44	0.82	2.3
B33	3.04	446	0.592	33.9	558	113.3	79.4	1.60	1.44	1.30	0.90	2.2
B34	3.04	489	0.557	31.8	611	115.2	83.4	1.71	1.33	1.20	0.95	2.1
B35	3.04	657	0.467	29.5	821	119.7	90.2	1.97	1.07	0.95	1.08	2.0
B36	3.04	644	0.445	35.8	805	120.7	84.9	2.03	1.01	0.89	1.12	2.0
B37	3.04	780	0.388	32.4	975	123.0	90.6	2.18	0.86	0.76	1.19	1.9

Table C-2 Summary of Dehbi (1991) Experimental Results for 3.5 m Height Continued

Test ID	P _b	0.8·h _{tot}	W _{nc}	T _b -T _w	h _{tot}	T _b	T _w	P _{v,b}	P _{nc,b}	ρ _{nc,b}	ρ _{v,b}	ρ _b
	bar	W/m ² -C		°C	W/m ² -°C	°C	°C	bar	bar	kg/m ³	kg/m ³	kg/m ³
B38	3.04	802	0.357	35.4	1003	124.1	88.7	2.26	0.78	0.68	1.23	1.9
B39	3.04	854	0.342	34.5	1068	124.6	90.1	2.30	0.74	0.65	1.25	1.9
B40	3.04	1037	0.278	31.0	1296	126.8	95.8	2.45	0.59	0.51	1.33	1.8
C1	4.56	316	0.724	44.0	395	115.7	71.7	1.73	2.83	2.53	0.97	3.5
C2	4.56	435	0.631	43.0	544	123.4	80.4	2.21	2.35	2.07	1.21	3.3
C3	4.56	516	0.593	40.0	645	126.0	86.0	2.39	2.17	1.89	1.30	3.2
C4	4.56	547	0.557	42.0	684	128.2	86.2	2.56	2.00	1.74	1.38	3.1
C5	4.56	244	0.783	43.0	305	109.4	66.4	1.41	3.15	2.87	0.80	3.7
C6	4.56	335	0.725	34.0	419	115.7	81.7	1.73	2.83	2.54	0.96	3.5
C7	4.56	148	0.889	35.0	185	92.2	57.2	0.76	3.80	3.62	0.45	4.1
C8	4.56	254	0.800	37.0	318	107.3	70.3	1.31	3.25	2.98	0.74	3.7
C9	4.56	144	0.877	35.0	180	94.7	59.7	0.84	3.72	3.52	0.49	4.0
C10	4.56	342	0.730	34.0	428	115.2	81.2	1.70	2.86	2.56	0.95	3.5
C11	4.56	357	0.712	34.0	446	116.8	82.8	1.80	2.76	2.47	1.00	3.5
C12	4.56	373	0.692	36.0	466	118.6	82.6	1.90	2.66	2.36	1.05	3.4
C13	4.56	416	0.669	33.0	520	120.5	87.5	2.02	2.54	2.25	1.11	3.4
C14	4.56	409	0.645	40.0	511	122.4	82.4	2.14	2.42	2.13	1.17	3.3
C15	4.56	456	0.614	38.0	570	124.6	86.6	2.29	2.27	1.99	1.25	3.2
C16	4.56	491	0.577	40.0	614	126.9	86.9	2.46	2.09	1.82	1.33	3.2
C17	4.56	539	0.559	38.0	674	128.1	90.1	2.55	2.01	1.74	1.38	3.1
C18	4.56	521	0.532	45.0	651	129.6	84.6	2.67	1.89	1.64	1.44	3.1
C19	4.56	595	0.498	43.0	744	131.4	88.4	2.82	1.74	1.50	1.51	3.0
C20	4.56	633	0.476	41.0	791	132.5	91.5	2.91	1.65	1.42	1.56	3.0
C21	4.56	677	0.456	40.0	846	133.5	93.5	3.00	1.56	1.34	1.60	2.9
C22	4.56	657	0.438	47.0	821	134.3	87.3	3.07	1.49	1.27	1.63	2.9
C23	4.56	817	0.395	38.0	1021	136.2	98.2	3.24	1.32	1.12	1.72	2.8
C24	4.56	859	0.383	40.0	1074	136.7	96.7	3.29	1.27	1.08	1.74	2.8
C25	4.56	888	0.353	39.0	1110	137.9	98.9	3.40	1.15	0.98	1.79	2.8
C26	4.56	923	0.333	38.0	1154	138.7	100.7	3.48	1.08	0.91	1.83	2.7
C27	4.56	972	0.324	35.0	1215	139.0	104.0	3.51	1.05	0.89	1.85	2.7

C.2 Kataoka et al. (1994) Database

Kataoka et al. (1994) reports results of condensation on a 0.5 m wide, 4.5 m height vertical wall. Localized heat transfer coefficient results at three elevations are given as a function of wetwell temperature. Plots that relate the wetwell temperature, T_w , and outer pool temperature, T_{op} , are used to determine the inner wetwell wall temperature, T_w , by solving the outer pool natural convection heat transfer problem using the McAdams correlation. The approach is justified since Kataoka et al. demonstrates that the McAdams correlation fits the experimental results within a standard deviation of 11%.

Figure C-1 shows the Kataoka et al. (1994) heat transfer coefficient results at the 0.5 m, 2.0 m and 4 m measurement locations. Table C-3 provides the localized and averaged heat transfer coefficient at each wetwell temperature. Figure C-2 shows the wetwell and outer pool temperatures as a function of time. Note that Figure C-1 and Figure C-2 are a reproduction of plots from Kataoka et al. (1994).

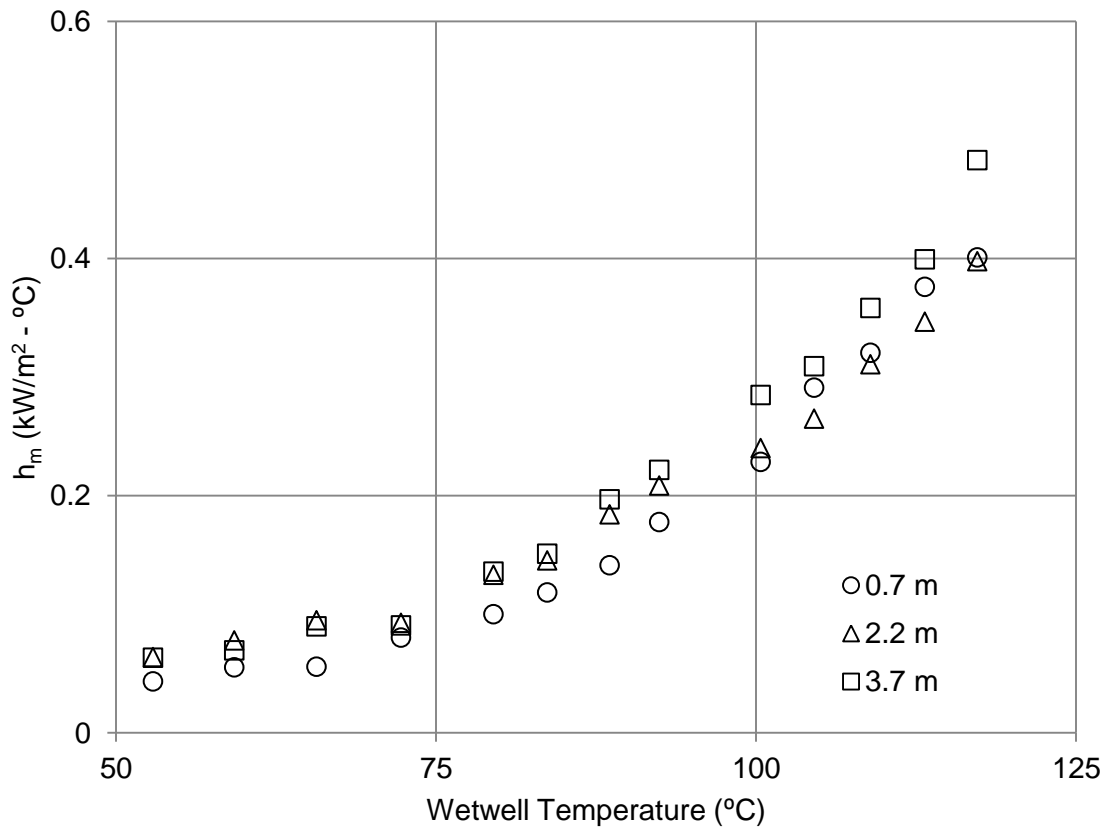


Figure C-1 Kataoka et al. (1994) Measured Condensation Heat Transfer Coefficients

T_b	$h_m (L = 0.7 \text{ m})$	$h_m (L = 2.2 \text{ m})$	$h_m (L = 3.7 \text{ m})$	$h_{m,ave}$
$^{\circ}\text{C}$	$\text{W}/\text{m}^2\text{-K}$	$\text{W}/\text{m}^2\text{-K}$	$\text{W}/\text{m}^2\text{-K}$	$\text{W}/\text{m}^2\text{-K}$
52.9	43	64	63	57
59.2	55	78	69	68
65.7	56	95	90	80
72.2	80	93	91	88
79.5	100	133	136	123
83.7	118	145	151	138
88.6	141	184	197	174
92.4	178	208	222	203
100.4	229	240	285	251
104.5	291	265	309	288
108.9	321	311	358	330
113.2	376	347	399	374
117.3	401	398	483	427

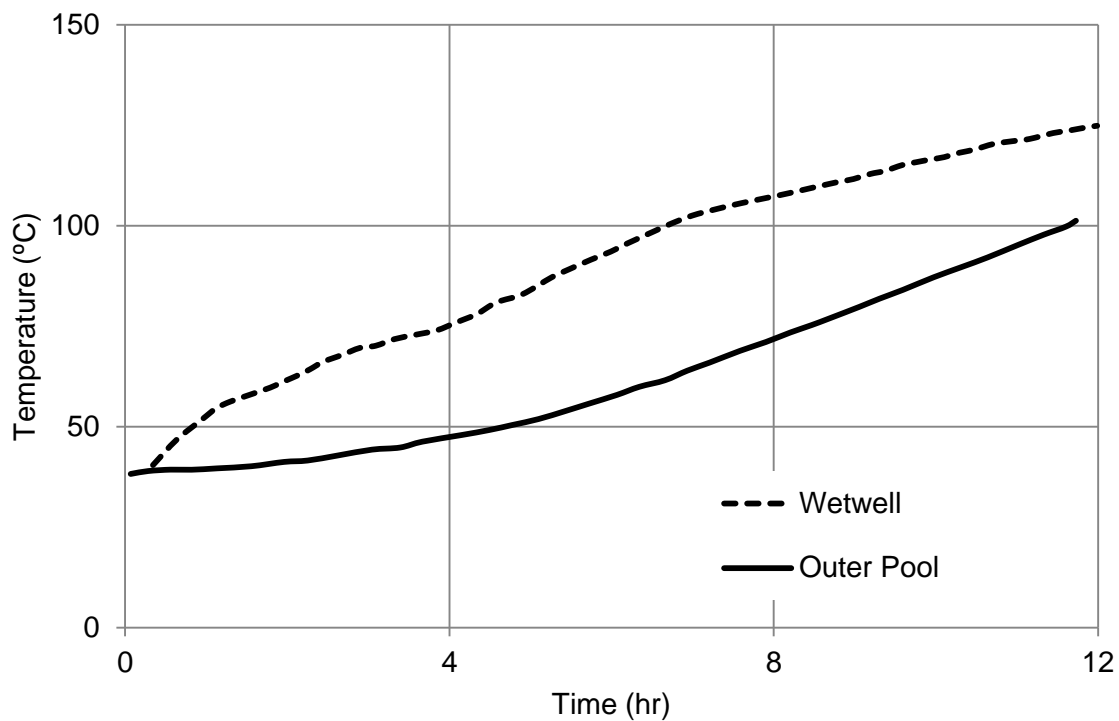


Figure C-2 Kataoka et al. (1994) Measured Wetwell and Outer Pool Temperatures

From Section 2 of Kataoka et al. (1994), the thickness of the stainless steel wall between the wetwell and outer pool, t_{ss} , is 12 mm. The thermal conductivity of stainless steel, k_{ss} , is assumed to be 16 W/m-K, and the wall heat transfer coefficient is defined as:

$$h_{ss} = \frac{k_{ss}}{t_{ss}} \quad \text{Equation C-1}$$

For the assumed thermal conductivity and given stainless steel thickness, the stainless steel heat transfer coefficient is 1333 W/m²-K. Comparing this value to the outer pool natural convection heat transfer coefficient calculated below, and the measured condensation heat transfer coefficients shown in Figure C-1, it is evident that the transfer rates are not highly dependent on the assumed stainless steel thermal conductivity.

The heat transfer coefficient between the outer pool and outer wall, h_{op} , using the McAdams natural convection correlation is:

$$\frac{h_{op}L}{k_f} = 0.13(Gr_L \cdot Pr)^{1/3} \quad \text{Equation C-2}$$

Since natural convection in the outer pool occurs in water, the standard form of the Grashoff number can be used:

$$Gr_L = \frac{g\rho_{op}^2\beta(T_{ow} - T_{op})L^3}{\mu_f^2} \quad \text{Equation C-3}$$

, where β is the volumetric coefficient of thermal expansion, ρ_{op} is the bulk density of the outer pool water and T_{ow} is the outer wall temperature. Therefore the heat transfer coefficient between the outer pool and wall is:

$$h_{op} = 0.13 \left(\frac{k_f^2 C_{p,f} g \rho_{op}^2 \beta (T_{ow} - T_{op})}{\mu_f} \right)^{1/3} \quad \text{Equation C-4}$$

The total heat transfer coefficient is calculated by combining the measured condensation heat transfer coefficient in the wetwell, h_m , with the stainless steel wall and outer pool heat transfer coefficients

assuming series heat transfer:

$$\frac{1}{h_t} = \frac{1}{h_{op}} + \frac{1}{h_{ss}} + \frac{1}{h_m} \quad \text{Equation C-5}$$

Given the measured outer pool and inner pool temperature and total heat transfer coefficient, the heat flux is calculated as follows:

$$q'' = h_t(T_w - T_{op}) \quad \text{Equation C-6}$$

The heat flux considering the outer pool heat transfer coefficient and temperature differential is:

$$q'' = h_{op}(T_{ow} - T_{op}) = 0.13 \left(\frac{k_f^2 C_{p,f} g \rho_{op}^2 \beta (T_{ow} - T_{op})}{\mu_l} \right)^{1/3} (T_{ow} - T_{op}) \quad \text{Equation C-7}$$

Equation C-6 and Equation C-7 above are solved by iterating the outer wall temperature, T_{ow} , until the heat fluxes are equal.

Finally, the inner stainless steel surface temperature is calculated as follows:

$$T_w = T_b - \frac{q''}{h_m} \quad \text{Equation C-8}$$

A summary of the analysis inputs results necessary to calculate the interface temperature for each test condition is provided in Table C-4.

Kataoka et al. (1994) conducted tests by initially closing the system with 1 bar of air at standard conditions. Experiments were also conducted with an initial air pressure of 1.5 bar, unfortunately the interface temperature cannot be determined from the data provided. The gas mixture properties are determined using the ideal gas law for wetwell air partial pressure, assuming dry air initially at 1 bar and 20°C, and using the IAPWS script, as described in Appendix D, to determine the steam partial pressure.

Table C-5 summarizes the Kataoka et al. (1994) test conditions.

Time	T_b	T_{op}	T_w	T_{ow}	$h_{m\ ave}$	β	k_f	C_p	ρ_{op}	μ_f	h_{op}	h_{tot}	q''
hr	°C	°C	°C	°C	W/m ² -K	1/°C	W/m-K	kJ/kg-K	kg/m ³	μPa-s	W/m ² -K	W/m ² -K	W/m ²
1.02	52.9	39.3	41.7	41.2	56.9	3.80E-04	0.630	4.18	992	662	337	47	637
1.72	59.2	40.2	43.7	42.9	67.6	3.87E-04	0.631	4.18	992	651	385	55	1049
2.40	65.7	41.7	46.4	45.2	80.1	3.98E-04	0.633	4.18	992	633	431	64	1543
3.43	72.2	45.0	50.5	49.0	87.9	4.22E-04	0.637	4.18	990	597	470	70	1915
4.46	79.5	49.4	56.7	54.6	123.1	4.54E-04	0.643	4.18	988	552	538	93	2803
4.96	83.7	51.9	60.1	57.7	138.3	4.71E-04	0.646	4.18	987	529	571	103	3260
5.41	88.6	54.4	64.4	61.2	174.2	4.87E-04	0.649	4.18	986	509	621	123	4214
5.85	92.4	57.0	68.1	64.5	202.7	5.04E-04	0.651	4.18	985	488	659	139	4918
6.72	100.4	62.5	75.7	71.0	251.3	5.39E-04	0.657	4.19	982	449	727	164	6201
7.37	104.5	67.0	81.0	75.9	288.5	5.66E-04	0.661	4.19	979	421	766	181	6799
8.37	108.9	74.3	88.0	82.8	330.0	6.09E-04	0.666	4.19	975	381	805	199	6905
9.26	113.2	81.2	94.6	89.4	374.0	6.48E-04	0.671	4.20	971	349	838	217	6936
10.14	117.3	88.2	101.2	96.1	427.3	6.87E-04	0.674	4.20	967	321	867	236	6853

P_b	T_b	T_w	P_{vb}	P_{ncb}	ρ_{ncb}	ρ_{vb}	ρ_b	W_{nc}
bar	°C	°C	bar	bar	kg/m ³	kg/m ³	kg/m ³	
1.25	52.9	41.7	0.14	1.11	1.19	0.09	1.28	0.93
1.33	59.2	43.7	0.19	1.13	1.19	0.13	1.31	0.90
1.41	65.7	46.4	0.26	1.16	1.19	0.16	1.35	0.88
1.52	72.2	50.5	0.34	1.18	1.19	0.22	1.40	0.85
1.67	79.5	56.7	0.46	1.20	1.19	0.29	1.47	0.81
1.77	83.7	60.1	0.55	1.22	1.19	0.33	1.52	0.78
1.90	88.6	64.4	0.66	1.23	1.19	0.40	1.59	0.75
2.02	92.4	68.1	0.77	1.25	1.19	0.46	1.64	0.72
2.30	100.4	75.7	1.03	1.27	1.19	0.60	1.79	0.67
2.48	104.5	81.0	1.19	1.29	1.19	0.68	1.87	0.64
2.69	108.9	88.0	1.38	1.30	1.19	0.78	1.97	0.60
2.91	113.2	94.6	1.59	1.32	1.19	0.89	2.08	0.57
3.15	117.3	101.2	1.82	1.33	1.19	1.01	2.20	0.54

C.3 Uchida et al. (1965) Database

Uchida et al. (1965) reports results for condensation on a 0.14 m wide by 0.3 m length condensing plate. Results are given for condensation in air, nitrogen and argon, although the argon results are not analyzed as part of this assessment. Measured heat transfer coefficients are given as a function of non-condensable gas to vapor weight ratio. Figure C-3 provides a reproduction of the results plot from Uchida et al. (1965).

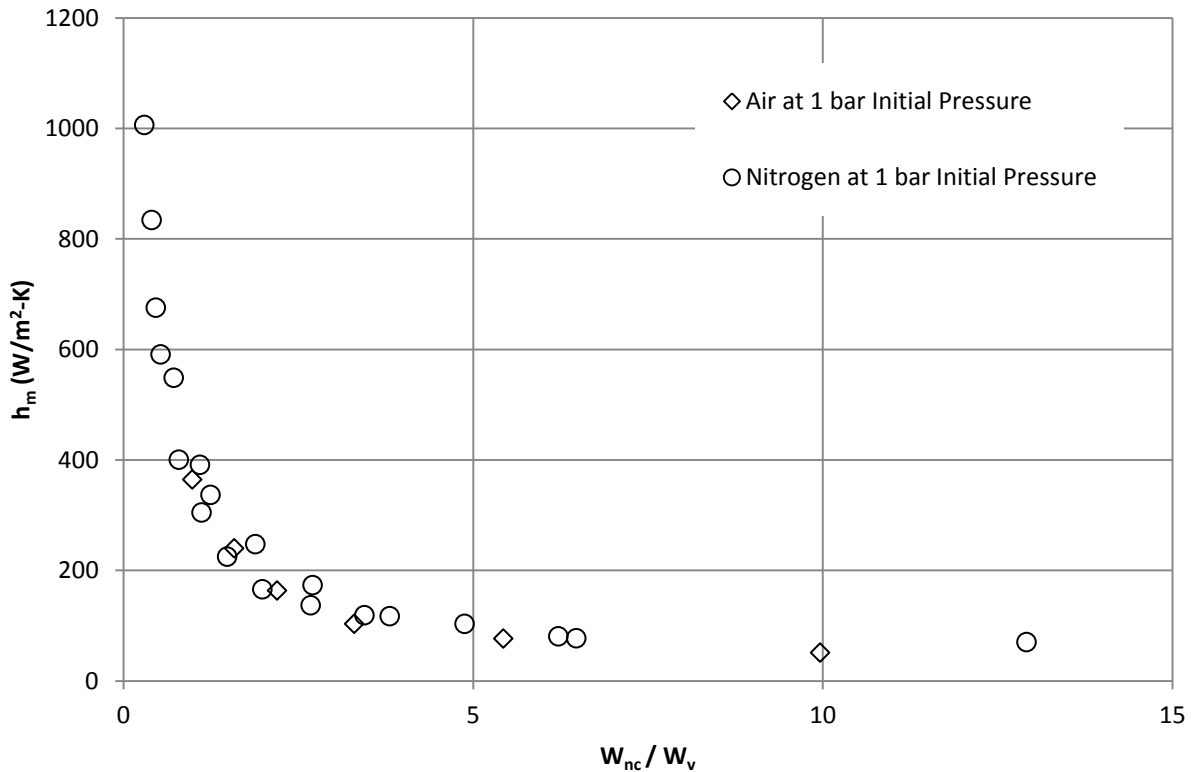


Figure C-3 Uchida et al. (1965) Measured Heat Transfer Coefficients

The Uchida et al. (1965) experiments were conducted with a constant wall temperature of 322 K. Bulk gas mixture properties are determined using the ideal gas law for air partial pressure, assuming dry air or nitrogen initially at 1 bar and 20°C, and using the IAPWS script, as described in Appendix D, to determine the steam partial pressure. Table C-6 summarizes the Uchida et al. (1965) test results for air and Table C-7 summarizes the results for nitrogen.

Table C-6 Uchida et al. (1965) Air Data								
P_b	T_b	T_w	P_{vb}	P_{ncb}	ρ_{ncb}	ρ_{vb}	ρ_b	W_{nc}
bar	C	C	bar	bar	kg/m³	kg/m³	kg/m³	
1.31	58.0	48.9	0.18	1.13	1.19	0.12	1.31	0.909
1.53	72.4	48.9	0.35	1.18	1.19	0.22	1.41	0.845
1.81	85.5	48.9	0.59	1.22	1.19	0.36	1.55	0.768
2.17	97.0	48.9	0.91	1.26	1.19	0.54	1.73	0.688
2.59	106.9	48.9	1.29	1.30	1.19	0.75	1.94	0.613
3.50	122.4	48.9	2.15	1.35	1.19	1.21	2.40	0.497

Table C-7 Uchida et al. (1965) Nitrogen Data								
P_b	T_b	T_w	P_{vb}	P_{ncb}	ρ_{ncb}	ρ_{vb}	ρ_b	W_{nc}
bar	C	C	bar	bar	kg/m³	kg/m³	kg/m³	
1.24	51.5	48.9	0.13	1.11	1.15	0.09	1.24	0.928
1.44	67.3	48.9	0.28	1.16	1.15	0.18	1.33	0.866
1.45	68.3	48.9	0.29	1.17	1.15	0.18	1.33	0.862
1.56	74.3	48.9	0.37	1.19	1.15	0.24	1.39	0.830
1.70	80.7	48.9	0.49	1.21	1.15	0.30	1.45	0.792
1.76	83.4	48.9	0.54	1.22	1.15	0.33	1.48	0.775
1.94	90.1	48.9	0.70	1.24	1.15	0.42	1.57	0.730
1.95	90.3	48.9	0.71	1.24	1.15	0.43	1.58	0.728
2.25	99.0	48.9	0.98	1.27	1.15	0.58	1.73	0.665
2.31	100.5	48.9	1.03	1.28	1.15	0.61	1.76	0.654
2.64	107.9	48.9	1.34	1.30	1.15	0.77	1.92	0.597
2.93	113.5	48.9	1.61	1.32	1.15	0.92	2.07	0.555
3.15	117.1	48.9	1.81	1.33	1.15	1.03	2.18	0.527
3.19	117.8	48.9	1.85	1.33	1.15	1.05	2.20	0.522
3.99	128.9	48.9	2.62	1.37	1.15	1.45	2.60	0.442
4.29	132.4	48.9	2.90	1.38	1.15	1.60	2.75	0.418
5.41	143.5	48.9	3.99	1.42	1.15	2.16	3.31	0.348
6.04	148.7	48.9	4.60	1.44	1.15	2.47	3.62	0.318
6.78	154.2	48.9	5.32	1.46	1.15	2.83	3.98	0.289
8.83	166.8	48.9	7.33	1.50	1.15	3.83	4.98	0.231

C.4 Tagami (1965) Database

Tagami (1965) reports results for condensation on 0.3 m and 0.9 m height, 15 cm diameter vertical cylinders. For access to the experimental data and a description of the facility the Tagami (1965) results are also provided by Corradini (1984). The Tagami (1965) results are obtained by extracting data from a plot of heat transfer coefficient versus vapor to non-condensable gas weight ratio. Figure C-4 provides a reproduction of the results plot from Tagami (1965).

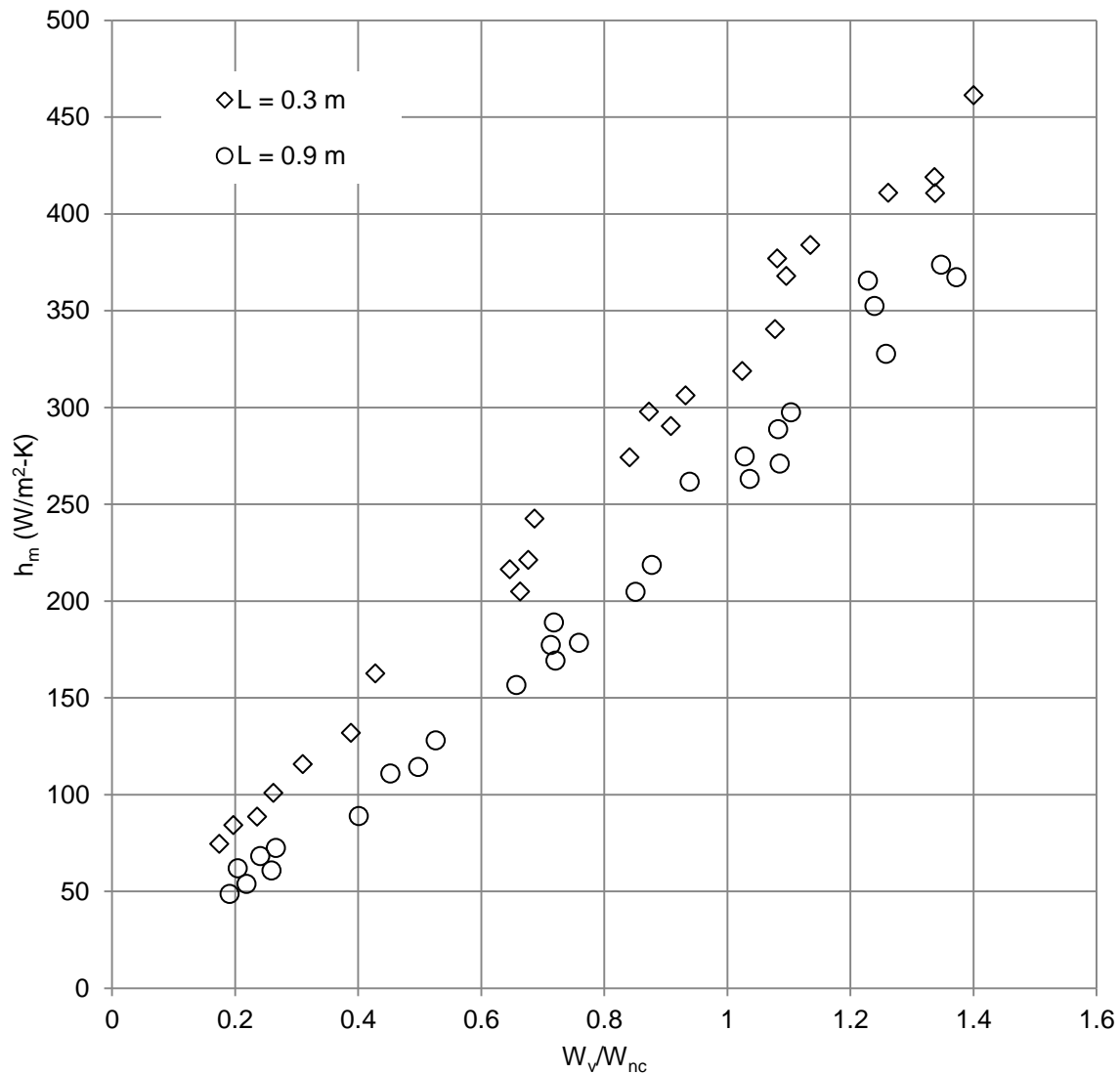


Figure C-4 Tagami (1965) Measured Heat Transfer Coefficients

The Tagami (1965) experiments were conducted with a constant wall temperature of 322 K. Bulk gas mixture properties are determined using the ideal gas law for air partial pressure, assuming dry air initially at 1 bar and 20°C, and using the IAPWS script, as described in Appendix D, to determine the steam partial pressure. Table C-8 summarizes the Tagami (1965) test results for the 0.3 m height cylinder and Table C-9 summarizes the results for the 0.9 m height cylinder.

Table C-8 Tagami (1965) 0.3 m Height Cylinder Data								
P_b	T_b	T_w	P_{vb}	P_{ncb}	ρ_{ncb}	ρ_{vb}	ρ_b	W_{nc}
bar	C	C	bar	bar	kg/m ³	kg/m ³	kg/m ³	
1.50	71.1	48.9	0.33	1.18	1.19	0.21	1.40	0.851
1.56	74.2	48.9	0.37	1.19	1.19	0.23	1.42	0.835
1.65	78.8	48.9	0.45	1.20	1.19	0.28	1.47	0.809
1.72	81.6	48.9	0.51	1.21	1.19	0.31	1.50	0.792
1.83	86.2	48.9	0.61	1.23	1.19	0.37	1.56	0.763
2.02	92.5	48.9	0.77	1.25	1.19	0.46	1.65	0.720
2.11	95.2	48.9	0.85	1.26	1.19	0.51	1.70	0.700
2.67	108.5	48.9	1.36	1.30	1.19	0.79	1.98	0.601
2.63	107.7	48.9	1.33	1.30	1.19	0.77	1.96	0.607
2.70	109.1	48.9	1.39	1.30	1.19	0.80	1.99	0.596
2.72	109.6	48.9	1.42	1.31	1.19	0.82	2.01	0.593
3.09	116.2	48.9	1.76	1.33	1.19	1.00	2.19	0.543
3.25	118.7	48.9	1.91	1.34	1.19	1.08	2.27	0.524
3.16	117.4	48.9	1.83	1.33	1.19	1.04	2.23	0.534
3.30	119.6	48.9	1.96	1.34	1.19	1.11	2.30	0.518
3.52	122.8	48.9	2.17	1.35	1.19	1.22	2.41	0.494
3.65	124.5	48.9	2.29	1.36	1.19	1.28	2.47	0.481
3.69	125.1	48.9	2.33	1.36	1.19	1.30	2.49	0.477
3.66	124.7	48.9	2.30	1.36	1.19	1.29	2.48	0.481
3.78	126.3	48.9	2.42	1.36	1.19	1.35	2.54	0.469
4.09	130.1	48.9	2.71	1.38	1.19	1.50	2.69	0.442
4.27	132.2	48.9	2.89	1.38	1.19	1.59	2.78	0.428
4.27	132.2	48.9	2.88	1.38	1.19	1.59	2.78	0.428
4.42	133.9	48.9	3.03	1.39	1.19	1.67	2.86	0.417

Table C-9 Tagami (1965) 0.9 m Height Cylinder Data

P_b	T_b	T_w	P_{vb}	P_{ncb}	ρ_{ncb}	ρ_{vb}	ρ_b	W_{nc}
bar	C	C	bar	bar	kg/m³	kg/m³	kg/m³	
4.42	133.9	48.9	3.03	1.39	1.19	1.67	2.86	0.417
4.51	134.9	48.9	3.12	1.39	1.19	1.71	2.90	0.410
4.61	135.9	48.9	3.21	1.40	1.19	1.76	2.95	0.403
4.70	136.9	48.9	3.31	1.40	1.19	1.81	3.00	0.397
4.80	137.9	48.9	3.40	1.40	1.19	1.86	3.05	0.390
4.91	138.9	48.9	3.50	1.41	1.19	1.91	3.10	0.384
5.01	139.9	48.9	3.60	1.41	1.19	1.96	3.15	0.378
5.12	140.9	48.9	3.70	1.41	1.19	2.01	3.20	0.372
5.23	141.9	48.9	3.81	1.42	1.19	2.07	3.26	0.365
5.34	142.9	48.9	3.92	1.42	1.19	2.12	3.31	0.359
5.45	143.9	48.9	4.03	1.42	1.19	2.18	3.37	0.353
5.57	144.9	48.9	4.14	1.43	1.19	2.23	3.42	0.347
5.69	145.9	48.9	4.26	1.43	1.19	2.29	3.48	0.342
5.81	146.9	48.9	4.37	1.43	1.19	2.35	3.54	0.336
5.93	147.9	48.9	4.49	1.44	1.19	2.41	3.60	0.330
6.06	148.9	48.9	4.62	1.44	1.19	2.48	3.66	0.325
6.19	149.9	48.9	4.74	1.44	1.19	2.54	3.73	0.319
6.32	150.9	48.9	4.87	1.45	1.19	2.60	3.79	0.314
6.45	151.9	48.9	5.00	1.45	1.19	2.67	3.86	0.308
6.59	152.9	48.9	5.14	1.45	1.19	2.74	3.93	0.303
6.73	153.9	48.9	5.27	1.46	1.19	2.81	4.00	0.298
6.88	154.9	48.9	5.41	1.46	1.19	2.88	4.07	0.293
7.02	155.9	48.9	5.56	1.46	1.19	2.95	4.14	0.288
7.17	156.9	48.9	5.70	1.47	1.19	3.02	4.21	0.283
7.32	157.9	48.9	5.85	1.47	1.19	3.10	4.28	0.278
7.48	158.9	48.9	6.00	1.47	1.19	3.17	4.36	0.273
7.64	159.9	48.9	6.16	1.48	1.19	3.25	4.44	0.268
7.80	160.9	48.9	6.32	1.48	1.19	3.33	4.52	0.263

C.5 Su et al. (2013 and 2014) Database

Su et al. (2013 and 2014) reports the experimental results of condensation on a 2.0 m height, 0.038 m diameter vertical cylinder. The bulk non-condensable gas mass fraction, bulk pressure, bulk to wall temperature difference and measured heat transfer coefficients are reported for each experiment in graphical form. Figure C-5 and Figure C-6 are reproductions of figures from Su et al. (2013). Figure C-7 is a reproduction from Su et al. (2014). The plot used to extract data shown in Figure C-5 was originally produced with logarithmic axes, and a number of the data points were tightly grouped. Therefore, it is possible that some data points were missed or erroneous data points selected. In the instance an erroneous data point was selected, it would be very close to an actual experimental condition, and well within the reported experimental error. The data extracted from each image and gas properties, calculated as described in Appendix D, are provided in Table C-10, Table C-11 and Table C-12.

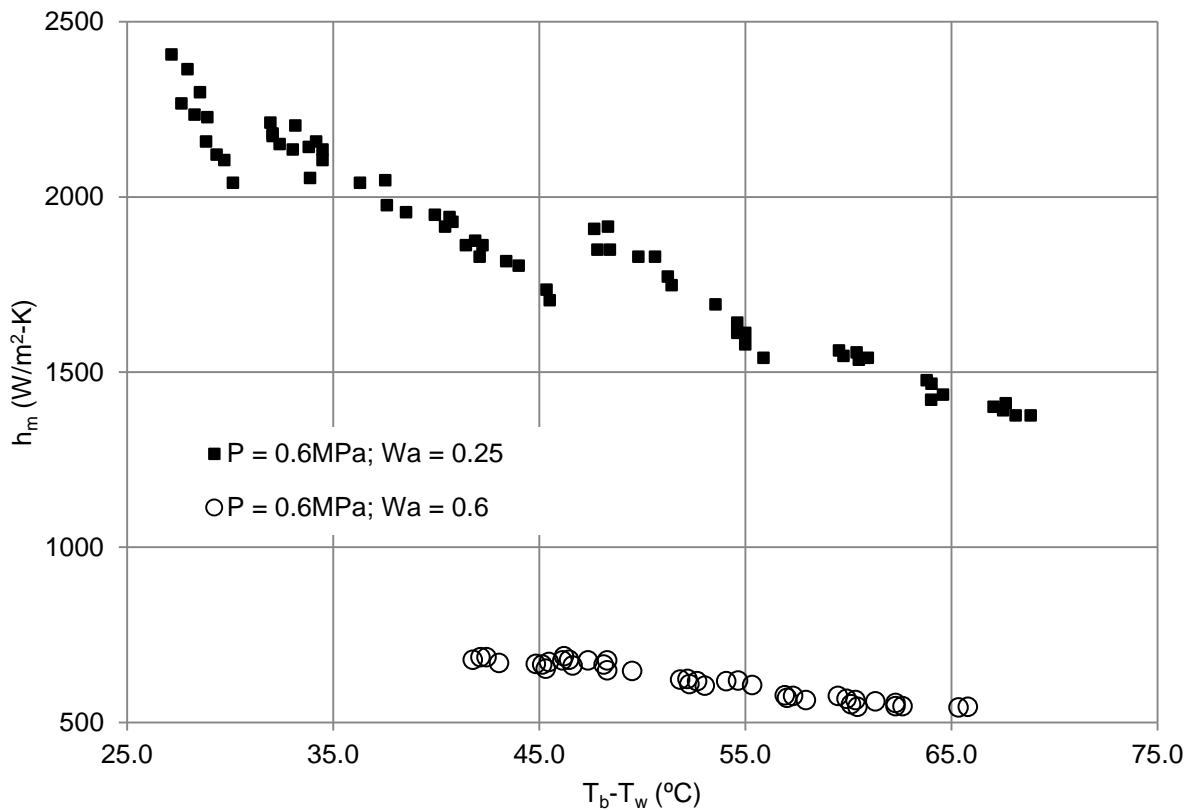


Figure C-5 Su et al. (2013) Measured Heat Transfer Coefficients at 6 bar

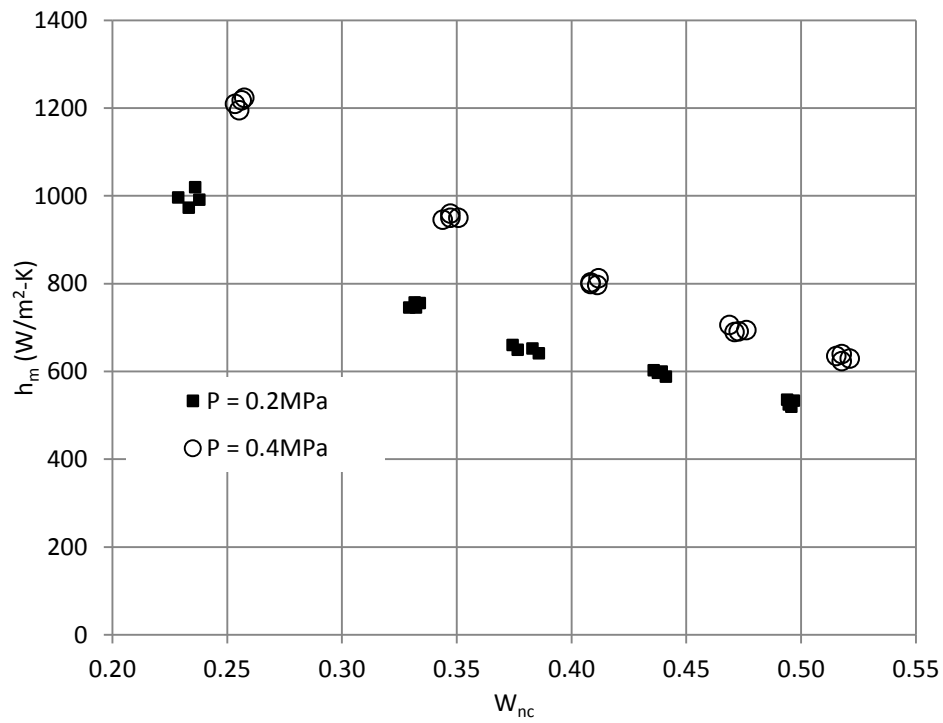
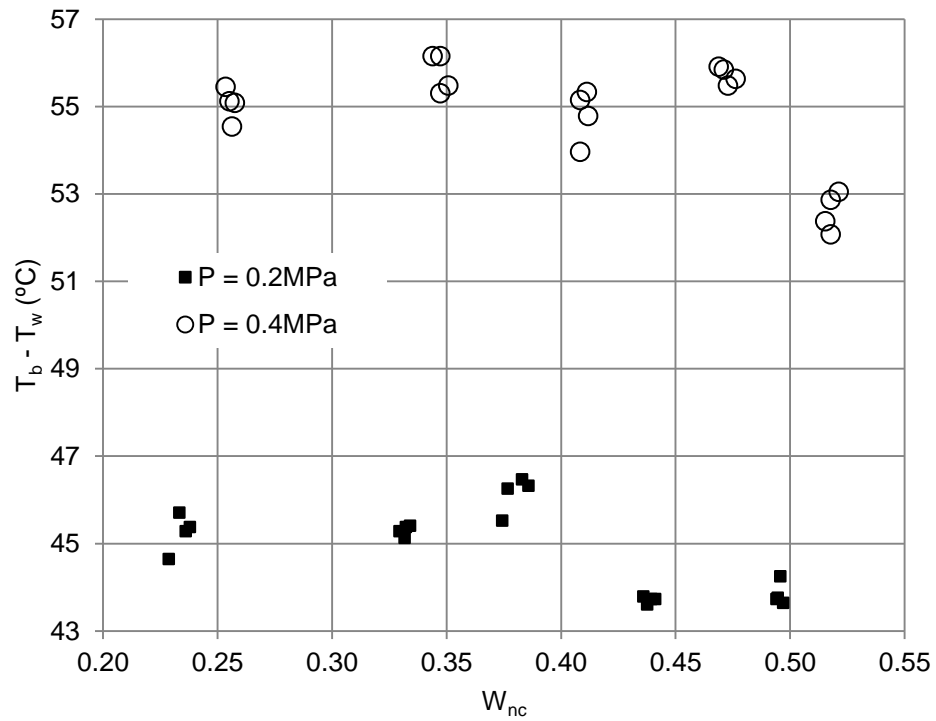


Figure C-6 Su et al. (2013) Measured Heat Transfer Coefficients at 2 and 4 bar

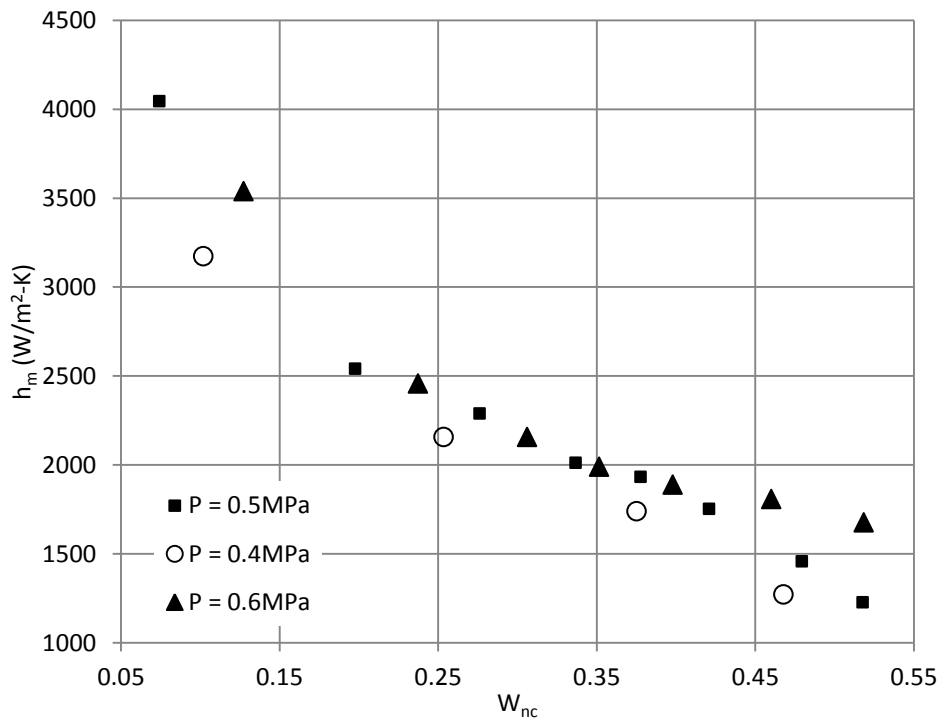
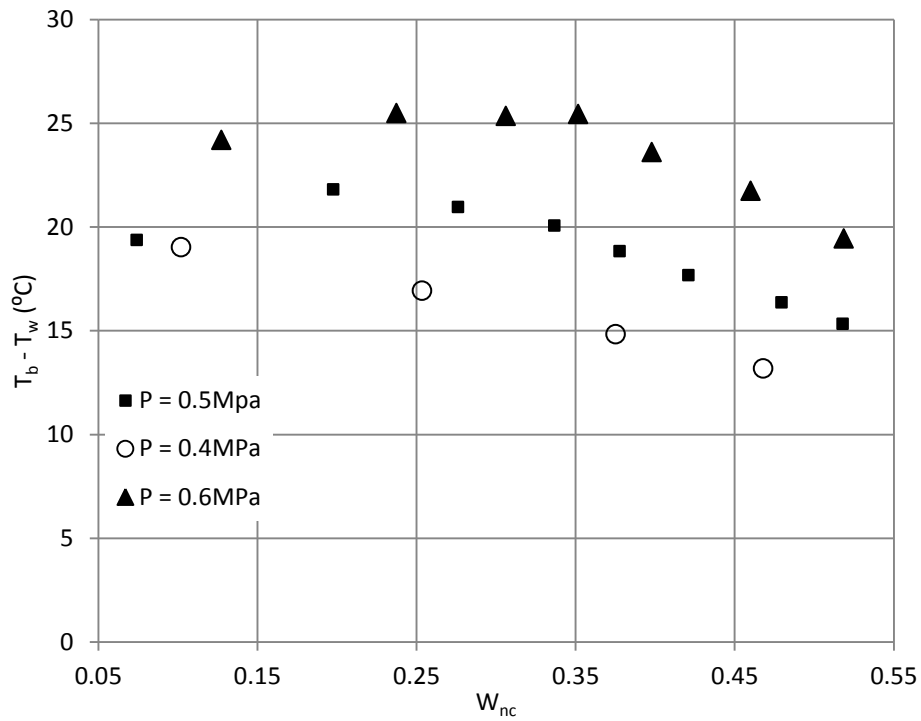


Figure C-7 Su et al. (2014) Measured Heat Transfer Coefficients

Table C-10 Su et al. (2013) Experimental Results at 6 bar									
h_m	T_b	T_w	P_b	P_{vb}	P_{ncb}	ρ_{ncb}	ρ_{vb}	ρ_b	W_{nc}
W/m^2-C	$^{\circ}C$	$^{\circ}C$	bar	bar	bar	kg/m^3	kg/m^3	kg/m^3	
2405	151.6	124.4	6	4.97	1.03	0.84	2.54	3.38	0.25
2363	151.6	123.7	6	4.97	1.03	0.84	2.54	3.38	0.25
2266	151.6	123.9	6	4.97	1.03	0.84	2.54	3.38	0.25
2234	151.6	123.3	6	4.97	1.03	0.84	2.54	3.38	0.25
2298	151.6	123.1	6	4.97	1.03	0.84	2.54	3.38	0.25
2157	151.6	122.8	6	4.97	1.03	0.84	2.54	3.38	0.25
2226	151.6	122.7	6	4.97	1.03	0.84	2.54	3.38	0.25
2119	151.6	122.2	6	4.97	1.03	0.84	2.54	3.38	0.25
2105	151.6	121.9	6	4.97	1.03	0.84	2.54	3.38	0.25
2039	151.6	121.4	6	4.97	1.03	0.84	2.54	3.38	0.25
2211	151.6	119.6	6	4.97	1.03	0.84	2.54	3.38	0.25
2180	151.6	119.5	6	4.97	1.03	0.84	2.54	3.38	0.25
2172	151.6	119.5	6	4.97	1.03	0.84	2.54	3.38	0.25
2149	151.6	119.2	6	4.97	1.03	0.84	2.54	3.38	0.25
2134	151.6	118.5	6	4.97	1.03	0.84	2.54	3.38	0.25
2203	151.6	118.4	6	4.97	1.03	0.84	2.54	3.38	0.25
2142	151.6	117.8	6	4.97	1.03	0.84	2.54	3.38	0.25
2157	151.6	117.4	6	4.97	1.03	0.84	2.54	3.38	0.25
2134	151.6	117.1	6	4.97	1.03	0.84	2.54	3.38	0.25
2105	151.6	117.1	6	4.97	1.03	0.84	2.54	3.38	0.25
2053	151.6	117.7	6	4.97	1.03	0.84	2.54	3.38	0.25
2039	151.6	115.3	6	4.97	1.03	0.84	2.54	3.38	0.25
2046	151.6	114.1	6	4.97	1.03	0.84	2.54	3.38	0.25
1976	151.6	114.0	6	4.97	1.03	0.84	2.54	3.38	0.25
1955	151.6	113.0	6	4.97	1.03	0.84	2.54	3.38	0.25
1948	151.6	111.7	6	4.97	1.03	0.84	2.54	3.38	0.25
1914	151.6	111.2	6	4.97	1.03	0.84	2.54	3.38	0.25
1941	151.6	110.9	6	4.97	1.03	0.84	2.54	3.38	0.25
1928	151.6	110.8	6	4.97	1.03	0.84	2.54	3.38	0.25
1861	151.6	110.1	6	4.97	1.03	0.84	2.54	3.38	0.25
1874	151.6	109.7	6	4.97	1.03	0.84	2.54	3.38	0.25
1861	151.6	109.3	6	4.97	1.03	0.84	2.54	3.38	0.25
1829	151.6	109.5	6	4.97	1.03	0.84	2.54	3.38	0.25
1816	151.6	108.2	6	4.97	1.03	0.84	2.54	3.38	0.25
1803	151.6	107.6	6	4.97	1.03	0.84	2.54	3.38	0.25
1735	151.6	106.2	6	4.97	1.03	0.84	2.54	3.38	0.25
1704	151.6	106.1	6	4.97	1.03	0.84	2.54	3.38	0.25
1907	151.6	103.9	6	4.97	1.03	0.84	2.54	3.38	0.25
1914	151.6	103.2	6	4.97	1.03	0.84	2.54	3.38	0.25

Table C-10 Su et al. (2013) Experimental Results at 6 bar Continued									
h_m	T_b	T_w	P_b	P_{vb}	P_{ncb}	ρ_{ncb}	ρ_{vb}	ρ_b	W_{nc}
W/m^2-C	$^{\circ}C$	$^{\circ}C$	bar	bar	bar	kg/m^3	kg/m^3	kg/m^3	
1848	151.6	103.2	6	4.97	1.03	0.84	2.54	3.38	0.25
1848	151.6	103.8	6	4.97	1.03	0.84	2.54	3.38	0.25
1829	151.6	101.8	6	4.97	1.03	0.84	2.54	3.38	0.25
1829	151.6	101.0	6	4.97	1.03	0.84	2.54	3.38	0.25
1772	151.6	100.3	6	4.97	1.03	0.84	2.54	3.38	0.25
1747	151.6	100.2	6	4.97	1.03	0.84	2.54	3.38	0.25
1693	151.6	98.0	6	4.97	1.03	0.84	2.54	3.38	0.25
1640	151.6	97.0	6	4.97	1.03	0.84	2.54	3.38	0.25
1611	151.6	97.0	6	4.97	1.03	0.84	2.54	3.38	0.25
1611	151.6	96.6	6	4.97	1.03	0.84	2.54	3.38	0.25
1578	151.6	96.6	6	4.97	1.03	0.84	2.54	3.38	0.25
1539	151.6	95.7	6	4.97	1.03	0.84	2.54	3.38	0.25
1561	151.6	92.0	6	4.97	1.03	0.84	2.54	3.38	0.25
1556	151.6	91.2	6	4.97	1.03	0.84	2.54	3.38	0.25
1539	151.6	90.7	6	4.97	1.03	0.84	2.54	3.38	0.25
1545	151.6	91.8	6	4.97	1.03	0.84	2.54	3.38	0.25
1534	151.6	91.1	6	4.97	1.03	0.84	2.54	3.38	0.25
1476	151.6	87.8	6	4.97	1.03	0.84	2.54	3.38	0.25
1420	151.6	87.6	6	4.97	1.03	0.84	2.54	3.38	0.25
1435	151.6	87.0	6	4.97	1.03	0.84	2.54	3.38	0.25
1465	151.6	87.6	6	4.97	1.03	0.84	2.54	3.38	0.25
1400	151.6	84.5	6	4.97	1.03	0.84	2.54	3.38	0.25
1390	151.6	84.1	6	4.97	1.03	0.84	2.54	3.38	0.25
1410	151.6	84.0	6	4.97	1.03	0.84	2.54	3.38	0.25
1376	151.6	83.5	6	4.97	1.03	0.84	2.54	3.38	0.25
1376	151.6	82.7	6	4.97	1.03	0.84	2.54	3.38	0.25
679	134.7	92.9	6	3.10	2.90	2.47	1.65	4.12	0.60
686	134.7	92.5	6	3.10	2.90	2.47	1.65	4.12	0.60
686	134.7	92.2	6	3.10	2.90	2.47	1.65	4.12	0.60
669	134.7	91.6	6	3.10	2.90	2.47	1.65	4.12	0.60
667	134.7	89.8	6	3.10	2.90	2.47	1.65	4.12	0.60
665	134.7	89.5	6	3.10	2.90	2.47	1.65	4.12	0.60
653	134.7	89.4	6	3.10	2.90	2.47	1.65	4.12	0.60
672	134.7	89.2	6	3.10	2.90	2.47	1.65	4.12	0.60
679	134.7	88.2	6	3.10	2.90	2.47	1.65	4.12	0.60
688	134.7	88.5	6	3.10	2.90	2.47	1.65	4.12	0.60
662	134.7	88.1	6	3.10	2.90	2.47	1.65	4.12	0.60
676	134.7	88.6	6	3.10	2.90	2.47	1.65	4.12	0.60
676	134.7	87.3	6	3.10	2.90	2.47	1.65	4.12	0.60

Table C-10 Su et al. (2013) Experimental Results at 6 bar Continued									
h_m	T_b	T_w	P_b	P_{vb}	P_{ncb}	ρ_{ncb}	ρ_{vb}	ρ_b	W_{nc}
W/m^2-C	$^{\circ}C$	$^{\circ}C$	bar	bar	bar	kg/m^3	kg/m^3	kg/m^3	
665	134.7	86.6	6	3.10	2.90	2.47	1.65	4.12	0.60
648	134.7	86.4	6	3.10	2.90	2.47	1.65	4.12	0.60
676	134.7	86.4	6	3.10	2.90	2.47	1.65	4.12	0.60
646	134.7	85.2	6	3.10	2.90	2.47	1.65	4.12	0.60
622	134.7	82.9	6	3.10	2.90	2.47	1.65	4.12	0.60
609	134.7	82.4	6	3.10	2.90	2.47	1.65	4.12	0.60
617	134.7	82.0	6	3.10	2.90	2.47	1.65	4.12	0.60
624	134.7	82.5	6	3.10	2.90	2.47	1.65	4.12	0.60
604	134.7	81.6	6	3.10	2.90	2.47	1.65	4.12	0.60
617	134.7	80.6	6	3.10	2.90	2.47	1.65	4.12	0.60
620	134.7	80.0	6	3.10	2.90	2.47	1.65	4.12	0.60
607	134.7	79.3	6	3.10	2.90	2.47	1.65	4.12	0.60
575	134.7	77.4	6	3.10	2.90	2.47	1.65	4.12	0.60
569	134.7	77.7	6	3.10	2.90	2.47	1.65	4.12	0.60
577	134.7	77.8	6	3.10	2.90	2.47	1.65	4.12	0.60
563	134.7	76.7	6	3.10	2.90	2.47	1.65	4.12	0.60
575	134.7	75.2	6	3.10	2.90	2.47	1.65	4.12	0.60
567	134.7	74.8	6	3.10	2.90	2.47	1.65	4.12	0.60
563	134.7	74.3	6	3.10	2.90	2.47	1.65	4.12	0.60
552	134.7	74.6	6	3.10	2.90	2.47	1.65	4.12	0.60
544	134.7	74.2	6	3.10	2.90	2.47	1.65	4.12	0.60
560	134.7	73.4	6	3.10	2.90	2.47	1.65	4.12	0.60
556	134.7	72.4	6	3.10	2.90	2.47	1.65	4.12	0.60
546	134.7	72.4	6	3.10	2.90	2.47	1.65	4.12	0.60
546	134.7	72.1	6	3.10	2.90	2.47	1.65	4.12	0.60
542	134.7	69.3	6	3.10	2.90	2.47	1.65	4.12	0.60
544	134.7	68.9	6	3.10	2.90	2.47	1.65	4.12	0.60

Table C-11 Su et al. (2013) Experimental Results at 2 and 4 bar									
h_m	T_b	T_w	P_b	P_{vb}	P_{ncb}	ρ_{ncb}	ρ_{vb}	ρ_b	W_{nc}
W/m^2-C	$^{\circ}C$	$^{\circ}C$	bar	bar	bar	kg/m^3	kg/m^3	kg/m^3	
995	114.9	70.3	2	1.69	0.31	0.28	0.94	1.22	0.23
972	114.8	69.1	2	1.68	0.32	0.29	0.94	1.23	0.23
1019	114.7	69.5	2	1.68	0.32	0.29	0.94	1.23	0.24
991	114.7	69.3	2	1.67	0.33	0.29	0.94	1.23	0.24
745	112.0	66.7	2	1.53	0.47	0.42	0.86	1.29	0.33
757	111.9	66.8	2	1.53	0.47	0.43	0.86	1.29	0.33
745	111.9	66.5	2	1.53	0.47	0.43	0.86	1.29	0.33
755	111.8	66.4	2	1.52	0.48	0.43	0.86	1.29	0.33
659	110.5	65.0	2	1.46	0.54	0.49	0.82	1.32	0.37
648	110.4	64.2	2	1.45	0.55	0.50	0.82	1.32	0.38
651	110.2	63.7	2	1.44	0.56	0.51	0.82	1.32	0.38
641	110.1	63.8	2	1.44	0.56	0.51	0.81	1.32	0.39
602	108.2	64.4	2	1.35	0.65	0.59	0.77	1.36	0.44
596	108.2	64.6	2	1.35	0.65	0.60	0.77	1.36	0.44
599	108.1	64.4	2	1.34	0.66	0.60	0.76	1.36	0.44
588	108.0	64.3	2	1.34	0.66	0.60	0.76	1.36	0.44
535	105.8	62.1	2	1.24	0.76	0.69	0.71	1.41	0.49
524	105.8	62.0	2	1.24	0.76	0.70	0.71	1.41	0.49
519	105.8	61.5	2	1.24	0.76	0.70	0.71	1.41	0.50
533	105.7	62.1	2	1.24	0.76	0.70	0.71	1.41	0.50
1209	136.8	81.4	4	3.30	0.70	0.59	1.75	2.34	0.25
1195	136.8	81.7	4	3.30	0.70	0.60	1.74	2.34	0.26
1217	136.7	82.2	4	3.29	0.71	0.60	1.74	2.34	0.26
1223	136.7	81.6	4	3.29	0.71	0.60	1.74	2.34	0.26
945	133.7	77.6	4	3.02	0.98	0.84	1.61	2.45	0.34
950	133.6	77.4	4	3.01	0.99	0.85	1.60	2.45	0.35
959	133.6	78.3	4	3.01	0.99	0.85	1.60	2.45	0.35
950	133.5	78.0	4	2.99	1.01	0.86	1.60	2.46	0.35
802	131.2	77.2	4	2.80	1.20	1.03	1.50	2.53	0.41
799	131.2	76.0	4	2.80	1.20	1.03	1.50	2.53	0.41
797	131.1	75.7	4	2.79	1.21	1.04	1.50	2.54	0.41
812	131.0	76.2	4	2.78	1.22	1.05	1.49	2.54	0.41
705	128.5	72.6	4	2.58	1.42	1.23	1.39	2.62	0.47
689	128.4	72.5	4	2.57	1.43	1.24	1.39	2.63	0.47
691	128.3	72.8	4	2.57	1.43	1.24	1.39	2.63	0.47
694	128.1	72.5	4	2.56	1.44	1.25	1.38	2.63	0.48
635	126.2	73.8	4	2.41	1.59	1.39	1.31	2.69	0.52
639	126.1	73.2	4	2.40	1.60	1.40	1.30	2.70	0.52
623	126.1	74.0	4	2.40	1.60	1.40	1.30	2.70	0.52
629	125.9	72.8	4	2.39	1.61	1.41	1.30	2.70	0.52

Table C-12 Su et al. (2014) Experimental Results									
h_m	T_b	T_w	P_b	P_{vb}	P_{ncb}	ρ_{ncb}	ρ_{vb}	ρ_b	W_{nc}
W/m^2-C	$^{\circ}C$	$^{\circ}C$	bar	bar	bar	kg/m^3	kg/m^3	kg/m^3	
1271	128.5	115.4	4	2.59	1.41	1.23	1.40	2.62	0.47
1738	132.5	117.7	4	2.91	1.09	0.94	1.55	2.49	0.38
2157	136.8	119.9	4	3.30	0.70	0.59	1.75	2.34	0.25
3173	141.2	122.1	4	3.74	0.26	0.22	1.95	2.18	0.10
1227	133.5	118.2	5	3.00	2.00	1.71	1.60	3.31	0.52
1456	135.5	119.1	5	3.18	1.82	1.55	1.69	3.24	0.48
1751	138.3	120.6	5	3.44	1.56	1.32	1.81	3.13	0.42
1931	140.1	121.3	5	3.63	1.37	1.15	1.90	3.06	0.38
2011	141.8	121.7	5	3.80	1.20	1.01	1.99	2.99	0.34
2288	144.0	123.0	5	4.04	0.96	0.80	2.10	2.90	0.28
2540	146.5	124.7	5	4.33	0.67	0.55	2.24	2.79	0.20
4044	150.0	130.6	5	4.76	0.24	0.20	2.44	2.63	0.07
1675	139.8	120.3	6	3.59	2.41	2.03	1.89	3.91	0.52
1807	142.9	121.2	6	3.92	2.08	1.74	2.04	3.78	0.46
1887	145.8	122.2	6	4.25	1.75	1.45	2.20	3.65	0.40
1989	147.8	122.4	6	4.49	1.51	1.25	2.31	3.56	0.35
2156	149.6	124.2	6	4.71	1.29	1.06	2.41	3.48	0.31
2456	152.0	126.6	6	5.03	0.97	0.80	2.56	3.36	0.24
3538	155.5	131.3	6	5.50	0.50	0.41	2.78	3.19	0.13

C.6 Kim et al. (2009) Database

Kim et al. (2009) reports experimental results for condensation on a 0.65 m height, 0.038 m diameter vertical cylinder with nitrogen as the non-condensable gas. The bulk non-condensable gas mass fraction, bulk pressure, bulk to wall temperature difference and measured heat transfer coefficients are reported for each experiment in graphical form. Figure C-8 through Figure C-12 are reproductions of figures from Kim et al. (2009).

As noted by Kim et al. (2009) using the ideal gas law for properties prediction at the 20 bar test conditions results in significant error. As described in Appendix D, gas properties are determined using a script based on the International Association for the Properties of Water and Steam (IAPWS) 1995 formulation for steam, and nitrogen properties are determined using the National Institute of Standards and Technology (NIST) Fluid Thermodynamic and Transport Properties (REFPROP) database. The data extracted from each image and gas properties, calculated as described in Appendix D, are provided in Table C-13.

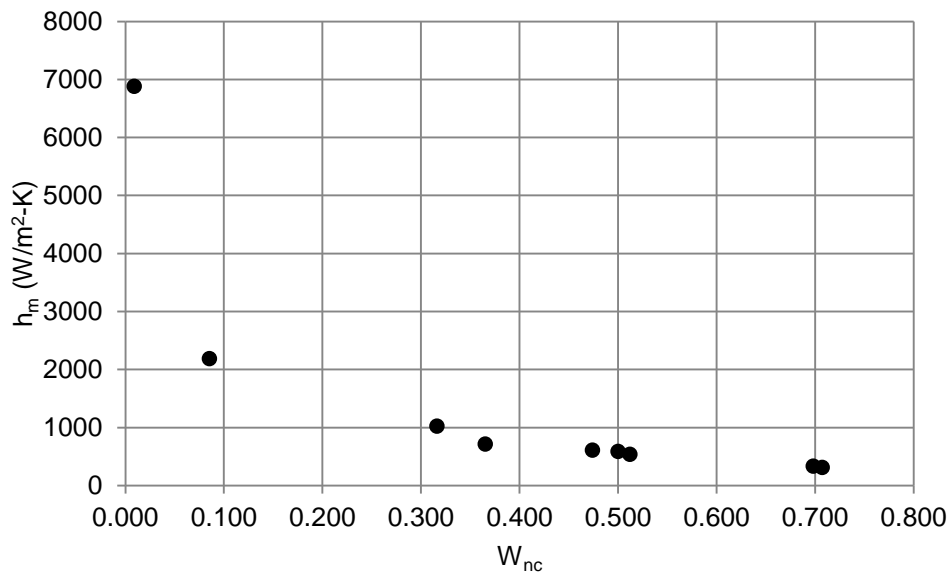


Figure C-8 Kim et al. (2009) Results at 4 bar and 50°C Wall Sub-cooling

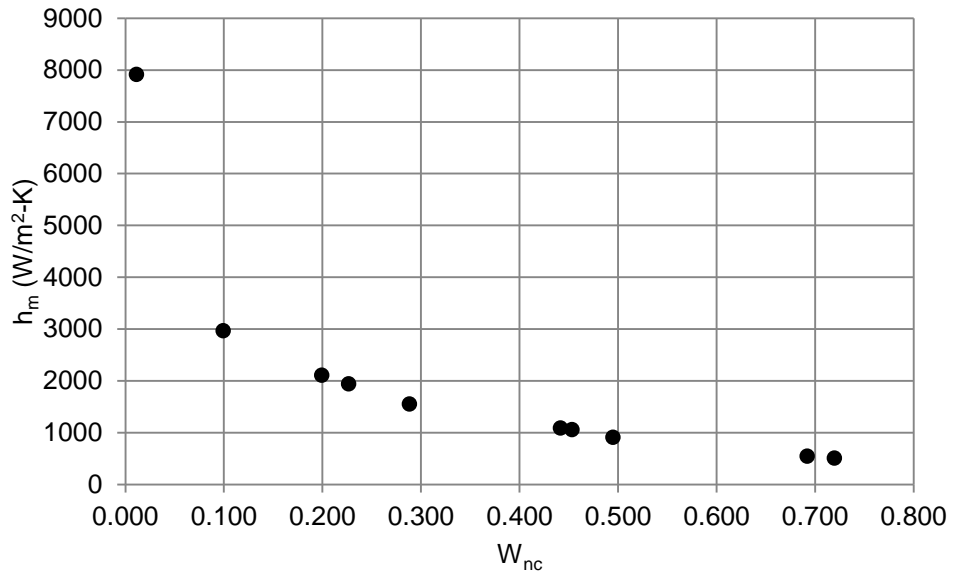


Figure C-9 Kim et al. (2009) Results at 7 bar and 50°C Wall Sub-cooling

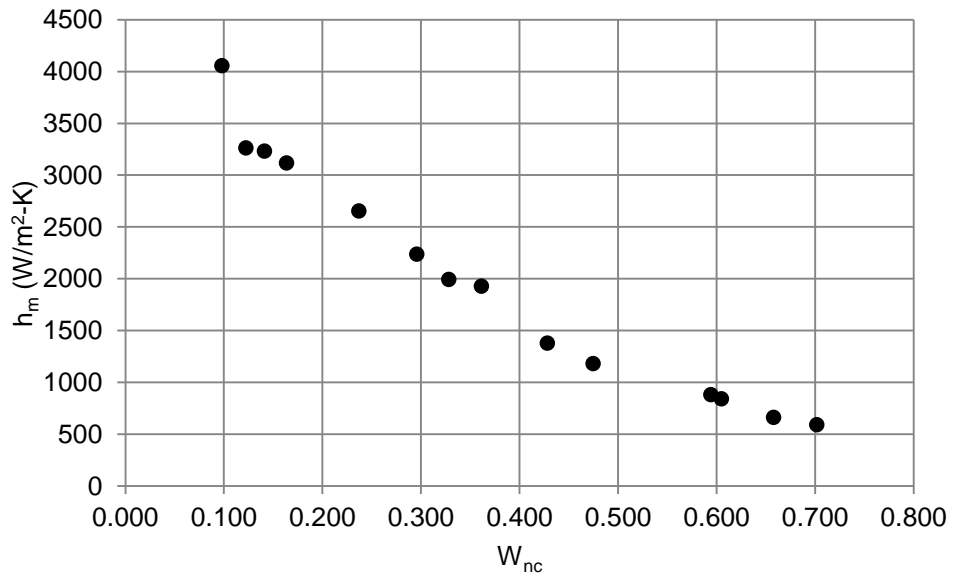


Figure C-10 Kim et al. (2009) Results at 12 bar and 50°C Wall Sub-cooling

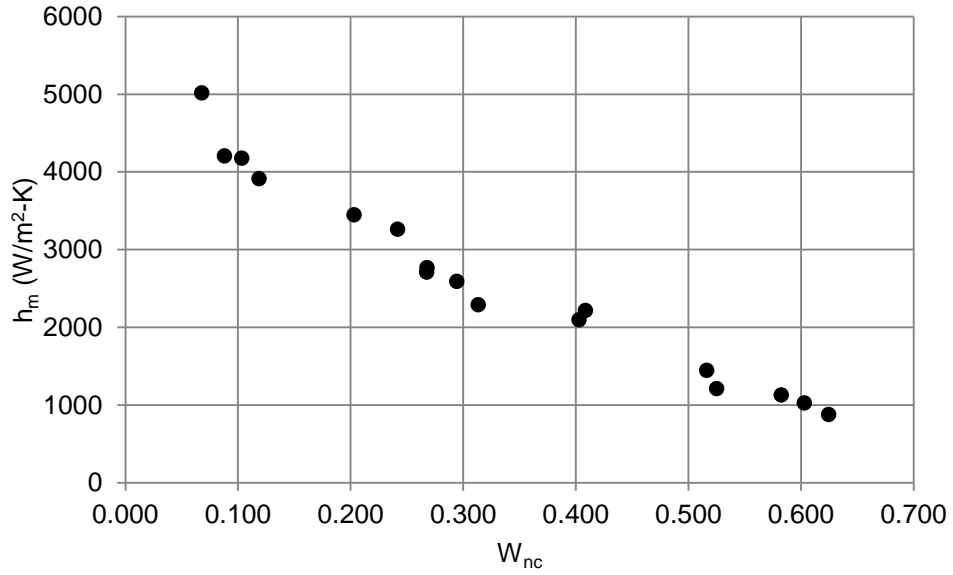


Figure C-11 Kim et al. (2009) Results at 15 bar and 55°C Wall Sub-cooling

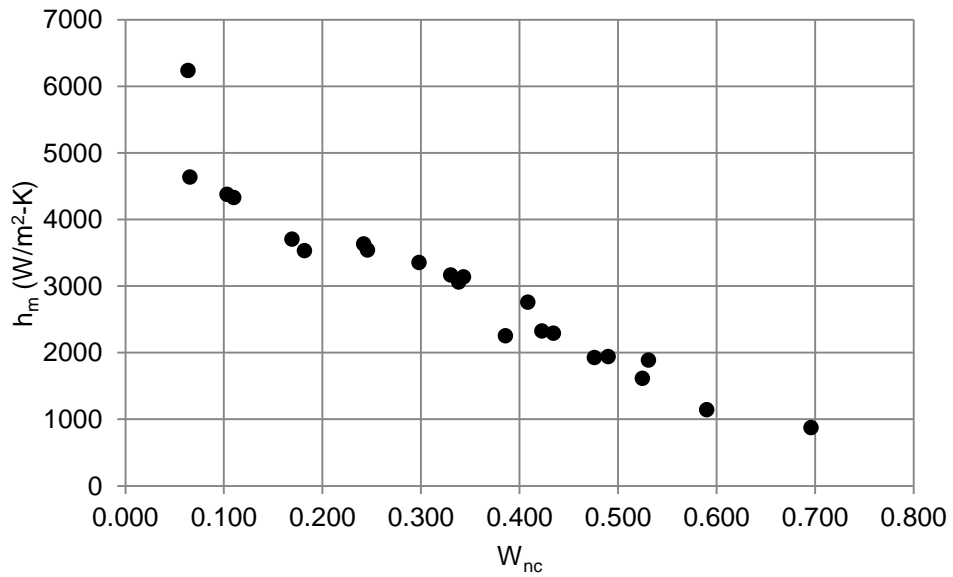


Figure C-12 Kim et al. (2009) Results at 20 bar and 60°C Wall Sub-cooling

Table C-13 Kim et al. (2009) Experimental Results									
h_m	T_b	T_w	P_b	P_{vb}	P_{ncb}	ρ_{ncb}	ρ_{vb}	ρ_b	W_{nc}
W/m^2-C	$^{\circ}C$	$^{\circ}C$	bar	bar	bar	kg/m^3	kg/m^3	kg/m^3	
6879	143.4	93.4	4	3.98	0.02	0.02	2.15	2.17	0.009
2184	141.5	91.5	4	3.77	0.23	0.19	2.05	2.24	0.085
1021	134.5	84.5	4	3.08	0.92	0.78	1.69	2.48	0.316
711	132.6	82.6	4	2.92	1.08	0.93	1.61	2.54	0.365
611	127.9	77.9	4	2.54	1.46	1.27	1.41	2.68	0.474
586	126.6	76.6	4	2.44	1.56	1.36	1.36	2.72	0.500
536	126.0	76.0	4	2.39	1.61	1.40	1.34	2.74	0.512
335	113.7	63.7	4	1.62	2.38	2.14	0.93	3.07	0.698
310	112.9	62.9	4	1.58	2.42	2.18	0.90	3.09	0.707
509	129.3	79.3	7	2.65	4.35	3.76	1.47	5.23	0.720
547	132.0	82.0	7	2.87	4.13	3.55	1.58	5.13	0.692
908	146.1	96.1	7	4.28	2.72	2.26	2.31	4.56	0.495
1056	148.3	98.3	7	4.55	2.45	2.02	2.44	4.46	0.453
1089	148.9	98.9	7	4.62	2.38	1.96	2.48	4.44	0.442
1554	155.7	105.7	7	5.53	1.47	1.19	2.94	4.13	0.288
1943	158.0	108.0	7	5.87	1.13	0.91	3.11	4.02	0.227
2107	158.9	108.9	7	6.02	0.98	0.79	3.18	3.97	0.199
2966	162.1	112.1	7	6.53	0.47	0.38	3.43	3.81	0.099
7912	164.7	114.7	7	6.95	0.05	0.04	3.64	3.68	0.011
591	149.9	99.9	12	4.74	7.26	5.96	2.54	8.50	0.702
660	154.2	104.2	12	5.32	6.68	5.43	2.83	8.26	0.658
840	158.8	108.8	12	5.99	6.01	4.84	3.16	8.00	0.605
881	159.6	109.6	12	6.12	5.88	4.72	3.23	7.95	0.594
1182	167.8	117.8	12	7.51	4.49	3.54	3.92	7.46	0.475
1379	170.5	120.5	12	8.02	3.98	3.12	4.17	7.29	0.429
1929	174.0	124.0	12	8.72	3.28	2.55	4.51	7.07	0.361
1993	175.6	125.6	12	9.05	2.95	2.29	4.68	6.97	0.328
2236	177.1	127.1	12	9.37	2.63	2.03	4.84	6.87	0.296
2653	179.6	129.6	12	9.93	2.07	1.59	5.11	6.70	0.237
3117	182.4	132.4	12	10.61	1.39	1.07	5.44	6.51	0.164
3232	183.3	133.3	12	10.80	1.20	0.91	5.54	6.45	0.141
3261	183.9	133.9	12	10.97	1.03	0.79	5.62	6.41	0.122
4055	184.8	134.8	12	11.18	0.82	0.62	5.72	6.35	0.098
878	165.8	110.8	15	7.16	7.84	6.21	3.74	9.95	0.625
1025	167.7	112.7	15	7.49	7.51	5.92	3.91	9.83	0.603
1130	169.4	114.4	15	7.80	7.20	5.65	4.06	9.72	0.583
1212	173.7	118.7	15	8.65	6.35	4.94	4.48	9.42	0.525
1447	174.3	119.3	15	8.77	6.23	4.84	4.54	9.38	0.516
2099	181.3	126.3	15	10.33	4.67	3.58	5.31	8.88	0.403

Table C-13 Kim et al. (2009) Experimental Results Continued

h_m	T_b	T_w	P_b	P_{vb}	P_{ncb}	ρ_{ncb}	ρ_{vb}	ρ_b	W_{nc}
W/m^2-C	$^{\circ}C$	$^{\circ}C$	bar	bar	bar	kg/m^3	kg/m^3	kg/m^3	
2217	181.0	126.0	15	10.25	4.75	3.64	5.27	8.91	0.409
2292	185.9	130.9	15	11.47	3.53	2.68	5.86	8.54	0.314
2592	186.8	131.8	15	11.70	3.30	2.49	5.98	8.47	0.294
2709	188.1	133.1	15	12.03	2.97	2.24	6.14	8.38	0.268
2768	188.0	133.0	15	12.02	2.98	2.25	6.14	8.38	0.268
3262	189.2	134.2	15	12.34	2.66	2.01	6.29	8.29	0.242
3449	190.8	135.8	15	12.79	2.21	1.66	6.51	8.17	0.203
3913	194.2	139.2	15	13.74	1.26	0.94	6.97	7.92	0.119
4178	194.7	139.7	15	13.90	1.10	0.82	7.06	7.87	0.103
4207	195.3	140.3	15	14.07	0.93	0.69	7.14	7.83	0.088
5018	196.0	141.0	15	14.29	0.71	0.53	7.24	7.77	0.068
877	170.2	110.2	20	7.95	12.05	9.43	4.14	13.57	0.696
1142	180.7	120.7	20	10.18	9.82	7.51	5.24	12.75	0.590
1615	185.9	125.9	20	11.47	8.53	6.46	5.86	12.32	0.525
1887	185.4	125.4	20	11.35	8.65	6.55	5.81	12.36	0.531
1943	188.4	128.4	20	12.12	7.88	5.93	6.19	12.11	0.490
1929	189.4	129.4	20	12.38	7.62	5.72	6.31	12.03	0.476
2291	192.1	132.1	20	13.14	6.86	5.12	6.68	11.81	0.435
2326	192.8	132.8	20	13.35	6.65	4.96	6.78	11.75	0.423
2757	193.7	133.7	20	13.60	6.40	4.76	6.91	11.67	0.408
2256	195.0	135.0	20	14.00	6.00	4.46	7.10	11.56	0.386
3064	197.7	137.7	20	14.81	5.19	3.83	7.50	11.33	0.339
3140	197.4	137.4	20	14.73	5.27	3.89	7.46	11.35	0.343
3168	198.1	138.1	20	14.95	5.05	3.73	7.57	11.29	0.330
3356	199.8	139.8	20	15.48	4.52	3.32	7.83	11.15	0.298
3544	202.3	142.3	20	16.33	3.67	2.69	8.24	10.93	0.246
3634	202.5	142.5	20	16.39	3.61	2.64	8.27	10.91	0.242
3530	205.2	145.2	20	17.33	2.67	1.94	8.73	10.67	0.182
3704	205.8	145.8	20	17.53	2.47	1.80	8.83	10.63	0.169
4331	208.2	148.2	20	18.41	1.59	1.15	9.26	10.41	0.110
4379	208.5	148.5	20	18.52	1.48	1.07	9.31	10.39	0.103
4637	210.0	150.0	20	19.07	0.93	0.67	9.58	10.26	0.066
6238	210.0	150.0	20	19.09	0.91	0.65	9.60	10.25	0.064

C.7 Liu (1999) Database

Liu (1999) reports experimental results for condensation on a 2 m height, 0.038 m diameter vertical cylinder. Results are provided in tabular form in Appendix A of Liu (1999). The bulk and wall temperatures, measured heat transfer coefficient and bulk pressure are reported for each experiment, and gas mixture properties are calculated as described in Appendix D. Table C-14 summarizes the results. The vapor mole fractions, x_v , shown in Table C-14 are inconsistent with the values reported in Liu (1990) by up to 15%. This discrepancy in the results of Liu (1999) is due to either a calculation error or a different method of calculating the steam partial pressure.

h_m	T_b	T_w	P_b	P_{vb}	P_{ncb}	ρ_{ncb}	ρ_{vb}	ρ_b	W_{nc}	x_v
W/m^2-C	$^{\circ}C$	$^{\circ}C$	bar	bar	bar	kg/m^3	kg/m^3	kg/m^3		
524	108.2	104.4	2.53	1.35	1.18	1.079	0.782	1.861	0.580	0.53
1203	114.2	104.3	2.53	1.65	0.88	0.795	0.942	1.737	0.457	0.65
1319	117.4	105.7	2.53	1.83	0.71	0.630	1.037	1.667	0.378	0.72
1947	120.4	106.4	2.53	2.01	0.52	0.463	1.134	1.597	0.290	0.79
2404	122.8	108.3	2.53	2.17	0.36	0.318	1.219	1.537	0.207	0.86
422	110.5	104.0	3.04	1.46	1.58	1.436	0.839	2.275	0.631	0.48
735	115.7	104.5	3.04	1.73	1.31	1.171	0.986	2.158	0.543	0.57
1127	119.7	105.2	3.04	1.97	1.07	0.949	1.112	2.062	0.461	0.65
1399	122.2	106.0	3.04	2.13	0.91	0.801	1.197	1.999	0.401	0.70
1795	125.8	107.3	3.04	2.38	0.66	0.578	1.327	1.905	0.303	0.78
2494	129.8	109.4	3.04	2.69	0.35	0.305	1.489	1.793	0.170	0.88
329	110.5	104.3	3.55	1.46	2.09	1.897	0.839	2.736	0.693	0.41
707	116.5	104.8	3.55	1.78	1.77	1.579	1.011	2.591	0.610	0.50
954	119.9	105.2	3.55	1.98	1.56	1.385	1.120	2.504	0.553	0.56
1262	124.0	106.3	3.55	2.25	1.29	1.132	1.263	2.395	0.473	0.64
1775	127.9	107.3	3.55	2.54	1.01	0.873	1.413	2.285	0.382	0.72
332	111.3	103.4	4.05	1.50	2.56	2.315	0.860	3.175	0.729	0.37
564	115.1	103.7	4.05	1.70	2.35	2.110	0.969	3.079	0.685	0.42
889	121.7	104.4	4.05	2.10	1.95	1.722	1.181	2.903	0.593	0.52
1241	128.8	105.8	4.05	2.61	1.45	1.252	1.447	2.699	0.464	0.64
1816	132.6	108.0	4.05	2.92	1.14	0.975	1.607	2.583	0.378	0.72
394	112.7	104.9	4.56	1.57	2.99	2.695	0.901	3.596	0.750	0.34
720	119.4	104.1	4.56	1.95	2.61	2.315	1.102	3.417	0.678	0.43
1116	127.5	105.7	4.56	2.51	2.05	1.781	1.396	3.177	0.561	0.55
1368	130.9	106.4	4.56	2.78	1.78	1.533	1.536	3.070	0.499	0.61
1774	135.0	108.2	4.56	3.13	1.43	1.220	1.717	2.937	0.415	0.69

C.8 Anderson (1998a) Database

Anderson (1998a) reports results of testing that modeled a 1:12 scale radial slice of the AP600 nuclear plant containment vessel. Results from an atmospheric facility and pressurized facility with different geometries are available. The test geometries included vertical, inclined and horizontal condensing surfaces. The length of the vertical condensing surface for the atmospheric facility is 0.91 m and the vertical component of the pressurized facility is 1.13 m.

Anderson (1998a) utilized two independent methods of heat flux measurement. Localized heat flux meter (HFM) measurements based on temperature gradient across the condensing plate and coolant channel energy balance (CEB) results are provided for each of the condensing plates. The atmospheric facility results are shown in Table C-15.

Test ID	HFM	CEB	T_b	T_w	P_b
	W/m ² -K	W/m ² -K	C	C	bar
202	70.53	71.07	60.65	28.6	1
203	99.96	102.77	69.23	29.4	1
204	96.9	100.04	69.04	29.4	1
211	95.24	99.79	68.15	29.2	1
212	168.4	173.33	79.68	29.2	1
213	157.57	172.57	79.68	34	1
214	183.08	204.03	79.35	31.8	1
215	182.77	201.06	85.12	28.43	1
216	178.02	201.74	85.25	29.76	1
217	174.56	201.86	84.55	29.47	1
218	239.96	263.78	89.53	30.6	1
219	234.93	268.65	89.72	30.3	1
220	230.66	267.45	89.68	29.96	1
326	150.01	172.62	81.46	27.76	1
328	150.55	188.12	80.8	31.74	1
329	147.52	174.51	80.58	29.58	1

A total of 47 separate air steam condensation experimental results were documented by Anderson (1998a). However, local measurement results for each of the cooling channels are only available for 17 of these experiments. Since the pressurized facility included horizontal, inclined and vertical condensing surfaces, it is necessary to analyze the local results to determine the average values for the vertical condensing wall. Table C-16 provides the bulk temperature, wall temperature and heat transfer coefficients based on the average results from the three vertical condensing plates. The complete listing of local measurement results from Anderson (1998a) is provided in Table C-17. This information was reproduced here due to poor image quality in Anderson (1998a). All values were checked through back-calculation using multiple methods to confirm the correct values.

Table C-16 Anderson (1999a) Pressurized Facility Averaged Experimental Results					
Test ID	T_b (°C)	T_w (°C)	HFM (W/m ² -K)	CEB (W/m ² -K)	P_b (bar)
1000s	90.1	49.4	343	403	1.00
1001s	89.3	59.9	381	460	1.00
1002s	89.3	67.4	461	674	1.00
1003s	89.7	77.9	454	483	1.00
1004s	90.0	32.7	280	376	1.00
1005s	89.9	45.4	353	389	1.00
1006s	87.4	45.2	321	375	1.00
2000a	73.7	32.9	106	86	1.49
2001a	93.8	51.8	242	250	2.01
2002a	106.6	67.3	422	371	2.50
2003a	117.3	75.8	532	576	3.08
2100a	77.1	35.4	139	145	1.50
2101a	108.8	67.6	407	388	2.53
3000a	117.2	89.0	676	555	3.00
3001a	116.8	95.2	694	573	3.04
3002a	117.0	81.3	637	556	3.04
3003a	117.6	70.2	530	499	3.06

Table C-17 Anderson (1999a) Pressurized Facility Local Experimental Results

Test ID	Plate #	1	2	3	4	5	6	7	8	9	10	11	12	13	14
	Angle	90 (Hor.)	5	75	75	75	75	60	60	45	45	30	0	0	0 (Vert.)
1000s	T _b (°C)	90.3	90.3	90.1	90.1	90.0	90.0	90.1	90.1	90.1	90.1	89.9	89.9	90.1	90.1
	T _w (°C)	55.4	53.5	51.2	50.9	50.5	51.2	49.8	49.6	51.6	53.2	52.2	50.3	49.5	48.5
	HFM (W/m ² -K)	460	473	312	442	461	402	520	423	464	511	497	324	348	355
	CEB (W/m ² -K)	436	N/A	444	430	444	445	426	455	440	464	449	405	393	412
1001s	T _b (°C)	89.8	89.8	89.2	89.2	89.5	89.5	89.5	89.5	89.4	89.4	89.2	89.2	89.3	89.3
	T _w (°C)	65.2	63.7	63.4	62.4	62.4	62.4	61.7	61.6	62.3	63.2	62.2	60.9	59.8	59.1
	HFM (W/m ² -K)	555	558	534	528	548	456	589	465	535	534	567	354	397	392
	CEB (W/m ² -K)	489	N/A	507	454	475	463	496	494	532	552	535	436	470	475
1002s	T _b (°C)	89.4	89.4	88.7	88.7	89.5	89.5	89.3	89.3	89.4	89.4	89.4	89.4	89.3	89.3
	T _w (°C)	69.4	67.7	65.8	65.1	69.3	69.1	69.1	68.8	70.8	71.4	70.6	69.2	66.9	66.3
	HFM (W/m ² -K)	627	626	537	561	679	546	700	546	639	615	693	424	485	473
	CEB (W/m ² -K)	684	N/A	542	507	512	469	461	497	485	484	772	671	689	663
1003s	T _b (°C)	89.9	89.9	88.1	88.1	87.6	87.6	88.9	88.9	89.2	89.2	89.5	89.5	89.7	89.7
	T _w (°C)	80.6	79.7	79.0	78.5	77.7	77.5	77.8	77.6	78.5	78.6	78.6	77.8	78.1	77.7
	HFM (W/m ² -K)	918	556	744	720	661	447	769	542	696	587	715	390	526	446
	CEB (W/m ² -K)	702	N/A	732	651	588	566	553	585	579	578	539	465	523	460
1004s	T _b (°C)	90.3	90.3	90.1	90.1	90.1	90.1	90.0	90.0	54.5	54.5	90.0	90.0	90.1	90.1
	T _w (°C)	39.7	36.4	36.8	35.8	35.1	35.5	33.7	34.5	22.7	23.9	35.7	33.4	32.7	31.9
	HFM (W/m ² -K)	361	370	360	390	425	382	442	395	369	412	391	275	281	284
	CEB (W/m ² -K)	430	436	448	418	436	426	430	443	421	418	411	381	370	377
1005s	T _b (°C)	90.9	90.9	90.2	90.2	90.0	90.0	90.2	90.2	90.3	90.3	90.0	90.0	89.9	89.9
	T _w (°C)	51.1	49.2	48.9	49.0	48.4	48.5	47.3	47.7	48.6	49.7	49.3	42.7	47.0	46.5
	HFM (W/m ² -K)	430	405	425	456	465	415	499	440	452	446	497	N/A	356	350
	CEB (W/m ² -K)	386	477	428	431	444	440	445	469	439	457	433	370	395	400
1006s	T _b (°C)	88.8	88.8	88.4	88.4	88.0	88.0	87.8	87.8	88.0	88.0	87.4	87.4	87.4	87.4
	T _w (°C)	50.1	48.7	48.0	47.4	47.4	47.2	45.0	45.8	46.8	48.3	48.2	46.2	45.1	44.4
	HFM (W/m ² -K)	431	362	375	383	465	391	514	400	422	444	539	320	330	312
	CEB (W/m ² -K)	420	452	428	409	424	415	436	426	405	429	410	380	377	368
2000a	T _b (°C)	73.5	73.5	75.1	75.1	73.9	73.9	73.1	73.1	74.4	74.4	73.9	73.9	73.6	73.6
	T _w (°C)	33.6	32.2	33.6	33.1	32.6	32.4	32.3	32.4	32.8	32.9	33.4	32.8	33.3	32.8
	HFM (W/m ² -K)	183	76	151	113	137	147	190	129	139	115	149	104	124	89
	CEB (W/m ² -K)	106	121	140	128	148	148	137	136	126	120	87	79	86	93
2001a	T _b (°C)	93.5	93.5	93.9	93.9	94.0	94.0	93.8	93.8	93.7	93.7	93.6	93.6	93.8	93.8
	T _w (°C)	53.5	52.1	54.0	53.1	53.9	52.8	52.5	53.3	53.4	53.9	53.4	52.5	51.8	51.0
	HFM (W/m ² -K)	318	183	326	226	334	290	342	273	265	249	314	252	250	225
	CEB (W/m ² -K)	183	207	136	214	255	276	287	291	284	294	271	253	245	252

Table C-17 Anderson (1998a) Pressurized Facility Experimental Results Cont.

Test ID	Plate #	1	2	3	4	5	6	7	8	9	10	11	12	13	14
	Angle	90 (Hor.)	5	75	75	75	75	60	60	45	45	30	0	0	0 (Vert.)
2002a	T _b (°C)	106.5	106.5	106.6	106.6	106.7	106.7	106.6	106.6	106.7	106.7	106.4	106.4	106.7	106.7
	T _w (°C)	68.7	67.1	68.2	66.8	63.4	65.8	67.2	67.1	67.1	68.0	68.0	67.8	67.5	66.6
	HFM (W/m ² -K)	507	332	510	367	141	457	541	475	393	404	490	436	446	385
	CEB (W/m ² -K)	343	388	430	386	360	414	391	417	374	395	381	362	359	393
2003a	T _b (°C)	116.3	116.3	116.8	116.8	117.0	117.0	116.9	116.9	116.9	116.9	117.1	117.1	117.4	117.4
	T _w (°C)	78.9	77.0	79.0	77.0	76.9	75.6	76.7	76.5	76.9	78.2	78.0	77.1	75.5	74.7
	HFM (W/m ² -K)	672	435	741	498	567	598	704	602	520	566	663	553	538	504
	CEB (W/m ² -K)	454	504	561	500	508	541	604	533	491	517	596	564	584	580
2100a	T _b (°C)	77.7	77.7	77.9	77.9	76.9	76.9	78.0	78.0	77.4	77.4	77.0	77.0	77.1	77.1
	T _w (°C)	38.1	35.6	36.2	36.2	35.0	34.9	36.2	36.2	36.5	36.6	35.9	35.8	35.6	35.0
	HFM (W/m ² -K)	222	113	199	177	210	191	199	179	225	184	142	147	150	120
	CEB (W/m ² -K)	N/A	199	177	160	183	164	125	191	171	165	154	133	144	159
2101a	T _b (°C)	109.3	109.3	109.5	109.5	109.2	109.2	109.5	109.5	109.1	109.1	109.0	109.0	108.7	108.7
	T _w (°C)	68.8	67.9	69.1	68.9	68.6	68.1	69.1	68.9	70.7	70.8	69.8	68.0	67.6	67.2
	HFM (W/m ² -K)	470	362	522	474	530	520	525	476	730	571	482	436	409	376
	CEB (W/m ² -K)	370	431	440	389	442	461	318	479	441	455	415	379	388	398
3000a	T _b (°C)	116.7	116.7	117.0	117.0	117.0	117.0	117.1	117.1	117.1	117.1	117.1	117.1	117.2	117.2
	T _w (°C)	89.8	88.6	90.1	88.5	88.2	87.5	87.9	86.6	87.9	89.6	89.6	89.1	89.0	88.9
	HFM (W/m ² -K)	823	559	886	602	782	729	834	646	609	572	792	733	793	502
	CEB (W/m ² -K)	566	628	678	592	642	630	656	630	590	576	627	572	573	521
3001a	T _b (°C)	116.3	116.3	116.7	116.7	116.8	116.8	116.5	116.5	117.0	117.0	116.7	116.7	116.8	116.8
	T _w (°C)	97.9	96.8	98.3	97.2	97.9	98.0	97.9	97.3	97.4	97.9	96.8	95.7	95.2	94.8
	HFM (W/m ² -K)	865	529	896	606	797	836	905	691	701	697	875	741	718	622
	CEB (W/m ² -K)	546	564	635	576	601	681	646	668	592	750	692	442	632	647
3002a	T _b (°C)	115.4	115.4	115.9	115.9	116.3	116.3	116.5	116.5	116.7	116.7	116.8	116.8	117.2	117.2
	T _w (°C)	80.4	78.9	81.0	78.6	78.7	78.4	79.1	79.3	80.4	81.7	82.5	81.1	81.9	81.1
	HFM (W/m ² -K)	688	427	796	511	692	645	716	615	573	586	729	628	700	584
	CEB (W/m ² -K)	503	528	577	531	560	559	574	547	540	556	539	519	535	612
3003a	T _b (°C)	117.1	117.1	117.0	117.0	117.1	117.1	118.0	118.0	117.7	117.7	117.5	117.5	117.7	117.7
	T _w (°C)	73.5	69.3	70.0	67.9	67.9	68.7	68.4	68.2	68.6	69.7	69.6	70.0	71.0	69.6
	HFM (W/m ² -K)	701	446	680	478	609	605	692	584	479	518	612	535	562	492
	CEB (W/m ² -K)	524	551	462	415	442	443	423	459	404	401	425	419	533	545

Appendix D Fluid and Gas Properties

The properties of water and steam (thermal conductivity, viscosity, enthalpy, specific heat, surface tension and density) are determined using a script based on the International Association for the Properties of Water and Steam (IAPWS) 1995 formulation (Wagner 2002). The properties of air and nitrogen are determined using the National Institute of Standards and Technology (NIST) Fluid Thermodynamic and Transport Properties (REFPROP) database, Version 9.1.

The average coefficient of viscosity of the air vapor mixture within the boundary layer is calculated as the average of the bulk and interface mixture viscosities. The mixture viscosity at the bulk and interface is calculated using Wilkes method as reported by Poling et al. (2001).

$$\mu_m = \frac{x_1\mu_1}{x_1 + x_2\phi_{1,2}} + \frac{x_2\mu_2}{x_2 + x_1\phi_{2,1}} \quad \text{Equation D-1}$$

The quantity $\phi_{1,2}$ is found by interchanging the subscripts in the following equation:

$$\phi_{i,j} = \frac{1}{2\sqrt{2}} \left(1 + \frac{M_i}{M_j} \right)^{-1/2} \left[1 + \left(\frac{\mu_i}{\mu_j} \right)^{1/2} \left(\frac{M_j}{M_i} \right)^{1/4} \right]^2 \quad \text{Equation D-2}$$

, where M_i and M_j are the molecular weights of the individual components and μ_i and μ_j are the viscosities of the individual components.

The average diffusion coefficient, D , within the boundary layer for the binary air vapor mixture is evaluated at the average bulk and interface temperature using the Wilke and Lee method as reported by Poling et al. (2001).

$$D = \frac{10^{-3} \cdot T^{1.5} \left(3.03 - \frac{0.98}{M_{AB}^{0.5}} \right)}{P M_{AB}^{0.5} \sigma_{AB}^2 \Omega_D} \quad \text{Equation D-3}$$

The parameter σ_{AB} represents the characteristic length for the intermolecular force law and is calculated as the average of the individual gas component scale parameters, σ , for each component, with no weighting applied. The air and nitrogen gas component scale parameters are 3.14 Å and 3.798 Å respectively based on those recommended by Poling et al. (2001). The steam scale parameter is 3.62 Å based on the relationship $\sigma = V_b^{1/3}$, where V_b is the liquid molar volume at the normal boiling temperature in cm^3/mol . The collision integral for diffusion, Ω_D , is given as a function of temperature:

$$\Omega_D = \frac{A}{\left(\frac{T}{\varepsilon_{AB}/k}\right)^B} + \frac{C}{\exp\left(D\frac{T}{\varepsilon_{AB}/k}\right)} + \frac{E}{\exp\left(F\frac{T}{\varepsilon_{AB}/k}\right)} + \frac{G}{\exp\left(H\frac{T}{\varepsilon_{AB}/k}\right)} \quad \text{Equation D-4}$$

, where $A = 1.06036$, $B = 0.15610$, $C = 0.19300$, $D = 0.47635$, $E = 1.03587$, $F = 1.52996$, $G = 1.76474$, and $H = 3.89411$. The parameter ε_{AB}/k is evaluated using the following relationship:

$$\frac{\varepsilon_{AB}}{k} = \left(\frac{\varepsilon_A}{k} \frac{\varepsilon_B}{k}\right)^{1/2} \quad \text{Equation D-5}$$

, where the values of ε_A/k and ε_B/k are defined for each gas component. The value of ε/k for air and nitrogen gas components are 97 K and 71.4 K respectively based on recommended values by Poling et al. (2001). The value of ε/k for steam is 429.1 K based on the relationship $\varepsilon/k = 1.15T_b$, where T_b is the normal boiling point at 1.01 bar in Kelvin.

In order to reproduce the results of Dehbi (2015) shown in Figure 9-3, the values σ and ε_{AB}/k for the diffusion coefficient calculation were taken from Dehbi (2015). Furthermore, the ideal gas law was used to calculate steam, air and nitrogen densities.

Appendix E Experimental Results

E.1 Tabulated Results for 0.457 m Width Plate

Table E-1 and Table E-2 provide the measured temperatures, absolute pressure and plate inclination results for the 0.457 m plate width consistent with the instrumentation defined in Table 5-1. An example of the graphical results for these experiments is given in Section 7.1. The graphical results show the entire data collection period after the system had stabilized. In most cases the gutter and trough collection tanks were drained and refilled several times to assure the condensation rates had stabilized. The values shown in Table E-1 and Table E-2 represent the average measurement over the last fill cycle of the gutter collection container.

Table E-3 provides the measured mass flow rates from the Coriolis flow meters, as described in Table 5-1, and the gutter and trough collection tank mass flow rates, \dot{m}_g and \dot{m}_t . The Coriolis flow meter results represent the average measurement over the last fill cycle of the gutter collection container. The collection tank mass flow rates are calculated from the differential pressure transducer, DP1 and DP2, readings as described in Appendix B.1. The gutter collection tank mass flow rate is based on the difference in the DP1 measurement from the start to the end of the last gutter fill cycle, $\Delta DP1$, and the time period of the last gutter fill cycle, $DP1 \Delta t$. The trough collection tank mass flow rate is based on the difference in the DP2 measurement from the start to the end of the last trough fill cycle, $\Delta DP2$, and the time period of the last trough fill cycle, $DP2 \Delta t$.

Table E-4 gives the measured heat transfer coefficient results and measurement uncertainties for the coolant channel calorimetric and condensate mass based measurement methods. The analysis methodology is presented in Appendix B.

Table E-1 Inclination, Pressure and RTD Results for 0.457 m Width Plate

Test ID	Inc	P1	RTD1	RTD2	RTD3	RTD4	RTD5	RTD6	RTD7	RTD8	RTD9	RTD10
	°	bar	°C									
T457_001	0	0.980	51.7	54.1	47.4	47.4	43.1	43.2	47.7	48.0	99.2	94.3
T457_002	0	0.978	56.6	57.6	54.9	55.0	54.9	55.1	56.6	56.8	93.7	85.7
T457_003	0	0.972	56.6	58.1	54.9	55.0	54.9	55.1	56.8	56.8	95.0	86.1
T457_004	0	0.970	47.6	50.2	45.3	45.4	45.2	45.3	47.6	47.8	95.5	87.4
T457_005	15	0.970	48.0	50.1	45.3	45.4	45.2	45.3	47.7	48.1	95.4	87.2
T457_006	30	0.970	48.2	50.1	45.3	45.4	45.2	45.3	47.8	48.1	95.4	86.8
T457_007	45	0.970	48.2	50.0	45.3	45.4	45.2	45.3	47.9	48.2	95.5	86.5
T457_008	60	0.970	48.1	49.7	45.2	45.4	45.2	45.3	47.9	48.2	95.4	86.2
T457_009	75	0.970	48.0	48.8	45.2	45.4	45.2	45.3	47.7	47.9	94.5	85.7
T457_010	75	0.970	48.1	49.7	45.2	45.3	45.2	45.3	47.8	48.1	95.1	86.2
T457_011	75	0.971	47.8	48.2	45.2	45.4	45.2	45.3	47.7	47.9	95.0	85.8
T457_012	60	0.971	47.8	48.7	45.2	45.4	45.2	45.3	47.7	47.9	94.8	85.5
T457_013	45	0.972	47.8	48.9	45.2	45.4	45.2	45.3	47.7	47.8	94.8	85.6
T457_014	45	0.972	48.1	50.5	45.2	45.4	45.2	45.3	47.8	48.0	94.9	85.7
T457_015	45	0.972	47.9	49.3	45.2	45.4	45.2	45.3	47.7	47.9	94.9	85.7
T457_016	0	0.974	47.4	48.2	45.3	45.2	45.3	45.4	47.8	48.0	94.7	88.0
T457_017	15	0.974	47.9	48.2	45.2	45.2	45.3	45.4	47.9	48.3	94.6	87.6
T457_018	31	0.974	48.1	48.4	45.3	45.3	45.3	45.3	47.9	48.3	94.4	86.9
T457_019	45	0.973	48.1	48.5	45.2	45.2	45.3	45.3	48.0	48.3	94.4	86.5
T457_020	60	0.973	48.1	48.4	45.2	45.2	45.3	45.4	48.0	48.4	94.4	86.5
T457_021	75	0.973	48.0	48.4	45.2	45.3	45.3	45.4	48.0	48.3	94.4	86.6
T457_022	75	0.973	47.9	48.1	45.2	45.2	45.3	45.3	47.8	48.1	94.2	86.2
T457_023	60	0.972	47.9	48.4	45.2	45.2	45.3	45.3	47.9	48.2	94.2	86.0
T457_024	76	0.972	47.8	47.9	45.2	45.2	45.3	45.3	47.8	48.1	94.1	85.9
T457_025	60	0.972	47.8	48.0	45.2	45.2	45.2	45.3	47.8	48.0	93.9	85.5
T457_026	0	0.971	47.6	48.0	45.3	45.2	45.2	45.3	47.9	48.0	93.9	86.1
T457_027	0	0.971	47.6	48.1	45.2	45.2	45.2	45.3	47.9	47.9	93.8	86.1
T457_028	0	0.970	47.3	47.9	45.3	45.3	45.3	45.4	47.6	47.8	93.9	86.5
T457_029	0	0.974	47.4	48.0	45.2	45.2	45.2	45.3	47.5	47.7	96.1	87.4
T457_030	15	0.974	47.7	48.1	45.2	45.2	45.2	45.3	47.6	48.0	96.1	87.4
T457_031	30	0.973	47.9	48.2	45.2	45.2	45.2	45.3	47.7	48.0	96.1	86.9
T457_032	45	0.974	47.9	48.3	45.2	45.2	45.2	45.3	47.7	48.0	96.0	86.3
T457_033	60	0.975	47.9	48.2	45.2	45.2	45.2	45.3	47.7	48.0	95.9	86.1
T457_034	75	0.974	47.9	48.2	45.2	45.2	45.2	45.3	47.7	48.0	95.9	86.1
T457_035	75	0.974	47.7	47.9	45.2	45.2	45.2	45.3	47.6	47.8	95.6	85.6
T457_036	45	0.974	47.7	47.8	45.2	45.2	45.2	45.3	47.6	47.8	95.4	85.4
T457_037	45	0.974	47.7	47.8	45.2	45.2	45.2	45.3	47.6	47.8	95.4	85.4
T457_038	30	0.974	47.6	47.9	45.2	45.2	45.2	45.3	47.7	47.8	95.5	85.5

Table E-1 Inclination, Pressure and RTD Results for 0.457 m Width Plate Continued

Test ID	Inc	P1	RTD1	RTD2	RTD3	RTD4	RTD5	RTD6	RTD7	RTD8	RTD9	RTD10
	°	bar	°C	°C								
T457_039	15	0.973	47.6	47.9	45.2	45.2	45.2	45.3	47.7	47.8	95.5	85.7
T457_040	0	0.972	47.5	47.9	45.2	45.2	45.2	45.3	47.6	47.8	95.4	85.7
T457_041	0	0.977	16.2	16.7	14.7	14.7	14.9	14.8	16.4	16.6	88.0	76.3
T457_042	0	0.974	18.4	18.7	16.6	16.6	16.7	16.6	18.4	18.6	87.1	74.5
T457_043	0	0.973	23.8	24.0	22.2	22.2	22.3	22.2	23.9	24.1	87.2	74.7
T457_044	0	0.975	30.4	31.4	28.0	28.0	28.0	28.0	30.7	30.8	95.6	87.6
T457_045	0	0.974	30.3	31.6	28.0	28.0	28.0	28.0	30.7	30.8	95.5	87.3
T457_046	0	0.974	30.3	31.7	28.0	28.0	28.0	28.0	30.7	30.8	95.5	87.2
T457_047	0	0.973	30.8	31.6	28.0	28.0	28.0	28.0	30.8	31.1	95.2	86.3
T457_048	0	0.973	30.7	31.4	27.9	27.9	27.9	27.9	30.7	31.0	95.2	86.2
T457_049	0	0.972	30.6	30.7	28.0	28.0	27.9	27.9	30.8	31.0	94.9	85.6
T457_050	0	0.972	30.3	30.4	27.9	27.9	27.9	27.9	30.7	30.7	94.8	85.2
T457_051	15	0.972	30.4	30.5	28.0	27.9	27.9	27.9	30.6	30.7	94.7	84.8
T457_052	30	0.971	30.4	30.3	27.9	27.9	27.9	27.9	30.5	30.7	94.5	83.9
T457_053	30	0.971	31.1	31.3	28.0	28.0	27.9	27.9	30.6	31.0	95.2	84.9
T457_054	30	0.969	31.0	31.2	28.0	28.0	27.9	27.9	30.7	31.0	94.7	83.8
T457_055	45	0.969	30.9	31.1	28.0	28.0	27.9	27.9	30.6	31.0	94.6	83.2
T457_056	61	0.968	30.8	31.1	28.0	28.0	27.9	27.9	30.5	30.9	94.6	83.0
T457_057	75	0.967	30.9	31.2	28.0	28.0	27.9	27.9	30.6	30.9	94.6	83.5
T457_058	75	0.966	31.2	31.8	28.3	28.3	27.9	27.9	30.5	30.8	94.6	83.4
T457_059	60	0.966	31.0	31.5	28.1	28.1	27.9	27.9	30.5	30.9	94.5	83.0
T457_060	60	0.965	30.8	31.2	27.9	27.9	27.9	27.9	30.5	30.9	94.5	83.1
T457_061	60	0.966	30.7	30.9	28.0	28.0	27.9	27.9	30.4	30.8	94.0	82.4
T457_062	45	0.966	30.7	30.9	27.9	27.9	27.9	27.9	30.5	30.8	94.2	82.4
T457_063_A	45	0.966	30.7	30.8	27.9	27.9	27.9	27.9	30.6	30.8	94.1	82.5
T457_063_B	45	0.966	30.7	30.8	27.9	27.9	27.9	27.9	30.5	30.7	94.1	82.4
T457_064_A	0	0.966	30.5	30.8	27.9	27.9	27.9	27.9	30.5	30.7	94.2	83.6
T457_064_B	0	0.966	30.5	30.8	27.9	27.9	27.9	27.9	30.5	30.7	94.2	83.7
T457_065_A	0	0.966	30.5	31.2	27.9	27.9	27.9	27.9	30.4	30.7	94.3	83.8
T457_065_B	0	0.966	30.4	31.1	27.9	27.9	27.9	27.9	30.3	30.6	94.3	83.9
T457_066	0	0.964	30.1	30.8	27.9	27.9	27.9	27.9	30.1	30.4	94.1	84.8
T457_067	0	0.962	29.9	31.0	27.9	27.9	27.9	27.9	30.1	30.3	94.3	84.8
T457_068	0	0.963	30.0	31.2	27.9	27.9	27.9	27.8	30.1	30.3	93.7	84.3
T457_069	0	0.962	30.0	31.1	27.9	27.9	27.8	27.8	30.1	30.3	93.6	84.0
T457_070	0	0.962	30.2	31.1	27.9	27.9	27.9	27.9	30.1	30.4	93.4	83.6
T457_071	0	0.971	29.9	30.6	27.9	27.9	27.9	27.9	30.0	30.2	93.7	84.1
T457_072	0	2.792	80.6	81.3	76.8	76.7	76.8	77.0	80.6	80.9	124.4	118.1

Table E-2 Thermocouple Results for 0.457 m Width Plate

Test ID	TC1	TC2	TC3	TC4	TC5	TC6	TC7	TC8	TC9	TC10	TC11	TC12	TC13	TC14	TC15	TC16	TC17	TC18	TC19
	°C																		
T457_001	62.8	60.4	59.1	58.6	58.6	59.2	57.1	57.2	58.1	57.8	56.9	55.5	60.9	59.0	58.4	57.2	94.3	94.2	93.8
T457_002	60.5	59.3	59.1	59.3	59.3	59.5	59.9	60.0	60.3	60.0	59.7	58.8	59.4	59.4	60.1	60.4	84.8	85.1	85.4
T457_003	61.0	59.8	59.0	59.1	58.9	59.0	59.6	59.9	60.4	60.3	60.0	59.1	59.2	59.0	60.1	60.3	85.9	85.8	85.7
T457_004	53.9	52.2	51.2	51.1	50.9	51.4	52.0	52.2	52.8	52.6	52.2	51.0	51.3	51.2	52.7	53.0	87.0	87.0	86.9
T457_005	53.7	52.1	51.5	52.5	52.7	52.9	53.0	53.1	53.7	53.4	52.7	51.7	52.8	53.1	53.3	54.2	86.9	86.8	86.8
T457_006	53.5	52.5	52.4	53.4	53.2	53.1	53.1	53.1	53.7	53.4	52.7	51.9	53.5	53.5	53.7	54.1	86.7	86.7	86.9
T457_007	53.7	53.3	52.7	53.5	53.2	53.3	53.4	53.4	53.9	53.4	52.8	52.3	53.7	53.5	54.1	53.9	86.5	86.5	86.7
T457_008	53.9	53.3	52.5	53.3	53.1	53.2	53.4	53.5	54.0	53.5	52.9	52.6	53.6	53.6	54.0	53.9	86.3	86.4	86.5
T457_009	53.6	52.5	51.7	52.7	52.5	52.7	52.8	52.8	53.2	52.7	52.3	52.2	53.3	53.5	53.4	53.4	85.6	85.6	85.8
T457_010	59.0	55.4	53.3	53.4	53.0	52.8	53.0	52.9	53.1	52.9	52.5	52.5	53.5	54.1	53.9	54.0	N/A	86.2	86.1
T457_011	50.9	51.3	50.8	51.9	51.6	52.0	52.2	52.4	52.7	52.5	52.2	52.3	52.8	52.6	53.2	53.3	41.7	85.8	85.9
T457_012	50.7	51.3	51.0	51.9	51.8	52.0	52.3	52.5	52.8	52.7	52.2	52.2	52.7	52.4	53.3	53.2	N/A	85.6	85.6
T457_013	50.6	51.2	51.1	52.0	51.9	52.1	52.3	52.4	52.8	52.6	52.2	51.8	52.5	52.1	53.2	53.0	N/A	85.5	85.6
T457_014	59.2	54.8	53.0	53.4	53.3	53.2	53.3	53.2	53.4	53.3	52.8	52.7	53.1	53.3	53.7	53.6	N/A	85.7	85.7
T457_015	52.5	52.2	51.8	52.7	52.6	52.6	52.8	52.7	52.9	52.9	52.4	52.2	52.8	52.6	53.2	53.1	48.5	85.6	85.5
T457_016	53.3	51.3	50.4	51.2	51.0	51.5	52.5	52.9	53.4	53.1	52.8	51.0	51.7	51.0	53.6	52.6	87.7	87.7	87.5
T457_017	53.0	51.4	50.8	52.3	52.6	53.0	53.6	53.5	54.0	53.5	53.3	51.3	53.0	53.3	54.0	54.3	87.4	87.4	87.3
T457_018	52.9	52.0	51.9	53.5	53.3	53.3	53.6	53.5	53.9	53.5	53.4	51.5	53.7	53.6	54.2	54.5	87.0	86.9	86.8
T457_019	53.1	52.9	52.3	53.5	53.3	53.3	53.7	53.8	54.2	53.6	53.4	52.1	53.7	53.5	54.4	54.2	86.7	86.7	86.6
T457_020	53.2	52.9	52.2	53.4	53.2	53.3	53.6	53.8	54.2	53.7	53.3	52.6	53.6	53.5	54.2	54.1	86.5	86.6	86.5
T457_021	53.6	52.7	51.9	53.1	53.0	53.1	53.5	53.5	53.9	53.5	52.9	52.6	53.7	53.8	53.9	54.3	86.4	86.5	86.4
T457_022	53.0	52.6	51.7	52.6	52.4	52.5	52.9	53.0	53.2	53.0	52.5	52.4	53.2	53.2	53.6	53.8	52.4	86.1	86.0
T457_023	53.0	52.6	52.0	53.1	52.8	52.9	53.3	53.5	53.9	53.3	53.0	52.2	53.3	53.1	53.8	53.7	66.3	86.1	85.9
T457_024	52.2	52.3	51.6	52.5	52.3	52.4	52.7	52.8	53.1	52.9	52.4	52.3	53.0	53.1	53.4	53.6	51.4	85.9	85.7
T457_025	52.8	52.1	51.5	52.8	52.8	52.8	53.0	53.0	53.3	53.0	52.5	52.0	52.9	52.7	53.4	53.4	51.8	85.6	85.4
T457_026	53.2	52.2	51.1	51.9	52.1	52.4	52.9	53.1	53.4	53.4	53.0	52.6	52.4	52.0	53.6	53.1	52.8	85.7	85.6

Table E-2 Thermocouple Results for 0.457 m Width Plate Continued

Test ID	TC1	TC2	TC3	TC4	TC5	TC6	TC7	TC8	TC9	TC10	TC11	TC12	TC13	TC14	TC15	TC16	TC17	TC18	TC19
	°C																		
T457_027	52.9	52.6	51.7	52.3	52.2	52.3	52.8	52.9	53.1	53.1	52.8	52.7	52.1	52.4	53.3	53.1	N/A	85.7	85.6
T457_028	52.4	50.7	49.9	50.8	50.8	51.3	52.1	52.3	52.7	52.4	52.1	50.3	51.4	50.7	52.8	52.4	85.9	86.2	86.1
T457_029	52.7	50.9	50.1	50.9	50.9	51.4	52.1	52.3	52.8	52.5	52.1	50.5	51.9	51.0	53.0	52.6	86.8	86.8	87.3
T457_030	52.6	50.9	50.3	51.8	52.1	52.5	52.9	52.8	53.2	52.8	52.6	50.9	52.7	52.9	53.4	54.0	86.7	86.6	87.1
T457_031	52.5	51.5	51.6	53.0	52.8	52.8	53.1	53.1	53.6	53.2	52.9	51.2	53.2	53.1	53.6	54.0	86.4	86.4	86.8
T457_032	52.6	52.3	51.8	53.0	52.7	52.8	53.0	53.1	53.6	53.1	52.8	51.6	53.2	53.0	53.7	53.7	86.0	86.0	86.5
T457_033	52.7	52.2	51.6	52.9	52.7	52.8	53.1	53.2	53.6	53.1	52.6	52.2	53.1	53.3	53.5	53.5	85.9	85.8	86.2
T457_034	53.1	52.4	51.5	52.7	52.5	52.6	52.9	52.9	53.3	52.9	52.4	52.3	53.0	53.3	53.5	53.4	85.7	85.7	86.1
T457_035	52.2	52.0	51.3	52.3	52.1	52.1	52.3	52.3	52.6	52.3	51.9	52.0	52.6	52.8	53.0	53.2	52.0	85.4	85.4
T457_036	52.3	51.7	51.0	52.1	52.2	52.3	52.6	52.7	52.9	52.9	52.5	52.2	52.4	52.2	53.0	52.8	52.9	85.1	85.2
T457_037	52.3	51.7	51.0	52.1	52.2	52.3	52.6	52.7	52.9	52.9	52.5	52.2	52.4	52.2	53.0	52.8	52.9	85.1	85.2
T457_038	52.3	51.7	50.9	52.0	52.2	52.3	52.7	52.8	53.0	53.0	52.7	52.4	52.4	52.2	52.9	53.0	52.8	85.2	85.3
T457_039	52.6	51.8	50.8	51.7	52.0	52.3	52.7	52.8	53.1	53.2	52.8	52.4	52.3	52.2	53.2	53.1	52.8	85.2	85.6
T457_040	52.5	51.9	50.9	51.5	51.7	51.9	52.4	52.5	52.8	52.8	52.5	52.2	51.8	51.9	52.9	53.0	52.9	85.3	85.6
T457_041	19.8	18.4	18.0	18.6	18.5	19.3	19.9	19.9	20.2	19.8	19.5	18.2	19.1	18.5	20.6	20.0	75.4	75.5	76.1
T457_042	22.5	22.0	21.5	21.8	21.7	22.0	22.2	22.2	22.3	22.3	22.0	22.0	21.8	21.9	22.7	22.4	N/A	73.7	73.8
T457_043	26.8	26.4	25.9	26.4	26.4	26.8	27.1	27.1	27.3	27.4	27.1	27.1	27.0	26.8	28.0	27.6	27.4	74.0	74.3
T457_044	37.4	35.0	34.1	34.7	34.5	34.9	35.8	36.3	37.2	37.2	36.6	34.8	35.2	34.9	37.4	36.5	86.9	86.9	86.7
T457_045	38.4	35.1	34.1	34.5	34.2	34.6	35.5	36.2	37.2	37.2	36.4	34.9	35.0	34.7	37.2	36.2	82.9	86.6	86.6
T457_046	39.9	35.3	34.1	34.5	34.2	34.6	35.7	36.4	37.3	37.2	36.3	35.4	34.6	34.8	37.0	37.1	70.0	86.4	86.4
T457_047	39.5	37.0	35.5	36.6	37.0	37.1	37.4	37.3	37.6	37.5	36.9	36.5	35.3	37.5	37.4	38.4	39.7	85.6	85.5
T457_048	39.0	36.8	35.4	36.5	36.9	37.1	37.4	37.2	37.5	37.5	36.9	36.4	34.9	37.4	37.4	38.3	39.0	85.4	85.4
T457_049	33.8	34.3	33.8	35.0	35.4	36.0	36.6	36.8	37.2	37.4	37.0	36.9	36.4	36.2	38.0	37.7	N/A	84.8	84.7
T457_050	33.3	33.6	33.4	34.4	34.5	35.2	35.8	36.1	36.5	36.7	36.4	36.5	35.9	34.7	37.6	36.2	34.5	84.4	84.2
T457_051	33.2	33.7	33.3	34.4	34.6	35.3	35.8	36.2	36.4	36.6	36.3	36.5	36.5	34.9	37.5	36.2	34.3	84.2	84.0
T457_052	32.8	33.3	33.0	34.2	34.4	35.0	35.4	35.8	35.9	36.1	35.9	36.1	36.4	34.7	37.2	35.9	34.1	83.8	83.3

Table E-2 Thermocouple Results for 0.457 m Width Plate Continued																			
Test ID	TC1	TC2	TC3	TC4	TC5	TC6	TC7	TC8	TC9	TC10	TC11	TC12	TC13	TC14	TC15	TC16	TC17	TC18	TC19
	°C	°C	°C																
T457_053	36.3	35.1	35.2	37.2	36.9	37.0	37.0	36.7	37.2	36.8	36.5	35.0	37.3	37.7	38.0	38.1	84.9	84.9	84.9
T457_054	37.6	35.9	35.2	36.9	37.1	37.3	37.3	37.1	37.3	37.2	36.8	36.3	36.7	37.1	37.6	38.0	37.8	83.7	83.5
T457_055	37.2	35.7	35.3	36.8	37.0	37.1	37.2	37.0	37.4	37.3	36.7	36.1	36.7	36.7	37.5	37.4	37.6	83.3	83.1
T457_056	36.9	35.8	35.2	36.6	36.5	36.5	36.6	36.6	37.0	36.7	36.1	35.6	36.7	36.3	37.2	37.0	37.4	83.2	83.0
T457_057	36.9	35.7	35.0	36.3	36.1	36.4	36.5	36.3	36.7	36.5	35.7	35.9	36.9	37.5	37.0	37.3	82.8	83.5	83.4
T457_058	40.0	37.0	36.0	36.8	36.5	36.5	36.3	36.2	36.5	36.2	35.5	35.6	37.1	37.4	37.1	37.3	47.9	83.4	83.2
T457_059	36.7	35.8	35.3	36.4	36.2	36.4	36.4	36.5	36.9	36.5	35.9	35.4	36.7	37.3	37.2	37.6	48.9	83.2	83.1
T457_060	36.3	35.6	34.9	36.1	35.9	36.2	36.4	36.6	36.9	36.4	35.9	35.4	36.8	36.7	37.3	37.0	83.1	83.4	83.3
T457_061	36.6	35.5	34.9	36.1	36.1	36.2	36.3	36.2	36.5	36.3	35.7	35.2	36.2	36.0	36.8	36.7	37.4	82.6	82.4
T457_062	37.1	35.3	34.9	36.3	36.4	36.5	36.7	36.5	36.9	36.9	36.3	35.6	36.2	36.3	37.0	37.0	38.4	82.6	82.4
T457_063_A	35.9	35.2	34.5	35.7	35.9	36.2	36.5	36.5	36.7	36.8	36.2	36.0	36.4	35.8	37.3	36.6	37.6	82.5	82.3
T457_063_B	35.9	35.2	34.5	35.7	35.8	36.1	36.4	36.3	36.6	36.6	36.1	35.9	36.3	35.7	37.2	36.5	37.5	82.5	82.2
T457_064_A	35.8	35.4	34.4	35.1	35.2	35.6	36.0	36.0	36.3	36.4	36.0	35.9	35.7	35.6	37.0	36.6	37.3	82.9	82.8
T457_064_B	35.6	35.2	34.3	35.0	35.2	35.6	36.0	36.1	36.4	36.4	36.1	35.9	35.7	35.6	37.0	36.6	36.9	83.0	83.1
T457_065_A	38.4	36.0	34.6	35.6	35.8	36.0	36.2	36.1	36.3	36.2	35.6	35.3	36.0	36.1	36.9	36.7	39.9	83.2	83.3
T457_065_B	38.5	36.1	34.6	35.5	35.7	36.0	36.3	36.2	36.5	36.4	35.8	35.4	34.6	36.0	36.0	36.8	40.4	83.2	83.4
T457_066	35.6	33.7	33.0	33.8	33.8	34.6	35.2	35.3	35.8	35.4	34.9	33.3	34.8	33.8	36.1	35.4	83.8	83.8	84.0
T457_067	35.7	33.7	32.9	33.3	33.0	33.5	34.2	34.6	35.4	35.3	34.8	33.2	33.8	33.8	35.7	35.2	79.0	83.8	84.3
T457_068	39.1	34.1	33.0	33.4	33.3	33.9	34.8	35.1	35.6	35.4	34.7	34.1	33.7	34.1	35.4	35.6	61.3	83.4	83.8
T457_069	36.7	33.7	32.9	33.3	33.3	33.8	34.5	34.6	35.3	35.1	34.6	33.6	33.5	35.5	35.1	36.2	52.1	83.0	83.4
T457_070	39.7	35.5	34.1	34.8	35.0	35.2	35.5	35.4	35.7	35.6	35.0	34.6	33.7	35.6	35.4	36.3	44.6	82.7	83.1
T457_071	35.2	33.3	32.6	33.1	33.0	33.7	34.5	34.8	35.3	34.9	34.4	32.8	33.7	33.1	35.5	34.7	83.1	83.2	83.6
T457_072	87.8	85.8	84.9	87.0	87.6	87.9	88.6	88.5	88.9	88.5	88.0	87.9	88.1	87.4	89.1	88.6	117.6	117.6	117.5

Table E-3 Mass Flow Rate Results for 0.457 m Width Plate

Test ID	CFM1	CFM2	CFM3	Δ DP1	Δ DP2	DP1 Δ t	DP2 Δ t	\dot{m}_g	\dot{m}_t
	kg/hr	kg/hr	kg/hr	Pa	Pa	s	s	kg/s	kg/s
T457_001	1361	1373	0	1511	1567	200	65	0.00510	0.00148
T457_002	1353	1358	0	1849	1508	613	214	0.00203	0.00043
T457_003	1350	1359	0	1889	1192	624	124	0.00204	0.00059
T457_004	1357	1379	0	1821	1422	441	73	0.00279	0.00119
T457_005	1356	1380	0	1879	1336	400	75	0.00317	0.00109
T457_006	1356	1378	0	1744	1400	352	85	0.00334	0.00101
T457_007	1357	1380	0	1815	1413	351	112	0.00349	0.00077
T457_008	1357	1379	0	1855	1309	351	117	0.00356	0.00069
T457_009	1356	1379	0	1769	1285	356	192	0.00335	0.00041
T457_010	1356	1380	66.47	1848	1423	379	49	0.00329	0.00178
T457_011	1357	1378	56.10	1720	1411	342	78	0.00339	0.00111
T457_012	1357	1379	54.42	1829	1453	372	88	0.00332	0.00101
T457_013	1358	1379	57.96	1733	1488	371	90	0.00315	0.00101
T457_014	1357	1379	60.56	1838	1347	389	84	0.00319	0.00098
T457_015	1356	1378	57.85	1694	1521	356	102	0.00321	0.00091
T457_016	1389	1320	0	1801	1045	399	399	0.00304	0.00016
T457_017	1391	1321	0	1763	1100	362	454	0.00329	0.00015
T457_018	1391	1321	0	1649	652	319	319	0.00349	0.00013
T457_019	1390	1320	0	1683	1116	317	643	0.00358	0.00011
T457_020	1390	1320	0	1649	1211	309	738	0.00360	0.00010
T457_021	1390	1321	0	1639	1178	310	728	0.00357	0.00010
T457_022	1390	1321	44.40	1312	329	255	255	0.00347	0.00008
T457_023	1390	1321	11.40	1633	370	323	323	0.00341	0.00007
T457_024	1390	1321	54.07	1394	279	287	287	0.00328	0.00006
T457_025	1389	1321	51.25	1331	260	276	276	0.00325	0.00006
T457_026	1390	1321	79.86	1289	915	273	1103	0.00318	0.00005
T457_027	1390	1322	201.91	857	490	186	647	0.00311	0.00005
T457_028	1390	1321	0	1276	558	319	769	0.00270	0.00004
T457_029	1383	1377	0	1576	1242	375	272	0.00284	0.00028
T457_030	1383	1378	0	1620	1448	351	351	0.00311	0.00025
T457_031	1383	1378	0	1682	1299	344	344	0.00330	0.00023
T457_032	1382	1378	0	1547	1092	314	314	0.00332	0.00021
T457_033	1383	1378	0	1674	922	337	492	0.00335	0.00011
T457_034	1383	1379	0	1673	748	337	368	0.00335	0.00012
T457_035	1382	1379	54.66	1260	1265	267	267	0.00318	0.00029
T457_036	1382	1378	102.15	1342	1569	300	452	0.00302	0.00021
T457_037	1382	1378	102.15	1342	1569	300	452	0.00302	0.00021
T457_038	1382	1379	102.71	1341	1640	291	453	0.00311	0.00022

Table E-3 Mass Flow Rate Results for 0.457 m Width Plate Continued

Test ID	CFM1	CFM2	CFM3	Δ DP1	Δ DP2	DP1 Δ t	DP2 Δ t	\dot{m}_g	\dot{m}_t
	kg/hr	kg/hr	kg/hr	Pa	Pa	s	s	kg/s	kg/s
T457_039	1383	1380	102.35	1663	1595	354	458	0.00317	0.00021
T457_040	1382	1379	102.18	1436	1244	335	335	0.00289	0.00023
T457_041	1371	1344	0	1720	935	704	261	0.00165	0.00022
T457_042	1366	1343	233.13	611	815	230	157	0.00179	0.00032
T457_043	1378	1355	104.28	1388	941	570	196	0.00164	0.00029
T457_044	1391	1403	0	1646	1151	347	171	0.00320	0.00041
T457_045	1391	1403	4.26	940	1568	210	210	0.00302	0.00046
T457_046	1391	1403	8.60	1012	1554	230	230	0.00297	0.00041
T457_047	1391	1403	40.18	1056	1500	206	206	0.00346	0.00045
T457_048	1390	1403	42.29	774	1503	151	217	0.00346	0.00042
T457_049	1392	1403	120.49	1128	1539	217	222	0.00351	0.00042
T457_050	1392	1404	237.74	1127	1510	221	183	0.00344	0.00051
T457_051	1392	1403	242.31	887	1536	164	232	0.00365	0.00041
T457_052	1392	1403	249.04	778	1561	144	290	0.00364	0.00033
T457_053	1390	1405	0	1261	1367	237	287	0.00359	0.00029
T457_054	1389	1406	56.03	687	1402	132	286	0.00351	0.00030
T457_055	1389	1406	57.04	631	1402	123	315	0.00346	0.00027
T457_056	1389	1407	58.34	900	1527	174	360	0.00349	0.00026
T457_057	1390	1407	0	1047	1008	199	360	0.00355	0.00017
T457_058	1389	1407	24.71	1208	1571	231	439	0.00353	0.00022
T457_059	1389	1407	22.67	1160	1568	228	327	0.00343	0.00029
T457_060	1389	1402	0	1031	1229	199	309	0.00350	0.00024
T457_061	1389	1402	58.61	786	1652	160	426	0.00331	0.00024
T457_062	1389	1401	53.71	1084	1451	218	349	0.00335	0.00025
T457_063_A	1390	1400	124.70	962	1266	187	288	0.00347	0.00027
T457_063_B	1391	1401	123.05	1443	1446	292	332	0.00333	0.00027
T457_064_A	1390	1400	122.39	1064	1493	225	362	0.00319	0.00025
T457_064_B	1390	1400	120.92	1286	1654	277	368	0.00313	0.00028
T457_065_A	1390	1401	51.84	848	1360	183	235	0.00313	0.00035
T457_065_B	1391	1401	50.20	1473	1360	324	235	0.00307	0.00035
T457_066	1389	1403	0	1124	1189	281	190	0.00270	0.00038
T457_067	1389	1405	4.73	1136	1305	302	203	0.00254	0.00039
T457_068	1388	1405	11.81	1137	1302	295	174	0.00260	0.00046
T457_069	1389	1405	18.27	1714	1565	441	250	0.00262	0.00038
T457_070	1389	1406	29.64	1181	1130	291	183	0.00274	0.00038
T457_071	1389	1406	0	1134	950	312	173	0.00245	0.00034
T457_072	1379	1351	0	1333	1559	185	185	0.00486	0.00052

Table E-4 Heat Transfer Coefficient Results for 0.457 m Width Plate

Test ID	Calorimetric Measurements				Condensate Mass Based Measurements			
	q''	h	u _h		q''	h	u _h	
	W/m ²	W/m ² -K	W/m ² -K	%	W/m ²	W/m ² -K	W/m ² -K	%
T457_001	12924	372	26	7%	12477	359	7	2.1%
T457_002	5168	202	34	17%	5025	196	5	2.7%
T457_003	5155	198	34	17%	5039	194	5	2.7%
T457_004	6765	194	25	13%	6942	199	4	2.1%
T457_005	7689	228	26	12%	7887	233	5	2.2%
T457_006	8146	246	27	11%	8318	252	6	2.2%
T457_007	8703	268	27	10%	8682	267	6	2.3%
T457_008	8708	271	28	10%	8872	276	6	2.3%
T457_009	8234	254	28	11%	8359	258	6	2.3%
T457_010	N/A	N/A	N/A	N/A	8179	257	6	2.3%
T457_011	9048	273	27	10%	8460	255	6	2.2%
T457_012	N/A	N/A	N/A	N/A	8277	252	6	2.3%
T457_013	N/A	N/A	N/A	N/A	7861	238	5	2.2%
T457_014	N/A	N/A	N/A	N/A	7930	254	6	2.3%
T457_015	8584	264	27	10%	8002	246	6	2.3%
T457_016	7804	221	25	11%	7580	215	5	2.1%
T457_017	8577	251	26	10%	8174	239	5	2.2%
T457_018	9029	272	27	10%	8677	262	6	2.2%
T457_019	9238	284	27	10%	8911	274	6	2.3%
T457_020	9252	285	27	10%	8956	276	6	2.3%
T457_021	9050	276	27	10%	8877	271	6	2.3%
T457_022	8721	266	27	10%	8644	264	6	2.3%
T457_023	8402	260	27	11%	8493	263	6	2.3%
T457_024	8776	268	27	10%	8162	249	6	2.3%
T457_025	8776	273	28	10%	8109	252	6	2.3%
T457_026	8515	260	27	10%	7930	242	6	2.3%
T457_027	N/A	N/A	N/A	N/A	7741	236	6	2.4%
T457_028	7513	218	26	12%	6732	195	4	2.2%
T457_029	7163	203	25	12%	7070	201	4	2.1%
T457_030	7867	227	26	11%	7753	224	5	2.2%
T457_031	8349	248	27	11%	8213	244	5	2.2%
T457_032	8462	257	27	11%	8281	252	6	2.3%
T457_033	8701	267	28	10%	8351	256	6	2.3%
T457_034	8463	258	27	11%	8347	255	6	2.3%
T457_035	7713	235	27	12%	7941	242	6	2.3%
T457_036	7707	238	28	12%	7524	232	5	2.3%
T457_037	7707	238	28	12%	7524	232	5	2.3%
T457_038	7775	240	28	12%	7751	239	5	2.3%

Table E-4 Heat Transfer Coefficient Results for 0.457 m Width Plate Continued

Test ID	Calorimetric Measurements				Condensate Mass Based Measurements			
	q''	h	u _h		q''	h	u _h	
	W/m ²	W/m ² -K	W/m ² -K	%	W/m ²	W/m ² -K	W/m ² -K	%
T457_039	7849	240	27	11%	7899	242	5	2.3%
T457_040	7480	227	27	12%	7211	219	5	2.3%
T457_041	4847	85	15	18%	4411	78	2	2.2%
T457_042	N/A	N/A	N/A	N/A	4776	92	2	2.5%
T457_043	4630	97	18	19%	4345	91	2	2.3%
T457_044	8363	163	18	11%	8155	159	3	1.7%
T457_045	7364	144	18	12%	7702	151	3	1.9%
T457_046	7169	142	18	13%	7567	149	3	1.8%
T457_047	8773	181	19	10%	8807	182	3	1.9%
T457_048	8834	183	19	10%	8813	182	4	2.0%
T457_049	N/A	N/A	N/A	N/A	8951	183	3	1.9%
T457_050	9134	186	18	10%	8792	179	3	1.9%
T457_051	9660	198	19	9%	9320	191	4	1.9%
T457_052	9486	197	19	10%	9329	193	4	2.0%
T457_053	9431	198	19	10%	9172	192	4	1.9%
T457_054	9243	200	20	10%	8971	194	4	2.1%
T457_055	9127	200	20	10%	8852	194	4	2.2%
T457_056	8908	194	20	10%	8939	195	4	2.0%
T457_057	9315	200	19	10%	9092	196	4	2.0%
T457_058	8245	179	20	11%	9031	196	4	2.0%
T457_059	8040	175	20	11%	8796	191	4	2.0%
T457_060	9166	198	19	10%	8965	194	4	2.0%
T457_061	8472	185	20	11%	8496	186	4	2.1%
T457_062	8520	188	20	11%	8597	189	4	2.0%
T457_063_A	8166	179	20	11%	8893	195	4	2.0%
T457_063_B	8126	178	20	11%	8547	187	4	1.9%
T457_064_A	7861	166	19	11%	8167	173	3	1.9%
T457_064_B	8018	169	19	11%	8016	169	3	1.9%
T457_065_A	7673	163	19	12%	7999	170	3	2.0%
T457_065_B	7429	158	19	12%	7850	167	3	1.9%
T457_066	7148	144	18	13%	6916	139	3	1.9%
T457_067	6151	123	18	15%	6509	130	2	1.9%
T457_068	5718	117	18	16%	6670	136	3	1.9%
T457_069	5934	121	18	15%	6730	137	3	1.8%
T457_070	6466	136	19	14%	7018	148	3	1.9%
T457_071	6599	133	18	14%	6304	127	2	1.9%
T457_072	11953	406	31	8%	11636	395	10	2.5%

E.2 Tabulated Results for 0.914 m Width Plate

Table E-5 provides the measured temperatures, absolute pressure and plate inclination results for the 0.914 m plate width consistent with the instrumentation defined in Table 5-2. An example of the graphical results for these experiments is given in Section 7.1. The graphical results show the entire data collection period after the system had stabilized. In most cases the gutter and trough collection tanks were drained and refilled several times to assure the condensation rates had stabilized. The values shown in Table E-5 represent the average measurement over the last fill cycle of the gutter collection container.

Table E-6 provides the measured mass flow rates from the Coriolis flow meters, as described in Table 5-2, and the gutter and trough collection tank mass flow rates, \dot{m}_g and \dot{m}_t . The Coriolis flow meter results represent the average measurement over the last fill cycle of the gutter collection container. The collection tank mass flow rates are calculated from the differential pressure transducer, DP1 and DP2, readings as described in Appendix B.1. The gutter collection tank mass flow rate is based on the difference in the DP1 measurement from the start to the end of the last gutter fill cycle, $\Delta DP1$, and the time period of the last gutter fill cycle, $DP1 \Delta t$. The trough collection tank mass flow rate is based on the difference in the DP2 measurement from the start to the end of the last trough fill cycle, $\Delta DP2$, and the time period of the last trough fill cycle, $DP2 \Delta t$.

Table E-7 gives the measured heat transfer coefficient results and measurement uncertainties for the coolant channel calorimetric and condensate mass based measurement methods. The analysis methodology is presented in Appendix B.

Table E-5 Inclination, Pressure and Temperature Results for 0.914 m Width Plate

Test ID	Inc	P1	RTD1	RTD2	RTD3	RTD5	RTD7	RTD12	TC6	TC13	TC14	TC16
	°	bar	°C	°C	°C	°C	°C	°C	°C	°C	°C	°C
T914_001	82	1.606	88.3	52.7	54.3	54.6	52.7	75.5	57.2	76.2	76.2	88.4
T914_002	80	1.604	88.2	52.7	54.4	54.6	52.7	75.5	57.2	76.2	76.1	88.3
T914_003	78	1.603	88.1	52.7	54.3	54.6	52.6	75.4	57.3	76.1	76.0	88.2
T914_004	78	2.371	117.1	54.9	61.5	62.1	54.9	101.5	69.6	102.4	102.3	117.1
T914_005	78	2.366	117.2	54.9	61.4	62.0	54.9	101.4	69.4	102.3	102.2	117.3
T914_006	75	1.601	88.0	52.7	54.3	54.6	52.7	75.3	57.3	76.0	76.0	88.1
T914_007	75	2.372	117.3	54.9	61.5	62.2	54.8	101.5	69.7	102.5	102.4	117.2
T914_008	57	1.587	82.5	63.6	64.2	64.6	63.1	75.2	66.1	75.9	76.0	82.6
T914_009	57	2.369	117.3	55.2	62.2	63.0	55.1	101.7	70.0	102.3	102.2	117.2
T914_010	50	1.592	87.2	53.8	55.3	55.6	53.7	75.4	58.1	75.7	75.6	87.2
T914_011	37	1.592	87.5	53.8	55.3	55.6	53.7	75.4	58.1	75.7	75.6	87.6
T914_012	37	2.356	117.4	55.3	63.0	63.2	55.2	101.5	69.7	102.1	101.9	117.4
T914_013	15	1.594	87.7	53.8	55.3	55.6	53.7	75.8	57.9	75.9	75.8	87.8
T914_014	15	2.355	117.3	55.4	63.1	63.5	55.3	101.7	69.4	102.1	102.0	117.4
T914_015	0	2.300	117.2	56.5	63.6	65.0	55.6	101.9	69.6	102.2	102.0	117.3
T914_016	0	1.609	87.7	53.7	55.3	55.5	53.7	75.3	57.8	75.7	75.7	87.8
T914_017	0	2.317	118.3	56.9	63.8	65.7	55.4	101.8	69.4	102.1	102.2	118.7
T914_018	0	1.596	87.8	53.8	55.3	55.6	53.7	75.8	58.0	76.0	75.9	87.9
T914_019	0	1.583	82.4	63.6	64.1	64.5	63.1	75.4	66.0	75.9	75.9	82.5
T914_020	0	2.357	117.3	55.6	62.9	64.0	55.3	101.8	69.0	102.2	102.1	117.3

Table E-6 Mass Flow Rate Results for 0.914 m Width Plate

Test ID	CFM1	CFM2	CFM3	Δ DP1	Δ DP2	DP1 Δ t	DP2 Δ t	\dot{m}_g	\dot{m}_t
	kg/hr	kg/hr	kg/hr	Pa	Pa	s	s	kg/s	kg/s
T914_001	1009	998	0	421	1408	1722	1722	0.00111	0.00055
T914_002	1009	998	0	388	1092	1512	1512	0.00117	0.00049
T914_003	1010	1000	0	574	1216	2096	2096	0.00124	0.00039
T914_004	950	948	0	1215	1554	987	987	0.00559	0.00106
T914_005	948	949	0	1592	1970	1299	1299	0.00557	0.00102
T914_006	1009	999	0	784	729	2538	2538	0.00140	0.00019
T914_007	950	948	0	1178	1677	957	957	0.00559	0.00118
T914_008	948	946	0	722	221	4425	4425	0.00074	0.00003
T914_009	950	948	0	839	1681	673	673	0.00566	0.00168
T914_010	1006	996	0	537	789	1899	1899	0.00128	0.00028
T914_011	1006	997	0	722	1131	2559	2559	0.00128	0.00030
T914_012	949	948	0	663	1773	565	565	0.00533	0.00212
T914_013	996	995	0	764	1532	2946	2946	0.00118	0.00035
T914_014	937	944	0	552	1736	480	480	0.00522	0.00244
T914_015	912	935	0	395	1907	399	399	0.00449	0.00322
T914_016	981	995	0	550	1918	2523	2523	0.00099	0.00051
T914_017	919	934	0	371	2129	395	395	0.00426	0.00364
T914_018	986	993	0	579	1152	2457	2457	0.00107	0.00032
T914_019	925	920	0	139	99	1098	1098	0.00057	0.00006
T914_020	922	942	0	390	1726	399	399	0.00444	0.00292

Table E-7 Heat Transfer Coefficient Results for 0.914 m Width Plate								
Test ID	Calorimetric Measurements				Condensate Mass Based Measurements			
	q''	h	u _h		q''	h	u _h	
	W/m ²	W/m ² -K	W/m ² -K	%	W/m ²	W/m ² -K	W/m ² -K	%
T914_001	1409	78	18	23%	1437	79	4	4.5%
T914_002	1524	84	18	21%	1508	83	4	4.6%
T914_003	1634	91	18	20%	1610	90	4	4.4%
T914_004	6553	209	11	5%	6966	222	6	2.6%
T914_005	6514	208	11	5%	6937	221	6	2.5%
T914_006	1880	105	18	17%	1815	102	4	4.3%
T914_007	6486	208	11	5%	6965	223	6	2.6%
T914_008	1058	117	35	30%	940	104	8	7.5%
T914_009	6499	209	11	5%	7045	227	6	2.7%
T914_010	1682	98	19	19%	1658	97	4	4.5%
T914_011	1659	97	19	20%	1655	97	4	4.4%
T914_012	6375	204	11	5%	6637	212	6	2.7%
T914_013	1573	89	18	21%	1521	86	4	4.3%
T914_014	6065	192	10	5%	6502	205	6	2.8%
T914_015	5275	166	10	6%	5586	175	5	3.1%
T914_016	1311	76	18	24%	1281	74	3	4.5%
T914_017	5105	160	10	6%	5306	166	5	3.2%
T914_018	1553	88	18	21%	1383	78	3	4.4%
T914_019	912	98	32	33%	728	78	7	9.0%
T914_020	5357	166	10	6%	5532	171	5	3.1%

Appendix F Condensation Conductivity Derivation

The condensing heat transfer component is governed by diffusion through the non-condensable gas layer. Fick's law of diffusion for binary mixtures with a non-zero net flux is:

$$J_g = -cD \frac{\partial x_g}{\partial y} + Jx_g \quad \text{Equation F-1}$$

Where

J is the total flux of vapor and non-condensable ($\text{mol} / \text{m}^2 \cdot \text{s}$)

J_g is the total flux of non-condensable gas ($\text{mol} / \text{m}^2 \cdot \text{s}$)

D is the diffusion coefficient (m^2/s)

c is the total molar concentration of solute (mol/m^3)

x_g is the non-condensable gas mole fraction

Considering a developed non-condensable gas layer, the diffusion flux of non-condensable gas is zero and the total flux reduces to the vapor flux, J_v . Equation F-1 can be reduced to:

$$J_v x_g = cD \frac{\partial x_g}{\partial y} \quad \text{Equation F-2}$$

Rewriting Equation F-2 in terms of species mole fractions, total concentration and velocity yields:

$$cv_v x_g = cD \frac{\partial x_g}{\partial y} \quad \text{Equation F-3}$$

, where v_v is the average vapor molar velocity away from the interface. Solving for the vapor velocity yields:

$$v_v = \frac{D}{x_g} \frac{\partial x_g}{\partial y} = D \frac{\partial}{\partial y} \ln(x_g) \quad \text{Equation F-4}$$

Assuming the vapor velocity and $\ln(x_g)$ vary linearly through the diffusion layer, Equation F-4 can be integrated over the diffusion boundary layer thickness, δ

$$v_{vi} = \frac{D}{\delta} [\ln(x_{gb}) - \ln(x_{gi})] \quad \text{Equation F-5}$$

Defining a log mean mole fraction, x_{avg} , the condensate velocity can be rewritten in the form of Equation F-7.

$$x_{avg} = \frac{x_b - x_i}{\ln(x_b/x_i)} \quad \text{Equation F-6}$$

$$v_{vi} = \frac{D}{\delta x_{g,avg}} (x_{gb} - x_{gi}) \quad \text{Equation F-7}$$

For the two component mixture the non-condensable mole fractions can be replaced with vapor mole fractions.

$$v_{vi} = \frac{D}{\delta x_{g,avg}} (x_{vi} - x_{vb}) \quad \text{Equation F-8}$$

Assuming ideal gas behavior, Dalton's law of partial pressure can be used to form the condensate velocity in terms of vapor partial pressures at the bulk and interface.

$$v_{vi} = \frac{D}{P_t \delta x_{g,avg}} (P_{vi} - P_{vb}) \quad \text{Equation F-9}$$

In order to convert the pressure difference to temperature difference the Clapeyron equation is used.

$$\frac{dP}{dT} = \frac{i_{fg}}{T v_{fg}} \quad \text{Equation F-10}$$

Anderson (1998) integrated the Clapeyron equation over the boundary layer assuming the steam volume can be described by the ideal gas law and the liquid volume remains constant. The analysis also assumes constant latent heat and that the quantity $(v_f P_v / R_v)$ is small compared to the temperature. This is slightly different than the assumptions used to develop the Clausius-Clapeyron equation in the fact that the result of the integration remains in the form of differential temperature, which is ideal for typical heat transfer analyses. This integration results in a relationship between differential temperature and pressure as shown in Equation F-11.

$$P_{vi} - P_{vb} = \frac{h_{fg} M_v x_{v,avg} P_t}{T_b T_i R} (T_i - T_b) \quad \text{Equation F-11}$$

Substituting into Equation F-11 into Equation F-9 yields the relationship for v_{vi} :

$$v_{vi} = \frac{D h_{fg} M_v x_{v,avg}}{R T_b T_i x_{g,avg} \delta} (T_i - T_b) = \frac{D h_{fg} M_v}{\phi R T_b T_i \delta} (T_i - T_b) \quad \text{Equation F-12}$$

, where ϕ is given by

$$\phi = \frac{x_{g,avg}}{x_{v,avg}} = - \frac{\ln[(1 - x_{gb}) / (1 - x_{gi})]}{\ln[x_{gb} / x_{gi}]} \quad \text{Equation F-13}$$

The latent heat transfer rate at the interface q_l'' can be described in terms of the condensate velocity v_{vi} as follows:

$$q_l'' = -h_{fg} c M_v v_{vi} = -h_{fg} \frac{P_t}{R T_i} M_v v_{vi} \quad \text{Equation F-14}$$

To be consistent with Equation F-3, the total concentration, c , should be used in Equation F-14 since v_{vi} has been defined as the average molar velocity.

Substituting the relationship for v_{vi} from Equation F-12 into Equation F-14 results in a relationship between the condensing heat flux and temperature difference across the boundary layer:

$$q_1'' = \frac{P_t D h_{fg}^2}{\phi R_v^2 T_b T_i^2 \delta} (T_b - T_i) \quad \text{Equation F-15}$$

$$\delta = \frac{P_t D h_{fg}^2}{\phi R_v^2 T_b T_i^2 q_1''} (T_b - T_i) \quad \text{Equation F-16}$$

The Sherwood number can now be approximated as the ratio of the thermal to mass diffusion length scales:

$$\text{Sh} = \frac{h_1 L}{k_c} = \frac{L}{\delta} = \frac{q_1''}{(T_b - T_i)} L \phi \frac{R_v^2 T_b T_i^2}{P_t D h_{fg}^2} \quad \text{Equation F-17}$$

$$h = \frac{D}{\delta} = \frac{q_1''}{(T_b - T_i)} D \phi \frac{R_v^2 T_b T_i^2}{P_t D h_{fg}^2} \quad \text{Equation F-18}$$

From the relationship in Equation F-17 it can be easily shown that the effective condensation mass transfer thermal conductivity can be determined using Equation F-19.

$$k_c = \frac{1}{\phi T_b T_i^2} \left(\frac{P_t D h_{fg}^2}{R_v^2} \right) \quad \text{Equation F-19}$$

Equation F-19 is consistent with the formulation reported by Anderson (1998a). This formulation is similar to that proposed by Peterson et al. (1993).

Appendix G Average Film Thickness and Wave Velocity Calculation

In an effort to demonstrate the importance of surface waves on heat transfer enhancement, it is useful to compare the observed wave velocity to the wave-less film interface velocity. The wave velocity is calculated from an analysis of the video recordings acquired during testing and the corresponding wave free interface velocity is calculated using the Nusselt laminar film theory. The analysis method implemented to calculate the average liquid film thickness for conditions in which water is applied at the top of the test plate is also given as part of the Nusselt laminar film theory analysis.

Figure G-1 shows two images acquired during test T457_048. The video frame rate was set at 60 frames per second and the time lapse between the image on the left of Figure G-1 and the right is 0.5 s. Over the course of 30 frames, wave features were manually tracked using the light reflected from each wave, or series of waves. The tracked wave features are highlighted with red markers in the images.



Figure G-1 Wave Feature Tracking to Determine Average Wave Velocity for Test T457_048

Light reflected from the wave features is from a point source, and there is some uncertainty in the wave feature tracking method due to the angle at which light is reflected. However, the length scale of the reflections and wave features is small such that the uncertainty is bounded by one wavelength. Since the features were tracked for more than 10 wavelengths, the effect would result in less than $\pm 10\%$ error. Finally, the camera was centered and located perpendicular to the test surface. Spherical aberrations in the camera lenses and uncertainty in the camera positioning were not accounted for as part of this analysis. The uncertainty due to these effects can be conservatively approximated as $\pm 10\%$ using judgment.

Table G-1 shows the results of the feature tracking method used to determine the wave velocity during test T457_048. A total of 10 wave features were tracked over a 0.5 s time interval. Based on this analysis, the average wave velocity is 0.48 m/s, with a standard deviation of 0.06 m/s.

Table G-1 Wave Velocity Results for T457_048			
Tracking Point ID	dx	dt	Wave Velocity (dx/dt)
	m	s	m/s
1	0.22	0.5	0.44
2	0.26	0.5	0.51
3	0.24	0.5	0.48
4	0.27	0.5	0.54
5	0.26	0.5	0.52
6	0.25	0.5	0.51
7	0.24	0.5	0.47
8	0.20	0.5	0.40
9	0.19	0.5	0.38
10	0.29	0.5	0.58
Average			0.48
Standard Deviation			0.06

Considering a surface with condensation as the only source of film flow, Equation 3-2 gives the film heat transfer coefficient and film thickness integrated over the plate surface. However, for the T457_048 test condition, film is applied at the top of the test plate and Equation 3-2 is not applicable since it assumes that the condensate mass flow rate at the top of the plate is zero. Instead, the film thickness is calculated locally at 11 points along the plate surface and averaged to determine the film thickness assuming a

laminar, wave-less flow. The points are defined with a reference of $x = 0$ at the top of the plate. Since the applied liquid film mass flow rate, \dot{m}_{ap} , and the mass flow rate of condensate exiting the plate are directly measured for each experiment, the mass flow rate per unit width, Γ , can be directly calculated assuming uniform condensation rate on the test surface. The cumulative mass flow rate of condensate at each station, \dot{m}_{cond} , is calculated by dividing the condensate mass flow rate as measured at the gutter collection tank, \dot{m}_g , in equal increments along the plate length.

For experiment T457_048, the applied film mass flow rate is 42.3 kg/s, the condensate mass flow rate at the bottom of the plate is 12.5 kg/s and the plate width is 0.457 m. Assuming uniform condensation rate on the plate surface, the mass flow rate per unit width and film Reynolds number ($Re_\Gamma = \Gamma/\mu_f$) are calculated at 11 elevations along the plate surface as shown in Table G-2.

Table G-2 Nusselt Laminar Film Calculation Results for T457_048								
Station	x	\dot{m}_{ap}	\dot{m}_{cond}	\dot{m}_{tot}	Γ	Re_Γ	δ_{loc}	u
	m	kg/hr	kg/hr	kg/hr	kg/m-hr		μm	m/s
1	0.19	42.3	1.1	43.4	95.0	39.4	176	0.23
2	0.39	42.3	2.3	44.6	97.5	40.4	178	0.23
3	0.58	42.3	3.4	45.7	100.0	41.5	179	0.23
4	0.77	42.3	4.5	46.8	102.5	42.5	181	0.24
5	0.97	42.3	5.7	48.0	104.9	43.5	182	0.24
6	1.16	42.3	6.8	49.1	107.4	44.5	184	0.25
7	1.36	42.3	7.9	50.2	109.9	45.6	185	0.25
8	1.55	42.3	9.1	51.4	112.4	46.6	187	0.25
9	1.74	42.3	10.2	52.5	114.9	47.6	188	0.26
10	1.94	42.3	11.3	53.6	117.3	48.6	189	0.26
11	2.13	42.3	12.5	54.8	119.8	49.7	191	0.26

From Collier and Thome (1994), the Nusselt laminar film theory can be used to calculate the local film thickness, δ_{loc} , and velocity, u, of the film at the interface ($y = \delta_{loc}$) using the following equations:

$$\delta_{loc} = \left[\frac{3\Gamma\mu_f}{\rho_f(\rho_f - \rho_g)g} \right]^{1/3} \quad \text{Equation 12-1}$$

$$u = \frac{\delta_{loc}^2 (\rho_f - \rho_g) g}{2 \mu_f} \quad \text{Equation 12-2}$$

The local film thickness and film interface velocity at each station are shown in Table G-2. The measured average wall temperature of 37.8°C is used to calculate the liquid viscosity, thermal conductivity and density.

Comparing the results of Table G-2 and Table G-1, the measured wave velocity is approximately 100% greater than calculated interface velocity assuming laminar, wave-less film flow. This observation provides some insights into the physical mechanisms that promote enhanced heat and mass transfer due to surface waves.